Simulation numérique directe des vagues déferlantes en eaux peu profondes en interaction avec les nappes de pétrole

Shuo Liu

HESAM UNIVERSITÉ

Arts et Métiers Sciences et Technologies

ÉCOLE DOCTORALE SCIENCES ET MÉTIERS DE L'INGÉNIEUR
[Laboratoire de Mécanique des Fluides de Lille - Campus de Lille]

THÈSE

présentée par : **Shuo Liu**
soutenue le : **4 Décembre 2023**

pour obtenir le grade de : **Docteur d'HESAM Université**

préparée à : **École Nationale Supérieure d'Arts et Métiers**

Spécialité : **Mécanique des Fluides**

Direct Numerical Simulation of Shallow-water Breaking Waves Interacted with Oil Slicks

THÈSE DIRIGÉE PAR :
[Mme Annie-Claude Bayeul-Lainé]

ET CO-DIRIGÉE PAR :
[M. Olivier Coutier-Delgosha]

Jury

M. Daniel Fuster	Directeur de recherche, Institut D'Alembert, CNRS / Sorbonne Université	Président
M. Wouter Mostert	Professeur, University of Oxford	Rapporteur
M. Joseph Katz	Professeur, Johns Hopkins University	Examinateur
M. Frédéric Dias	Professeur, University College Dublin / ENS-PARIS-SACLAY	Examinateur
M. Luc Deike	Professeur, Princeton University	Examinateur
Mme Annie-Claude Bayeul-Lainé	Maitre de Conférences HdR, Arts et Métiers ParisTech	Examinatrice
M. Olivier Coutier-Delgosha	Professeur, Arts et Métiers ParisTech / Virginia Tech	Examinateur

THÈSE

"We should consider every day lost on which we have not danced at least once."

– Friedrich Nietzsche

Anknowledgements

I express my sincere gratitude to my esteemed supervisors, Professor Annie-Claude Bayeul-Lainé and Professor Olivier Coutier-Delgosha, for their guidance and support throughout my doctoral journey. My thesis would not have been possible without their patience and encouragement. Professor Annie-Claude Bayeul-Lainé has been an outstanding mentor who continually supports me with her kindness and commitment to my academic growth. I am also deeply grateful to Professor Olivier Coutier-Delgosha for his generosity in providing me with sufficient computational resources, which proved to be indispensable in advancing my research project. His encouragement and belief in my abilities were a constant source of motivation during my moments of frustration and self-doubt. Over the past four years, I have gained valuable insights from them and I believe their influence will continue to shape my lifelong journey.

I sincerely thank all members of the thesis committee for their willingness to review my work and participate in my defense. I thank Daniel Fuster for agreeing to chair the committee and Wouter Mostert for serving as the rapporteur. I thank Joseph Katz, Frédéric Dias and Luc Deike for their valuable time and constructive comments, which greatly enhanced the quality of this thesis.

I am very grateful to the entire LMFL laboratory members for their friendship, support and companionship throughout this challenging yet rewarding research journey. Special thanks go to Professor Jean-Philippe Laval, Antoine Dazin and Francesco Romano for their helpful comments and support. I thank Hui Wang and Meng Fan for their engaging discussions and assistance in numerical realizations and result analysis. Thanks to Bo Wang, Hossameldin Abdelaziz, Miguel Martinez Valero, and Renjie Hao for their support throughout this journey.

Finally, I would like to thank Weiyu Zheng for her support and encouragement throughout my doctoral studies. Your presence and companionship means so much to me at this crucial stage of my life. I would also like to thank my parents for their unwavering support and encouragement. Your faith in me has always been a source of strength for me.

Résumé

Le pétrole déversé en mer forme des nappes de pétrole, qui sont ensuite entraînées dans l'eau et brisées en gouttelettes allant du submicronique à plusieurs millimètres par les vagues déferlantes. Ces phénomènes affectent de manière significative le devenir du film de pétrole, notamment son transfert de masse, son échange d'énergie et sa distribution de particules. Par conséquent, l'étude des caractéristiques des gouttelettes de pétrole résultantes est cruciale pour comprendre le processus de dispersion du pétrole et son interaction avec les vagues déferlantes en eaux peu profondes. Nous utilisons des simulations numériques directes (DNS) pour étudier l'évolution des vagues déferlantes et leur impact sur les nappes de pétrole en reproduisant les ondes expérimentales générées par une plaque ondulée de type piston. Tout d'abord, nous avons effectué une DNS bidimensionnelle des vagues déferlantes à l'aide du solveur Basilisk pour acquérir une compréhension détaillée du processus de déferlement des vagues, y compris l'évolution de la surface libre, de la vitesse et des champs de tourbillon. Nous avons constaté que la tension superficielle a un effet significatif sur le processus de renversement de la crête, en épaississant la largeur du jet plongeant et en raccourcissant la distance qui se projette vers l'avant de la vague. Nous avons également appliqué l'échelle de dissipation conventionnelle de la théorie de la turbulence au processus de déferlement des vagues, établissant un lien entre le taux de dissipation d'énergie et le rapport entre la crête de la vague déferlante et la profondeur de l'eau. Nous avons ensuite étendu le DNS bidimensionnel des ondes déferlantes à un cadre tridimensionnel pour tenir compte des effets tridimensionnels sur le processus de déferlement des vagues et pour évaluer les effets de la viscosité (représentée par le nombre de Reynolds, Re) et de la tension superficielle (représentée par Nombre de liaisons, Bo) sur les caractéristiques et la distribution de taille des bulles générées par le déferlement des vagues. Un Bo plus élevé conduit à un plus grand nombre de bulles, la différence étant plus prononcée dans la gamme des bulles plus petites. La vitesse verticale varie avec le rayon de la bulle, montrant des vitesses de montée variables selon les rayons des bulles sous l'effet de la flottabilité, les bulles plus grosses s'élevant plus rapidement vers la surface libre. Pendant la phase de rupture active, la profondeur du panache de bulles reste constante, cohérente avec la hauteur initiale de

la cavité principale. Enfin, nous avons étendu le DNS bidimensionnel des ondes déferlantes à des simulations triphasées en présence de nappes de pétrole à la surface de l'eau. Grâce à une étude paramétrique, nous avons analysé la dépendance quantitative de la taille caractéristique des gouttelettes d'huile sur l'intensité des vagues et la tension interfaciale. Nous avons identifié une forte dépendance du diamètre caractéristique des gouttelettes sur le taux de dissipation d'énergie maximal et la tension interfaciale, ce qui est cohérent avec les prédictions théoriques de mise à l'échelle. Cette recherche ouvre la voie à l'étude de la relation entre le déferlement des vagues et le comportement des nappes d'hydrocarbures lors des déversements d'hydrocarbures en mer grâce à des simulations numériques, contribuant ainsi à une compréhension plus approfondie des mécanismes régissant la dispersion et la propagation du pétrole en surface.

Mots-clés : Vagues déferlantes, Entraînement d'air, Simulation numérique directe, Taux de dissipation d'énergie, Distribution en tailles des bulles, Dispersion d'huile

Abstract

Oil spilled at sea forms oil slicks, which are subsequently entrained into the water and broken up into droplets ranging from submicron to several millimeters by breaking waves. These phenomena significantly affect the fate of the oil film, including its mass transfer, energy exchange, and particle distribution. Therefore, investigating the characteristics of the resulting oil droplets is crucial for understanding the oil dispersion process and its interaction with shallow-water breaking waves. We employ direct numerical simulations (DNS) to investigate the evolution of breaking waves and their impact on oil slicks by reproducing experimental waves generated by a piston-type wave plate. First, we performed two-dimensional DNS of breaking waves using the Basilisk solver to gain a detailed understanding of the wave-breaking process, including the evolution of the free surface, velocity, and vorticity fields. We found that surface tension has a significant effect on the crest overturning process, thickening the width of the plunging jet and shortening the distance that projects forward ahead of the wave. We also applied the conventional dissipation scaling of turbulence theory to the wave-breaking process, establishing a link between the energy dissipation rate and the ratio of the breaking wave crest to water depth. We then extended the two-dimensional breaking waves DNS to a three-dimensional framework to account for three-dimensional effects on the wave-breaking process and to evaluate the effects of viscosity (represented by Reynolds number, Re) and surface tension (represented by Bond number, Bo) on the characteristics and size distribution of bubbles generated by wave breaking. A higher Bo leads to a greater number of bubbles, with the difference being more pronounced in the range of smaller bubbles. The vertical velocity varies with the bubble radius, showing varying rise velocities at different bubble radii under the effect of buoyancy, with larger bubbles rising to the free surface at a faster rate. During the active breaking phase, the depth of the bubble plume remains constant, consistent with the initial height of the main cavity. Finally, we extended the two-dimensional DNS of breaking waves to three-phase simulations in the presence of oil slicks on the water surface. Through a parametric study, we analyzed the quantitative dependence of the characteristic oil droplet size on the wave intensity and interfacial tension. We identified a strong dependence of the characteristic droplet diameter on the

maximum energy dissipation rate and interfacial tension, consistent with theoretical scaling predictions. This research paves the way for investigating the relationship between wave breaking and oil slick behavior in marine oil spills through numerical simulations, contributing to a deeper understanding of the mechanisms governing oil dispersion and surface spreading.

Keywords : Breaking waves, Air entrainment, Direct numerical simulation, Energy dissipation rate, Bubble size distribution, Oil dispersion

Contents

List of Tables

List of Figures

Chapter 1

Introduction

Contents

1.1 Overview

Accidental oil spills from offshore oil production and transportation pose a significant threat to marine ecosystems, causing a wide range of adverse consequences. Oil dispersion by breaking waves is a process that occurs when oil spilled at sea forms thin slicks, which are subsequently fragmented into droplets of various sizes. These droplets are subjected to turbulent forces and vortices generated by breaking waves (Delvigne & Sweeney, 1988). Breaking waves play an important role in the air-sea interaction, such as the transfer of mass, momentum, and heat between the atmosphere and the ocean. Wave breaking improves the transfer of energy from the surface wave field to currents and turbulence, especially in the upper layers of the water column (Melville, 1996). When a wave breaks, it initiates wave overturning and air entrainment, thereby constituting a source of turbulent energy capable of mixing the upper ocean layers. This phenomenon results in the formation of bubbles and droplets, which enhances air-sea exchange between gases and particulate matter, such as spilled oil (Cokelet, 1977).

In the context of breaking waves, scaling arguments suggest a proportional relationship between energy dissipation and wave characteristics. The wave dissipation per unit length of the breaking crest, denoted as ϵ_l, is expected to be related to the expression $b\rho_w c^5/g$ in deep-water breaking waves, as documented in previous studies (Duncan, 1981, 1983). Here, ρ_w is the density of water, g is the acceleration due to gravity, and c is the phase speed of the breaking wave. The breaking parameter b, which quantifies the extent of energy dissipation during the wave-breaking process, has been demonstrated to correlate with wave slope and spectral bandwidth through various laboratory experiments (Kendall Melville, 1994; Deane & Stokes, 2002; Melville & Matusov, 2002). This relationship is characterized as $(hk)^{5/2}$ using an inertial scaling model proposed by Drazen *et al.* (2008), where hk is a local breaking slope parameter. In contrast to the conditions in deep water, wave breaking in shallow water environments (e.g., nearshore zone) requires distinct considerations for relating inertial energy dissipation to wave characteristics. Mostert & Deike (2020) has extended the inertial scaling to shallow-water breaking solitary waves, revealing a dependence of energy dissipation on local amplitude and water depth. This indicates that the wave dissipation per unit length of breaking crest ϵ_l should exhibit proportionality with $\rho g^{3/2} {h_b}^{7/2}/d_b$, where h_b is the wave amplitude at breaking, and d_b is the undisturbed depth at breaking.

To gain insight into the transport of dispersed oil by oceanic waves and turbulent flows, Li (2017) conducted experimental measurements in a wave flume to investigate the temporal evolution of subsurface oil droplet size distributions induced by a single breaking wave. They also aimed to establish correlations between oil droplet

size distributions and various parameters, such as interfacial tension, oil viscosity, density, and wave-breaking characteristics. Numerical simulations can play a crucial role in obtaining accurate hydrodynamic information related to breaking waves and assessing the influence of natural dispersion on the spreading of oil slicks formed in the water column. However, existing models for oil spill scenarios lack the capability to directly resolve the dispersion of oil droplets resulting from breaking waves. Given the significant advancements in numerical algorithms and computational resources, it is now imperative to depict oil dispersion processes through direct numerical simulations for enhanced accuracy in predicting the fate of spilled oil. Consequently, it is essential to achieve a comprehensive understanding of the effect of breaking waves on the breakup of oil slicks and the associated droplet size distribution. The droplet size distribution serves as the bridge connecting small-scale processes (such as droplet rise rate, dissolution, and biodegradation) and large-scale processes governing oil transport. As an initial step in the investigation of surface oil spills at sea, this study delves into the mechanisms of natural dispersion under the influence of breaking waves. Our primary focus is to simulate the processes of oil dispersion subject to breaking waves, with a particular emphasis on the transport and fate of spilled oil. It is important to note that in this study, we assume that oil dispersion is primarily governed by the horizontal spreading of the surface slick due to gravity, inertia, viscous, and surface tension forces, without considering chemical and biological processes.

1.2 Objectives

We perform direct numerical simulations of two-phase wave-breaking and three-phase oil dispersion to investigate the evolution of experimental waves generated by a wave plate and their impact on the oil droplet breakup. Direct numerical simulation of breaking waves has become a viable option in recent years, providing valuable insights into breaking onset predictions, energy dissipation, and the generation of bubbles and droplets.

In the context of breaking waves, we solve the incompressible variable-density Navier-Stokes equations with second-order spatial and temporal accuracy using the Basilisk solver. We track the air–water interface using a volume of fluid (VOF) scheme. Surface tension is treated with the balanced-force technique. To improve accuracy and efficiency in surface-tension-driven flows, we implement a generalized height-function (HF) curvature estimation method that addresses inconsistencies at low interface resolution. Additionally, we employ an adaptive mesh refinement scheme to concentrate computational resources on critical solution regions, thereby improving computational efficiency. To investigate the relationship between crest geometry and energy dissipation rate in breaking waves, we conduct an extensive parametric study of two-dimensional breakers as

computational analogues for three-dimensional processes. This is necessary because the extensive parametric study based on 3-D simulations is currently not feasible due to computational resource limitations. We propose a dimensional analysis for 2-D waves generated by a wave plate to facilitate this analysis. We numerically reproduce a piston-type wave plate to initiate a single breaking event at the desired location with the desired energy by specifying the stroke and frequency of the wave plate. We analyze wave characteristics at different breaking intensities during wave breaking and investigate the scaling of wave dynamics and kinematics to initial conditions using inertial-scaling arguments. Since directly investigating the bubble distribution is obviously not available within a two-dimensional study, it is essential to perform three-dimensional simulations of breaking waves. By varying the Reynolds number Re and Bond number Bo, we explore the effects of viscosity and surface tension on the bubble size distribution and identify possible connections between the energy dissipation rate and the size distribution of bubbles and droplets.

To study the interaction of an oil slick with breaking waves, we conduct a direct numerical simulation based on accurate modeling of breaking waves and the resulting turbulence regions. To obtain accurate dynamical information, we employ the VOF function and adaptive mesh techniques within the Basilisk solver to model the three-phase free surface evolution. We conduct 2-D oil dispersion simulations as a proxy for full 3-D processes to facilitate an extensive parametric analysis. This allows us to explore the potential impacts of wave intensities and interfacial tensions on the characteristic oil droplet sizes. Our numerical investigation of oil dispersion by breaking waves encompasses five sets of breaking-wave intensities and five different interfacial tensions. By simulating the horizontal movement of the surface oil slick, tracking the vertical distribution of oil particles, quantifying their concentration in the water column, and assessing the mass balance of spilled oil, we unveil the dependence of droplet characteristics on both the breaking-wave intensities and interfacial tensions.

1.3 Outline

This dissertation comprises seven chapters.

Following the introduction chapter, Chapter 2 provides essential background information on the current study and a comprehensive review on the topics of breaking waves and oil dispersion. Chapter 3 details the numerical scheme employed for direct numerical simulations, including the methodology used for tracking the free surface and treating surface tension in both two-phase and three-phase scenarios, and the approach employed to identify the energy budget, bubbles, and droplets. Chapter 4 presents the findings of 2-D breaking

wave simulations, beginning with a discussion of the characteristics of wave breaking, including the wave-breaking process and energy budget analysis. A parametric study is then conducted to assess the influence of the initial condition and Bond number on critical aspects such as the main cavity, breaking onset prediction, and energy dissipation due to breaking. Chapter 5 reports the numerical data obtained from 3-D breaking wave simulations. It begins by presenting general information about bubbles and droplets, facilitating an analysis of their formation and spatiotemporal evolution, as well as the associated size distribution. Subsequently, various bubble plumes generated at distinct wave-breaking stages are analysed separately, with the aim of investigating the bubble-breakup mechanisms. Chapter 6 presents the results of 2-D oil dispersion simulations. A parametric study is conducted to explore the effects of wave strength and interfacial tension on particle statistics. Chapter 7 brings the dissertation to a close with concluding remarks of key findings and perspectives.

Chapter 2

Background and literature review

Contents

2.1 Breaking waves

As a strongly nonlinear intermittent process occurring across a wide range of scales, wave breaking plays an important role in air–sea interactions by limiting the height of surface waves and enhancing the transfer of mass, momentum and heat between the atmosphere and the ocean (Melville, 1996; Perlin *et al.*, 2013). During wave breaking, notable alterations occur at the free surface, involving the entrainment of air into the ocean, ejection of spray into the atmosphere, production of bubbles and aerosols (Kiger & Duncan, 2012; Veron, 2015), and the generation of local turbulence near the free surface. Wave breaking also exerts a critical influence on various aspects of the upper ocean, such as the dispersion of oil spills and contaminants, the determination of the particle size distribution and dynamic transport, and the overall health of marine ecosystems (Delvigne & Sweeney, 1988; Deike *et al.*, 2017; Li *et al.*, 2017). The most visible manifestation of wave breaking is the initial overturning action of the wave crest, which forms spray and whitecaps and is typically accompanied by the forward projection of a jet of water. The processes associated with breaking waves have been extensively studied, with significant progress made in understanding their geometry, breaking onset criteria, energy dissipation due to breaking and air entrainment (Perlin *et al.*, 2013; Deike, 2022).

2.1.1 Energy dissipation due to breaking

Particularly, the energy transfers involved in waves have been studied extensively over the years, and the parameterization of the dissipation rate due to breaking has benefited greatly from laboratory experiments and numerical measurements. The parameterization derived from fundamental experimental studies by Duncan (1981) has indicated that the work done by the whitecap or energy dissipation rate per unit length of wave crest scales to the fifth power of a characteristic speed

$$\epsilon_l = b\rho c^5/g \tag{2.1}$$

Here, b is a dimensionless coefficient related to the wave-breaking strength, ρ is the density of the fluid, c is a characteristic speed associated with the breaking wave and g is the acceleration due to gravity. The breaking parameter b was first assumed to be a non-dimensional constant but subsequently shown by extensive experimental investigations to vary over several orders of magnitude when varying the breaking wave slope S (Rapp & Melville, 1990; Tian *et al.*, 2010). To establish possible relationships between the breaking parameter b and the initial conditions of breaking waves, the conventional dissipation scaling of turbulence theory has been applied to the wave-breaking process (Duncan, 1981; Drazen *et al.*, 2008; Mostert & Deike, 2020), following

the form of the turbulent dissipation rate based on dimensional analysis (Batchelor, 1953). The local turbulent energy dissipation rate during wave breaking can be estimated as $\epsilon = \chi(w^3/l)$, where χ is a proportionality constant, w is the representative velocity scale and l is the turbulent integral length scale characterizing the energy-containing turbulent eddies (Taylor, 1935; Vassilicos, 2015). Therefore, the energy dissipation rate per unit length of the crest is $\epsilon_l = \rho A \epsilon$ by assuming a turbulent cloud of cross-section A. Drazen *et al.* (2008) relates the local turbulent energy dissipation rate to the local breaking properties by inertial scaling, i.e., $\epsilon = \sqrt{gh}^3/h$, where h is the breaking height and $\sqrt{gh}$ is the ballistic velocity of the toe of the plunging breaker. The turbulence cloud is assumed to be a circle with a cross-section of $A = \pi h^2/4$. This indicates that the dissipation rate per unit length of breaking crest

$$\epsilon_l = \rho A \epsilon \propto \rho g^{3/2} h^{5/2} \propto (hk)^{5/2} \rho c^5/g \tag{2.2}$$

where k is the wavenumber, and $c = \sqrt{g/k}$ by the dispersion relation in deep water. This leads to $b \propto S^{5/2}$, with $S = hk$ being the breaking wave slope. Moreover, the threshold behavior of the energy dissipation associated with wave breaking has been identified through laboratory measurements, revealing that b must tend to zero for sufficiently small slopes (Rapp & Melville, 1990; Drazen *et al.*, 2008; Tian *et al.*, 2010; Grare *et al.*, 2013). To characterize this behavior, Romero *et al.* (2012) proposed a semi-empirical scaling by introducing a characteristic slope threshold

$$b = a(S - S_0)^{5/2} \tag{2.3}$$

with a constant $a = 0.4$ and a critical slope $S_0 = 0.08$ being determined based on the fit to the laboratory data. Subsequent numerical simulations have consistently validated this scaling relationship (Iafrati, 2009; Deike *et al.*, 2016; De Vita *et al.*, 2018). In addition to deep water breaking waves, the energy dissipated by breaking solitary waves on a beach slope has also been quantified by Mostert & Deike (2020). The representative velocity scale is considered to be the impact velocity, which is calculated ballistically as $w = \sqrt{2gH_b}$, where H_b is the wave amplitude at breaking. The turbulent integral length scale is estimated to be the undisturbed depth at breaking d_b, and the cross-section of the turbulence cloud is assumed to be $A = \pi {H_b}^2/4$. Consequently, the dissipation rate per unit length of a breaking crest is given by

$$\epsilon_l = \rho A \epsilon \propto \rho g^{3/2} {H_b}^{7/2}/d_b \propto (H_b/d_0)^{7/2} (d_b/d_0)^{-1} \rho c^5/g \tag{2.4}$$

where d_0 is the undisturbed depth prior to the beach slope, and $c = \sqrt{gd_0}$ is derived from the dispersion relation in shallow water. These efforts have led to a connection between the dynamics and kinematics of breaking waves, and a parameterization of the dynamics has been developed based on geometric properties.

While great progress has been made in previous studies of energy dissipation due to breaking, certain limitations persist, necessitating further research to attain a global understanding of breaking waves. First, the majority of research efforts have focused on the study of breaking waves in deep water. However, breaking waves in shallow and intermediate water depths undergo more pronounced changes in the free surface compared with deepwater breakers, which introduces additional complexities to the problem. Currently, there is a scarcity of studies addressing shallow water breaking, particularly in cases where breaking is solely attributed to nonlinearity in a tank with a level bottom. Although the direct numerical simulation (DNS) approach, which resolves all breaking processes in waves, has been successfully employed in deep-water studies (Iafrati, 2011; Deike *et al.*, 2016) and shallow-water breakers on a slope (Mostert & Deike, 2020), previous investigations have been constrained by limited computational resources, thus restricting the range of wave scales to smaller Reynolds and Bond numbers. Nonetheless, it is essential to consider shallow-water experimental waves encompassing a wide range of length scales, ranging from wave breaking at the meter scale to micron-scale air bubble entrainment. This research aims to comprehensively characterize experimental breaking waves and explore the dispersion of oil spills influenced by breaking waves. The experimental breaking waves, resembling solitary waves, provide a suitable platform for analyzing breaking characteristics in shallow water environments. Their higher energy levels render them instrumental in validating and expanding existing wave-breaking theories, including wave-breaking criteria, breaking dissipation scaling laws, and air entrainment mechanisms.

2.1.2 Bubble size distribution

The formation and interaction of the air bubbles in the upper ocean mixed layer provide vertical and horizontal distributions of bubbles. The measurement and interpretation of the sizes of air bubbles in the upper ocean are important for the evaluation of gas transports between the atmosphere and the ocean (Melville, 1996; Garrett *et al.*, 2000). Breaking waves form bubbles and create an ensemble of bubbles below the surface (Deane, 1997). The bubble cloud shapes are detectable using various sonar techniques and serve to label the surface layer turbulence, play a role in the exchange of gases between the atmosphere and the ocean, and influence the ambient noise spectrum (Banner & Peregrine, 1993). The goal of the air entrainment investigation was to characterize the size and spatial distribution of bubble plumes and clouds after the passage of a breaking wave. A complete solution to the bubble formation proposed by Garrett *et al.* (2000) has illustrated the connection between the size spectrum and the turbulent energy dissipation rate. Garrett *et al.* (2000) assumed that the air injected by breaking waves at a scale much larger than the Hinze scale is broken up by the turbulent pressure

fluctuations, and proposed a power law of $r^{-10/3}$ for the size spectrum of these larger bubbles, by considering the level of turbulence and the average rate of supply of air with a dimensional cascade argument. The experimental measurements conducted by Deane & Stokes (2002) have provided a quantitative description of bubble formation mechanisms, revealing a bubble density proportional to $r^{-10/3}$ for larger bubbles determined by turbulent fragmentation, and a $-3/2$ power law scaling for smaller bubbles created by jet and drop impact on the wave face. Experimental measurements by Blenkinsopp & Chaplin (2007) described the evolution of the bubble cloud generated beneath the free surface and the splashes above, by analyzing the time-varying distribution of void fraction in breaking waves. They revealed similar characteristics of the bubble plumes and splashes across different types of breakers. Numerical findings reported by Rivière *et al.* (2021) revealed a clear sup-Hinze bubble size distribution power-law $\mathcal{N}(r) \propto d^{-10/3}$ and sub-Hinze bubble size distribution power-law $\mathcal{N}(r) \propto d^{-3/2}$, consistent with the theoretical model and numerical simulations. Based on these favorable results, Rivière *et al.* (2021) proposed an alternative mechanism for the production of sub-Hinze bubbles. In contrast to the self-similar cascade of break-ups identified in super-Hinze bubbles by Garrett *et al.* (2000), they argued that the scaling law governing sub-Hinze bubbles is derived from capillary-driven bubble splitting events occurring within elongated filaments, which result in the creation of at least one sub-Hinze bubble during the bubble fragmentation process.

While the initiation of the breaking phenomenon and the turbulence generated by it have been characterized (Rapp & Melville, 1990; Melville & Matusov, 2002; Banner & Peirson, 2007; Drazen *et al.*, 2008; Drazen & Melville, 2009), the time and length scales of the transition process remain to be explored. The measurement of 3-D two-phase turbulence in the laboratory and in the field presents many technical challenges in terms of accessing successfully the turbulent flow field and the size distributions of drops and bubbles during the active time of breaking (Mostert *et al.*, 2022). Energetically, it remains to determine the particular transition characteristics of the fully 3-D flow, and to investigate the dependence of these characteristics on the flow Reynolds number, as well as on the evolution of the ingested bubble plume. Furthermore, the details of the 2-D/3-D transition physics in breaking waves constitute an open question.

2.2 Oil Dispersion

Accidental oil spills during offshore oil production and transportation can have a wide range of negative impacts on the marine environment, posing a serious threat to ecosystems. Oil spills can also contaminate water, releasing harmful chemicals into the air, which can have a devastating effect on animals and plants in

the affected area. To address the potential hazards of oil spills, considerable research has been conducted to understand and quantify the oil spill processes in order to predict the trajectory and fate of spilled oil (Guo & Wang, 2009). The transport and fate of spilled oil in water are dominated by a variety of physical, chemical, and biological processes. The most common oil weathering processes that occur in the early stages of an oil spill are spreading, advection, diffusion, evaporation, emulsification, dissolution, and dispersion. In the longer term, photo-oxidation, biodegradation, and sedimentation emerge as pivotal mechanisms that govern the ultimate trajectory of the spilled oil (Keramea *et al.*, 2021). As the main source of power after an oil spill accident, ocean dynamics processes mainly affect oil slicks in terms of spreading and dispersion under the combined effects of wind, waves, and currents. Spreading is the horizontal expansion of an oil slick due to mechanical forces such as gravity, inertia, viscous, and interfacial tension, and turbulent diffusion. When crude oil is spilled onto the sea surface, it spreads to form an oil slick, and the movement of the oil slick is governed by advection and turbulent diffusion due to current and wind action (Guo & Wang, 2009). Advection of surface oil is caused by the forces of surface current and wind drag on oil, while advection of suspended oil refers to the movement of oil droplets entrained in the water column due to the water current. Dispersion occurs when waves or turbulent events break over the oil slick, producing droplets of various sizes into the water column (Fingas, 2014). The natural dispersion of oil spilled at sea is a key process in determining the expected lifetime on the sea surface of a specific crude oil or petroleum product under specific environmental conditions. Calculating the residence time of oil on the sea surface is a key issue in evaluating alternative oil spill response strategies, determining the probability of impacting coastlines, and estimating potential effects on sea birds and marine mammals in the path of the slick (Reed *et al.*, 2009). In sea states characterized by frequent wave breaking, it is widely acknowledged that breaking waves are the primary driving mechanism for the natural dispersion of an oil slick (Naess, 1982). Therefore, it is highly desirable to study the breakup and mixing into the water of a surface oil slick by breaking waves.

2.2.1 Oil dispersion by breaking waves

Oil dispersion by breaking waves is a process that occurs when oil spilled at sea forms thin slicks, which are then broken up into droplets of various sizes by the turbulent forces and vortices generated by breaking waves (Delvigne & Sweeney, 1988). The droplets then penetrate into the water column, causing a mixing of oil into the water column. During this process, smaller droplet sizes are linked to higher energy levels, lower viscosity, and lower interfacial tension. A high energy input at this stage, such as a passing storm, may disperse

the entire slick into the water column, leaving only very thin oil sheens visible after the storm has passed. With the development of breaking waves, the upper layer of the water column becomes well mixed, extending to a depth of approximately wave height at breaking. Smaller droplets are more easily dispersed and diffused into the water column by subsurface currents and turbulent mixing force, while larger droplets tend to resurface and reform slicks (Delvigne & Sweeney, 1988). The initial break-up and submergence of a coherent oil surface slick, as well as the secondary break-up of the oil parcels into smaller droplets, depend on the turbulence structure near the water surface. Turbulence also plays a significant role in the vertical diffusion of oil droplets into the water column. Turbulence can be described in terms of eddies of different sizes. The energy of large eddies is transferred via smaller eddies to the smallest size class where the energy is dissipated ultimately into heat under the influence of viscosity. The large velocity gradients of the small eddies are important for the breakup of oil droplets and for the collision probability of droplets, whereas the large eddies are primarily responsible for the dispersive transport of the oil droplets. The break-up of coherent surface oil layers into droplets and the intrusion of the droplets into the water column due to breaking waves is a complex of mechanisms in which probably all eddy size classes in the breaking waves play important roles. Many studies have been conducted to examine the possible mechanisms for the generation of oil droplets (Hinze, 1955; Delvigne & Sweeney, 1988; Li & Garrett, 1998; Li *et al.*, 2008; Afshar-Mohajer *et al.*, 2018). The purpose of studying oil dispersion induced by breaking waves is to provide an oil spill model that incorporates equations and empirical data on the effects of breaking waves and turbulence on oil droplet size, vertical dispersion rate, and the resulting oil concentration profile. Hinze (1955) assumed that the dynamic pressure force of turbulent flows is the cause of droplet breakup, and obtained a formula for the maximum size of oil droplets that can survive the pressure force using dimensional analysis

$$d_{max} = c(\gamma/\rho)^{3/5}\epsilon^{-2/5} \tag{2.5}$$

where c is an empirical constant. However, Li & Garrett (1998) argued that the formula obtained by Hinze (1955) is only valid for large droplet Reynolds numbers, when droplet Reynolds numbers are small, viscous shear associated with small turbulent eddies is the cause of the breakup. Laboratory investigations performed by Delvigne & Sweeney (1988) on the natural dispersion of surface oil found a dependence of the droplet size on oil viscosity and mean energy dissipation rate. They hypothesized that small eddies in turbulent flows are responsible for oil droplets splitting. Mukherjee *et al.* (2012) investigated the droplet formation mechanisms by dimensionless and force balance analysis. They identified four distinct regimes of droplet formations: for $d > \eta$, d scales either with $\varepsilon^{-2/5}$ or $\varepsilon^{-1/4}$ and for $d < \eta$, d scales either with $\varepsilon^{-1/2}$ or $\varepsilon^{-1/4}$ depending on

whether the main restoring force against droplet breakage is provided by surface tension or oil viscosity. For $d > \eta$ and $d < \eta$, the external force, which tries to deform and break the droplet is provided by the pressure difference across the droplet diameter and viscous shear, respectively.

2.2.2 Oil droplet size distribution

Wave breaking is the primary mechanism by which oil spills enter the water in the form of droplets, and the generation and distribution of these oil droplets are important but still not thoroughly understood topics in this field. The droplet size distribution of dispersed oil is of particular interest for elucidating of the reduction and horizontal diffusion of the surface oil, the uptake of oil by marine life, and the adsorption of oil by suspended particulate matter and its subsequent sedimentation onto the sea floor. In the experiments of the small-scale oil flume for studying the effect of breaking waves on a surface oil film by (Delvigne & Sweeney, 1988), oil was poured onto the water surface in the test section of the flume, which resulted in an oil film with a thickness of 0.5 mm. The droplet size distributions were obtained with a series of oil droplet samplers, which consist of a small glass cylinder with a flat top. The sampled oil droplets rose to the top of the glass cylinder after a standing time of 20 h, and photographs were taken of the top glass to enable the oil droplets to be counted. These experimental data indicate a droplet size distribution, which follows the relationship

$$N_u(d_o) \propto d_o^{-2.30(\pm 0.06)} \tag{2.6}$$

independent of oil type, weathering state, oil layer thickness, and temperature. In this relationship, d_o is the diameter of oil droplets, and $N_u(d_o)$ is the number of droplets in a unit size interval Δd around d_o. The droplet size distribution depends on factors such as water-oil interfacial tension, oil viscosity, wave type and intensity. Oil dispersion by breaking waves and the resulting droplet size distribution is important for evaluating the environmental impact of oil spills and designing effective countermeasures such as dispersants. The application of dispersants has become an important measure for responding to oil spills. By reducing the surface tension between oil and water, dispersants can help break up the oil into smaller droplets, which can then be more easily dispersed by the action of waves and currents. Additionally, the use of dispersants can also delay the formation of high-viscosity oil-water emulsions that are difficult to decompose and can cause serious harm. Therefore, understanding the role of surface tension in oil droplet generation and distribution is critical for developing effective oil spill response strategies. Oil dispersion by breaking waves can be measured experimentally using techniques such as particle image velocimetry (PIV), laser-induced fluorescence (LIF), and high-speed imaging to obtain the velocity fields, droplet size distributions, and surface profiles of breaking waves. Peishi *et al.*

(2011) study mathematical simulation on the oil slick spreading and dispersion in nonuniform flow fields. Oil dispersion by breaking waves can be modeled using computational fluid dynamics (CFD) methods that couple Reynold-averaged Navier-Stokes (RANS) equations with volume of fluid (VOF) methods to capture the transient water-air interface and the turbulent kinetic energy field. A numerical model including spreading and dispersion was developed to describe the early movement of the oil slick in the open and ice-covered water. A two-phase Smoothed Particle Hydrodynamics (SPH) model has been developed on the basis of GPUSPH, which is an open-source implementation of the weakly compressible SPH method on graphics processing units, to investigate oil dispersion under breaking waves (Wei *et al.*, 2017). Carratelli *et al.* (2011) provided an indication of the effects of wave-induced movement of 10 oil on the sea surface in connection with the Deepwater Horizon oil spill. To estimate the combined effects of oil transport and oil weathering, seasonal drift patterns are analysed and alternative fairway designs are derived using a Monte Carlo technique (Murawski & Woge Nielsen, 2013). Zhang *et al.* (2021) present the simulation results of both models in a limited scale (a sub-area of the Gulf of Mexico) under the same oil spill condition using real ocean current data from the Unified Wave Interface-Coupled Model (UWIN-CM). Muin *et al.* (2022) present a further study of the effect of non-linear waves on the dispersion of oil in the Bay. In order to explore the influence of offshore wave breaking on the formation and transportation of oil-related hazardous material (OHM), the wave breaking process was simulated in a 2-D laboratory flume, and the behavior process of OHM was identified and tracked (Fang *et al.*, 2022).

However, a drawback of traditional Eulerian methods is that they do not directly resolve dispersion phenomena in a physical point resulting in numerical diffusion. For computational purposes, oil spill models divide the slick into Lagrangian elements or particles and track their movement, which does not directly provide an oil concentration or thickness at specific locations. Elliott *et al.* (1986) applied the random walk particle tracking (RWPT) for the description of oil droplet movement in the water column. A hybrid numerical oil spill model coupled with particle tracking and the Eulerian-Lagrangian approach was developed by Guo & Wang (2009). The initial oil patch is modeled by the release of particles and the oil processes are tracked based on a critical value of the oil slick thickness or the oil concentration with the capability to predict the horizontal and vertical distribution, the concentration in the water column, and the mass balance of spilled oil.

Chapter 3

Methodology

Contents

3.1 Numerical scheme

3.1.1 Basilisk Solver

The Navier-Stokes equations for incompressible multiphase flow with variable density and surface tension are simulated using the Basilisk library. The Basilisk package, developed as the successor to the Gerris framework (Popinet, 2003, 2009), is an open-source program for solving various systems of partial differential equations on regular adaptive Cartesian meshes with second-order spatial and temporal accuracy. A quadtree-based / octree-based adaptive mesh refinement (AMR) scheme is used in 2-D / 3-D calculations to improve computational efficiency by concentrating computational resources on important solution domains. The method identifies and finely resolves only the active portions of the simulated flow while using coarser local resolutions for roughly quiescent regions. In particular, the AMR approach more easily allows direct resolution of small-scale turbulence in water without the need for a turbulence model (Boswell *et al.*, 2023). The refinement criterion is determined through a wavelet algorithm, which estimates the discretization error in the velocity and VOF fields. The generic time loop is implemented in the numerical scheme and the time step is limited by the Courant–Friedrichs–Lewy (CFL) condition. The flow is described with the incompressible, variable density Navier-Stokes equations with a surface tension term treated by a continuous surface force (Brackbill *et al.*, 1992) which can be written as

$$\rho(\partial_t \boldsymbol{u} + (\boldsymbol{u} \cdot \nabla)\boldsymbol{u}) = -\nabla p + \nabla \cdot (2\mu \boldsymbol{D}) + \boldsymbol{f}_\gamma \tag{3.1}$$

$$\partial_t \rho + \nabla \cdot (\rho \boldsymbol{u}) = 0 \tag{3.2}$$

$$\nabla \cdot \boldsymbol{u} = 0 \tag{3.3}$$

where $\boldsymbol{u} = (u, v, w)$ is the fluid velocity, $\rho \equiv \rho(x, t)$ is the fluid density, p is the pressure, $\mu \equiv \mu(x, t)$ is the dynamic viscosity, $\boldsymbol{D}$ is the deformation tensor defined as $D_{ij} \equiv (\partial_i u_j + \partial_j u_i)/2$ and $\boldsymbol{f}_\gamma$ is the surface tension force per unit volume (Deike *et al.*, 2016).

3.1.2 Momentum-conserving volume-of-fluid method

The VOF method was originally developed by Hirt & Nichols (1981) and has been modified by Kothe *et al.* (1991), and further coupled with momentum conservation by Fuster & Popinet (2018), with the advantage of allowing variable spatial resolution and sharp representation along the interface, while restricting the appearance of spurious numerical parasitic currents. The interface of two-phase flow is reconstructed by a function $\alpha(x, t)$,

defined as the volume fraction of a given fluid in each cell of the computational mesh, assuming values 0 or 1 for each phase. The density and viscosity can thus be computed by arithmetic means as:

$$\rho(\alpha) = \alpha\rho_1 + (1-\alpha)\rho_2 \tag{3.4}$$

$$\mu(\alpha) = \alpha\mu_1 + (1-\alpha)\mu_2 \tag{3.5}$$

where ρ_1 and ρ_2, μ_1 and μ_2 are the density and viscosity of the first and second fluids, respectively.

The advection equation for the density can be replaced with an equivalent advection equation for the volume fraction, which can be obtained by replacing the advection equation for the density:

$$\partial_t \alpha + \nabla \cdot (\alpha \boldsymbol{u}) = 0 \tag{3.6}$$

The piecewise linear interface construction (PLIC) approach is applied. The interface normal is computed by the mixed-Youngs-centred (MYC) method (Aulisa *et al.*, 2007) and the location of the interface in the cell is calculated based on the method of Scardovelli & Zaleski (2000).

For tracking the interfaces of multiphase flows, a similar volume fraction function is applied. The density and viscosity of the multiple fluids are computed using the arithmetic means:

$$\rho(\alpha) = \sum_{i=1}^{N} \alpha_i \rho_i \tag{3.7}$$

$$\mu(\alpha) = \sum_{i=1}^{N} \alpha_i \mu_i \tag{3.8}$$

where ρ_i and μ_i are the density and viscosity of each phase, respectively. The advection equation for the volume fraction of a multiphase flow describes the transport of a phase within a mixture of phases. It can be constructed by considering polyphase points formed by multiple phases, where each phase has a distinct volume fraction:

$$\partial_t \alpha_i + \nabla \cdot (\alpha_i \boldsymbol{u}) = 0 \tag{3.9}$$

where α_i is the volume fraction of phase i. The volume fraction fields α_i are defined such that they satisfy the following condition:

$$\sum_{i=1}^{N} \alpha_i = 1 \tag{3.10}$$

where N is the total number of phases in the mixture. We have N = 3 for three-phase problems.

Momentum conserving scheme in the advective momentum fluxes near the interface has been proven to be essential to reduce numerical momentum transfer through the interface, especially for cases with large density

differences of the distinct phases. Total fluxes on each face are obtained by adding the diffusive flux due to the viscous term, which is computed by semi-implicit Crank–Nicholson scheme (Pairetti *et al.*, 2018). The Bell–Collela–Glaz (BCG) second-order upwind scheme is used for the reconstruction of the liquid and gas momentum per unit volume to be advected in the cell (Bell *et al.*, 1989). And the generalized minmod slope limiter is employed to compute the gradient. The implementation of momentum-conserving VOF advection of the velocity components prevents artifacts caused by momentum leakage between the dense and light phases (Fuster & Popinet, 2018; Zhang *et al.*, 2020).

3.1.3 Balanced-force surface tension formulation

Though the surface tension forces can be neglected for waves longer than centimeters, which are the majority of waves herein, they could be important for capturing the main cavity at impact and wave hydrodynamics post-breakup. The wave-breaking process emphasizes the importance of surface tension at a small scale so that the surface tension can not be neglected due to the highly curved free surface. Surface tension is treated with the method of Brackbill *et al.* (1992) and the balanced-force technique (Francois *et al.*, 2006) as further developed by Popinet (2009, 2018). A generalized version of the height-function (HF) curvature estimation is implemented to address the inconsistency at low interface resolution, giving accurate and efficient solutions for surface-tension-driven flows. The surface tension force per unit volume $\boldsymbol{f}_\gamma$ can be expressed as:

$$\boldsymbol{f}_\gamma = \gamma \kappa \delta_s \boldsymbol{n} \tag{3.11}$$

where γ is the surface tension coefficient; δ_s is the interface Dirac function, indicating that the surface tension term is concentrated on the interface; and κ and $\boldsymbol{n}$ are the curvatures and normal to the interface, respectively.

3.1.4 Energy identification

The integrals over the entire specific phase are performed numerically to identify the energy budget in this phase. The kinetic energy E_k and the gravitational potential energy E_p of the propagating wave are provided as follows:

$$E_k = \frac{1}{2} \int_V \rho |\boldsymbol{u} \cdot \boldsymbol{u}| \mathrm{d}V \tag{3.12}$$

$$E_p = \int_V \rho g y \mathrm{d}V - E_{p0} \tag{3.13}$$

where V is the domain occupied by water in the system and E_{p0} is the gravitational potential energy of the still water at the beginning. The mechanical energy E_m of the wave is calculated as the sum of the kinetic and

potential components:

$$E_m = E_k + E_p \tag{3.14}$$

The non-conservative energy dissipation from the action of viscosity, E_d, can be calculated directly from the deformation tensor:

$$E_d(t) = \int_0^t \int_v \mu \frac{\partial u_i}{\partial x_j} \frac{\partial u_j}{\partial x_i} \mathrm{d}V \mathrm{d}t \tag{3.15}$$

Thus, the total conserved energy budget is given by $E_t = E_k + E_p + E_d$.

3.1.5 Bubbles and droplets counting technique

We count the droplets and bubbles in a flow by tagging connected neighborhoods. by considering connected regions separated by interfacial cells, the volume and position of individual bubbles and droplets can be determined without ambiguity. In practice, this is done using an implementation of the classical "painter's algorithm", which is typically used in bitmap graphics editors to fill connected regions of an image with a given color. This method is exact to the order of the resolution of the Navier-Stokes equations and the associated VOF method. Notably, the advection errors of VOF interface reconstruction can be significant when the liquid structure is less than twice the grid spacing (Li *et al.*, 2010). As noted in previous studies (Wang *et al.*, 2016; Mostert *et al.*, 2022; Wang *et al.*, 2023), with more than 4 minimum computational cells per bubble/droplet diameter, the bubbles/droplets take on a spherical shape, consistent with the physical shape of bubbles/droplets with a ratio of the diameter to the capillary length of less than 0.37 when surface tension dominates (Clift *et al.*, 2005). Therefore, in this study, bubbles/droplets with diameters less than four computational cells are considered unsolved and will not be counted.

3.2 Problem description

3.2.1 Wave initialization

This study investigates oil dispersion by breaking waves through direct numerical simulations of experimental waves. A series of breaking-wave experiments were conducted in a 6 m long, 0.3 m wide and 0.6 m high wave flume to investigate breaking processes and the dispersion of oil spills by breaking waves (Li *et al.*, 2017; Wei *et al.*, 2018; Afshar-Mohajer *et al.*, 2018). Breaking waves were initialized by driving a piston-type wavemaker over a constant water depth d. A single-wave breaking event was produced by a single push of the wavemaker,

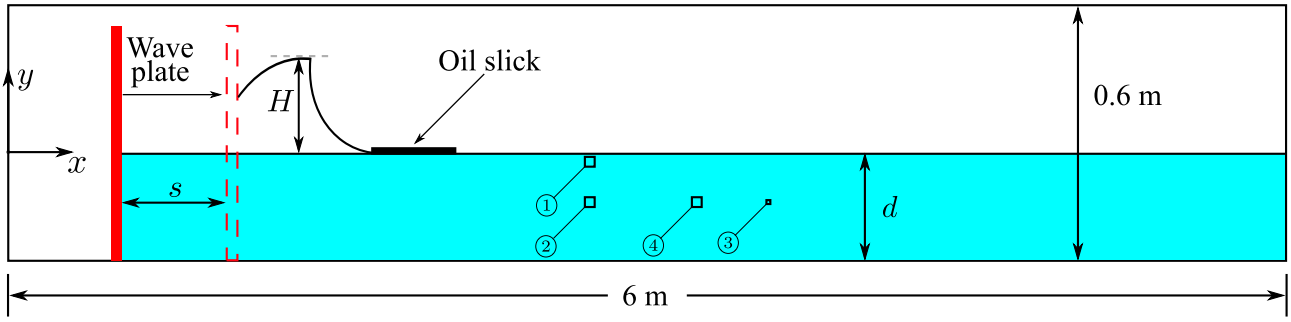

Figure 3.1: Sketch of laboratory breaking wave experiment and numerical domain.

and its trajectory $x(t)$ and associated wave plate velocity $U(t)$ were determined by the following functions:

$$x(t) = \frac{s}{2}(1 - \cos \sigma t), 0 \leq t \leq \frac{1}{2f} \tag{3.16}$$

$$U(t) = s\pi f \sin \sigma t, 0 \leq t \leq \frac{1}{2f} \tag{3.17}$$

where s is the wavemaker stroke length, $\sigma = 2\pi f$ is the angular frequency, and t is the time. A single push of the wavemaker for a half-period $1/(2f)$ was applied to produce a wave with a single crest. During the motion of the wave plate, the maximum wave plate stroke is s, and the maximum wave plate velocity is $U_{max} = s\pi f$. Multiple types of waves could be generated by varying the stroke s, frequency f and water depth d, ranging from non-breaking waves to breakers with different intensities. In comparison with the conventional motion of the piston-type wavemaker that produces sinusoidal waves with an oscillatory motion of $x(t) = s/2 \sin \sigma t$, the piston trajectory here can steepen the wave profile and promote the wave to break. The origin of the experimental domain was located at the undisturbed water surface on the left-hand boundary, where x represents the streamwise direction, and z is the vertical direction, with right and upwards being positive. The wavemaker was initially located at $x = 0.535$ m from the left-hand boundary (see figure 3.1). High-speed imaging was implemented to visualize the plunging jet impact and the subsequent breakup processes during wave breaking. The turbulence produced by breaking was characterized using particle image velocimetry (PIV). The PIV images were processed to calculate the time evolution of turbulence in the wave tank. Digital inline holography, a 3-D imaging technique, was employed to measure the size of the produced droplets and bubbles and to qualify the subsurface particle size distribution. On the basis of laboratory experiments, direct numerical simulations of a range of breaking waves were conducted using the Basilisk solver.

As a strongly nonlinear intermittent process that occurs over a wide range of scales, wave breaking plays an important role in air-sea interactions by limiting the height of surface waves and enhancing the transfer

of mass, momentum, and heat between the atmosphere and the ocean (Melville, 1996; Perlin *et al.*, 2013). When a wave breaks, the free surface undergoes dramatic changes, entraining air into the ocean and ejecting spray into the atmosphere, with the production of bubbles and aerosols (Kiger & Duncan, 2012; Veron, 2015), and the generation of local turbulence near the free surface. Wave breaking also controls the fate of oil spills and contaminants in the upper ocean, determines particle size distribution and dynamic transport, and further affects the health of marine environments (Delvigne & Sweeney, 1988; Deike *et al.*, 2017; Li *et al.*, 2017). The processes associated with breaking waves have received much research attention, and the greatest progress has been made in understanding the geometry of breaking, breaking onset criteria, dissipation due to breaking, and air entrainment (Perlin *et al.*, 2013; Deike, 2022).

The wave generated by the piston is assumed to be sufficiently long for the shallow water assumption. This assumption is supported by the wave speed measurement. Our numerical results indicate that the wave crest speed, calculated from the average speed of the moving wave crest, is greater than the wave speed predicted by shallow water theory. Moreover, the exact wavelength of the wave is difficult to determine, preventing us from accurately determining the depth regime d/L (ratio of water depth and wavelength). In the experiment, we measured the speed of the wave crest before breaking c_w directly. Assuming the wave plate frequency is equivalent to the wave frequency, and using the dispersion relation at a water depth of 0.25 m, we calculated the maximum wave speed to be 1.566 m/s. The experimentally measured wave speed c_w significantly exceeds this value, suggesting that linear wave theory is not applicable in this case. On the other hand, estimating the wave speed based on solitary wave theory yields values closer to the experimental measurements. Therefore, we conclude that the experimental wave exhibits characteristics similar to solitary waves.

The numerical methodology followed in this investigation involves the simulation of the incompressible flow of two / three immiscible fluids. To accurately capture the physical features of the three-phase interface profiles related to breaking waves, the Navier-Stokes equations should be solved numerically on grids sufficiently fine so that viscous and capillary effects could be retained. Based on Direct Numerical Simulations (DNS) of the water-air mixture resulting from the entrainment of droplets and bubbles, and the oil-water-air mixture resulting from the dispersion of the oil slick by breaking waves, in combination with previous experiments conducted at Johns Hopkins University, we intend to investigate the mechanisms of breaking waves and oil dispersion by breaking in terms of free-surface profiles, velocity fields, energy budget, and size distribution of bubbles and droplets.

3.2.2 Parameter space

In order to accurately simulate breaking waves and oil dispersion, we solve the two-phase Navier–Stokes equations with surface tension and using a momentum-conserving transport of each phase. Gravity is taken into account using the "reduced gravity approach" (Wroniszewski *et al.*, 2014). The domain is discretized using the adaptive mesh refinement scheme. A constant depth of water for the interface $\eta(x, y)_{(t=0)} = d$, with d the still water depth, is used as the initial condition in a square box of size $L = 6m$. The oil slick is placed on the undisturbed water surface, with a length of l_o and a thickness of h_o. The wave propagates in the x direction from left to right. The numerical resolution is given by $\Delta = L_0/2^{l_{max}}$, where l_{max} is the maximum level of refinement in the AMR scheme.

The piston is implemented by initializing a volume fraction field at each time step, which corresponds to the position and speed of the moving piston. This approach has been effectively employed in previous studies (Lin-Lin *et al.*, 2016; Wu & Wang, 2009). Since the moving piston is updated at each time step, the grids intersected with the piston are refined to the finest level all the time, thus ensuring the accurate representation of the moving boundary in the adaptive meshes. The refinement criterion is based on the wavelet-estimated discretization error in terms of the velocity and VOF fields. The corresponding mesh will be refined as required when initializing the wave. The refinement algorithm is invoked at every time step to refine the mesh whenever the estimated error of the wavelet exceeds the prescribed threshold for both the velocity and volume fraction fields.

3.2.3 Dimensional analysis for waves generated by wave plate

In this section, a dimensional analysis of the waves generated by wave plates is performed. Considering that the wave generated by the wave plate is assumed to be dependent on the fluid properties and the initial conditions. If the wave process is restricted to air–water systems close to standard temperature and pressure, then the density and kinematic viscosity ratios of the two phases are those of air and water in the experiments, which will not be regarded as altering the wave features. Then, the dependent variables for identifying this specific wave can be expressed as follows:

$$f(g, \nu, \rho, \gamma, s, f, d) \tag{3.18}$$

where g [dimension $\mathrm{L/T^2}$] is the gravitational acceleration, ν [$\mathrm{L^2/T}$] is the water kinematic viscosity, ρ [$\mathrm{M/L^3}$] is the water density and γ [$\mathrm{M/T^2}$] is the surface tension. The piston stroke s [L] and frequency f [T] of the

wave plate, and the undisturbed depth of water d [L] are referred to as the initial conditions. Buckingham's theorem can be used to construct the following dimensionless parameters by selecting ρ, g and d as the repeating variables:

$$\frac{g^{1/2}d^{3/2}}{\nu} = Re, \quad \frac{\rho g d^2}{\gamma} = Bo, \quad \frac{s}{d}, \quad \frac{f}{\sqrt{g/d}} = \frac{fd}{c} \tag{3.19}$$

The above dimensional analysis indicates that wave characteristics are determined by the Reynolds number Re, Bond number Bo, s/d and fd/c, where $c = \sqrt{gd}$ is the wave speed in shallow water. Of particular interest in this study is the maximum wave height before breaking H [L], the breaking wave crest H_b [L] of the plunging breaker, the total energy per unit length transferred by the motion of wave plate E_l [$\mathrm{ML/T^2}$] and the dissipation of the wave energy per unit length of the breaking crest, ϵ_l [$\mathrm{ML/T^3}$]. These wave characteristics should be dimensionless to connect to the dimensionless parameters representing the fluid properties and the initial conditions in (3.19). Using dimensional analysis, the dimensionless parameters for these wave features are as follows:

$$\frac{H}{d}, \quad \frac{H_b}{d}, \quad \frac{E_l}{\rho g d^3}, \quad \frac{\epsilon_l}{\rho g^{3/2} d^{5/2}} \tag{3.20}$$

Quantifying the influence of these dimensionless parameters is of great significance for elucidating the wave shape evolution, energy transfer and air entrainment mechanisms.

Chapter 4

2-D breaking waves simulations

Contents

Plunging breakers are characterized by the presence of a well-defined cavity beneath the overturning jet. This chapter investigates the dynamics of waves, the evolution of the plunging jet and the energy budget during wave breaking. The goal is to establish quantitative relationships of the main cavity, breaking criteria and energy dissipation with respect to the fluid properties and initial conditions, by reproducing experimental waves through 2-D DNS.

4.1 Numerical set-up

Two-dimensional direct numerical simulations of breaking waves reproduce the way to generate waves in the wave flume by exerting the motion of the piston-type wave plate (Li, 2017). The origin is located on the undisturbed water surface, with the x-axis pointing downstream and y-axis upward. The corresponding instantaneous velocity components are u and v, respectively. The density ($\mathrm{kg/m^3}$) and kinematic viscosity ($\mathrm{m^2/s}$) ratios of the two phases are those of air and water in the experiments, which are $1.29/1018.3$ and $1.39 \times 10^{-5}/1.01 \times 10^{-6}$, respectively. The Reynolds number in the breaking wave event generated by the wave plate can be defined by $Re = g^{1/2}d^{3/2}/\nu = cd/\nu$, where $c = \sqrt{gd}$ is the wave phase speed in shallow water. Due to the limitation of computational resources, combined with the decreasing effects of the Reynolds number on the evolution of wave breaking (Mostert & Deike, 2020), it is possible to use a Reynolds number that is smaller than the actual value. Breaking waves are normalized using the reference length and velocity scales, which in this case are the still water depth d and wave speed in shallow water c, respectively; the reference time scale is defined as $t_0 = d/c = \sqrt{d/g}$. It is worth noting that the fundamental nature of the breaking processes is not expected to be significantly altered by Reynolds number effects. The surface tension can be expressed by the Bond number $Bo = \rho g d^2/\gamma$, where γ is the constant surface tension coefficient between water and air. The physical value of the water surface tension coefficient with air, $\gamma = 0.0728\ \mathrm{kg/s^2}$, is used to analyze the effect of surface tension on the formation of the main cavity.

Three different experimental breaking waves are simulated to reproduce the breaking characteristics numerically. The wave plate stroke s, frequency f and water depth d for generating the three breakers are summarized in table 4.1. One of the breakers, a typical plunging breaker with $s = 0.5334$ m and $f = 0.75$ Hz, is chosen for model verification and detailed analysis. Furthermore, a parametric study is performed to relate the wave characteristics to the initial conditions by extensively varying the stroke s, frequency f, and water depth d. As the surface tension scheme is time-explicit, the maximum time step is the oscillation period of the smallest capillary wave. For the maximum level of refinement $l_{max} = 15$, the corresponding maximum time step $\Delta t/t_0$

Wave	s(m)	f(Hz)	d(m)	U_{max}(m s^{-1})	c(m s^{-1})	U_{max}/c
1	0.5334	0.75	0.25	1.257	1.566	0.803
2	0.4572	0.75	0.25	1.077	1.566	0.688
3	0.4572	0.625	0.25	0.898	1.566	0.573

Table 4.1: Parameter space for generating three different breaking waves. The column labels are as follows: s, wave plate stroke; f, frequency; d, water depth; U_{max}, maximum piston speed; c, shallow water wave speed; U_{max}/c, the ratio of the maximum piston speed to the shallow water wave speed.

should not be larger than 4×10^{-4}. A CFL number of 0.5 is utilized to ensure numerical stability. The VOF tracers are used to capture the water-air interfaces and the moving boundary of the wave plate. This capability of local dynamic grid refinement significantly reduces the computational cost of representing a breaking wave that propagates within an extended physical domain at a high resolution. This makes it especially appropriate for the present application where wave profile evolution and wave breaking are expected. The wave plate boundary and the air–water interface are initially refined to the finest level, while the remainder of the domain remains at a level of refinement of 10.

4.2 Mesh convergence

The choice of the effective numerical resolution is related to the numerical convergence. A key physical feature of simulating two-phase breaking waves is the thickness δ of the viscous boundary layer at the free surface. The estimation from Batchelor's method suggests the defining length scale $\delta \sim d/\sqrt{Re} \approx 0.004d = 1.0$ mm (Deike et al. 2015, 2016). Based on this estimation, the viscous sublayer is resolved with more than five grid cells at l_{max} = 15, allowing us to resolve the dissipation rate associated with the breaking waves (Mostert *et al.*, 2022). Furthermore, the grid convergence of the numerical results is analysed by considering three sets of simulations with l_{max} = 13, 14 and 15, corresponding to the effective resolution, which is equivalent to 4096^2, 8192^2 and 16384^2 on a regular grid, respectively. The numerical convergence is discussed in terms of the evolution of the free surface, velocity field, energy budget, and size distribution of the bubbles entrapped by wave breaking. Figure 4.1(a) and (b) illustrate the influence of mesh resolution on the development of the free surface for wave 1. The wave breaks at t/t_0 = 3.25, characterized by a vertical slope at the front of the wave (a). As the maximum level of refinement l_{max} increases from 13 to 15, the differences at the tip of the overturning jet become progressively smaller. The overturning jet curls over itself and impacts the surface of the wavefront at t/t_0 = 4.25 (b). Although slight phase shifts can be observed at different resolutions, the shape and size of

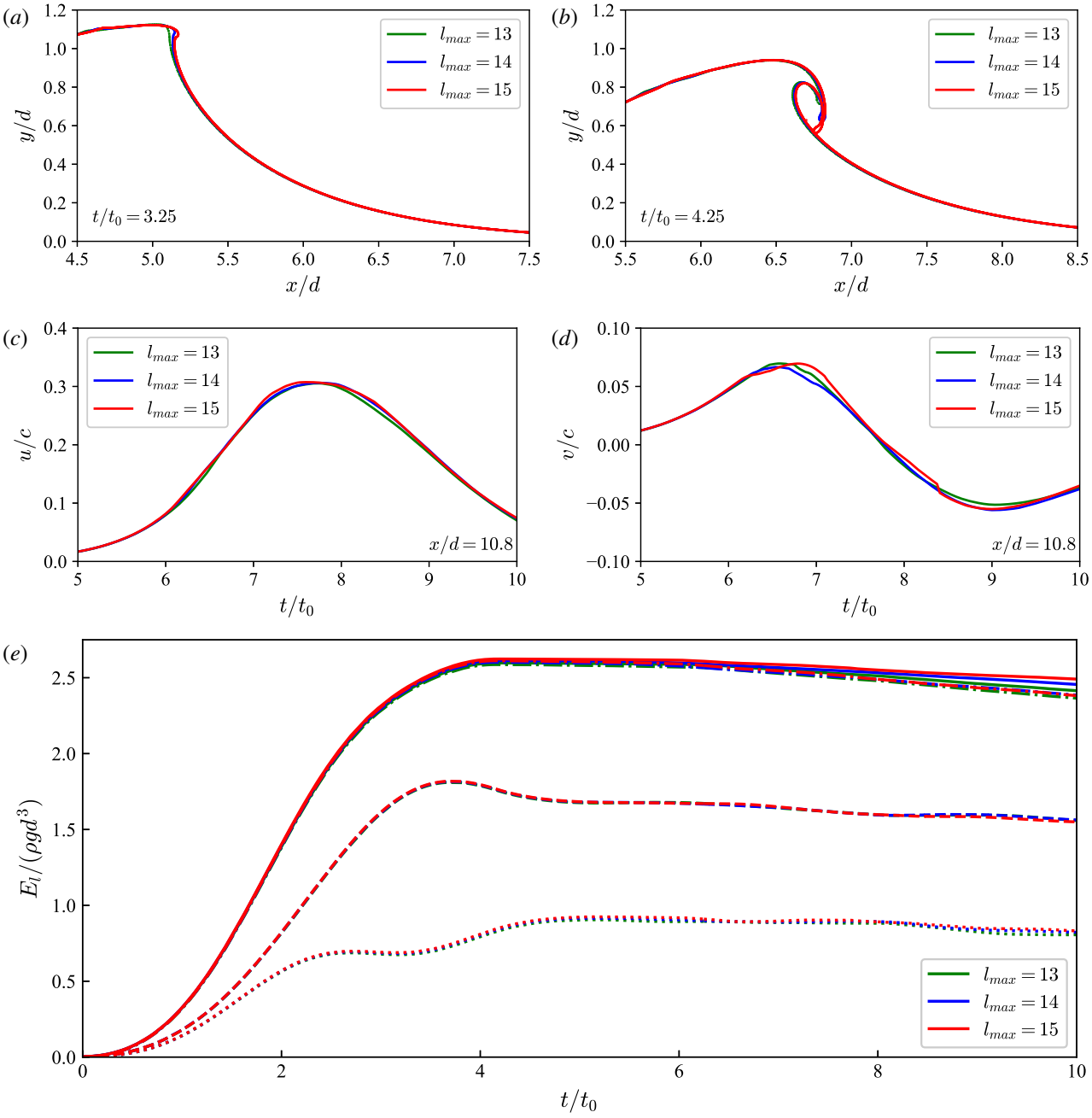

Figure 4.1: Convergence study at three different mesh resolutions for wave 1 with s/d = 2.13 and fd/c = 0.12; green, 2^{13}; blue, 2^{14}; red, 2^{15}. Grid convergence of the free surface during wave breaking at t/t_0 = 3.25 (a) and jet impact at t/t_0 = 4.25 (b); the temporal evolution for horizontal component u (c) and vertical component v (d) of the velocity field in the broken bore propagation region at x/d = 10.8; and the energy budget (e) for kinetic energy E_k (dotted), gravitational potential energy E_p (dashed), mechanical energy E_m (dash–dot), and total conserved energy E_t (solid).

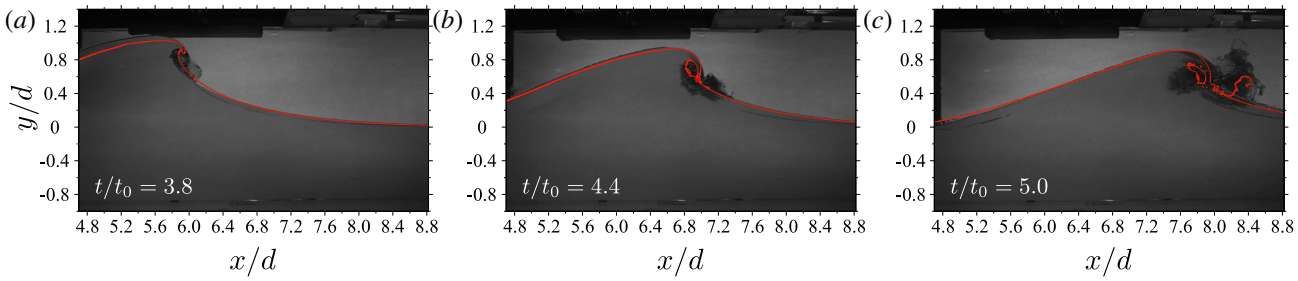

Figure 4.2: Qualitative comparison of free surface profiles between laboratory images and numerical results for wave 1 with s/d = 2.13 and fd/c = 0.12.

the entrained air by the plunging jet remain similar. Figures 4.1(c) and (d) show the temporal evolution of the horizontal component (c) and vertical component (d) of the velocity field in the broken-bore propagation region at x/d = 10.8. A better agreement is observed between the cases with resolutions of 2^{14} and 2^{15} compared with those between 2^{13} and 2^{14}. Regarding the energy budget, figure 4.1(e) indicates numerical convergence in the evolution of kinetic energy E_k, gravitational potential energy E_p, and conservative energy $E_m = E_k + E_p$ for all cases. This convergence suggests that numerical accuracy is achieved in the energy transfer between E_k and E_p. However, differences in $E_t = E_k + E_p + E_d$ at different resolutions imply that the dissipated energy cannot be fully captured by the current grid cells directly. Nevertheless, as the wave dissipation rate can be calculated based on the conservative energy E_m, numerical convergence is also attained in estimating energy dissipation when calculated from the loss of E_m.

The above convergence studies have confirmed that all results are well converged, with no significant changes observed as the maximum level of refinement increases from 13 to 15. The resolution of 2^{15} is used to realize a more precise parametric study to determine the wave characteristics as a function of the fluid properties and initial conditions. Consequently, all presented results in the following sections have attained convergence with respect to grid resolution.

4.3 Model verification

A high-speed camera with a frame rate of 500 frames per second is used in the experiments to visualize the development of wave breaking and subsequent breakup processes. The field of view, 4.12 $\times$ 4.12, is centered horizontally at $x/d = 6.74$, with left and right view sides of 4.68 and 8.8, respectively. The vertical center of the camera is adjusted to the initial free surface. The numerical results of the temporal evolution of the free surface for wave 1 are compared with experimental snapshots for model verification. Comparisons of the free-surface

profile between the simulation results and snapshots taken during the experiments are shown in figure 4.2. The camera is located upstream of the wave direction close to the side of the wave plate. This device is primarily responsible for recording the development of the plunging jet, jet impact and air entrapment, and the generation of the first splash-up. Comparisons of the free-surface evolution at t/t_0 = 3.8, 4.4, and 5.0 show excellent agreement between the current simulation and the experimental results. The configuration in the motion of the wave plate leads to the formation of a highly asymmetric wave profile during the prebreaking period. As the wave slope increases and the wave crest curls over, the formation of a plunging jet becomes evident at t/t_0 = 3.8, with a downwards projection towards the water surface. At t/t_0 = 4.4, the plunging jet impacts the rising wavefront, leading to the formation of the main cavity through the entrapment of an air tube. At t/t_0 = 5.0, a splash-up is generated, propelled by the primary plunging jet, moving upwards. It is accompanied by the emission of droplets from fractured ligaments. The slight discrepancy between the height of the splash-up and the development of the aerated region is attributed to the 3-D instability in the spanwise direction, which falls beyond the scope of this study. Overall, the evolution of the free surface during the breaking process, including the curvature of the overturning wave crest, the size of the main cavity, and the height and location of the first splash-up, can be accurately predicted by our numerical simulations.

Furthermore, figure 4.3 shows the simulated free-surface profiles over time for wave 1 recorded at three designated positions (x/d = 4.8, 7.2, and 9.6) corresponding to the prebreaking, breaking, and postbreaking regions, respectively, with a comparison with the experimental high-speed imaging results. The free-surface profile at the first position (x/d = 4.8) remains smoothly curved, which corresponds to the prebreaking stage where the free surface is smooth, without the formation of the vertical interface and the generation of bubbles and droplets. The numerical simulation accurately reproduces the evolution of the free surface, including the development of the rise and fall of the wave profile, with only a slight underestimation at the peak value of the wave profile at t/t_0 = 3.1. The second position is located at x/d = 7.2, within the wave-breaking region, near the main cavity entrapped by the plunging jet. In the experiment, the free surface exhibits an immediate increase after jet impact at approximately t/t_0 = 4.4, indicating the penetration of the plunging jet into the wavefront and the formation of the main cavity. Figure 4.3(b) shows that our numerical simulation can closely capture the phenomenon of how waves break. The only discrepancy can be caused by the lack of small ejections when the plunging jet penetrates into the wavefront due to the absence of the 3-D effect. The wave propagates to the third position and develops into turbulent flow, forming a large amount of spray and bubbles. There are apparent fluctuations in the free surface between t/t_0 = 5.6 and 8.8, showing a strongly turbulent phenomenon in this

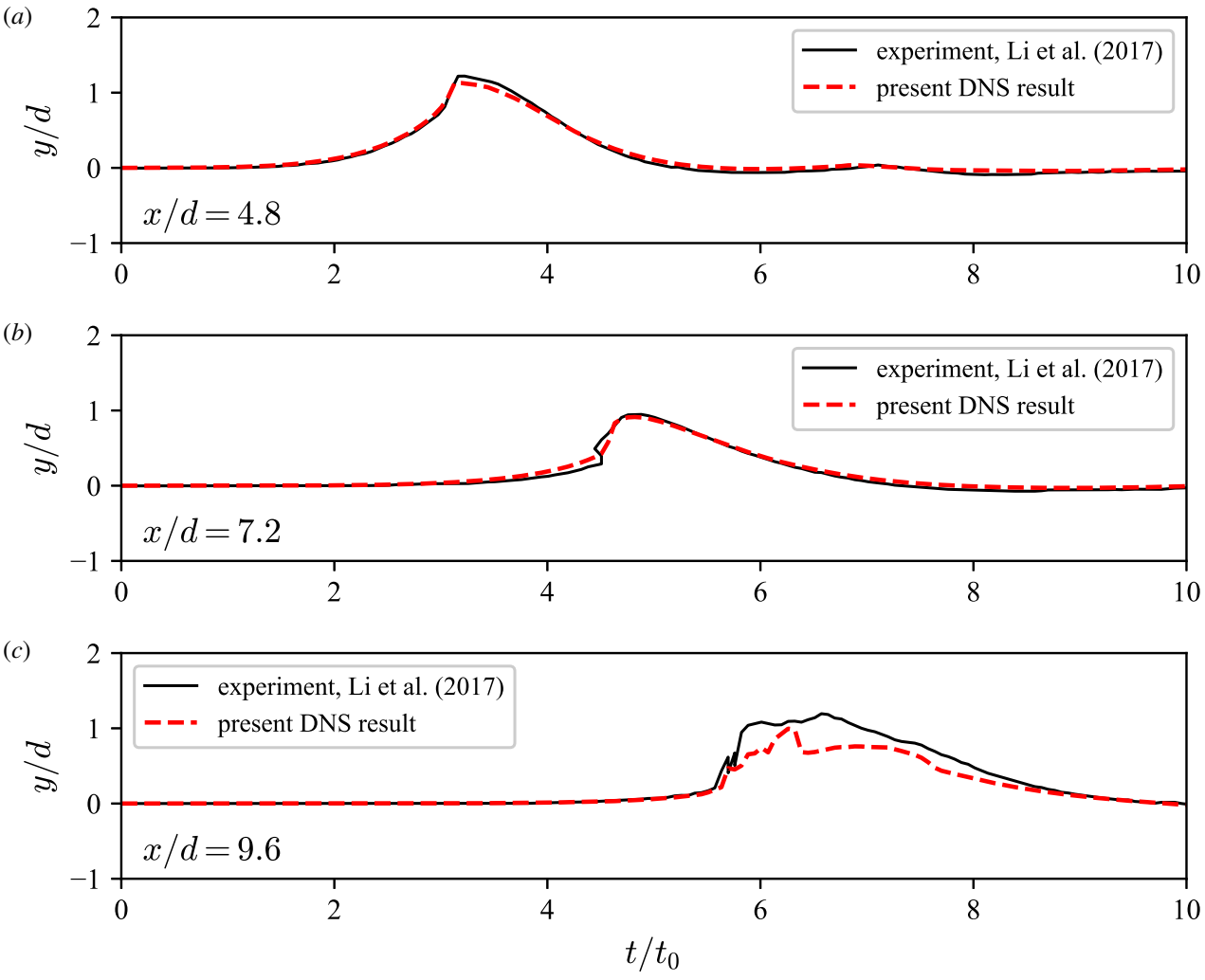

Figure 4.3: Qualitative comparison of surface elevations over time at x/d = 4.8 (a), 7.2 (b), and 9.6 (c) for wave 1 with s/d = 2.13 and fd/c = 0.12.

region. Figure 4.3(c) shows an overall underestimation of the free-surface elevations from t/t_0 = 5.6 to 8.8 by our numerical simulation. This result is most likely due to differences in the recordings of the free-surface elevations from the experiments and numerical simulations. In the experiment, the value of the free-surface elevations is the maximum elevation of the wave profile, splashing bubbles, and droplets, as the free-surface elevations are recorded from the black region in the experimental snapshots. However, in the numerical simulation, the free-surface elevations are primarily determined by wave profiles rather than splashing droplets scattered above the water surface. In general, the temporal evolution of free-surface profiles can be precisely reproduced by our simulation when compared with laboratory experiments at each location.

In summary, although our 2-D simulation has limitations in capturing droplets and ligaments in the spanwise direction, the model demonstrates its capability to accurately depict wave hydrodynamics. This is evidenced by its ability to reproduce the wave height, wave speed, and wave-breaking process, as demonstrated in the aforementioned comparisons.

4.4 Breaking characteristics

4.4.1 Wave breaking dynamics

Sequences of wave 1 with contours of the normalized velocity magnitude $(u, v)/c$ are shown in figure 4.4. For wave 1, we show the very early time evolution of the pre-broken wave at t/t_0 = 1.25 and t/t_0 = 2.25, as well as the wave crest steepening at t/t_0 = 3.25 and the jet impact which forms a closed cavity at t/t_0 = 4.25.

Sequences of three different plunging breakers with contours of the normalized velocity magnitude $(u, v)/c$ are shown in figure 4.5. For wave 1, the wave begins to break as the wave crest steepens and becomes multivalued at t/t_0 = 3.19. A curled jet is formed projecting ahead of the wave, and a high and flat interface accumulates at the rear side of the wave crest. The overturning jet develops further and impacts the wavefront, forming a closed cavity from the entrapped air at t/t_0 = 4.25. The phenomena of the breaking event from wave breaking and jet impact to splash-up formation among waves 1, 2, and 3 are quite similar. However, some differences exist at the rear side of the wave crest and regarding the size and shape of the closed cavity. Due to the highly unsteady and rapidly evolving breaking crest, determining the location and speed of the crest is challenging. Instead, the maximum horizontal particle velocity u is used to analyze the speed evolution from incipient breaking to jet impact. Notably, the phase speed in shallow water c, calculated using linear wave theory, exhibits significant discrepancies when compared with the measured wave phase speed, which can be determined by the distance

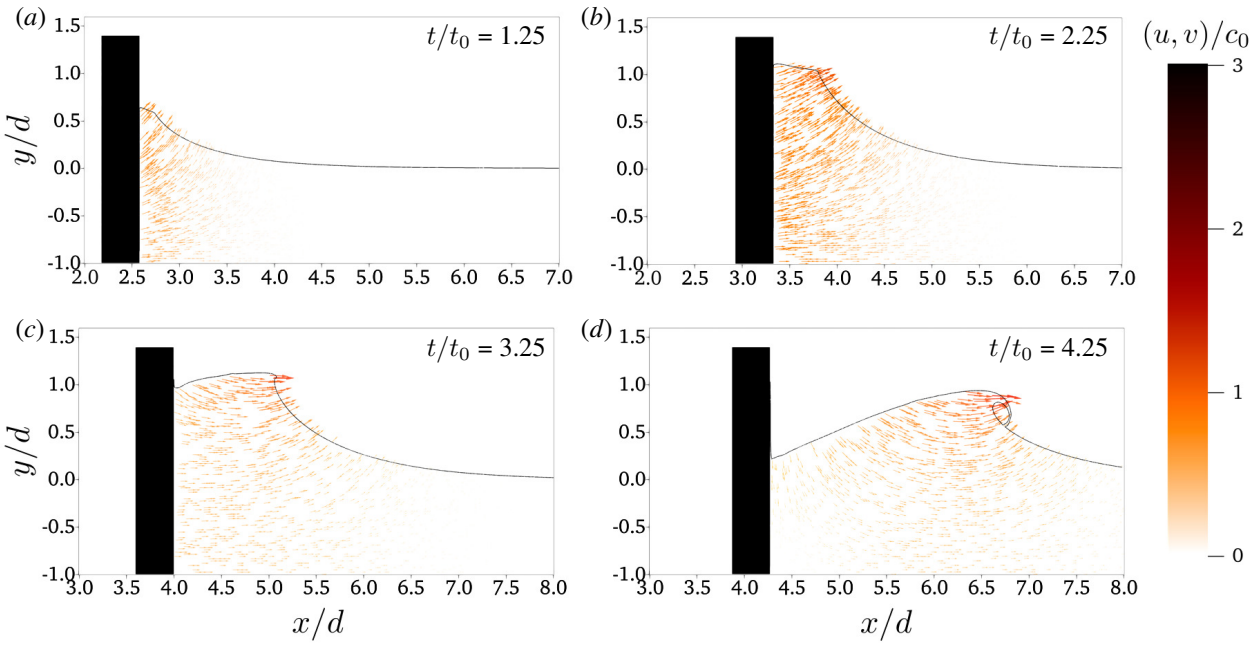

Figure 4.4: Evolution of the free surface for wave 1, labeled with the normalized velocity vectors $(u, v)/c$.

between two crests. These discrepancies may arise from the highly nonlinear and asymmetric wave profile, as well as the persistent motion of the wave plate during wave breaking. For simplicity, we continue to use the shallow water phase speed c here. Prior to wave breaking, the maximum horizontal particle velocity is located at the wave crest. The green star in figure 4.5 indicates the position where the maximum horizontal particle velocity is located at that moment. As the wavefront approaches vertical, the particle velocities become almost horizontal with the order of the phase speed. The location of the maximum horizontal particle velocity then shifts downwards to the vertical plane along the longitudinal direction. At this stage, the maximum horizontal particle velocity begins to increase until the plunging jet impacts, reaching its maximum value at the top of the entrapped air cavity within the curling jet. For wave 1, the front face becomes nearly vertical at $t/t_0 = 3.19$, with a horizontal crest particle velocity of $u/c = 1.57$. Upon impact of the plunging jet at $t/t_0 = 4.25$, the horizontal crest particle velocity increases to $u/c = 1.99$, representing a 27% increase. For wave 2 and wave 3, the front face becomes nearly vertical at $t/t_0 = 2.88$ and $t/t_0 = 4.51$, respectively, with velocity increases of 40% and 14% up to the impact of the plunging jet at $t/t_0 = 4.19$ and $t/t_0 = 5.63$, respectively.

The wave-breaking process is illustrated using wave 1 as a representative example. Figure 4.6 shows the normalized streamwise velocity u/c, vertical velocity v/c, and vorticity ω/ω_0 at different stages of wave

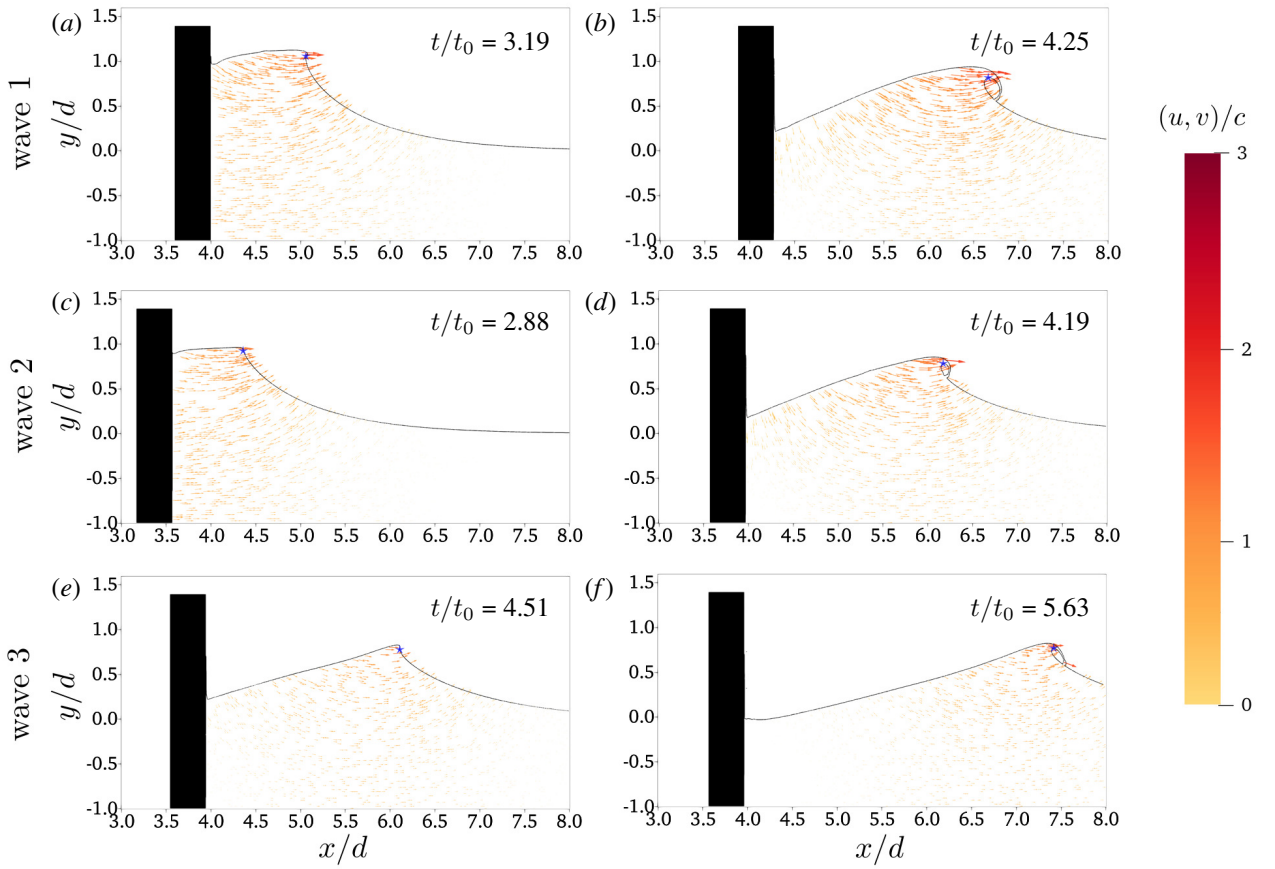

Figure 4.5: Evolution of the free surface for the three different plunging breakers, labeled with the normalized velocity vectors $(u, v)/c$. Panels (a, c, e) correspond to the time when the wavefront nears vertical, while (b, d, f) indicate the time when the plunging jet impacts the wavefront. The green star indicates the position where the maximum horizontal particle velocity is located at that moment.

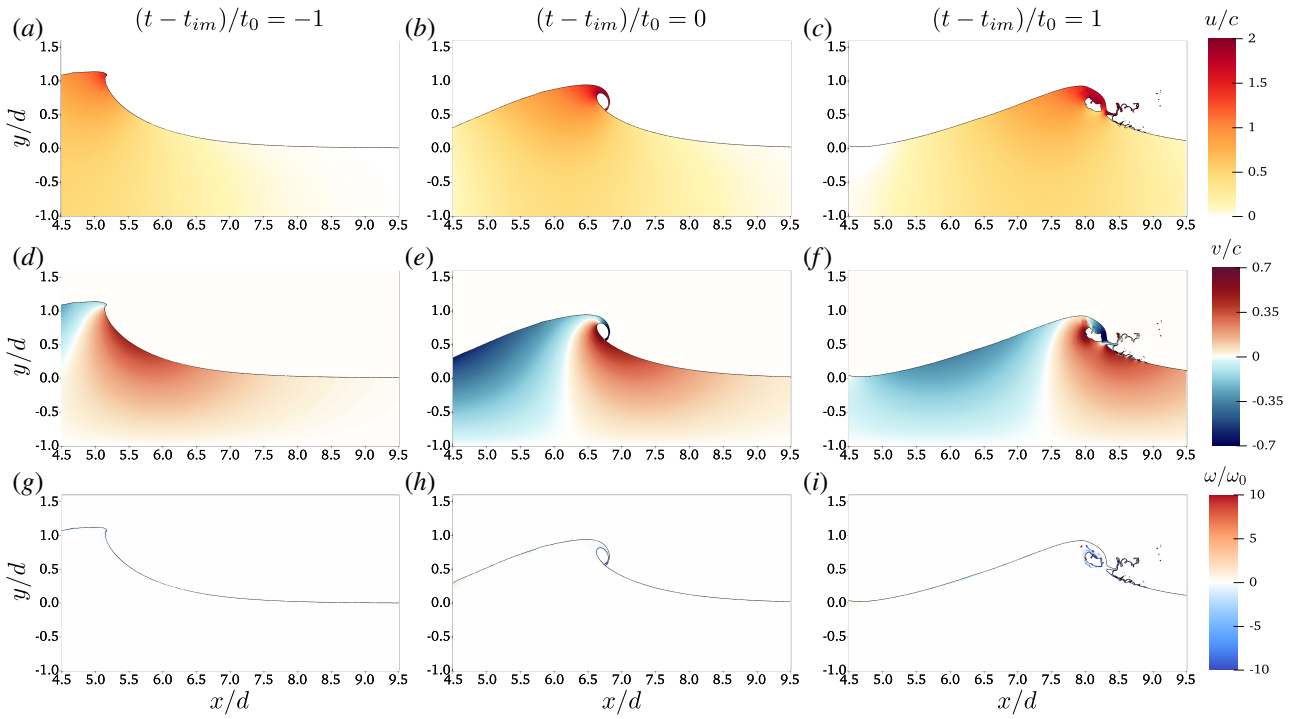

Figure 4.6: Detailed normalized streamwise velocity u/c (a-c), vertical velocity v/c (d-f), and vorticity ω/ω_0 (g-i) for wave 1 with s/d = 2.13 and fd/c = 0.12 during wave overturning (a, d, g), $(t - t_{im})/t_0$ = -1; jet impact (b, e, h), $(t - t_{im})/t_0$ = 0; and splash-up (c, f, i), $(t - t_{im})/t_0$ = 1.

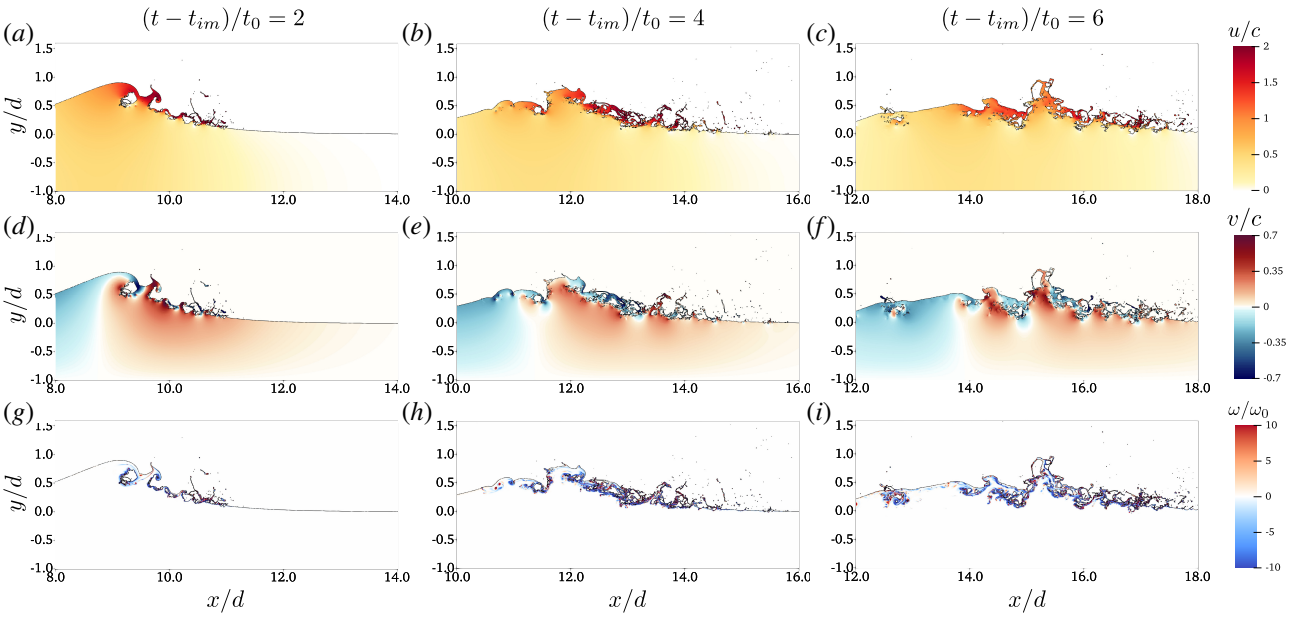

Figure 4.7: Detailed normalized streamwise velocity u/c, vertical velocity v/c and vorticity ω/ω_0 in the late stage after wave breaking at $(t - t_{im})/t_0$ = 2, 4 and 6 for wave 1 with s/d = 2.13 and fd/c = 0.12.

overturning (left column, $(t - t_{im})/t_0$ = -1), jet impingement (middle column, $(t - t_{im})/t_0$ = 0), and splash-up (right column, $(t - t_{im})/t_0$ = 1), where t_{im} denotes the time when the plunging jet impacts the wavefront, and $\omega_0 = \sqrt{g/d}$ represents a reference vorticity. Figure 4.6(a-c) presents the distribution of the streamwise velocity component, with the maximum values u/c = 1.62 (a) at the neck below the wave crest, 2.21 (b) at the impact point where the toe of the jet connects with the wavefront, and 2.65 (c) near the tip of the splash-up. Combined with the distribution of the vertical velocity, the water–particle velocities of the wave crest are found to be approximately horizontal, as shown by PIV measurements of breaking waves by Perlin *et al.* (1996). The vertical asymmetry can be clearly observed from the distribution of the vertical velocity. Vortices are identified as concentrated at the free surface as the wave overturns, becoming more intense during cavity closure and subsequent splash-ups.

Figure 4.7 illustrates the normalized streamwise velocity u/c, vertical velocity v/c, and vorticity ω/ω_0 during the late stage of wave breaking at $(t - t_{im})/t_0$ = 2, 4 and 6. Notably, the highest streamwise velocity components are concentrated on the ruptured ligaments and ejected droplets resulting from the splash-ups, reaching a maximum value of u/c = 2.65, as decipted in figure 4.7(a-c). By examining the distribution of the vertical velocity component in Figure 4.7(d-f), we can identify the location of the original wave crest, as well as the number and positioning of the primary splash-up processes, since the vertical velocity component v/c

equals zero at the positions of the original wave crest and impact point. As the wave experiences repetitive jet impacts and splash-ups, the wavefront interfaces become turbulent, resulting in irregular turbulent patches. Figure 4.7(g-i) demonstrates that the vortices do not interact with the bottom, suggesting that the wave depth does not significantly influence the turbulent clouds induced by wave breaking in our study.

4.4.2 Energy budget

This section investigates the temporal evolution of the energy input by the wave plate, energy loss during wave breaking and the corresponding dissipation rate. Before proceeding, we acknowledge the inherent three-dimensional nature of turbulence and the potential controversies surrounding the use of 2-D simulations. Although 2-D simulations may not fully capture the complexities of three-dimensional turbulence, they have been widely employed in studying breaking waves due to their ability to reproduce key features and capture the dominant mechanisms governing the breaking process. Specific aspects of breaking waves, such as wave overturning and energy evolution, have been found to yield valuable insights through 2-D simulations. Previous studies, such as Iafrati (2009), have indicated that the overturning of the jet and the initial jet impact are primarily two-dimensional processes. Moreover, the assumption of two-dimensionality is reasonable, particularly in the early stages after the onset of breaking, when large air bubbles are entrapped. The use of two-dimensional DNS has also proven effective in capturing the dissipative scales of the breaking wave process, as demonstrated by Deike *et al.* (2015). Three-dimensional effects are expected to become significant only in the subsequent stage, where instabilities in the cross-direction strongly influence both the fragmentation process of the air cavity and the dynamics of large vortical structures.

Figures 4.8 (a), (b), and (c) illustrate the energy evolution in the wave tank for each case. Initially, there is no energy in the system, but as the wave plate begins to move and interact with the water body, the generation of waves leads to a simultaneous increase in gravitational potential energy and kinetic energy. The total energy continues to increase until the moment when the plunging jet impacts the wavefront. For waves 1, 2, and 3, this occurs at t/t_0 = 4.25, 4.19, and 5.63, respectively. Prior to the jet impact, two visible energy transfers between kinetic and potential energy can be observed, resulting from wave steepening and the descent of the plunging jet. Figures 4.8(d), (e), and (f) present the temporal evolution of the total mechanical energy starting from the initial jet impact for three different waves. The associated dissipation rate is also depicted using dashed lines. Examining wave 1 in Figure 4.8(d), the energy dissipation rate remains relatively small and constant from the impact of the plunging jet until just before the first splash-up impact, occurring at approximately $(t - t_{im})/t_0$

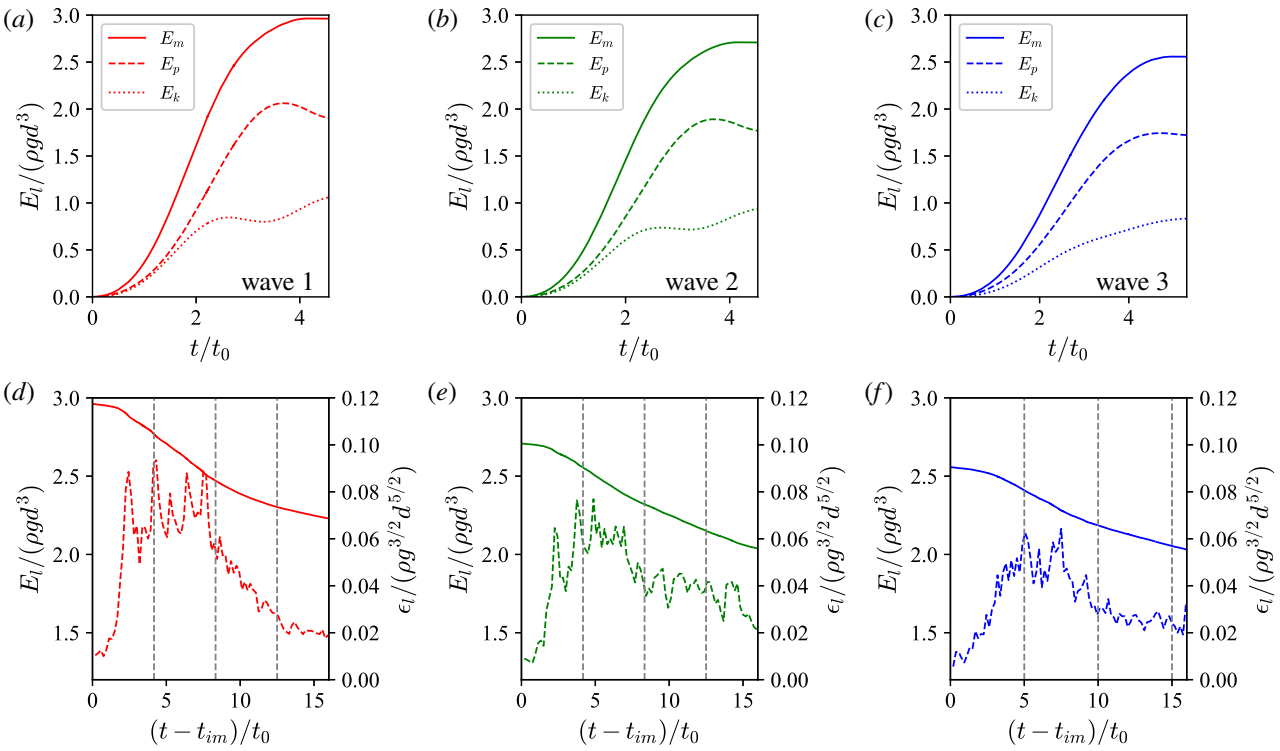

Figure 4.8: The temporal evolution of the normalized energy per unit length $E_l/(\rho g d^3)$ for wave 1 (a), wave 2 (b) and wave 3 (c) from the initiation of wave plate motion until the moment of jet impact. The motion of the wave plate transfers energy to the stationary water column, resulting in the propagation of waves at a constant water depth. Jet impact occurs at t/t_0 = 4.25, 4.19 and 5.63 for waves 1, 2 and 3, respectively. Panels $(d - f)$ present the normalized energy per unit length $E_l/(\rho g d^3)$ and the normalized energy dissipation rate per unit length $\epsilon_l/(\rho g^{3/2} d^{5/2})$ starting from the time of jet impact for the three different waves. The energy dissipation is enhanced upon the plunging jet striking the wavefront. The dissipation rate first increases and then remains relatively constant for a period. Subsequently, the energy dissipation rate starts to decline, marking the end of the active breaking stage. Three grey lines indicate specific time points at $(t - t_{im})/t_0 = (1/(2f))/t_0$, $(1/f)/t_0$ and $(3/(2f))/t_0$.

= 1. Subsequently, as the first splash-up and its associated shedding droplets collide with the water surface, the energy dissipation rate begins to increase. From $(t - t_{im})/t_0$ = 1 onwards, the wavefront interface undergoes significant perturbations due to multiple jet impacts, splashing events, and the formation of entrapped bubbles and ejected droplets. These breaking processes enhance energy transfer and dissipation, leading to a rapid increase in the energy dissipation rate and a continuous decay of the total mechanical energy. After $(t - t_{im})/t_0$ = 3, as the wave becomes more turbulent, the dissipation rate reaches its maximum, entering a plateau that remains relatively constant until approximately $(t - t_{im})/t_0$ = 8. Following the intense dissipation caused by turbulence, the dissipation rate starts to decrease at a constant rate, with a noticeable reduction observed at approximately $(t - t_{im})/t_0$ = 13. A similar trend is observed in waves 2 and 3, with a weaker energy transfer and turbulence region due to wave breaking. Notably, all scales of the breaking wave, from energy dissipation to the formation and breakup of bubbles and droplets in a two-phase turbulent environment, must be resolved in order to accurately capture the physics of breaking waves. However, this is not feasible in two-dimensional direct numerical simulations. The energy dissipation rates presented in figure 4.8(d-f), which are based on the decay of the mechanical energy, were used as a way of determining the active breaking period. The natural end time of breaking is not immediately obvious, but examining the evolution of dissipation rates provides a way to identify the point at which the wave has stopped breaking. While our 2-D results on the energy budget and dissipation provide a brief overview of energy evolution during breaking and its associated causes from a two-dimensional perspective, some physical phenomena such as the rupture of the main air cavity cannot be represented due to the absence of 3-D information. Consequently, it is not advisable to extrapolate from these 2-D results to infer the complete physical processes occurring during breaking.

4.5 Parametric study

4.5.1 Influence of the Bond number

In this section, the effect of dimensionless parameters responsible for the wave evolution and breaking characteristics on the geometry of the main cavity at impact is investigated. The effect of the Reynolds number on the wave evolution is expected to be small before wave breaking, as the jet thickness is independent of the Reynolds number, and no apparent dependence of the cavity size on the Reynolds number is discovered (Iafrati, 2009; Mostert *et al.*, 2022). The Reynolds independence of the wave characteristics and main cavity features is checked by comparing the numerical results for distinct Reynolds numbers of 6×10^4 and 6×10^5 with

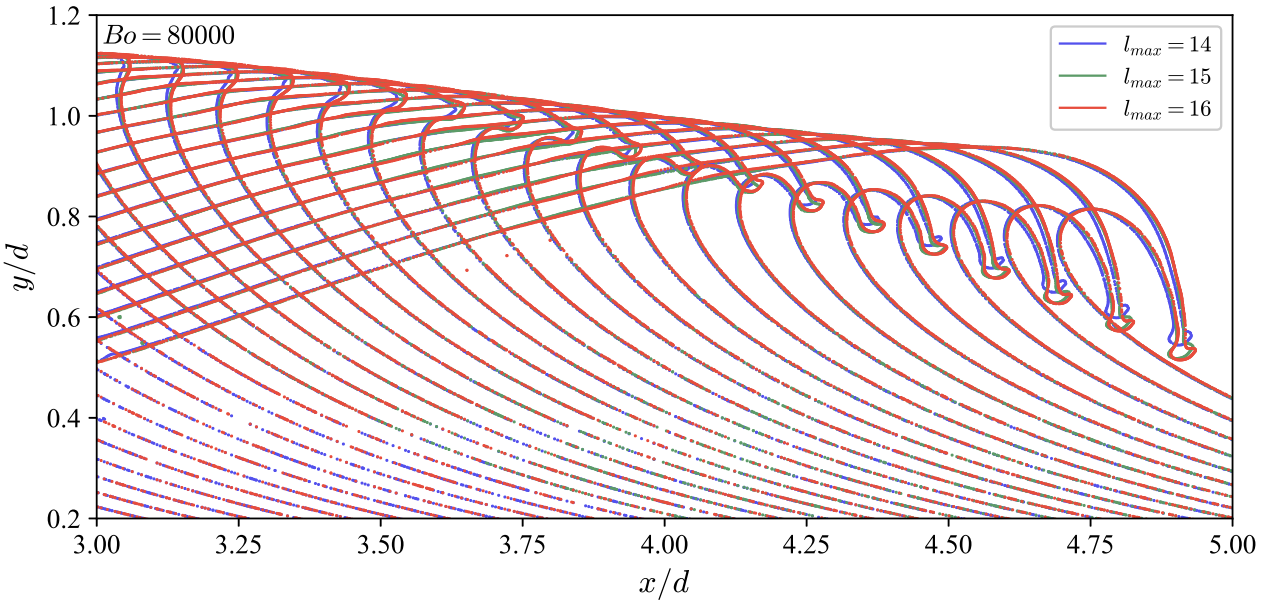

Figure 4.9: Evolution of the free surface, spanning from jet formation to jet impact, is examined with a time interval of $\Delta t/t_0 = 0.16$. A large Bond number of 80000, which represents a significant scale separation, is used for grid convergence analysis. The comparison between l_{max} = 15 and 16 exhibits better agreement compared with that between l_{max} = 14 and 15, indicating that l_{max} = 15 adequately achieves grid convergence, even for relatively high Bond numbers.

experimental data. These findings confirm the results obtained previously by Iafrati (2009). The influence of the Reynolds number on the wave features is neglected in this study since it has been shown to be negligible at high Reynolds numbers in breaking waves. Since our 2-D simulation provides a reasonable estimate of the wave profile and the formation of a plunging jet, which is considered the laminar structure before jet impingement occurs, the effects of the Bond number on the evolution of the wave profile and breaking characteristics of plunging breakers are determined by examining extensive cases with a wide range of Bond numbers. The Bond number increases from 6000 to 80000 in increments of 2000, while all other parameters remain constant. Note that $Bo = 8600$ refers to the surface tension between air and water in the experiments. Previous studies have revealed that a larger value of Bo results in greater separation between the wavelength and Hinze scale, necessitating the use of costly numerical resources if all scales are to be resolved (Wang *et al.*, 2016). Our high-resolution meshes that benefit from adaptive mesh refinement criteria can resolve breakers with greater separation between length scales, allowing us to vary Bo over a wide range. For instance, for $Bo = 80000$, the capillary length $l_c = \sqrt{d^2/Bo} = 0.884$ mm, and the capillary length relative to the smallest grid size $l_c/\Delta \sim 5$ at $l_{max} = 15$. A similar capillary length to the smallest grid size ratio was utilized in the three-dimensional

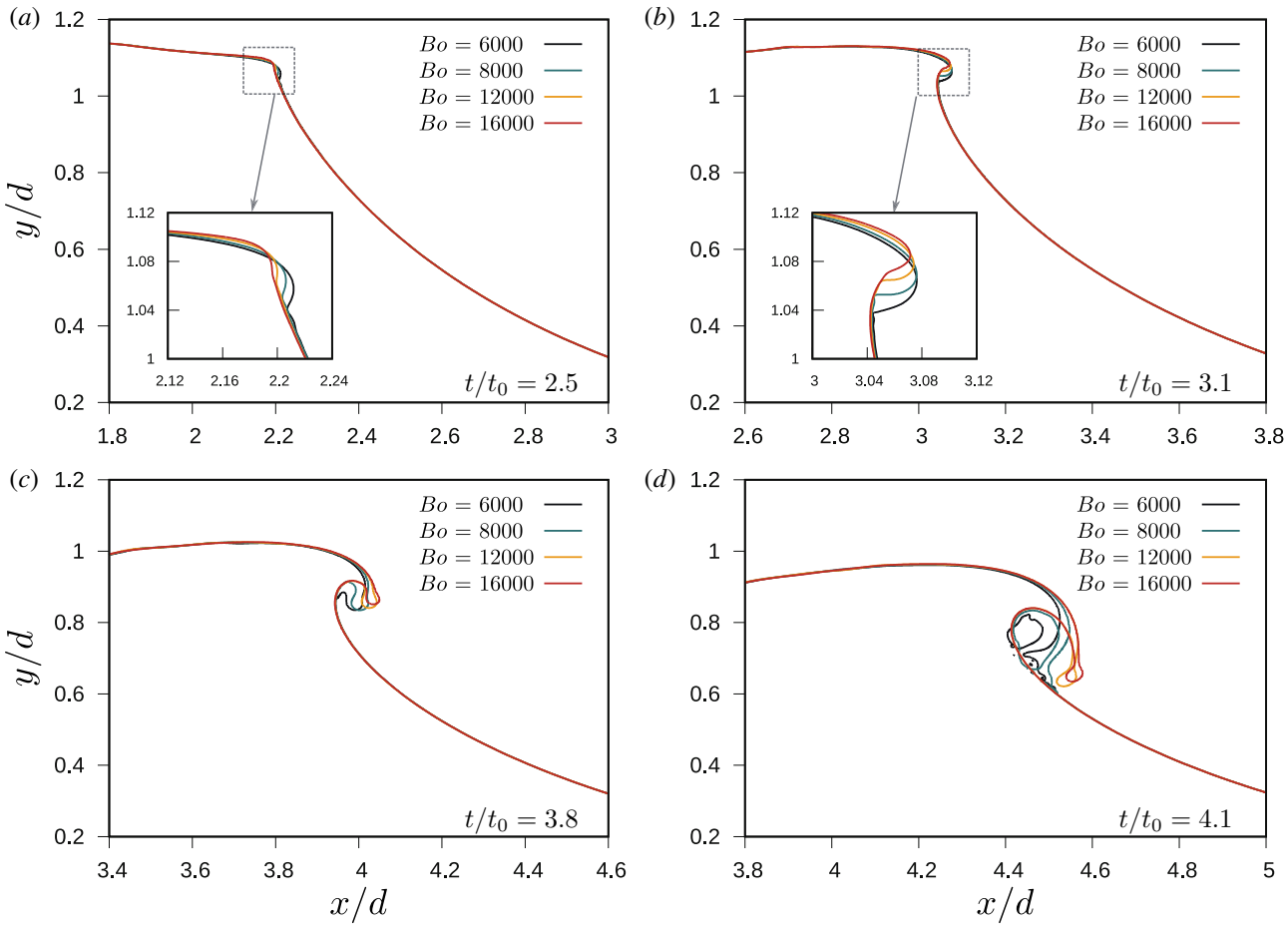

Figure 4.10: The spatial evolution of the free surface and the development of overturning jet for wave 1 at various Bond numbers when t/t_0 = (a) 2.5, (b) 3.1, (c) 3.8, (d) 4.1.

wave-breaking DNS of $Re = 100000$ and $Bo = 1000$ by Mostert *et al.* (2022). Additionally, a grid number of 6.4 was employed to represent the initial sheet for investigating the motion and stability of the edge of a liquid sheet in 2-D. A rim forms at the edge of the free end of the sheet, and a neck appears just behind the rim, resembling the phenomena observed in the stretching of the plunging jet (Fuster *et al.*, 2009). These applications suggest that the current grid resolution is adequate for capturing the formation and geometry of the plunging jet. In addition, a convergence study was conducted to assess the ability of our 2-D simulation to capture the formation and geometry of the plunging jet, considering three different l_{max} values of 14, 15, and 16 for $Bo = 80000$. As shown in figure 4.9, we observe that the agreement between l_{max} = 15 and 16 is better than that between l_{max} = 14 and 15, and the results for $l_{\max} = 15$ and 16 are nearly coincident. This suggests that l_{max} = 15 is sufficient for achieving grid convergence, even at relatively high Bond numbers.

Figure 4.10 illustrates the evolution of the wave profile under various Bond numbers at t/t_0 = 2.5, 3.1, 3.8,

and 4.1. Qualitatively, the wave profile evolution does not exhibit a significant influence of Bo. The impact of Bo primarily manifests in the development of the plunging jet, which features a rounded edge due to capillary retraction (Fuster *et al.*, 2009). At t/t_0 = 2.5, the generated wave crest experiences the effects of surface tension, resulting in a bulge on the front face of the steepening wave crest. The inset of figure 4.10(a) reveals a smaller bulge with an increasing Bond number, accompanied by a slightly larger wave height prior to breaking. This behavior indicates that surface tension induces capillary ripples on the forward face of the wave, leading to a bulge on the water surface. Experimental studies by Perlin *et al.* (1996) captured the appearance of parasitic capillary waves on the upper section of the vertical wavefront, specifically along the highest elevations of the lower front face of the plunging wave. Moreover, Diorio *et al.* (2009) observed that the bulge and capillary waves on the crest-front faces of the spillers at breaking onset are self-similar, independent of the breaking-wave-generation mechanism. This geometric similarity is limited to the crest-front profiles of the spillers and is attributed to the crest flow being dominated by surface tension and gravity. For larger Bond numbers where the influence of surface tension is negligible, a smaller bulge is formed. The slopes of the free surface upstream of the toe and the curvature of the bulge appear to increase with surface tension. The profile shapes and trends depicted in figure 4.10(a) exhibit qualitative similarities to numerical simulations of deep-water plunging and spilling breakers reported by Perlin *et al.* (1996) and Diorio *et al.* (2009). However, the detailed quantitative characteristics of the capillary ripples are beyond the scope of this study and are not discussed here. At t/t_0 = 3.1 (figure 4.10(b)), as the horizontal asymmetry of the wave profile develops further, the edge of the bulge erupts from a point just forwards of the crest and becomes tangent to the wave direction, presenting different widths of the bulge due to different surface tensions. The bulge due to surface tension projects forwards and develops into a plunging jet at t/t_0 = 3.8 (figure 4.10(c)), and a thicker jet can be observed at a smaller Bond number, indicating that jet thickness is dependent on the Bond number due to capillary effects caused by surface tension. Figure 4.10(d) shows that at t/t_0 = 4.1, the plunging jets at Bo = 6000 and 8000 impact the rising wavefront, ingesting a tube of air, while the plunging jets at Bo = 12000 and 16000 still need more time to form the cavity. As the Bond number increases, the instant at which the plunging jet impinges on the front of the wave is delayed, and the plunging jet becomes thinner and projects farther forwards ahead of the wave, entrapping more air into the wave.

The cross-sectional shape of the air cavity is affected by surface tension. Increasing the effect of surface tension causes the plunging jet to thicken and reduces the volume of air entrapped at the jet impact. The geometric properties of the main cavity caused by plunging breakers are identified by New (1983), showing that

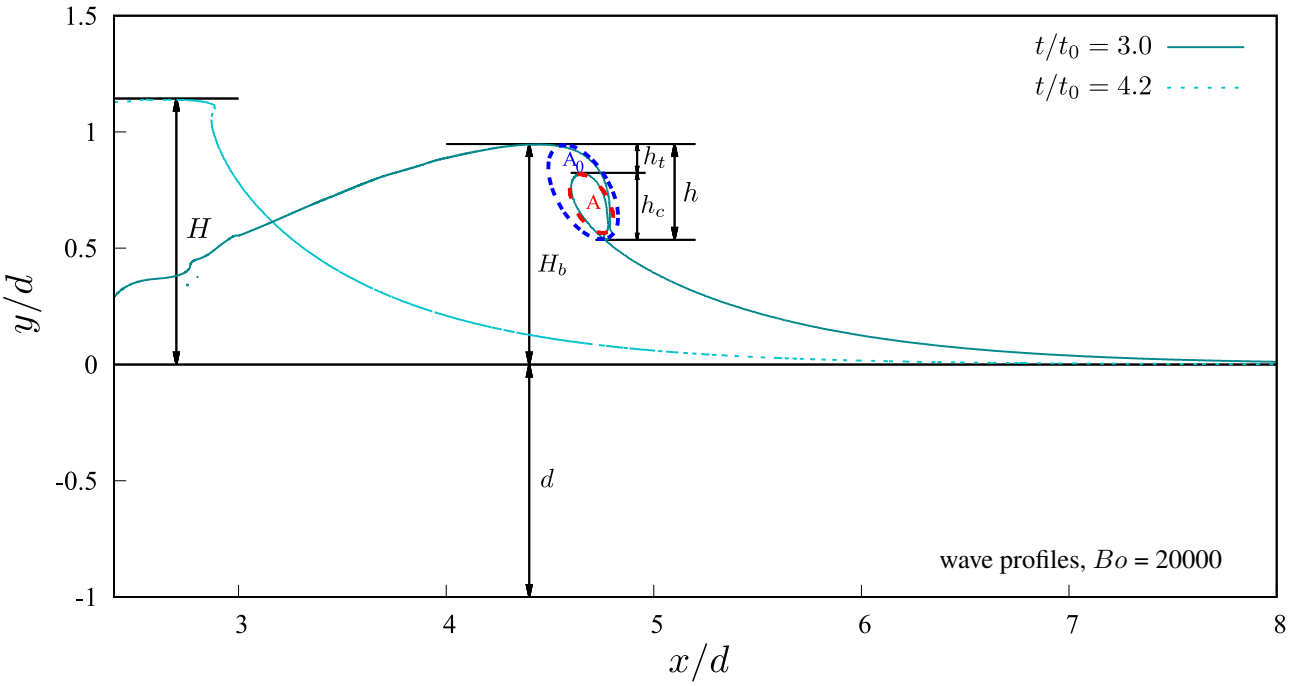

Figure 4.11: Estimation of the breaking height h, which is the sum of the height from the breaking crest to the cavity top h_t and the vertical height of the main cavity h_c. The main cavity size A is assumed to be proportional to ${h_c}^2$, which can be normalized by $A_0 \propto h^2$, giving that $A/A_0 \propto (h_c/h)^2$.

the surface profiles underneath the overturning crest may be represented by an ellipse of axes ratio $\sqrt{3}$, with its major axis rotated at an angle of approximately $60°$ to the horizontal. A similar shape can be confirmed in our cases as shown in figure 4.11. The vertical height of the main cavity h_c, calculated as $h_c = h - h_t$, is closely related to the size of the main cavity entrapped by the plunging jet, where h is the breaking height and h_t is the height from the breaking crest to the cavity top. The cross-sectional area of the initially ingested cavity in the breaking process can be estimated by applying the ellipse area formula $A = \pi(h_c/sin60°)^2/4\sqrt{3}$, where h_c is the vertical height of the main cavity. By normalizing the main cavity using the cross-sectional area A_0, we obtain $A/A_0 \propto (h_c/h)^2$. A new scaling regarding the cavity correction factor for the entrained cavity is proposed as $A/A_0 = ((h - \pi l_c)/h)^2$ by Mostert *et al.* (2022), with very good agreement at high Bond numbers and weaker agreement at lower Bond numbers. This indicates that $h_c = h - \pi l_c$, where l_c is the capillary length. Similar scaling can be proposed, but a coefficient of 0.6 should be used to mediate the difference between the width of the jet and the breaking height when it exhibits a greater separation between the wave scale and capillary length due to the larger Bond number in the present work, which gives $A/A_0 = (0.6(h - \pi lc)/h)^2$.

Figure 4.12(a) illustrates the geometry of the main cavity when the plunging jet connects with the front of

the wave at t/t_0 = 4.32. It is observed that the size of the main cavity appears to be independent of the surface tension when increasing the Bond number, indicating a convergence of the main cavity size as the Bond number increases. Figure 4.12(b) shows very good agreement between this scaling and the present DNS results. As previously stated, the wave jet becomes thinner and projects farther forwards ahead of the wave as the surface tension decreases. It exhibits a breaking height h_0 in the absence of surface tension, which represents the maximum value of all breaking heights when surface tension is considered. The decreased breaking height caused by the shortened project distance normalized by d is proportional to the cube of the capillary length normalized by d, which gives $(h_0 - h)/d \propto (l_c/d)^3$, as shown in figure 4.12(c), while h_t remains constant under a distinct Bond number. Figure 4.12(d) shows the comparison of the numerical results of h/d to the estimated values of h/d calculated using $h_0/d - C(l_c/d)^3$ by the proposed power-law scaling, with C being a proportionality constant.

4.5.2 Breaking onset criteria

This section develops the relationship between wave parameters, i.e., maximum wave height before breaking H [L], breaking-wave crest H_b [L] of the plunging breaker, and the initial conditions used to generate waves in this study by numerical data fitting, following the above dimensional analysis as stated in (3.19) and (3.20):

$$\frac{H}{d} = f_H(Re, Bo, \frac{s}{d}, \frac{fd}{c}) \tag{4.1}$$

$$\frac{H_b}{d} = f_{H_b}(Re, Bo, \frac{s}{d}, \frac{fd}{c}) \tag{4.2}$$

As discussed in section 4.5.1, Re and Bo do not significantly influence the wave characteristics, so the wave is considered independent of Re and Bo when discussing the scaling of H and H_b to the initial conditions. Thus,

$$\frac{H}{d} = f_H(\frac{s}{d}, \frac{fd}{c}) \propto (\frac{s}{d})^{\alpha_H}(\frac{fd}{c})^{\beta_H} \tag{4.3}$$

$$\frac{H_b}{d} = f_{H_b}(\frac{s}{d}, \frac{fd}{c}) \propto (\frac{s}{d})^{\alpha_{H_b}}(\frac{fd}{c})^{\beta_{H_b}} \tag{4.4}$$

This dimensional analysis demonstrates the dependence of the wave characteristics on the dominant dimensionless variables derived from the initial conditions. Their quantitative relations are investigated by conducting various cases for different combinations of s, f and d to determine the corresponding coefficients in the dimensionless expressions.

First, the wave characteristics are estimated from the simplified theory for plane wavemakers. In shallow water, a simple theory for the generation of waves by wavemakers was proposed by Galvin (1964), who reasoned

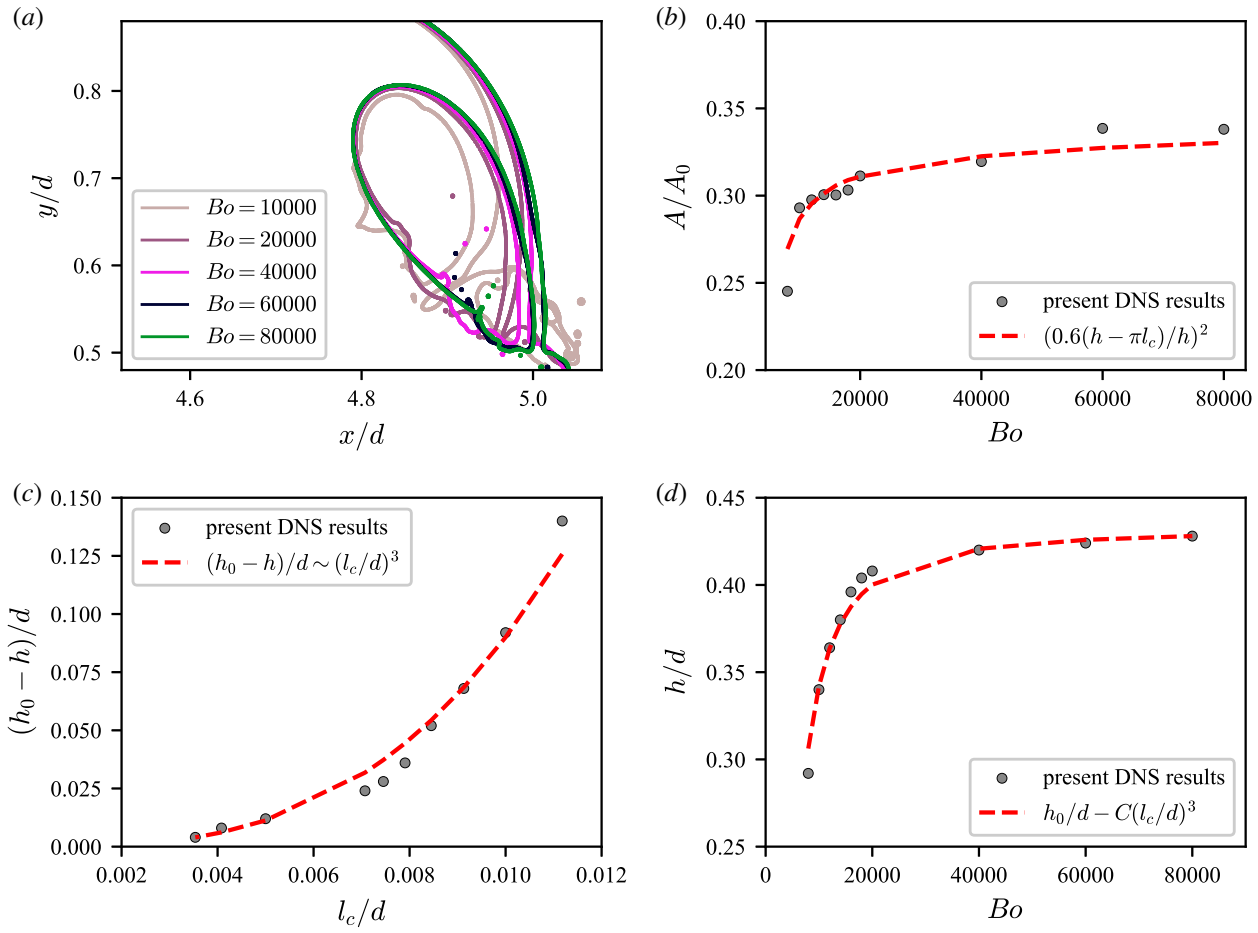

Figure 4.12: Estimation of the main cavity size and breaking height. (a) The geometry of the main cavity when the plunging jet connects with the front of the wave at $t/t_0 = 4.32$ under various Bond numbers. (b) Relationship between cavity area and Bond numbers. (c) A linear relationship between the decreased breaking height caused by shortened project distance and the capillary length, $(h_0 - h)/d \propto (l_c/d)^3$. (d) A scaling to estimate the breaking height at different Bond numbers.

that the water displaced by the wavemaker should be equal to the crest volume of the propagating wave form. As breaking waves are generated by a piston wavemaker with a stroke of s over a constant water depth d, the volume of water displaced over a whole stroke is sd. If the resulting waves are vertically symmetric with one single crest before breaking, then the crest volume of the propagating waveforms in a wavelength is $\int_0^{L/2}(H/2)(1-\cos kx)\mathrm{d}x = HL/4$, where L is the wavelength and $k = 2\pi/L$ is the wavenumber; equating the two volumes gives

$$sd = \frac{HL}{4} \tag{4.5}$$

According to the dispersion relation of shallow-water waves, the wavelength is $L = T\sqrt{gd}$. Then the resulting connection between the wave height and the initial conditions of the wave plate can be expressed as

$$\frac{H}{d} = \frac{4s}{T\sqrt{gd}} \tag{4.6}$$

Notably, the wave parameters H, L and T in this expression are theoretical values and do not represent the real values in actual waves, which already break before forming a symmetrical waveform, but it provides us with a possible relationship that can be used to determine the fit to the numerical data.

Then, the scaling of the maximum wave height before breaking H of the experimental waves generated by the wave plate is fitted through the numerical results under various initial conditions. It can be seen from (4.3) that $H/d \propto s^{\alpha_H} f^{\beta_H} d^{\beta_H/2-\alpha_H} g^{-\beta_H/2}$, so $H \propto s^{\alpha_H} f^{\beta_H} d^{\beta_H/2-\alpha_H+1} g^{-\beta_H/2}$. At the same frequency f, numerical results show that $H/d \propto sd^{-1/2}$ and $H \propto sd^{1/2}$, so we have $\alpha_H = 1$ and $\beta_H = 1$; thus, it gives

$$\frac{H}{d} \propto \frac{sf}{\sqrt{gd}} \propto \frac{U_{max}}{c} \tag{4.7}$$

where $U_{max} = s\pi f$ is the maximum wave plate velocity and $c = \sqrt{gd}$ is the linear velocity. This is quite similar to the theoretical result proposed in (4.6). Furthermore, the scaling of the breaking-wave crest H_b with the initial conditions is also fitted through the numerical results. Based on the same method of analyzing the numerical data, the exponents in the power-law scaling can be determined as $\alpha_{H_b} = 2/3$ and $\beta_{H_b} = 1/3$; thus

$$\frac{H_b}{d} \propto (\frac{s}{d})^{2/3}(\frac{fd}{c})^{1/3} \tag{4.8}$$

Figure 4.13 (a) and (b) show the relationship between the normalized maximum wave height before breaking H/d and breaking-wave crest H_b/d to the initial conditions. A linear correlation between the maximum wave height before breaking H and the maximum wave plate speed U_{max} is revealed, showing that the wave height increases as the maximum wave plate speed increases. As indicated in Table 4.2 and figure 4.13(a), the generated

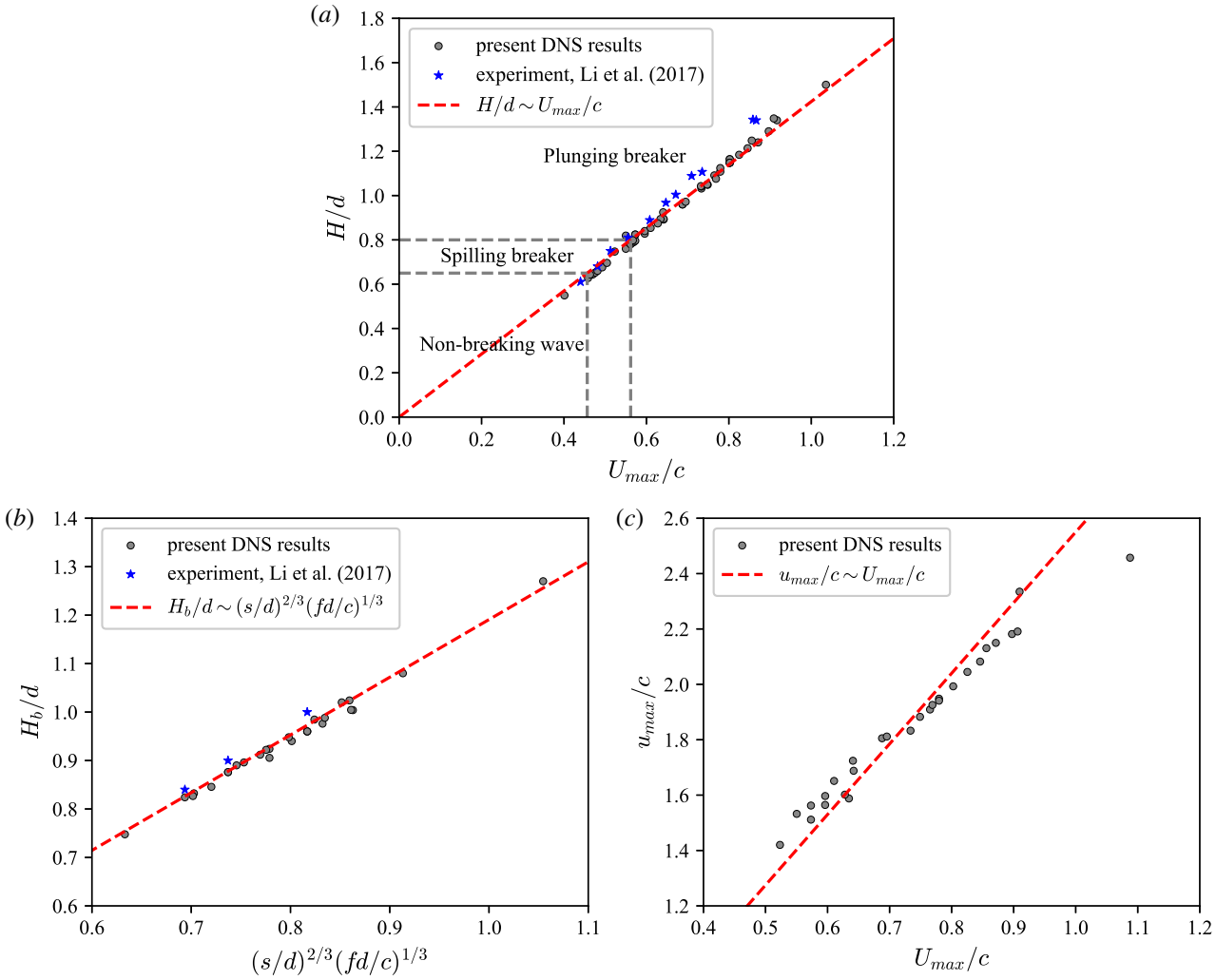

Figure 4.13: Scaling for the maximum wave height before breaking (a) and breaking wave crest (b) with respect to the initial conditions. Normalized wave height from (4.3) with the parameters $\alpha_H = 1$ and $\beta_H = 1$. This indicates that the wave height normalized by the water depth is proportional to the maximum wave plate velocity normalized by the wave phase speed. (b) The normalized breaking wave crest from (4.4) with the parameters $\alpha_{H_b} = 2/3$ and $\beta_{H_b} = 1/3$. (c) Relationship between the maximum fluid particle velocity before jet impact and the maximum wave plate speed.

U_{max}/c	H/d	regular	spilling	plunging
0.476	0.652	✓		
0.482	0.660		✓	
0.570	0.792		✓	
0.573	0.796			✓

Table 4.2: Breaking type identification at different ratios of wave height to water depth H/d.

wave remains non-breaking for $H/d \leq 0.652$, and breaks for $H/d \geq 0.660$. The breaking is of the spilling type for $0.660 \geq H/d \leq 0.792$ whereas it is of the plunging type for $H/d \geq 0.796$. The above results agree with the measurement done by Li (2017), who showed that the critical value for spilling and plunging wave is $H/d = 0.8$. For plunging breakers, a linear correlation between breaking-wave crest H_b and initial conditions is also proposed, which is in good agreement with the numerical results. We also present the relationship between the maximum fluid particle velocity at the moment of jet impact and the initial conditions. Figure 4.13 (c) demonstrates a generally linear dependence between $u_{\max}/c$ and $U_{\max}/c$, where lower values of $U_{\max}/c$ tend to correspond to higher values of $u_{\max}/c$, while larger values of $U_{\max}/c$ result in lower values of $u_{\max}/c$. Deviations from this linear dependence may be attributed to nonlinearity and asymmetry introduced by our wave-making method. Waves associated with larger $U_{\max}/c$ break earlier, limiting the acceleration of water particles, whereas waves corresponding to smaller $U_{\max}/c$ receive energy from the rear side of the wave crest. In addition, the shoaling effect induced by higher nonlinearity leads to an increase in wave height and a decrease in fluid particle velocity.

4.5.3 Energy dissipation due to breaking

The energy dissipation rate due to breaking can be defined as $\epsilon_l = \Delta E_m/\Delta t$, which is the average decrease in the conservative energy E_m over the active breaking period Δt. Notably, different studies have adopted varying definitions for the active breaking period. For instance, in the laboratory measurements conducted by Drazen and Kirby (2008) on deep-water breaking due to dispersive focusing, the duration of the breaking event is determined by differencing the start and stop times of breaking from the spectrogram of the hydrophone signal. On the other hand, when considering breaking solitary waves on plane slopes in shallow water, Mostert & Deike (2020) defined the active breaking period as commencing when the wave face becomes vertical and ending when the kinetic energy E_k equals the potential energy E_p. This definition ensures that the contribution of bottom boundary layer friction during run-up is excluded from the calculation of the dissipation during breaking. In the current case, where the wave breaks due solely to nonlinearity in a tank with a level bottom, the dominant mechanism of dissipation comes from viscous dissipation by turbulence in the upper layers. If we assume that most of the viscous dissipation occurs while the wave is actively breaking, then the active breaking phase ends when the energy dissipation rate slows. As shown in figure 4.8(d), (e), and (f), the energy dissipation rate initially exhibits a rapid increase with time, reaching its maximum at approximately $(t - t_{im})/t_0 = (1/(2f))/t_0$. Subsequently, the dissipation rate remains relatively constant for a duration of

$1/(2f)$, after which it begins to decay. A noticeable decay in the energy dissipation rate can be observed at approximately $(t - t_{im})/t_0 = (3/(2f))/t_0$, which may indicate the end of the active breaking stage. Therefore, in this study, the active breaking period is defined as the period starting when the jet impacts and lasting $\Delta t = 3/(2f)$, once the quasi-equilibrium stage has ended and the energy dissipation rate begins to decay.

The physical parameters for the energy budget are the total energy per unit length transferred by the motion of the wave plate E_l [ML/T^2] and the energy dissipation per unit length of the wave crest ϵ_l [ML/T^3] for plunging breakers. Then, the dimensional analysis for the energy budget gives

$$\frac{E_l}{\rho g d^3} = f_{E_l}(Re, Bo, \frac{s}{d}, \frac{fd}{c}) \tag{4.9}$$

$$\frac{\epsilon_l}{\rho g^{3/2} d^{5/2}} = f_{\epsilon_l}(Re, Bo, \frac{s}{d}, \frac{fd}{c}) \tag{4.10}$$

Likewise, the energy budget is assumed to be independent of the Reynolds number and Bond number. Thus,

$$\frac{E_l}{\rho g d^3} = f_{E_l}(\frac{s}{d}, \frac{fd}{c}) \propto (\frac{s}{d})^{\alpha_{E_l}} (\frac{fd}{c})^{\beta_{E_l}} \tag{4.11}$$

$$\frac{\epsilon_l}{\rho g^{3/2} d^{5/2}} = f_{\epsilon_l}(\frac{s}{d}, \frac{fd}{c}) \propto (\frac{s}{d})^{\alpha_{\epsilon_l}} (\frac{fd}{c})^{\beta_{\epsilon_l}} \tag{4.12}$$

We first determine the relationship between the total energy per unit length and the initial conditions. According to linear wave theory, the total energy per wave unit width is given by $E_l = \rho g H^2 L/8$. Thus, the dimensionless wave energy can be expressed as $E_l/(\rho g d^3) = H^2 L/(8d^3)$. Assuming that the generated wave has the same frequency as the wave plate, we can calculate the nominal wavelength L using the dispersion relationship in shallow water, i.e., $L = T\sqrt{gd} \propto \sqrt{gd}/f$. Furthermore, we have derived the scaling between wave height and the initial conditions as $H/d \propto sf/\sqrt{gd}$. Consequently, we find that $E_l/(\rho g d^3) = H^2 L/(8d^3) \propto (s/d)^2 (fd/c)$. Therefore, the scaling of the energy budget with respect to the initial conditions is determined by $\alpha_{E_l} = 2$ and $\beta_{E_l} = 1$ and can be described as

$$\frac{E_l}{\rho g d^3} \propto (\frac{s}{d})^2 (\frac{fd}{c}) \tag{4.13}$$

Figure 4.14 shows the relationships between the total energy transferred by the motion of the wave plate E_l and the initial conditions. It is evident that the measured total energy from the numerical data is generally in agreement with the estimated results from the initial conditions. However, in the lower range of total energy, which corresponds to lower nonlinearity, the estimated total energy derived from the initial conditions tends to underestimate the measured total energy.

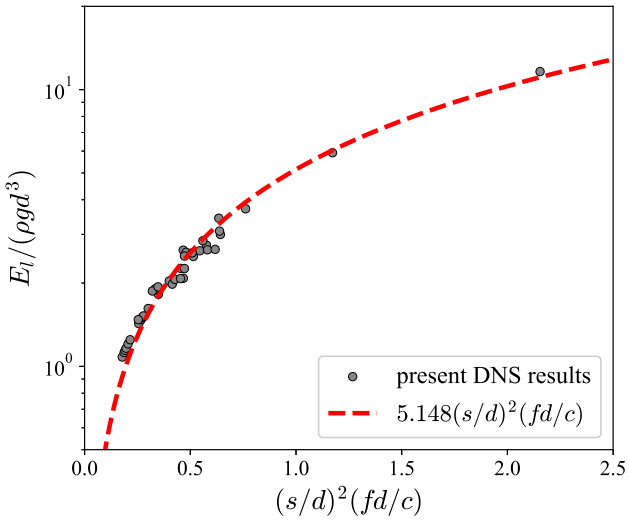

Figure 4.14: Scaling for the total energy transferred by the motion of wave plate E_l. Normalized total energy from (4.13) with the parameters $\alpha_{E_l} = 2$ and $\beta_{E_l} = 1$.

Next, we aim to establish a scaling relationship between the energy dissipation rate during wave breaking and the wave parameters. This scaling is based on an inertial model for estimating the energy dissipation rate, similar to the approach employed by Drazen *et al.* (2008) for deep-water breakers and Mostert & Deike (2020) for shallow-water breakers. We seek to validate the applicability of this framework in predicting energy dissipation during breaking in shallow water over a flat-bed geometry. To establish a connection between the isotropic turbulence assumption and the empirical relationship, accurate estimations are required for the turbulent integral length scale l, the characteristic velocity scale w, and the turbulent cloud cross-section A. In the study by Drazen *et al.* (2008) on plunging breaking waves in deep water, an inertial model is employed to estimate the dissipation rate, using the local wave height h and velocity at impact as the length and velocity scales, respectively. The trajectory of the toe, as measured in the experiment, indicates that the toe of the breaker is in freefall under gravity, descending a height h. Consequently, the vertical velocity of the toe at impact can be approximated as $w = \sqrt{2gh}$. By assuming a cylindrical cloud of turbulence of cross-sectional area $A = \pi h^2/4$ and applying the linear dispersion relationship in deep water, they argued that the breaking parameter b should be proportional to $S^{5/2}$, where $S = hk$ is the local slope at breaking. Following the same inertial model, Mostert & Deike (2020) quantified the energy dissipation caused by breaking solitary waves in shallow water on a gentle slope. They determined the impact velocity of the plunging jet as $w = \sqrt{2gH_b}$, where H_b is the wave height at breaking. The turbulent integral length scale l is estimated by the undisturbed depth at breaking d_b, as d_b sets the upper limit on the size of eddies that form from the breaking process. This was corroborated by examining

the vorticity in the liquid phase during the breaking event, which demonstrated that the mixing zone reaches the slope bed and is constrained by the depth. Utilizing the inertial model, they established a relationship between the dissipation resulting from wave breaking during the active breaking period and the local wave height, depth and beach slope, denoted as $b \propto (H_b/d_0)^{7/2}(d_b/d_0)^{-1}$, where d_0 is the water depth before the wave enters the slope. The same estimation method utilized by Mostert & Deike (2020) can be applied to our breaking waves in shallow water. However, there are notable distinctions between our breaking waves and the wave breaking on a slope examined in their work. Unlike waves breaking on a slope, our waves propagate in a tank with a flat bottom and break due to strong nonlinearity. Although in many cases the breaking height H_b exceeds the water depth d, since the plunging jet descends from a wave crest and impacts the wavefront, the mixing zone is situated near the initial water depth and is still bounded by the breaking height H_b. This can also be supported by the vorticity field during the postbreaking period, as depicted in figure 4.7. By considering a cylindrical cloud of turbulence with a cross-sectional area of $A = \pi {H_b}^2/4$, a vertical height of H_b and an impact velocity of the toe $w = \sqrt{2gH_b}$, the dissipation per unit length along the wave crest is

$$\epsilon_l = \rho A \epsilon = \rho \frac{\pi {H_b}^2}{4} \frac{\sqrt{2gH_b}^3}{H_b} \propto \rho g^{3/2} {H_b}^{5/2} \tag{4.14}$$

$$b = \frac{\epsilon_l}{\rho c^5/g} = \frac{\epsilon_l}{\rho g^{3/2} d^{5/2}} \propto (\frac{H_b}{d})^{5/2} \tag{4.15}$$

This scaling demonstrates that the dominant dimensionless variable describing the energy dissipation by breaking in shallow water is the ratio of H_b and d. Multiple experimental measurements have demonstrated that energy dissipation associated with wave breaking exhibits a threshold dependence on S, with the dissipation rapidly approaching zero at low values of S. Drawing on laboratory data from various sources, Romero *et al.* (2012) proposed a semiempirical result by introducing a slope-based breaking threshold S_0, which can be expressed as $b = a(S - S_0)^n$, where a is a constant and S_0 is a threshold slope for breaking. Based on a visual fit through the data, a power of $5/2$ consistent with the inertial scaling of Drazen *et al.* (2008), as well as a slope threshold of $S_0 = 0.08$ and a scaling factor of $a = 0.4$ were obtained. In the shallow-water cases, our numerical results also reveal a threshold behaviour in the energy dissipation associated with wave breaking. As shown in figure 4.15 (a), the green dotted line represents a fit to the inertial scaling $b = a(H_b/d)^{5/2}$ with a coefficient value of $a = 0.06$. However, when the inertial scaling is extended to smaller values of H_b/d, it overestimates the dissipation rate compared with the numerical data. This discrepancy clearly indicates that the energy dissipation approaches zero at low values of H_b/d, exhibiting threshold behaviour. To account for this observation, we adopt a semiempirical scaling relationship of the form $b = a(H_b/d - \chi_0)^n$, where χ_0 denotes

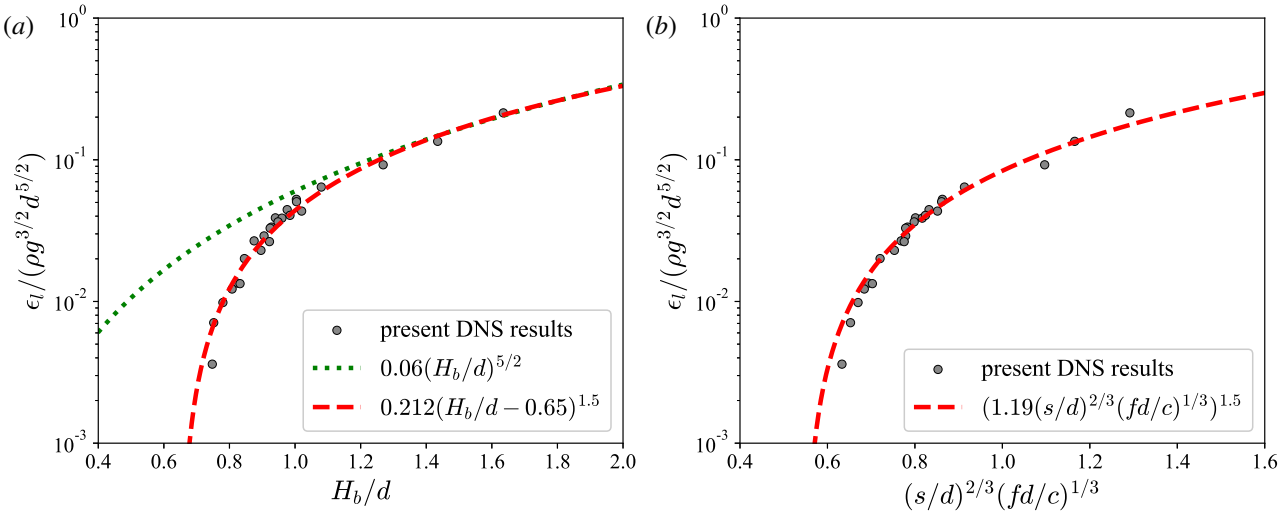

Figure 4.15: Scaling for the energy dissipation per unit length of the breaking wave ϵ_l (a) with respect to the initial conditions. (a) Scaling for energy dissipation per unit length of the breaking wave ϵ_l with respect to local breaking parameters H_b/d, as shown in (4.16). (b) Normalized energy dissipation rate based on the relationship between the breaking wave crest H_b/d and the initial conditions.

the critical value for H_b/d. By fitting the numerical data, we can obtain the best-fitting parameters for this scaling relationship

$$\frac{\epsilon_l}{\rho g^{3/2}d^{5/2}} = a(\frac{H_b}{d} - \chi_0)^n = 0.21(\frac{H_b}{d} - 0.65)^{1.5} \tag{4.16}$$

This reveals a threshold value of $\chi_0 = 0.65$ and a power law scaling of $n = 1.5$. Figure 4.15 (a) illustrates the fitted curve that smoothly connects all the numerical data. Notably, the obtained threshold χ_0 closely aligns with the breaking criterion $H/d = 0.65$, which distinguishes between breaking and non-breaking waves. Note that this link between the energy dissipation rate and the local breaking parameters is applicable to plunging breakers. Although spilling waves exist within the H_b/d range of 0.65-0.76, the dissipation associated with spilling breakers is not depicted in this context. The validation of the relationship between dissipation caused by spilling breakers and local breaking parameters would require additional data, but it exceeds the scope of this discussion. This critical value for H_b/d can be justified by the absence of energy dissipation in non-breaking waves. It is worth highlighting that in deep water scenarios, the scatter of the data at high values of S and the relatively small threshold slope S_0 allow for retaining the power law of $5/2$ in the inertial scaling proposed by Drazen *et al.* (2008) when the slope threshold is introduced. However, in shallow-water cases, the critical value $\chi_0 = 0.65$ significantly modifies the power law from the inertial scaling of $5/2$ to 1.5. As stated in section 4.5.2, based on the relationship of the normalized breaking-wave crest to the initial conditions $H_b/d = 1.19(s/d)^{2/3}(fd/c)^{1/3}$, the energy dissipation rate can also be connected to the initial conditions.

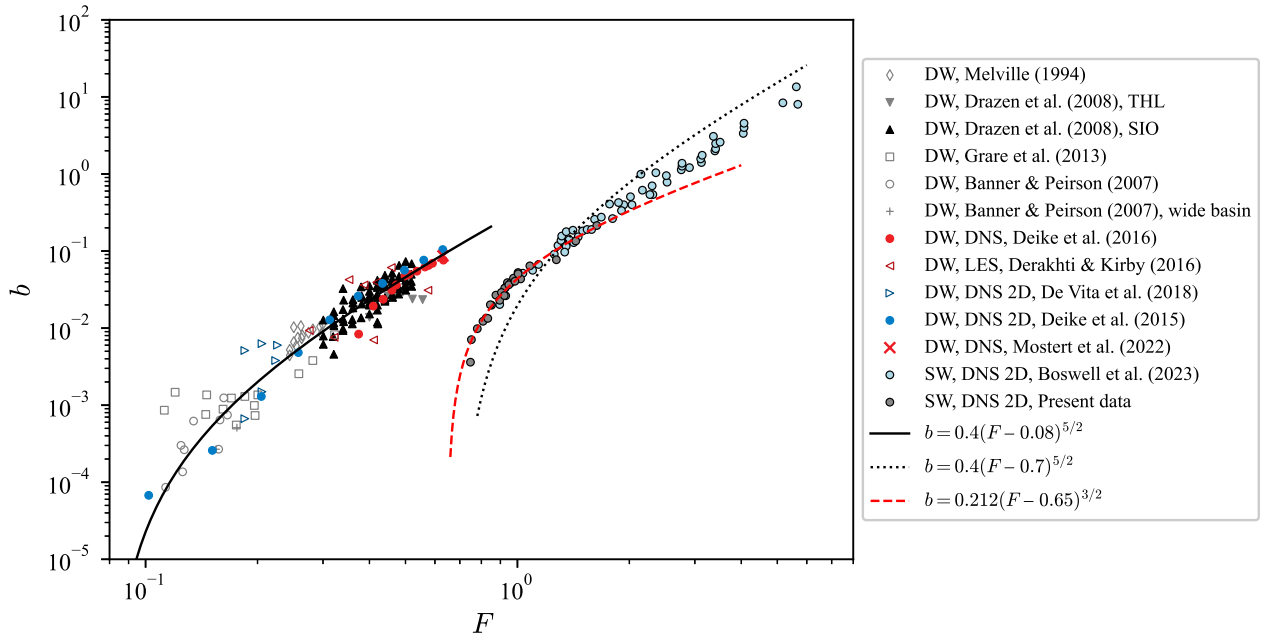

Figure 4.16: Energy dissipation from laboratory experiments and numerical simulations: DW, deep water; SW, shallow water. The solid line is the semiempirical formulation in deep water regimes, $b = 0.4(F - 0.08)^{5/2}$ (Romero *et al.* (2012)), with breaking threshold $F* = 0.08$, while the dotted line is the semiempirical formulation in deep water regimes proposed by Boswell *et al.* (2023) with $F* = 0.65$. The dashed line is a visual fit through the present data, giving $b = 0.212(F - 0.65)^{1.5}$.

Figure 4.15 (b) shows a good dependence between the energy dissipation rate and the initial conditions.

Based on the aforementioned analysis, the magnitude of the breaking parameter b in shallow-water breaking waves is influenced by the ratio of the local breaking crest height to the water depth, highlighting the significant role of water depth in energy dissipation in shallow water. The breaking parameter b exhibits a threshold dependence on H_b/d, rapidly tending to zero for low values of H_b/d. As H_b/d increases, the breaking parameter asymptotically converges to the inertial scaling of $5/2$. These findings, which combine a local inertial turbulent argument and empirical results through least squares fit to the numerical data, establish a relationship between the dissipation rate and wave parameters, providing predictive insights into the dissipation rate of breaking waves in shallow water. A comparative analysis was conducted using data from the literature in both deep water (sourced from Deike (2022)) and shallow water (sourced from Boswell *et al.* (2023)) conditions. As originally proposed by Beji (1995) and subsequently applied in the numerical investigation conducted by Boswell *et al.* (2023), a nonlinearity parameter $F = ga/c^2$ was used to connect the two distinct regimes, where a is a representative amplitude and c is a phase speed. In deep water, where $c = \sqrt{g/k}$, the nonlinearity parameter

$F \sim ak = S$ corresponds to the wave slope, while it converges to a/d in shallow water, with $c = \sqrt{gd}$. In our cases, F approaches H_b/d as $a \sim H_b$. Figure 4.16 shows the breaking parameter b for deep-water breakers from a variety of experimental and numerical sources (Kendall Melville, 1994; Drazen *et al.*, 2008; Grare *et al.*, 2013; Banner & Peirson, 2007; Deike *et al.*, 2016; Derakhti & Kirby, 2016; De Vita *et al.*, 2018; Deike *et al.*, 2015; Mostert *et al.*, 2022), along with the shallow-water dataset from Boswell *et al.* (2023) and the present study. The breaking dissipation in this study falls between the previously established deep-water regimes and the shallow-water breaking waves documented by Boswell *et al.* (2023), and shows favourable consistency within the range of overlap between our data and Boswell's data. Furthermore, our data extend the left-hand boundary of this range by extending the nonlinearity parameter, specifically, H_b/d from 0.85 to 0.75. This particular range displays a discernible diminishing trend in the breaking parameter b as the nonlinearity parameter F decreases. A similar trend can also be observed in Boswell's data. However, there is a clear discontinuity between the deep-water and shallow-water regimes, rendering a single power-law scaling inadequate for capturing both datasets. As introduced by Romero *et al.* (2012), a heuristic examination of the breaking threshold was undertaken to fit the extensive experimental and numerical observations in deep-water scenarios, yielding a semiempirical formulation $b = 0.4(S - 0.08)^{5/2}$, where $S \sim F$ under deep-water conditions. Notably, Boswell *et al.* (2023) made a commendable effort to address the discontinuity across various depth regimes using the same concept of breaking threshold dependence, and a slope threshold $F* = 0.7$ was determined in Boswell's shallow-water solitary wave cases. In our cases, the critical breaking threshold $F*$ was determined to be 0.65 through the best fit to our numerical data. The expression $b = 0.212(F - 0.65)^{1.5}$ collapses the DNS data presented in the present study favourably. However, the proposed semiempirical scaling fails to encompass the DNS data of shallow-water solitary breaking waves from Boswell *et al.* (2023).

Upon analyzing the wave speed, we infer the experimental wave to exhibit solitary wave characteristics. Employing these experimental waves, we can effectively examine the dissipation induced by breaking in shallow water. Nevertheless, for waves with F values bridging those of deep and shallow water datasets, the corresponding F values lack definitive physical significance. Accordingly, a supplementary investigation of breaking energy dissipation in theoretical intermediate water breaking waves is warranted to encompass various water depth regimes. The next step is to develop a comprehensive breaking parametrization. The available datasets summarized in figure 4.16 suggest the possibility of a varying breaking threshold, particularly in the context of transitioning between deep and shallow water conditions. We aim to propose a determination relation governing the breaking threshold to accommodate the different depth regimes. Based on the canonical

wave theory, the breaking boundary for deep-water waves is $H/L = 0.142$; for intermediate-water waves, the breaking boundary is $H/L = 0.142tanh(kd)$; and for shallow-water waves, the breaking boundary is $H/d = 0.78$. Considering the dependence of the threshold slope for breaking on the breaking parameter b, we deduce that the varying breaking boundary on different depth regimes plays a significant role in deriving the scaling law of the breaking dissipation if we want to develop a comprehensive breaking parametrization. To connect different depth regimes, the breaking parameter is determined as a function of a parameter H/L, where wavelength L is calculated based on the dispersion relation $\sigma^2 = gktanh(kd)$, with angular frequency $\sigma = 2\pi/T$, wavenumber $k = 2\pi/L$. The detailed analysis remains to be done in our future work.

4.6 Conclusion

This chapter was designed to determine the effect of the fluid properties and initial conditions on the dynamics, kinematics and energy dissipation in the breaking process by performing high-fidelity simulations of breaking waves generated by a piston-type wave plate using 2-D DNS. The investigation of the stroke and frequency of the wave plate has shown detailed information, including breaking characteristics, energy transfer and dissipation during wave breaking. A quantitative relationship between the main cavity size and the breaking height is presented based on the investigation of the influence of the Bond number on the evolution of the overturning jet. This reveals the effect of surface tension on the crest overturning process, which thickens the width of the plunging jet and shortens the distance that projects forwards ahead of the wave. The resulting wave height is estimated based on the simplified theory for plane wavemakers, and a reliable agreement is obtained between this theoretical result and our numerical data. The link between wave height and initial conditions indicates that waves can be classified as non-breaking waves, spilling breakers and plunging breakers based on the ratio of wave height to water depth H/d. The conventional dissipation scaling of turbulence theory is applied to the wave-breaking process, deriving a link between the energy dissipation rate and the ratio of the breaking-wave crest to the water depth H_b/d. By accounting for a threshold behaviour, an empirical scaling of the breaking parameter is proposed as $b = a(H_b/d - \chi_0)^n$, where $\chi_0 = 0.65$ represents the breaking threshold and $n = 1.5$ is a power law determined through the best fit to the numerical results. The proposed scaling laws quantitatively link the kinematics and dynamics of breaking waves to the local wave parameters and initial conditions, which may be of use for future theoretical analysis.

Chapter 5

3-D breaking waves simulations

Contents

Experimental measurements of wave breaking are typically confined to water due to technical constraints, and a comprehensive description of the energetic wave-breaking region is lacking (Wang *et al.*, 2016). Given the inherently three-dimensional nature of turbulence, bubbles, and droplets in wave breaking, we perform three-dimensional direct numerical simulations to resolve these structures in this chapter. Direct numerical simulations of wave breaking facilitate a detailed investigation of the small-scale physics directly, without the need for a turbulence model. However, one of the significant challenges in DNS is accurately resolving processes characterized by increasing separation of scales as the Reynolds number Re and Bond number Bo increase. Specifically, to faithfully capture the physics of breaking waves, the simulation must encompass all scales ranging from energy dissipation to the formation and breakup of bubbles and droplets within a two-phase turbulent environment. This requires capturing the full three-dimensional physics of the problem while retaining a qualitatively faithful representation of the breaking process in comparison with experimental observations. In this regard, the octree-based adaptive mesh refinement (AMR) scheme in the Basilisk solver emerges as an effective tool for attaining higher resolutions of small-scale turbulence than conventional uniform-grid approaches.

5.1 Numerical set-up

We numerically reproduce the wave flume experiments of Li (2017) by conducting three-dimensional direct numerical simulations of breaking waves. The numerical resolution is given by $\Delta = L_0/2^{l_{max}}$, where l_{max} is the maximum level of refinement in the AMR scheme. A CFL number of 0.5 is used to ensure numerical stability. The representation of water-air interfaces and the replication of the wave plate piston motion are achieved using VOF tracers. The piston is implemented by initializing a volume fraction field at each time step, which corresponds to the position and speed of the moving piston. This approach has been successfully employed in previous studies (Lin-Lin *et al.*, 2016; Wu & Wang, 2009). Since the moving piston is updated at each time step, the grids intersecting with the piston are consistently refined to the highest refinement level. This ensures an accurate representation of the moving boundary in the adaptive meshes. The refinement criteria are based on the wavelet-estimated discretization error in the velocity and VOF fields. Consequently, the mesh is refined as needed during wave initialization and propagation. The refinement algorithm is invoked at each time step to adjust the mesh whenever the wavelet-estimated error exceeds the prescribed threshold for both velocity and volume fraction fields. The default domain in Basilisk is a cube for 3-D simulations, so the initial numerical domain is 6 m $\times$ 6 m $\times$ 6 m. To optimize computational resources, we introduce a numerical wall,

Case	Re	Bo	Resolution	l_c/Δ
1	100 000	8 600	2048^3	0.920
2	100 000	8 600	4096^3	1.840
3	100 000	8 600	8192^3	3.681
4	50 000	8 600	8192^3	3.681
5	100 000	4 300	8192^3	5.205

Table 5.1: Parameter space for three-dimensional breaking waves. Case 1, 2, and 3, with maximum level of refinement l_{max} of 11, 12 and 13, respectively, are designed for mesh convergence study. Cases 3, 4, and 5, with varied Re and Bo, are used to investigate the effects of viscosity and surface tension. Δ/r_H, ratio of the smallest grid size to the Hinze scale, defined as $r_H = C(\gamma/\rho_w)^{3/5}\epsilon^{-2/5}$, where $C \approx 0.4$ is a dimensionless constant; l_c/Δ, ratio of the capillary length to the smallest grid size, where the capillary length is defined as $l_c = \sqrt{\gamma/\Delta\rho g}$; r_H/l_c, ratio of the Hinze scale to the capillary length.

narrowing the spanwise width in a manner similar to the numerical wave plate. The velocity is constrained to be zero outside the wall. Given that the mesh is refined according to the discretization error of velocity and volume fraction fields, the mesh outside the wall is maintained at the minimum level of refinement. This results in an effective spanwise width of 0.3 m, consistent with the dimensions of the experimental wave flume to be reproduced. We present three-dimensional simulations of breaking waves using air–water density and viscosity ratios of $1.29/1018.3$ and $1.39 \times 10^{-5}/1.01 \times 10^{-6}$, respectively, which are consistent with experimental values. Numerical simulations of breaking waves are confined typically to the highest Re accessible to available computation effort (Mostert *et al.*, 2022), we used a typical accessible Re of 100 000. We perform a convergence analysis for a case with s = 0.5334 m, f = 0.75 Hz, and d = 0.25 m, under the conditions of Re = 100 000 and Bo = 8 600. After validating mesh convergence, we conduct three numerical cases with varied viscosity and surface tension. A summary of these cases and their corresponding parameters is provided in Table 5.1.

5.2 Mesh convergence

The grid convergence of the numerical results is evaluated through an analysis of three distinct sets of simulations with l_{max} = 11, 12, and 13, corresponding to effective resolutions equivalent to 2048^3, 4096^3, and 8192^3 on a regular grid, respectively. The associated minimum mesh sizes Δ/d are 0.01172, 0.00586 and 0.00293, which correspond to 86, 171 and 342 grid cells representing water depth in each set, respectively.

The numerical convergence of wave-breaking simulations is discussed in terms of the energy budget and size distribution of bubbles and droplets produced by wave breaking. Figure 5.1(a) shows the evolution of kinetic

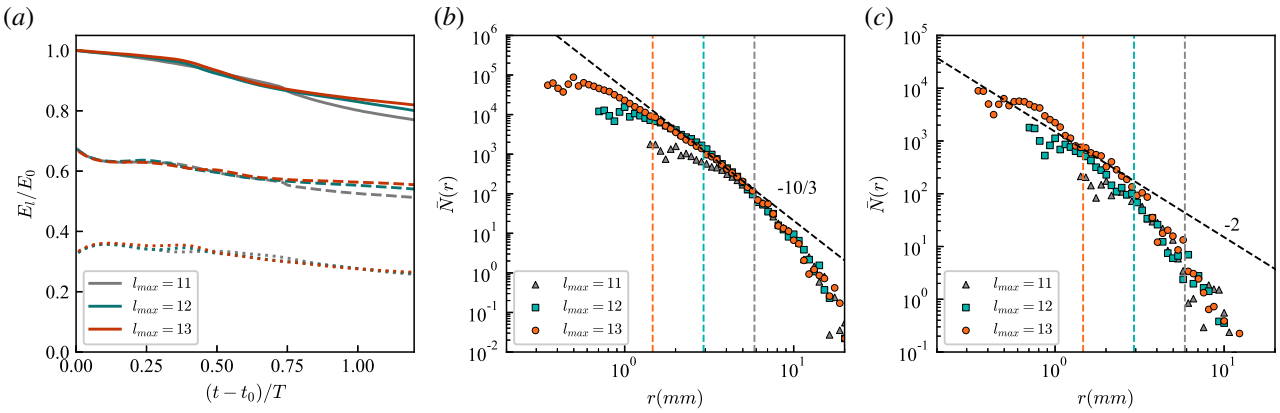

Figure 5.1: Mesh convergence study at three mesh resolutions for a wave with s = 0.5334 m, f = 0.75 Hz, and d = 0.25 m at Re = 100 000 and Bo = 8 600: green, 2^{11}; blue: 2^{12}; red: 2^{13}. Mesh convergence of (a) energy budget for the kinetic energy E_k (dotted), gravitational potential energy E_p (dashed), and mechanical energy E_m (solid); (b) time-averaged bubble size distribution during the active breaking phase; and (c) time-averaged water droplet size distribution during the active breaking phase.

energy E_k, gravitational potential energy E_p, and conservative energy $E_m = E_k + E_p$ normalized by the total mechanical energy E_0 when the plunging jet impacts the wavefront. While significant differences are seen between the coarse grid (2048^3) and the two finer grids (4096^3 and 8192^3), the 4096^3 and 8192^3 resolutions exhibit almost identical behavior during breaking. This suggests that the results of the energy budget remain relatively stable for resolutions finer than the grid equivalent to 8192^3. As the wave dissipation rate ϵ_l can be calculated based on the conservative energy E_m, we can conclude that we accurately resolve the dissipative scales in the breaking process, and the dissipation rate converges for a resolution of l_{max} = 13. Another indicator of numerical convergence for breaking waves is bubble generation due to air entrainment by breaking. Figure 5.1(b) shows the average bubble size distribution during the active breaking stage between $(t - t_{im})/T = 0.2$ and $(t - t_{im})/T = 1.2$. Smaller bubbles can be resolved and captured with increased mesh resolution due to further break-up. All cases collapse onto a similar curve, which follows the scaling law of -10/3 for large bubbles with approximately r > 1 mm. However, the -3/2 scaling law for sub-Hinze bubbles is not clearly evident in our simulations, as the Hinze scale is not fully reached, even in the finest grids. Figure 5.1(c) shows the time-averaged water droplet size distribution during the active breaking stage between $(t - t_{im})/T = 0.2$ and $(t - t_{im})/T = 1.2$. All three droplet size distributions are very close, following the scaling law of -2 for large droplets. Additionally, working with a finer grid enables the capture of smaller droplets created by further splashing.

The convergence studies confirm that all results are well converged, with no significant changes observed

as the maximum level of refinement increases from 11 to 13. A resolution of 2^{13} is used to perform a precise parametric study to determine the effect of Re and Bo on wave-breaking characteristics. Consequently, all presented results in the following sections have converged with respect to grid resolution.

5.3 Model verification

Three high-speed cameras with a frame rate of 500 frames per second were used in the experiments to visualize the development of wave breaking and the subsequent breakup processes. The horizontal centers of the three fields of view (FOVs), which measured 103×103, 75×75, and 75×75 cm^2, were located at x = 1.66, 2.43, and 3.07 m for cameras 1, 2, and 3, respectively. The vertical centers of all cameras were aligned with the initial free surface. We compare the numerical results of interface evolution over time for a plunging breaker generated by a wave plate motion with s = 0.5334 m, f = 0.75 Hz, and d = 0.25 m to the experimental snapshots taken with the high-speed cameras. Comparisons of the free surface profile between the simulation results and the experimental snapshots are shown in Figure 5.2, 5.3, and 5.4.

Camera 1, located upstream of the wave direction and near the side of the wave plate, is primarily responsible for recording the development of the plunging jet, the jet impact and air entrainment, and the generation of the first splash-up. As shown in figure 5.2, comparisons of the free surface evolution at t = 0.62 s, t = 0.72 s, and 0.82 s show good agreement between the present simulations and the experimental results from Camera 1. As the wave slope steepens and the wave crest curls, a plunging jet can be observed at t = 0.62 s, with a tendency to project downward to the water surface. At t = 0.72 s, the plunging jet impacts the rising wavefront, forming the main cavity by entrapping a tube of air. Before the jet impacts, the wave dynamics remain mostly two-dimensional. Then, at t = 0.82 s, subsequent splash events can be observed above the jet impact site. During this process, our numerical simulation accurately predicts the evolution of the free surface, including the development of the wave crest, the curvature of the overturning wave crest, the precise size of the main cavity, and the height and position of the first splash-up.

The subsequent development of the initial wave crest and the first splash-up was recorded by Camera 2, as illustrated in figure 5.3. At t = 0.92 s, the subsequent splash falls back to the surface under the influence of gravity, shedding numerous droplets. Concurrently, the air cavity deforms and elongates along the streamwise direction at t = 1.02 s, leading to the generation of relatively small bubbles and droplets from the impact of the subsequent splashes. At t = 1.22 s, the collapse of the air cavity can be clearly observed, creating larger bubbles,

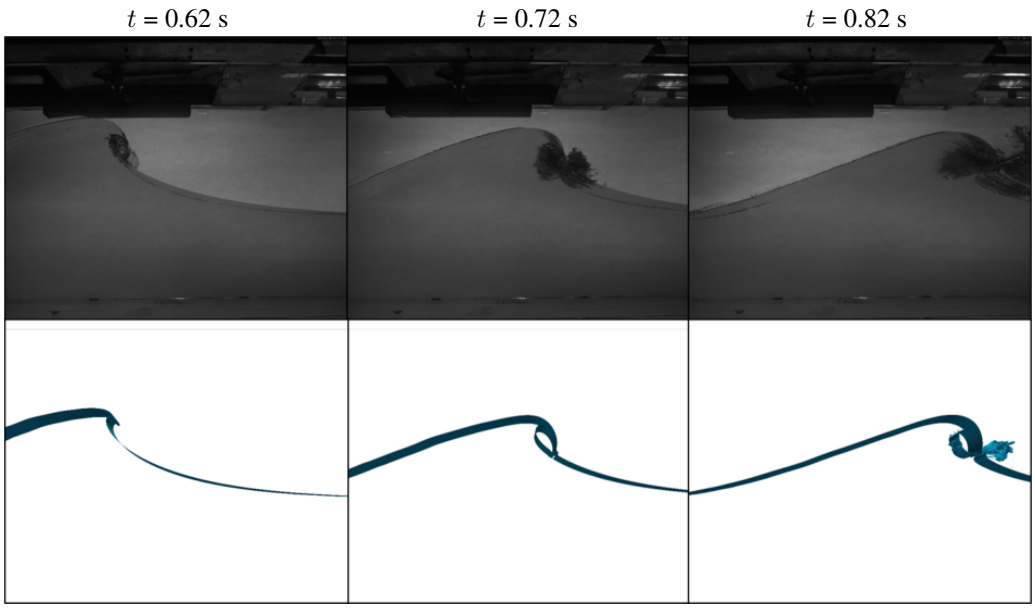

Figure 5.2: Comparisons of the free surface profiles for the wave with s/d = 2.13 and fd/c = 0.12 at Re = 100 000 and Bo = 8 600 between laboratory images (above) and numerical results (below), as recorded by camera 1.

which are subsequently fragmented by turbulent fluctuations (Deane & Stokes, 2002; Deike *et al.*, 2016). From t = 0.92 s to 1.02 s, the free surface beneath the ligaments and droplets of the first splash-up had already been disturbed due to the propagation of perturbations and capillaries at the main free surface prior to the impact of the first splash-up. Following this, the initial splash-up dives and reconnects with the free surface. During this process, more water droplets and ligaments were observed in the experiment compared with our numerical results, as indicated by the black region in the experimental snapshots. This discrepancy can be attributed to the fact that the grid scale employed in the numerical simulation is not fine enough to capture all the generated water droplets, air bubbles, and ligaments.

Figure 5.4 shows the interface evolution resulting from the turbulent breakdown of the forward face of the wave. During this process, two large dense bubble plumes with numerous bubbles of various sizes form in the water, along with ejected droplets in the air. The former plume is generated by the collapse of the initial air cavity, while the latter one results from the entrainment during subsequent splash events. Some differences were observed between the simulated free surface evolution and the snapshots taken by Camera 3. In comparison with experimental observations, similar phenomena were observed in the simulation, including the occurrence and rising of a secondary splash-up, as well as the gradual decay of the wave crest. However, the exact development of the second splash-up and the rising wavefront was not exactly reproduced. The distribution of

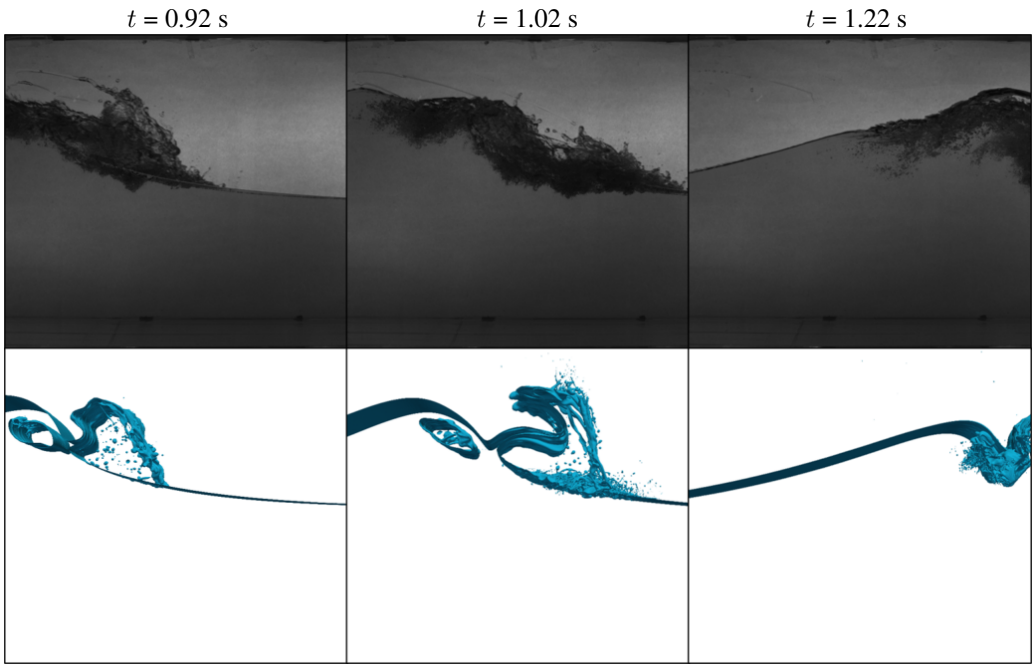

Figure 5.3: Comparisons of the free surface profiles for the wave with s/d = 2.13 and fd/c = 0.12 at Re = 100 000 and Bo = 8 600 between laboratory images (above) and numerical results (below), as recorded by camera 2.

the bubble cloud region exhibits a phase shift, but the size of the bubble cloud and penetration depth closely resemble what was observed in the experiments. These discrepancies can be explained by the fact that a slight perturbation at the wavefront can eventually lead to the development of drastically different breaking processes. This chaotic behavior of breaking waves has been investigated in laboratory experiments with the same set-ups, demonstrating that the breaking process is inherently non-repeatable, particularly in the post-breaking regions (Wei *et al.*, 2018).

The qualitative aspects of breaking wave dynamics are crucial for a faithful representation of the breaking process. In this respect, the evolution and dynamics of the breaker in our simulations closely resemble those observed in laboratory experiments with similar wave initializations, despite some Reynolds number influences (Mostert *et al.*, 2022). We recognize that the Re effect is evident when comparing numerical and experimental results, particularly in the distribution of bubbles towards the rear of the wave. However, direct numerical simulations of breaking waves are typically limited to the highest Re values attainable with available computational resources. When employing a Re matching the experimental value of 600 000, increasing the grid resolution leads to a more pronounced curling of the plunging jet, reducing the amount of air entrainment and the size of the main cavity. Achieving grid convergence is challenging, and the morphology of the main

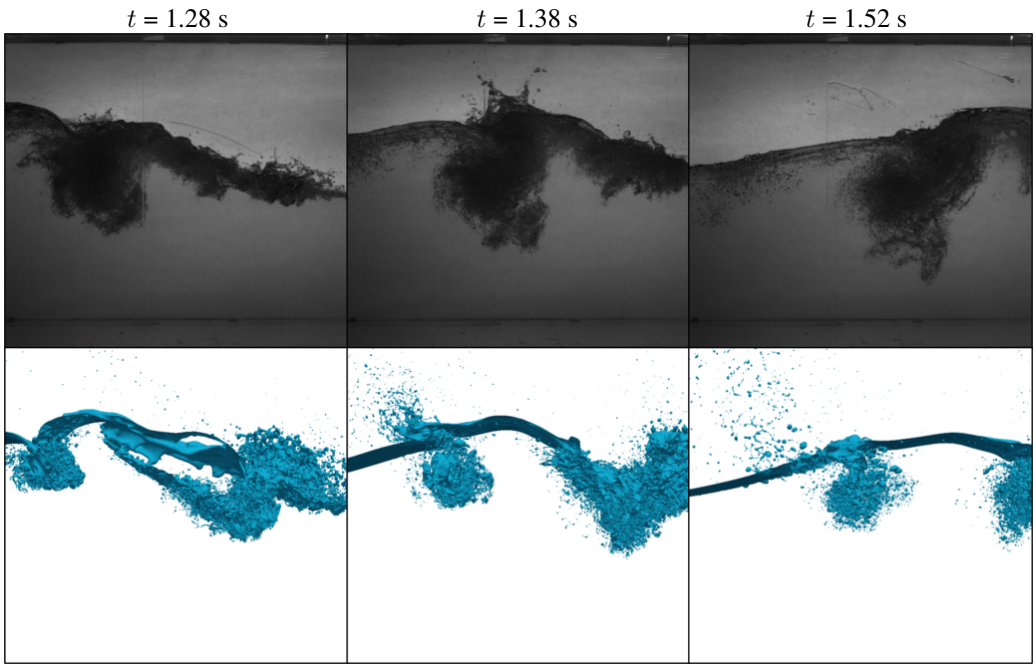

Figure 5.4: Comparisons of the free surface profiles for the wave with s/d = 2.13 and fd/c = 0.12 at Re = 100 000 and Bo = 8 600 between laboratory images (above) and numerical results (below), as recorded by camera 3.

cavity deviates from experimental observations at larger grid resolutions. Therefore, to preserve the overall wave-breaking process, we selected the highest Re value achievable by DNS that still produces a qualitatively accurate representation of the breaking process compared to experimental observations, which is Re = 100 000 for the present study. The accuracy of capturing the physical mechanisms of breaking waves is assessed based on the position and morphology of the plunging jet and main cavity during the period from jet formation to jet impact. The phenomena of steepening and overturning, together with the characteristics of the ingested cavity, exhibit striking similarity to their experimental counterparts. The subsequent fragmentation of entrained air and the sequence of droplet-producing splash also closely match the experimental observations. Overall, our numerical results demonstrate a reasonable agreement with experimental measurements in terms of wave shape and maximum wave height before breaking. A good agreement is also found between the simulated size of the main cavity entrapped by the plunging jet and the experimental data. However, some discrepancies can be seen in the post-breaking regions, notably in the inaccurate generation of water droplets, air bubbles, and ligaments. The profiles of the wavefront and the distribution of the bubble cloud region are also not well reproduced. These discrepancies can be attributed to the lack of numerical resolution and the inherently chaotic behavior of breaking waves in post-breaking regions.

5.4 Breaking characteristics

5.4.1 Wave breaking processes

We present the interface evolution over time for a plunging breaker generated by the motion of a wave plate with s/d = 2.13 and fd/c = 0.12 at Re = 100 000 and Bo = 8 600 to examine the detailed wave-breaking processes, as depicted in figures 5.5 through 5.7. The water–air interface is identified using an isosurface of the zero distance function. Droplets and bubbles are shown above and below the free surface, respectively. The interface is colored to represent the three velocity components: streamwise (u), vertical (v), and spanwise (w), displayed in three distinct columns. The wave-breaking processes shown in these figures include the development of the maximum wave height, the formation of the overturning jet, wave plunging, splash-ups, and subsequent wave-breaking events.

At t = 0.9 s, a splash-up forms following the jet impact, as can be seen in figure 5.5. Water ligaments are subsequently generated from the initial liquid sheet, driven by spanwise instability induced by both gravity and surface tension. Notably, the toe of the resulting splash-up exhibits the highest streamwise and downward vertical velocities. Following the laminar flow phase prior to wave breaking, three-dimensional effects become progressively more pronounced as a consequence of the jet impact, as illustrated by the spanwise velocity in both the main cavity and the splash-up (see figure 5.5c). The main cavity undergoes further deformation and elongation at t = 1.0 s (figure 5.5 d-f). As the primary splash-up evolves and impacts the free surface (figure 5.5 g-i), a secondary splash-up emerges, and an air cavity is entrained when the primary splash-up impacts the free surface at around t = 1.2 s. As can be seen in figure 5.5 (j-o), it becomes apparent that the second splash-up differs from the primary one; it is no longer planar and is characterized by the formation of numerous ligaments and droplets due to the spanwise instability. The rear portion of the splash collides with the upper surface of the plunging jet at t = 1.3 s, leading to the breakup of the main cavity (figure 5.5 m-o). It is worth noting that this backward-splash entrainment is the primary source of bubble generation, with the formation of a bubble cloud resulting from the breakup of the main cavity.

Figure 5.6 shows the temporal evolution of the free surface from t = 1.4 s to 1.8 s. During the collision between the rear side of the splash and the upper surface of the plunging jet, extensive bubbles of various sizes are produced due to the breakup of the main cavity, forming the first bubble plume. Simultaneously, a large number of droplets are ejected from the collision point into the air above the main cavity (figure 5.6 a-c). A second bubble plume is then formed through the fragmentation of this air cavity, induced by the collision between the

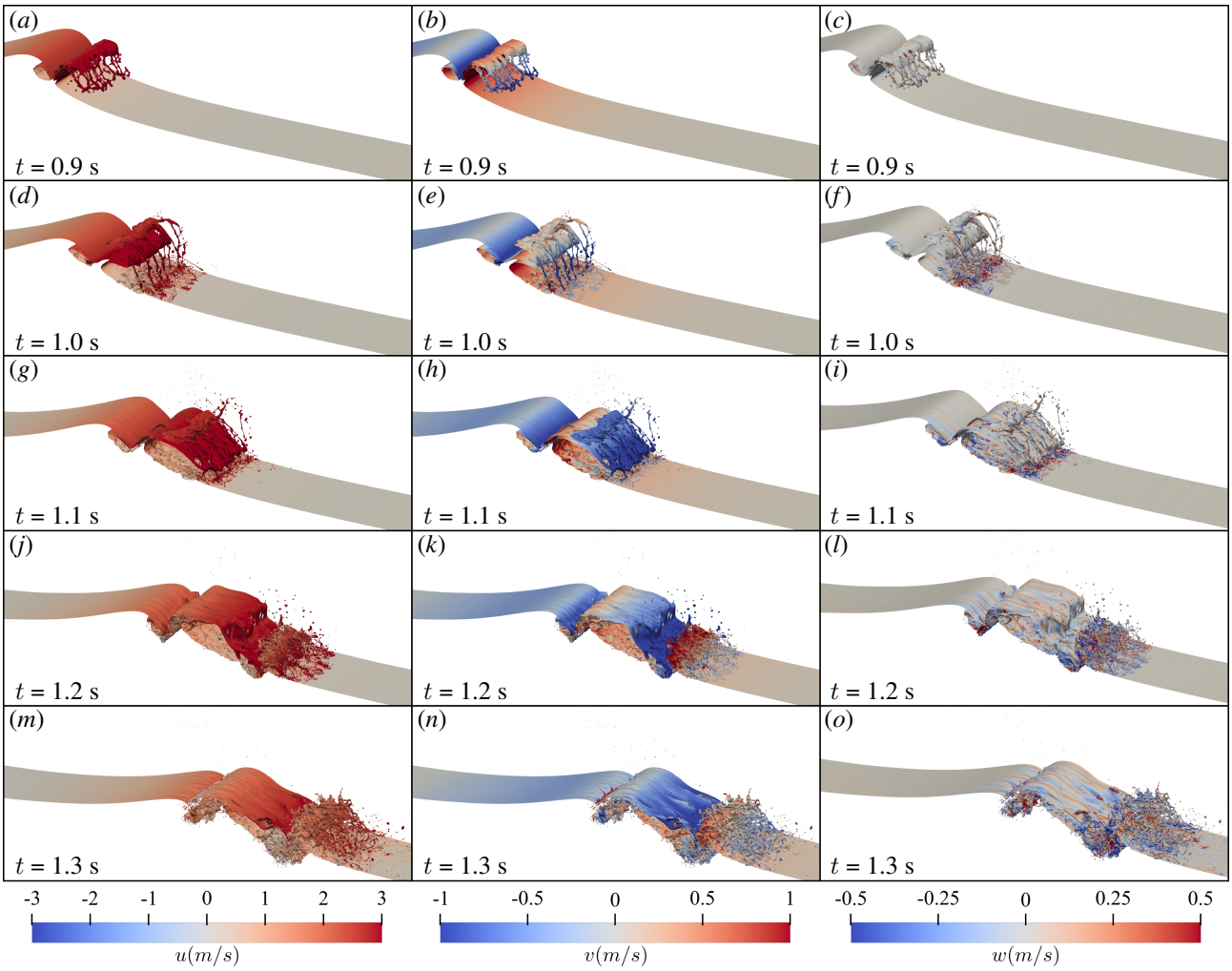

Figure 5.5: The free surface profiles for the wave with s/d = 2.13 and fd/c = 0.12 at Re = 100 000 and Bo = 8 600 from 0.9 s to 1.3 s. The surface is the air–water interface identified using the isosurface of the zero distance function, where the color represents the streamwise and vertical velocity components. The time interval between images Δt = 0.1 s.

rear side of the secondary splash and the upper surface of the plunging jet. This collision is distinguishable by the presence of ejected droplets with positive vertical velocities over the second air cavity, represented in red in figures 5.6 (e) and (f). These ejected droplets have relatively large sizes, which subsequently fall back into the water, as shown in figures 5.6 (k) and (n). The majority of bubbles during wave breaking are produced by air entrainment due to the disintegration of the first and second air cavities. From the front edge of the wave, it is evident that no obvious splash-up is formed because most of the energy has been dissipated due to breaking in the course of the first two splash-ups (figure 5.5 j-o).

Figure 5.7 shows the late stage of free-surface evolution between t = 1.9 s and 2.3 s. In addition to the two main bubble plumes, air is also entrained by turbulent regions at the leading edge of the wave because bubbles are produced underneath the free surface during wavefront propagation. Furthermore, bubbles start to vanish as they ascend towards the surface, with larger bubbles disappearing before smaller ones due to their higher buoyancy-induced rising speed. This phenomenon is more produced in the first bubble plume which forms at an earlier stage.

5.4.2 Vortex filaments

The curl of the velocity field of a fluid, which is generally termed vorticity ω, is $\omega = \nabla \times v$. A vortex line is a line whose tangent is everywhere parallel to the local vorticity vector. The vortex lines drawn through each point of a closed curve constitute the surface of a vortex tube. Finally, a vortex filament is a vortex tube whose cross-section is of infinitesimal dimensions. The product of the magnitude of the vorticity and the cross-sectional area, which is termed the vortex intensity, is constant along the filament. It follows that a vortex filament cannot terminate in the interior of the fluid. Thus, a vortex filament must either form a closed vortex ring, or must terminate at the fluid boundary (Fitzpatrick, 2017). Because a vortex tube can be regarded as a bundle of vortex filaments whose net intensity is the sum of the intensities of the constituent filaments, we conclude that the intensity of a vortex tube remains constant along the tube. A vortex sheet is defined as a planar array of parallel vortex filaments.

Streamwise vortex filaments are observed beneath the entrained air tube, a phenomenon also documented by Lubin & Glockner (2015) and Wang *et al.* (2016). In a more recent study by Lubin & Glockner (2015), nearly one billion mesh grid points were used to simulate the fine vortex filaments generated during the early stage of wave breaking. Figure 5.8 shows the temporal evolution of coherent vortical structures encircling the main air tube. These 3-D vortex structures are identified using the Q-criterion, which is defined as the second invariant of

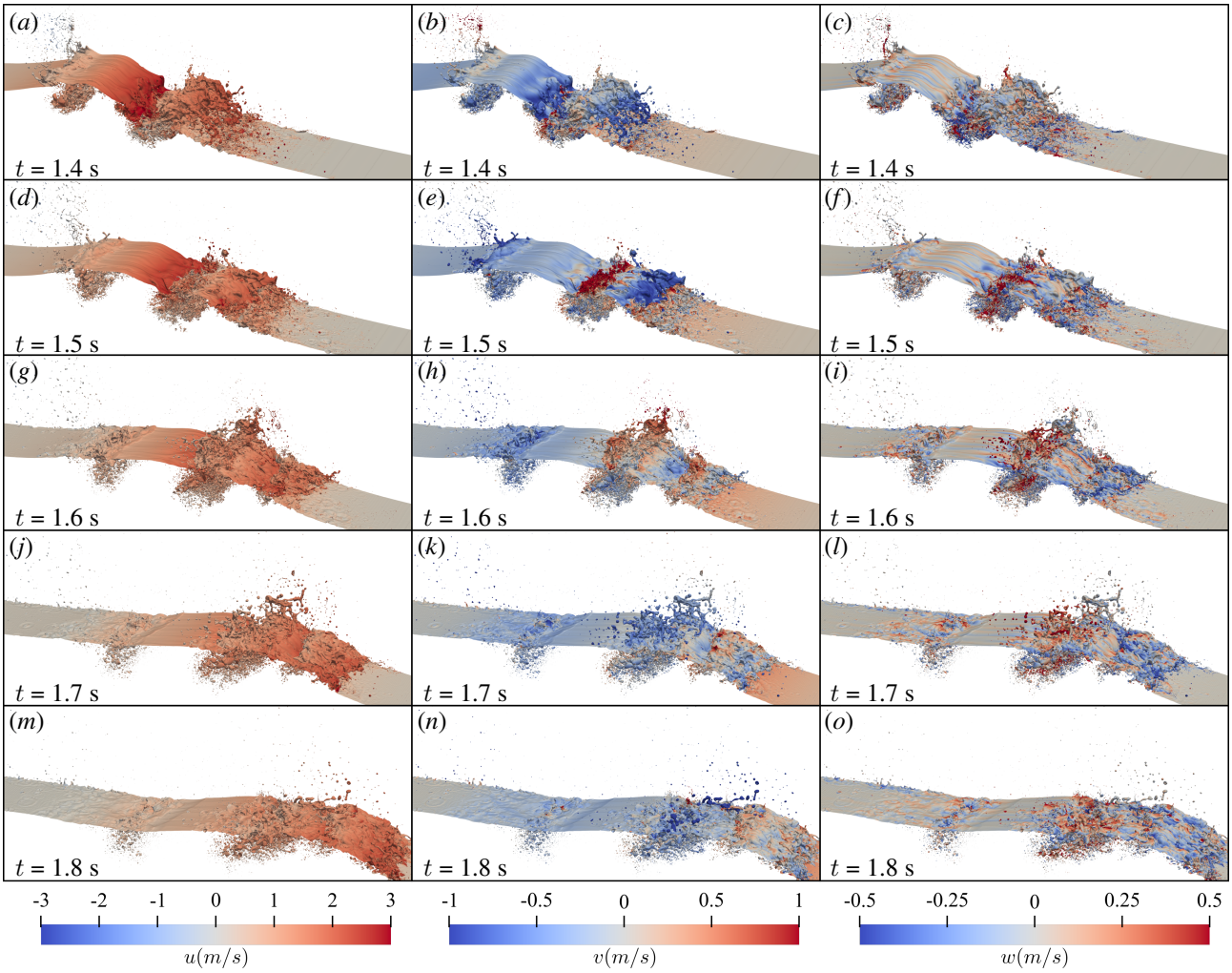

Figure 5.6: The free surface profiles for the wave with s/d = 2.13 and fd/c = 0.12 at Re = 100 000 and Bo = 8 600 from 1.4 s to 1.8 s. The surface is the air–water interface identified using the isosurface of the zero distance function, where the color represents the streamwise and vertical velocity components. The time interval between images Δt = 0.1 s.

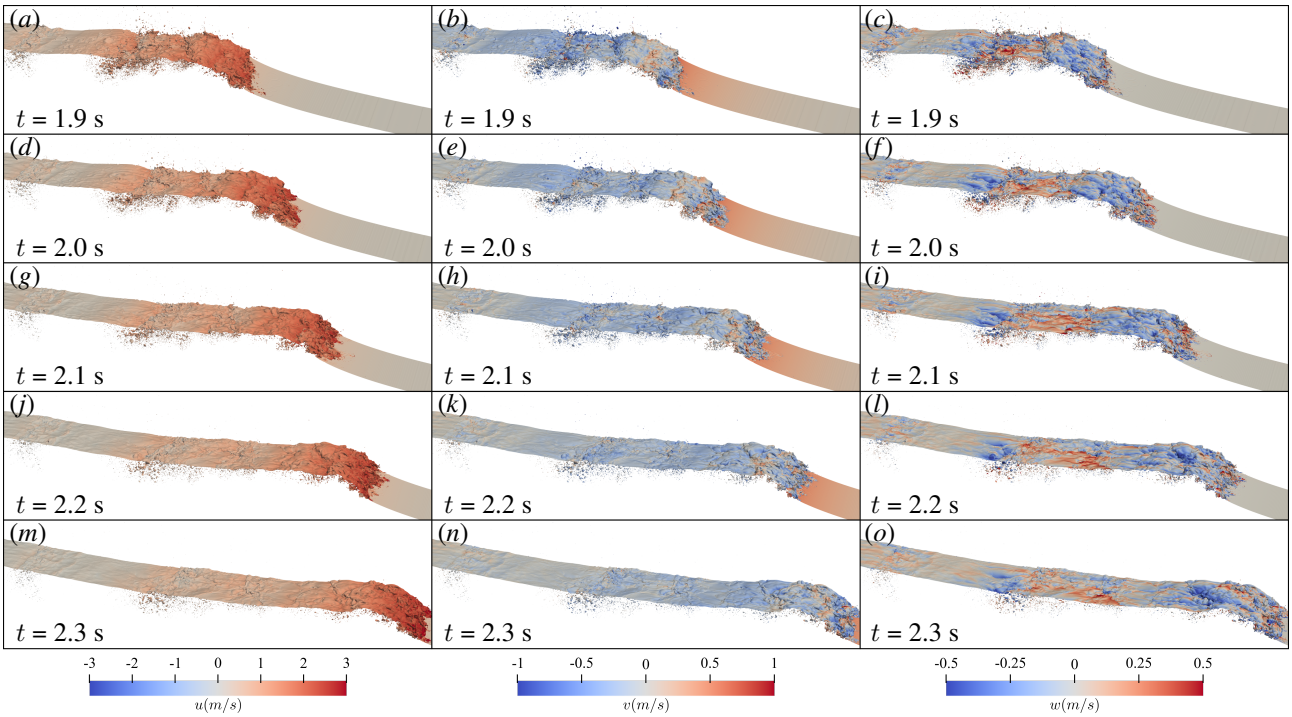

Figure 5.7: The free surface profiles for the wave with s/d = 2.13 and fd/c = 0.12 at Re = 100 000 and Bo = 8 600 from 1.9 s to 2.3 s. The surface is the air–water interface identified using the isosurface of the zero distance function, where the color represents the streamwise and vertical velocity components. The time interval between images Δt = 0.1 s.

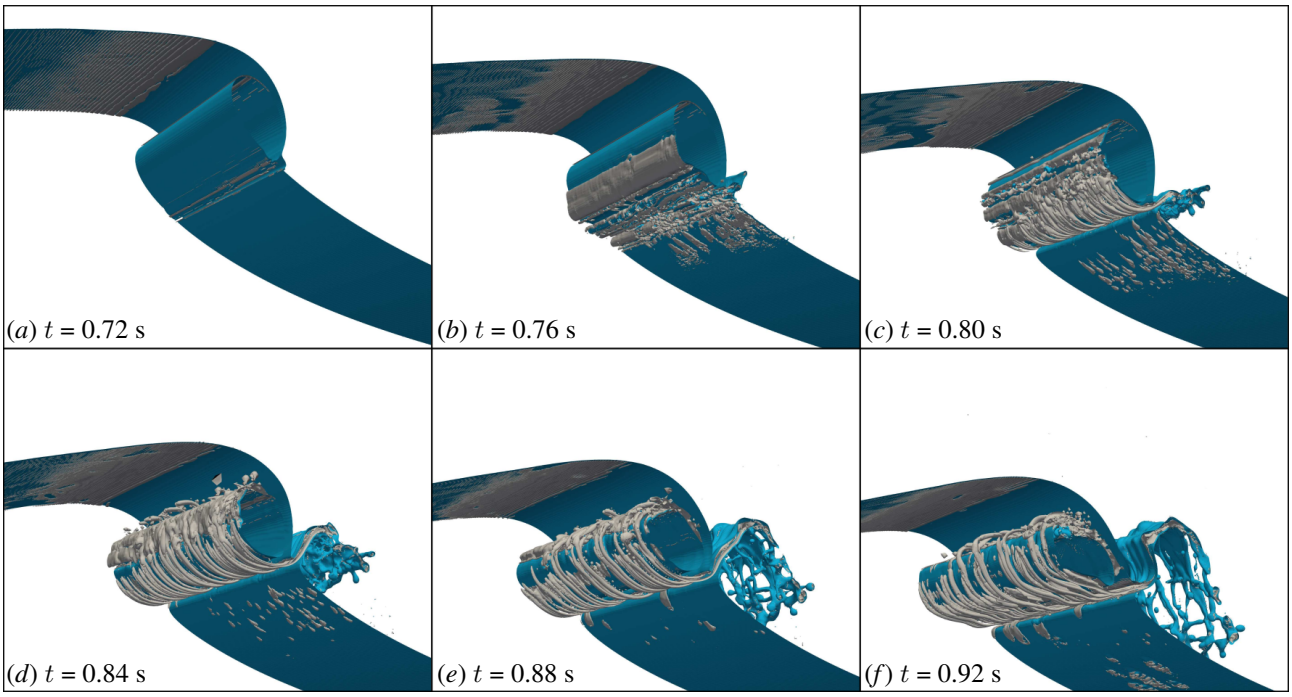

Figure 5.8: Time evolution of vortex filaments wrapped around the main tube of air for the wave with s/d = 2.13 and fd/c = 0.12 at Re = 100 000 and Bo = 8 600 from 0.72 s to 0.92 s. The time interval between images, Δt = 0.04 s.

the velocity gradient (Jeong & Hussain, 1995). The Q-criterion represents the balance between shear strain rate and vorticity magnitude and is a particularly valuable tool for identifying vortices in complex 3-D flows (Wang *et al.*, 2016). The Q isosurfaces, plotted for the water phase, show strong organized structures characterized by streamwise vortex filaments wrapping around the main air tube. These streamwise vortex filaments are related to the spanwise instabilities in the entrained air tube, contributing to the uneven deformation of the air cavity in the spanwise direction and the final collapse of the air cavity. As the filaments ascend towards the saddle point beneath the wave crest, They are observed to coil and then they form a buckle, with the loop bending and redirecting backwards and downwards (Lubin *et al.*, 2019).

5.5 Air entrainment

In the context of plunging breaking waves, air can be entrained by several mechanisms, such as air tube entrapment and jet impact, entrapment by forward splash, backward-splash entrainment, and turbulent entrainment, as discussed in Kiger & Duncan (2012). Air entrainment by breaking waves has been shown to be significant in multiple physical processes, including gas transfer at the air-sea surface, the generation of ambient sound in the

transition zone, and the production of aerosols when interacting with other materials. The dominant factor for these processes is the bubble size spectrum. Due to the inherently three-dimensional nature of bubble formation, three-dimensional simulations are necessary for its investigation. In this section, we present our simulations of air entrainment processes corresponding to several mechanisms. We investigate the air-entrainment properties and bubble-size statistics for different combinations of viscosities and surface tension coefficients.

The bubble size distribution can be associated with a turbulent break-up model introduced by Garrett *et al.* (2000). This model assumes an inertial subrange and a direct cascade process, where air is injected at large scales by the entrainment process and turbulent fluctuations break them into smaller bubbles. Assuming the size distribution per unit volume $\mathcal{N}(r)$, with r the bubble radius, to depend only on the local time-averaged turbulent dissipation rate $\bar{\epsilon}$, the bubble radius r and the source of bubbles, i.e., the constant air flow rate per unit volume of water Q, then dimensional analysis leads to:

$$\mathcal{N}(r) \propto Q\bar{\epsilon}^{-1/3}r^{-10/3} \tag{5.1}$$

This self-similar cascade process ends at the scale where surface tension prevents further bubble break-up, the Hinze scale:

$$r_H = C_0(\frac{\gamma}{\rho})^{3/5}\bar{\epsilon}^{-2/5} \tag{5.2}$$

where $C_0 \simeq 0.4$ is a dimensionless constant. The Hinze scale r_H is defined such that 95 % of the air is contained in bubbles with a radius less than r_H Hinze (1955):

$$\int_0^{r_H} r^3 N(r)dr = 0.95 \int_0^{\infty} r^3 N(r)dr \tag{5.3}$$

The breaking wave is transient, so the Hinze scale may vary with time. For the time-average bubble size distribution, the Hinze scale is estimated based on the averaged turbulence dissipation rate. Several experimental studies have identified a bubble size distribution following a power law of the bubble radius $\mathcal{N}(r) \propto r^{-m}$ with $m \in [2.5 : 3.5]$ (Loewen *et al.*, 1996; Deane & Stokes, 2002; Leifer & De Leeuw, 2006; Blenkinsopp & Chaplin, 2010). However, determining the exact value of the power law exponent m is difficult due to the rapid temporal variations in the bubble size distribution. As discussed in Deane & Stokes (2002), the bubble size distribution is controlled by two distinct mechanisms: large bubbles (r > 1.0 mm) are determined by turbulent fragmentation and exhibit a power-law scaling of -10/3, while smaller bubbles are created through jet and drop impact, showing a -3/2 power-law scaling. However, the scaling for large bubbles $\mathcal{N}(r) \propto r^{-m}$, with $m \in [2.5 : 3.5]$, is only valid during the active breaking time, which lasts for approximately one wave period.

Later on, the bubble size distribution is found to be much steeper. Therefore, a more complete description of the bubble size distribution during the breaking event and during the rise of the bubbles is required to investigate its temporal evolution and the corresponding bubble generation mechanism. If turbulent pressure fluctuations are the dominant mechanism for the breakup of both large and small bubbles, smaller bubbles should be able to resist the distortion by pressure and not likely to break up. Consequently, the air fraction is expected to accumulate in a large spectral peak that would only slowly disappear as the bubbles dissolve. However, such a peak is not observed.

Experimental studies have shown that large numbers of bubbles smaller than the Hinze scale are also entrained. While break-up events are self-similar, occurring on the eddy turnover time at the parent bubble scale, a distinct mechanism must be proposed for the size distribution of bubbles smaller than the Hinze scale. Deane & Stokes (2002) reported the statistics of bubbles below the Hinze scale as $N(r) \propto r^{-3/2}$. Recent DNS of breaking waves and bubble breakup have provided further evidence for this regime, with production due to entrainment at impact (Chan *et al.*, 2021; Mostert *et al.*, 2022) and the fragmentation of highly deformed, large super-Hinze bubbles, yielding a nonlocal cascade (Rivière *et al.*, 2021). Rivière *et al.* (2021) describe a break-up event as involving inertial deformation followed by capillary splitting events. Splitting events happen much faster and are capillary-driven, typically taking place on filament structures that have been prepared by break-up events. Sub-Hinze bubbles can be produced during splitting events by the capillary break-up mechanism when the elongated filaments are formed through a Rayleigh-Plateau instability. Considering the fragmentation dynamics as a succession of binary events, a population balance equation was employed to derive a -3/2 power-law scaling for sub-Hinze bubbles.

5.5.1 General bubble formation by breaking

We now discuss the formation and the time evolution of bubbles in shallow-water breaking waves. While the dynamics of deep and shallow-water waves differ, the process of air entrainment and breakup under the influence of turbulence is qualitatively similar, although the magnitude of the effects may vary. Figures 5.9(a) and (b) show the temporal evolution of the number $N(t)$ and volume $V(t)$ of entrained bubbles. The dimensionless time is normalized by the nominal wave period. The jet reconnects with the water surface at $t = t_{im}$, forming a main cavity characterized by a large pocket of entrained air. Bubbles then start to be produced, but the air tube is not included in the number and volume of entrained bubbles. When decreasing the Reynolds number Re from 100 000 to 50 000 at the same Bond number Bo of 8 600, the peak number of bubbles produced

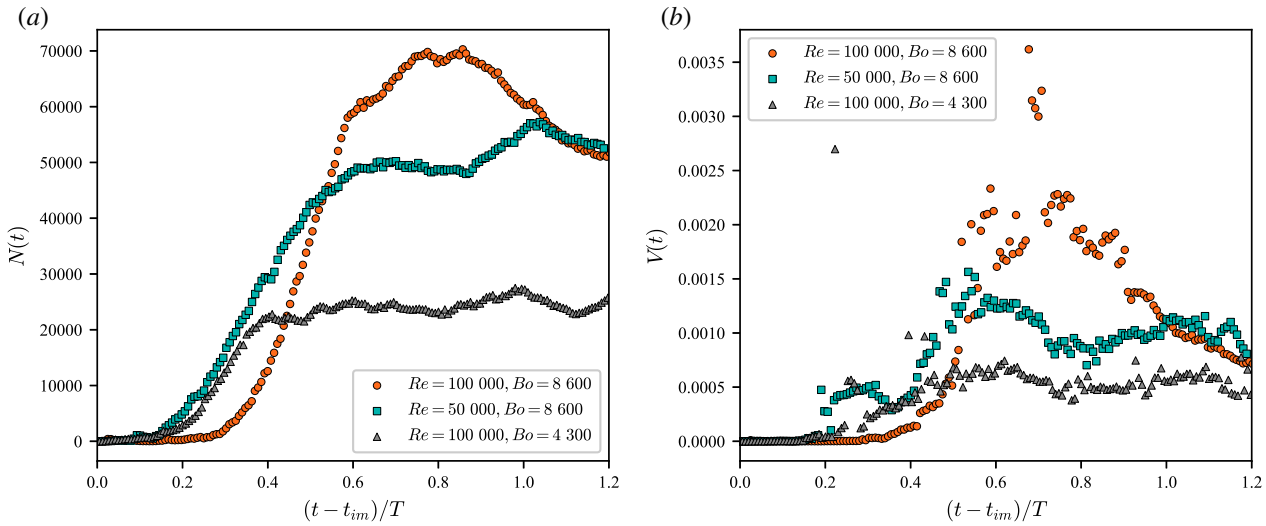

Figure 5.9: Time evolution of the total number $N(t)$ (a) and volume $V(t)$ of entrained air bubbles at different test cases with varying Re and Bo. (a) Base case: Re = 100 000, Bo = 8 600; (b) Small Re case: Re = 50 000, Bo = 8 600; (c) Small Bo case: Re = 100 000, Bo = 4 300. $(t - t_{im})/T$ shows the collapsing time after jet impact normalized by the theoretical wave period, where t_{im} represents the jet impact time.

decreases. However, when decreasing Bo from 8 600 to 4 300 at the same Re of 100 000, the entrained number of bubbles decreases almost three times in the peak number of bubbles. compared with the Reynolds number, the production of bubbles is more sensitive to the Bond number. For the small Bo case with Re = 100 000 and Bo = 4 300, a rapid and continuous increase in the total number and volume of bubbles is observed from $(t-t_{im})/T$ = 0.3 to $(t-t_{im})/T$ = 0.6, which can be attributed to the rupture and breakup of the main air cavity. This is followed by a slower increase in the total number and volume of bubbles over $0.6 \lesssim (t-t_{im})/T \lesssim 0.85$. Subsequently, $N(t)$ and $V(t)$ decrease. These processes correspond to the active breaking stage, which occurs over approximately one wave period, $0.2 \lesssim (t - t_{im})/T \lesssim 1.2$. For the small Re case with Re = 50 000 and Bo = 8 600, the rapid increase in the total number and volume of bubbles is observed earlier than the larger Re case, starting from $(t - t_{im})/T$ = 0.15. The bubble numbers reach a plateau at approximately $(t - t_{im})/T$ = 0.6. Starting from $(t - t_{im})/T$ = 0.85, the number of bubbles starts to increase again, followed by a decrease at $(t - t_{im})/T$ = 1.0. The small Bo case exhibits a similar temporal trend in the evolution of the number and volume of entrained bubbles but shows a lower level of bubble production.

Figure 5.10 shows the time evolution of the bubble size distribution $N(r, t)$. In the base case with Re = 100 000 and Bo = 8 600 (Figure 5.10a), bubbles of varying radii, ranging from the minimum mesh scale to 4.5 mm, are produced immediately upon impact at $(t - t_{im})/T = 0$. Most of the bubbles immediately disappear due to reconnection with the free surface under the effect of buoyancy, with larger bubbles disappearing first.

This disappearance process continues until the impact on the undisturbed free surface of the forward splash created by the plunging jet at $(t - t_{im})/T \approx 0.15$. Bubbles produced by the splash impact exhibit a smaller maximum radius of 2 mm compared with those resulting from the plunging jet impact. The subsequent bubble size distribution at $0.15 \lesssim (t - t_{im})/T \lesssim 0.3$ is formed by the bubbles created by a sustained splash impact and then disappear by reconnection with the free surface in the developed breaker. Starting from $(t - t_{im})/T$ = 0.3, a dramatic increase in the bubble number is observed, with the largest bubble reaching a radius of 10 mm. This is caused by the breakup of the main air cavity due to turbulent pressure fluctuations. During the breakup process, the entrained cavity collapses, and a large number of bubbles of various sizes are produced especially larger bubbles. The fragmentation of the two main aeration areas finishes at around $(t - t_{im})/T$ = 0.8. Afterwards, the bubbles start to rise to the free surface and disappear. The large void pockets outgas rapidly, causing the large bubbles to float up and vanish first due to their greater buoyancy. In the small Re case with Re = 50 000 and Bo = 8 600 (Figure 5.10b), bubbles produced after jet impact show a narrower range of radii, from the minimum mesh scale to 3.0 mm. Without the disappearance process that occurs in the base case, the rapid increase in the number and volume of bubbles starts earlier at $(t - t_{im})/T$ = 0.15. This difference is caused by the different wave breaking process: in the small Re case, there is entrapment between the rear side of the splash and the upper surface of the plunging jet, whereas the splash of the base case did not show this backward-splash entrainment. This is likely due to the stronger energy in the splash, which causes the upper surface of the plunging jet to be unable to catch the rear side of the splash at the first stage after impact in the base case. When the breakup of the main cavity starts, a rough constant increase in the total number and volume of bubbles is also observed, with a smaller increase rate compared with the base case. The small Bo case shows a similar but shorter increase rate compared with the small Re case. In addition, the overall number of entrained bubbles is smaller across the entire range of bubble radii.

Figure 5.11 shows the bubble size distribution $N(r, t)$ at different times t during the active breaking period. The amplitude of the bubble size distribution of the base case is smaller than the other two cases before $(t - t_{im})/T$ = 0.4 due to the delay of the backward-splash entrainment. During $(t - t_{im})/T$ = 0.6 to $(t - t_{im})/T$ = 0.8, the amplitude of the bubble size distribution becomes largest in the base case due to a greater increase rate of the bubbles produced by the breakup of the main cavity. At the late stage $(t - t_{im})/T$ = 1.0 and $(t - t_{im})/T$ = 1.2, the base case shows a more obvious decrease in the total number of bubbles and a similar amplitude of the bubble size distribution to the small Re case. The small Re case and small Bo case show a similar time evolution of the bubble size distribution. As the production of bubbles is more sensitive to the Bond number,

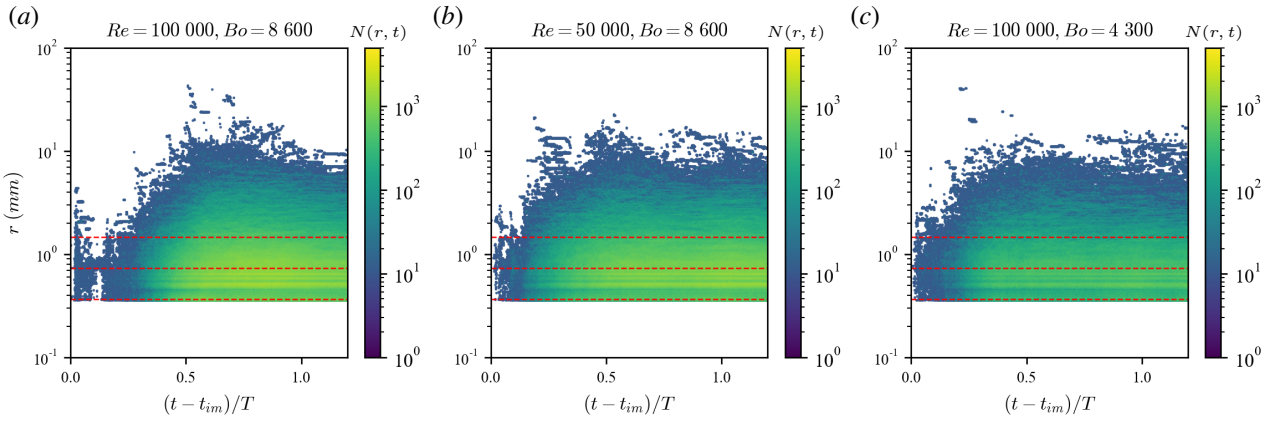

Figure 5.10: Contour of bubble size distribution over time. (a) Base case: Re = 100 000, Bo = 8 600; (b) Small Re case: Re = 50 000, Bo = 8 600; (c) Small Bo case: Re = 100 000, Bo = 4 300. The dashed lines from bottom to top represent space scales with 1, 2, and 4 times the minimum mesh resolution.

the smaller Re case shows a larger overall amplitude of the bubble size distribution during the active breaking period. Although the amplitude and time evolution of the bubble size distribution shows some discrepancies, the overall slope of the bubble size distribution is similar for all three cases, first growing, reaching a maximum, and then decaying. During the active breaking time, the size distribution follows $N(r,t) \propto r^{-10/3}$.

Figure 5.12 shows the time-averaged bubble size distribution $\bar{N}(r)$ over the active breaking period. The bubble inertial subrange, i.e. the range of bubble radii for which the power law is observed, starts close to the smallest resolved scale (approximately 0.7 mm) and ends at the radius of the largest bubble observed in the simulation (approximately 10 mm). The scale of the beginning of the bubble cascade corresponds to the Hinze scale, which is approximately 1 mm in this case. For sup-Hinze bubbles, the time-averaged size distribution follows $\bar{N}(r) \propto r^{-10/3}$, with a steeper slope in the size distribution for bubbles larger than 6 mm. This steeper slope can be attributed to the time chosen to average the bubble size distribution, due to the small number of bubbles in the early growth time and the disappearance of larger bubbles in the late decay time. For sub-Hinze bubbles, the mesh resolution is close to the Hinze scale, so the Hinze scale might not be fully resolved. Although the bubbles with radii ranging from 0.5 - 0.8 mm show a size distribution of $\bar{N}(r) \propto r^{-3/2}$, this observation should be taken with caution and cannot be used to validate the $-3/2$ scaling law in the sub-Hinze range observed in the experiments. During the active breaking period, the bubble size distribution is almost the same when varying the Reynolds number, with the small Re case showing a smaller number of large bubbles. More bubbles are observed at higher Bo, with the difference pronounced in the range of smaller bubbles. For bubbles larger than r > 10 mm, the bubble size distribution in the small Bo case is similar to that of the small Re case.

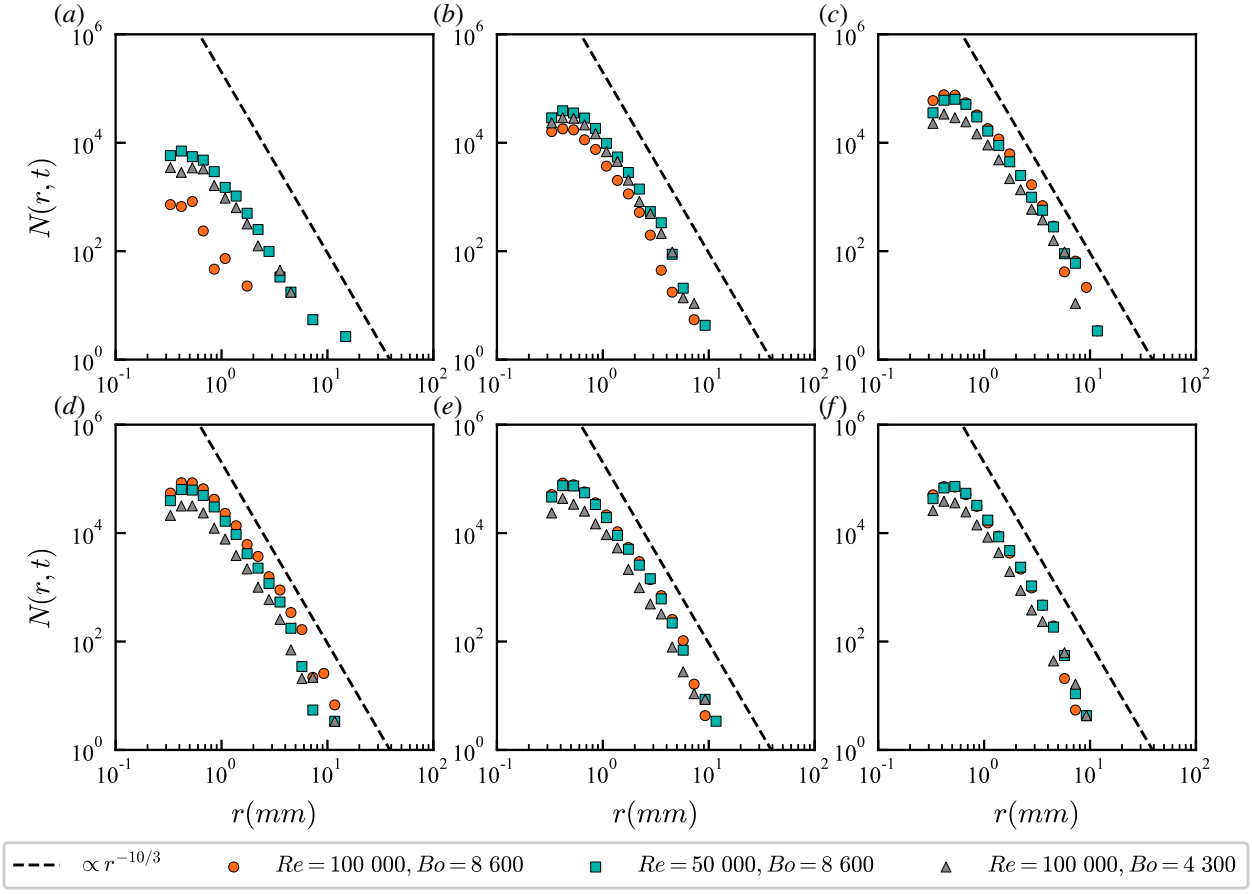

Figure 5.11: Bubble size distribution at different times during the active breaking period: (a) $(t - t_{im})/T$ = 0.2; (b) $(t - t_{im})/T$ = 0.4; (c) $(t - t_{im})/T$ = 0.6; (d) $(t - t_{im})/T$ = 0.8; (e) $(t - t_{im})/T$ = 1.0; (f) $(t - t_{im})/T$ = 1.2. Base case: Re = 100 000, Bo = 8 600; Small Re case: Re = 50 000, Bo = 8 600; Small Bo case: Re = 100 000, Bo = 4 300.

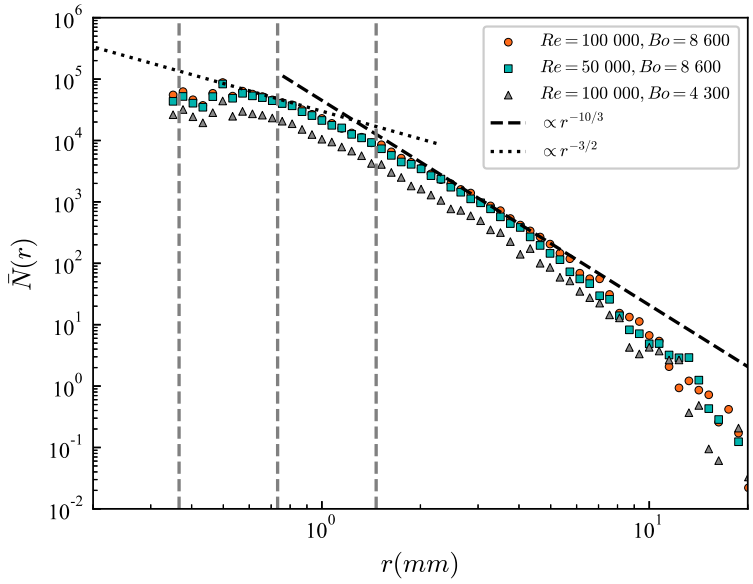

Figure 5.12: Active breaking time-averaged bubble size distribution. Base case: Re = 100 000, Bo = 8 600; Small Re case: Re = 50 000, Bo = 8 600; Small Bo case: Re = 100 000, Bo = 4 300. The dashed line is $\bar{N}(r) \propto r^{-10/3}$ for sup-Hinze bubbles and the dotted line is $\bar{N}(r) \propto r^{-3/2}$ for sub-Hinze bubbles.

Figure 5.13 shows the time evolution of the number of bubbles at various scales of bubble radii r, normalized by its maximum value $N(r,t)/N_0(r)$. In the base case, a large number of bubbles are created at various radii starting from $(t - t_{im})/T \simeq 0.3$, with a similar increase rate until $(t - t_{im})/T \simeq 0.7$. This indicates a rapid bubble breakup. Large bubbles then disappear first and much faster than smaller bubbles, as they collapse into smaller ones due to turbulent pressure fluctuations and rise up to the free surface with larger rise velocities due to buoyancy. The decay rate increases with decreasing bubble radius. In the small Re case (Figure 5.13b), the number of bubbles starts to increase earlier and shows a second increase starting from $(t - t_{im})/T$ = 0.85 after the rapid increase caused by the main cavity breakup. Although the bubble production evolution is different, the separation of the number of bubbles at various radii is observed at the same time at approximately $(t - t_{im})/T$ = 0.65, indicating the same mechanism of the rising of large bubbles. Figure 5.13(c) shows the time evolution of the number of bubbles for various radii in the small Bo case. In this case, the separation of the number of bubbles at various radii occurs much earlier, especially for large bubbles with r = 4 mm, which means that fewer large bubbles are produced during the main cavity breakup.

Breakup processes during active breaking can be reasonably well-captured, allowing us to capture the rise velocity of fragmented bubbles. Figure 5.14 shows the time evolution of the vertical velocity of bubbles at various bubble radii r, normalized by the impact velocity of the tip of the plunging jet. The vertical velocity

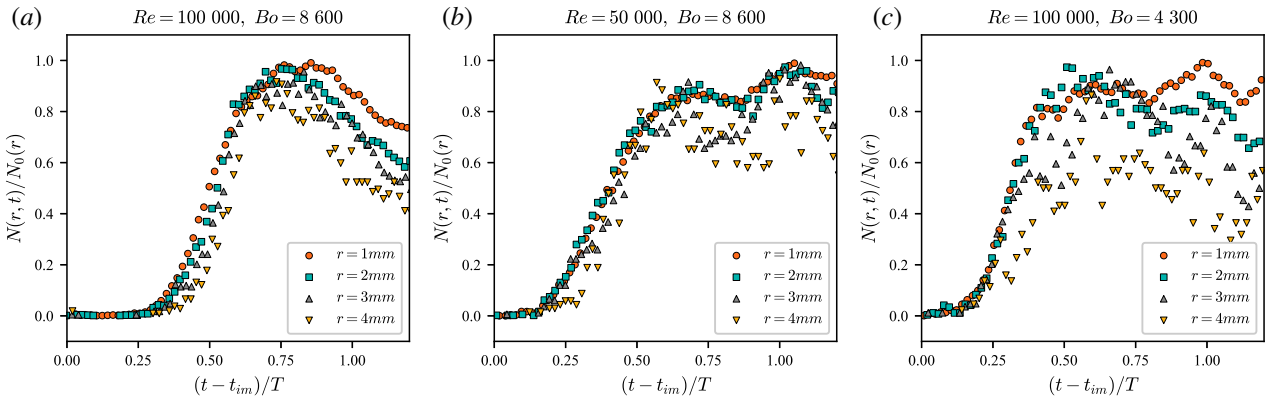

Figure 5.13: Time evolution of the number of bubbles $N(r,t)$ for various radii r: (a) Base case: Re = 100 000, Bo = 8 600; (b) Small Re case: Re = 50 000, Bo = 8 600; (c) Small Bo case: Re = 100 000, Bo = 4 300.

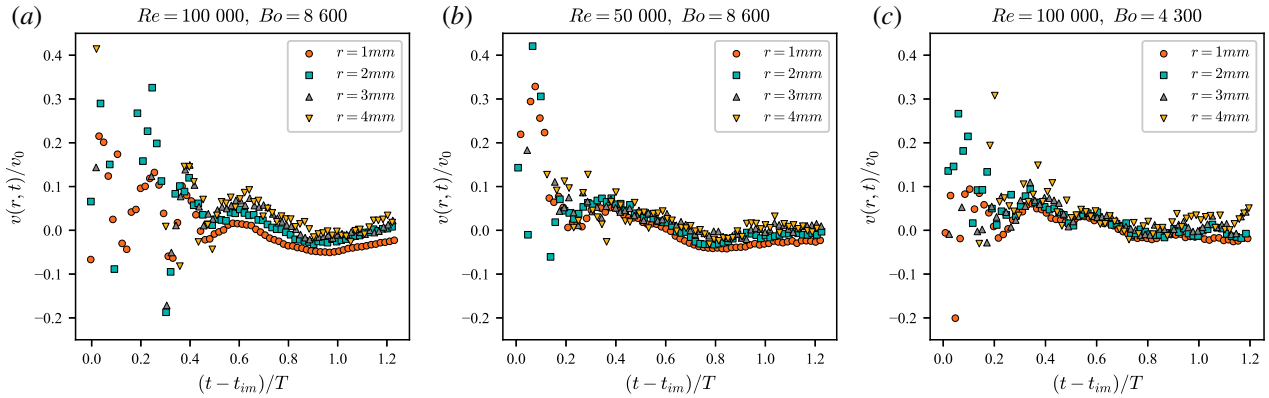

Figure 5.14: Time evolution of the vertical velocity of bubbles $v(r,t)$ for various radii r: (a) Base case: Re = 100 000, Bo = 8 600; (b) Small Re case: Re = 50 000, Bo = 8 600; (c) Small Bo case: Re = 100 000, Bo = 4 300.

increases with the increasing bubble radii, showing that buoyancy causes different rise velocities, with larger bubbles rising to the free surface faster. compared with cases with small Re and Bo, the separation of the vertical velocity of bubbles is more pronounced in the base case during the active breaking time.

5.5.2 Bubble plumes

To elucidate the air entrainment mechanism by wave breaking, we must identify the time and location of bubble production. Figures 5.15(a) and (b) show the time evolution of the bubble number distribution in the streamwise and vertical directions, respectively. These figures clearly depict the bubble location, number distribution, as well as the corresponding time evolution. Figure 5.15 (a) shows that bubbles entrained by

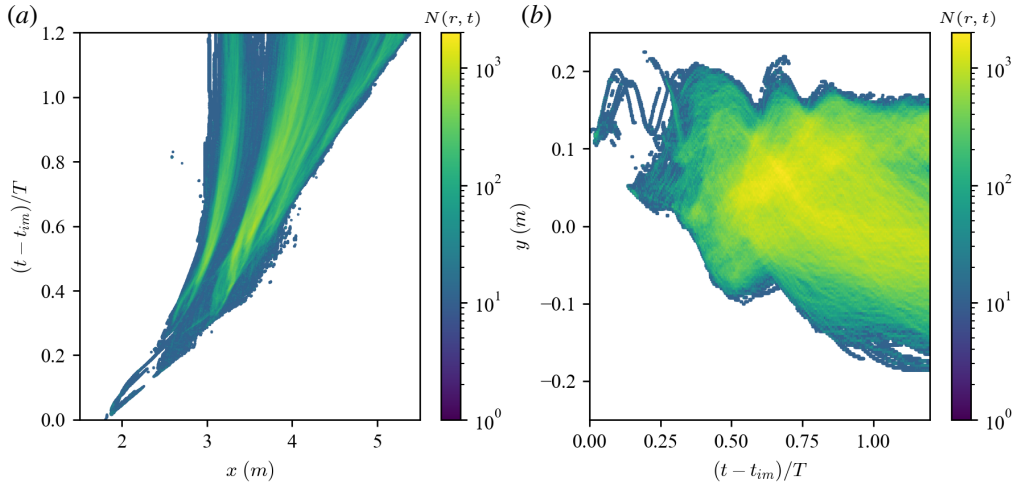

Figure 5.15: Time evolution of the bubble number distribution in the streamwise direction (a) and vertical direction (b) for the wave with s/d = 2.13 and fd/c = 0.12 at Re = 100 000 and Bo = 8 600.

a plunging breaker can be divided into three distinct visible clouds: the first bubble plume produced by the disintegration of the main air cavity, the second bubble plume entrapped by the forward splash, and the third bubble plume by turbulent entrapment (Derakhti & Kirby, 2014). Figure 5.15 (b) shows the bubble number distribution in the vertical direction. The initial lines of the number distribution before $(t - t_{im})/T$ = 0.2 indicate that bubbles are produced by the jet impact and move together with the wave motion. The lower envelope shows the maximum penetration depth at each time instant, and the descending amplitude of the upper envelope indicates the decreasing energy due to wave breaking.

Now we analyze the characteristics of the bubble plumes separately. Figure 5.16 shows the generation and evolution of the first bubble plume during active breaking. The plot is colored by the streamwise, vertical, and spanwise components of the velocity field, u, v, and w, respectively. The magnitude of the dots indicates the idealized bubble size by regarding all the bubbles as regular spheres. The horizontal velocity u in figure 5.17 shows a clear distinction between bubbles at upper and lower locations. A distinction of vertical velocity between front and behind bubbles can also be observed from the vertical velocity v. As the first bubble plume is produced by the breakup of the main cavity, we can deduce that there exists a large negative (clockwise) vortex in this region, which accelerates the upper bubbles and decelerates the lower bubbles in the horizontal direction, and drives the front bubbles downwards and the behind bubbles upwards vertically. At $(t - t_{im})/T$ = 0.6 in figures 5.17(a) and (b), the bubble plume has just been generated. The initial bubble plume is approximately semicircular and a great number of large bubbles can be observed. The bubble plume is left behind the crest

as the wave travels past, and the overall horizontal and vertical velocities decrease significantly at $(t - t_{im}/T$ = 0.8 in figures 5.17(c) and (d). Due to a phenomenon similar to wave drift caused by nonlinearity, the bubble plume is stretched into an inverted triangle shape. At $(t - t_{im})/T$ = 1.0 in figures 5.17(e) and (f), the bubble plume spreads out further, and we can observe that the large bubbles float up and gather near the free surface under the action of buoyancy. Until $(t - t_{im})/T$ = 1.2 in figures 5.17(g) and (h), the total number of bubbles in the bubble plume is significantly reduced as large bubbles rise to the surface, eventually collapsing and disappearing. Throughout the entire active breaking phase, the depth of the bubble plume remains constant, consistent with the initial height of the main cavity.

Figure 5.18 shows the generation and evolution of the second bubble plume during active breaking. compared with the first bubble plume, the second bubble plume exhibits a broader spatial extent and a higher density of bubbles. When the splash-up impacts the free surface, some bubbles can be generated underneath the impact site. A significant collision between the rear side of the splash-up and the front edge of the plunging jet can be observed at t = 1.6 s. This collision entraps lots of air into the water column, which is subsequently fragmented into bubbles. It is evident that large bubbles can be generated by this entrainment and fragmentation. Figure 5.19 also shows a clear separation in the distribution of horizontal velocity u and vertical velocity v and an overall increase in the velocity of bubbles when compared with the first bubble plume. The bubbles in the second bubble plume are produced by the entrainment of the forward splash and the negative (clockwise) vortices in the near-surface turbulent region.

Ocean spray consists of small water droplets ejected from the ocean surface following surface breaking wave events. These drops get transported in the marine atmospheric boundary layer, in which they exchange momentum and heat with the atmosphere. Small spary droplets are transported over large distances and can remain in the atmosphere for several days, where they will scatter radiation; evaporate entirely, leaving behind sea salt; participate in the aerosol chemical cycle; and act as cloud condensation nuclei. Large droplets remain close to the ocean surface and affect the air-sea fluxes of momentum and enthalpy, thereby enhancing the intensity of tropical cyclones (Veron, 2015). Breaking is responsible for the formation of sea spay throygh direct atomization, and while small bubbles may be dissolved into the water column, larger bubbles entrained by breaking rise back to the surface and collapse (Deike, 2022).

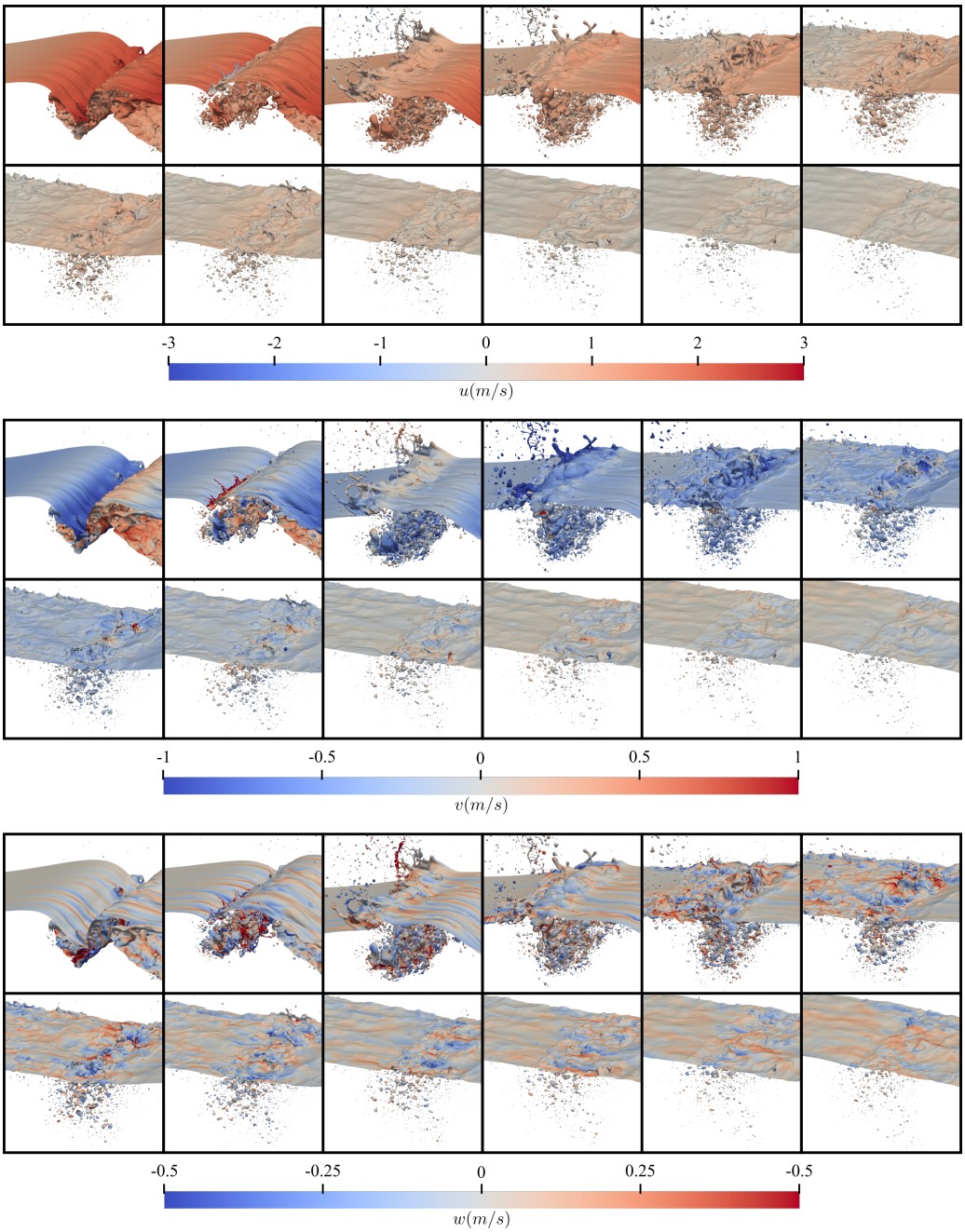

Figure 5.16: The spatial distribution and velocity of the bubbles in the first bubble plume during the active breaking phase from 1.2 s to 2.3 s for the wave with s/d = 2.13 and fd/c = 0.12 at Re = 100 000 and Bo = 8 600. The time interval between images, Δt = 0.1 s.

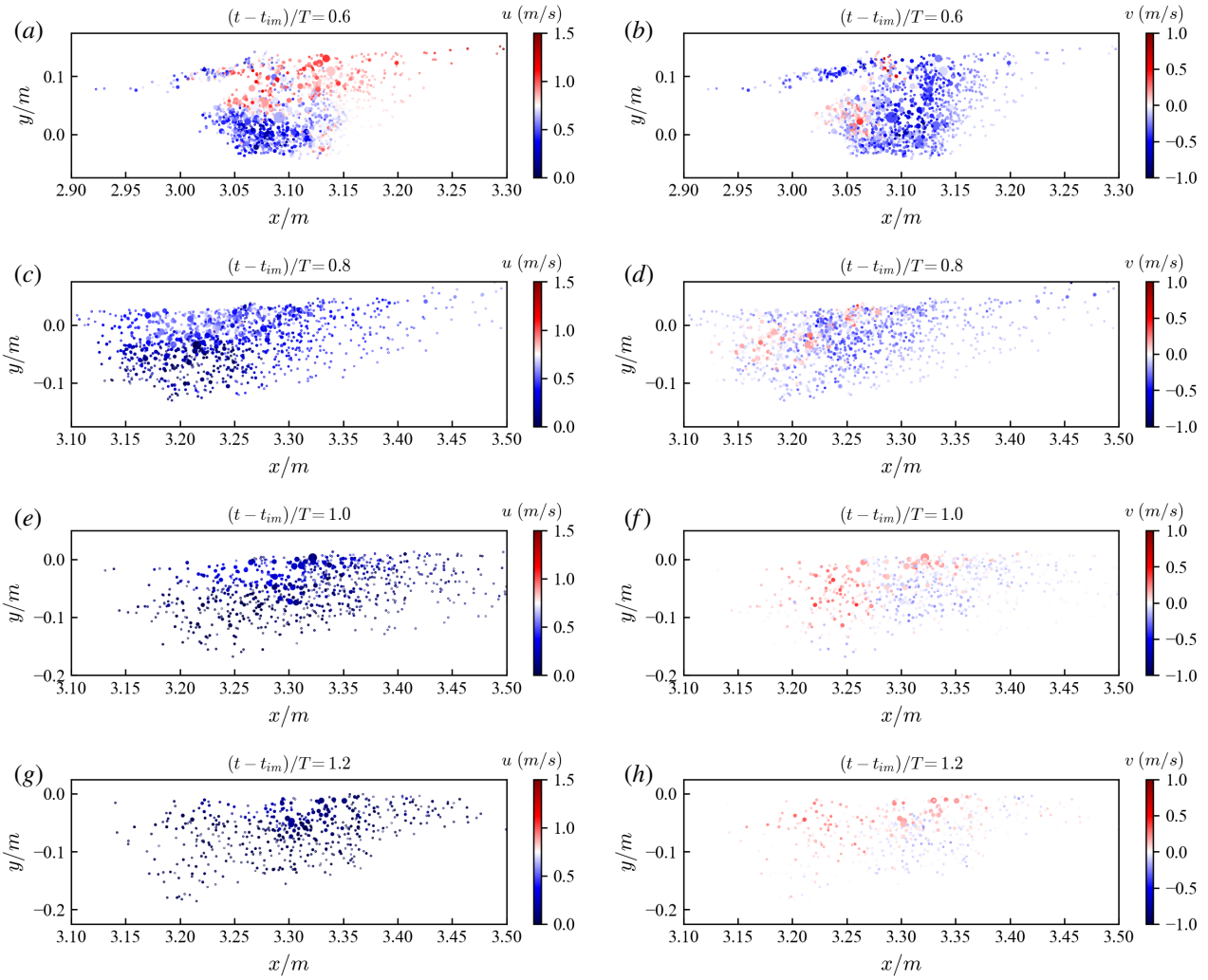

Figure 5.17: The spatial distribution and velocity of the bubbles in the first bubble plume during the active breaking phase for the wave with s/d = 2.13 and fd/c = 0.12 at Re = 100 000 and Bo = 8 600.

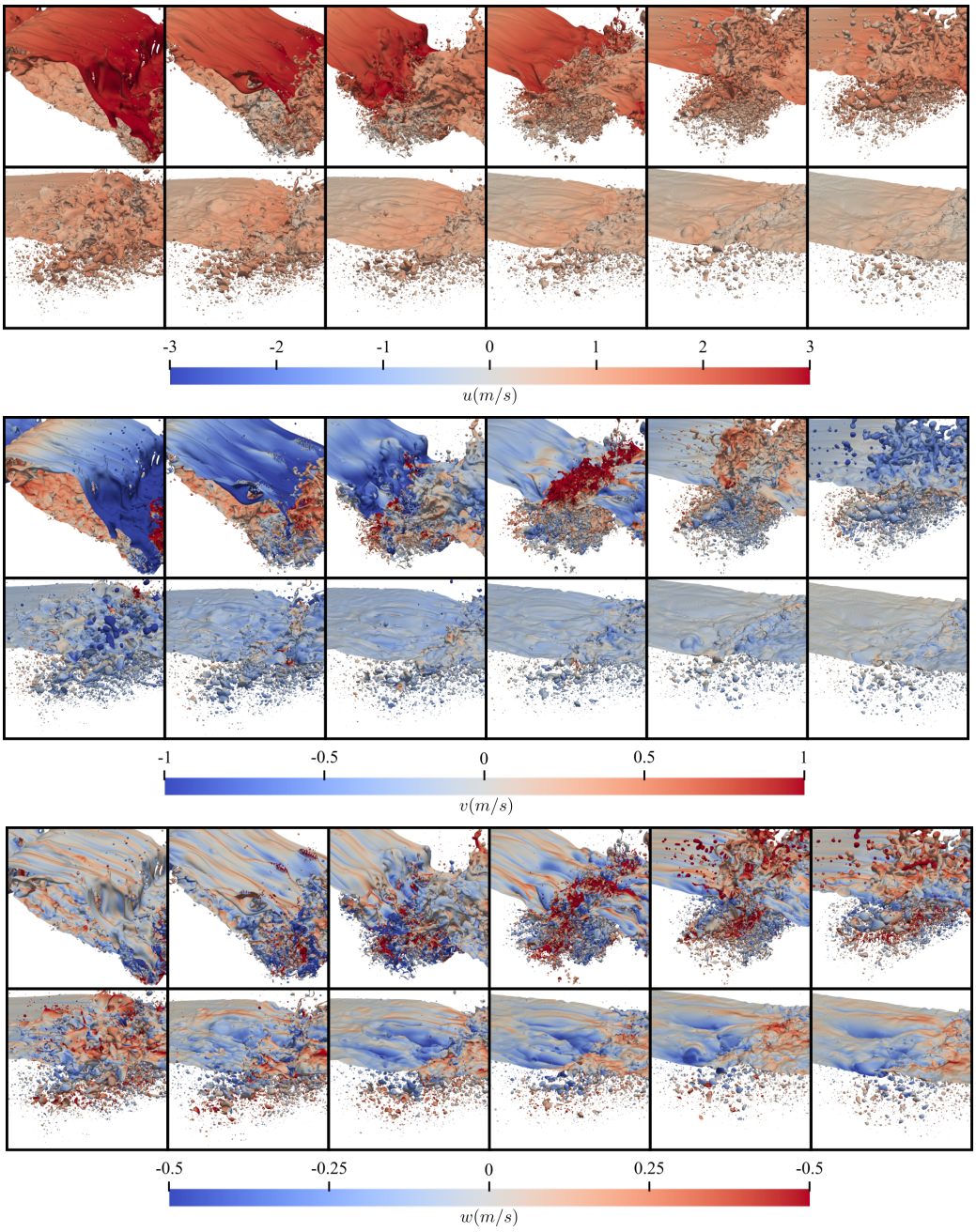

Figure 5.18: The spatial distribution and velocity of the bubbles in the second bubble plume during the active breaking phase from 1.2 s to 2.3 s for the wave with s/d = 2.13 and fd/c = 0.12 at Re = 100 000 and Bo = 8 600.

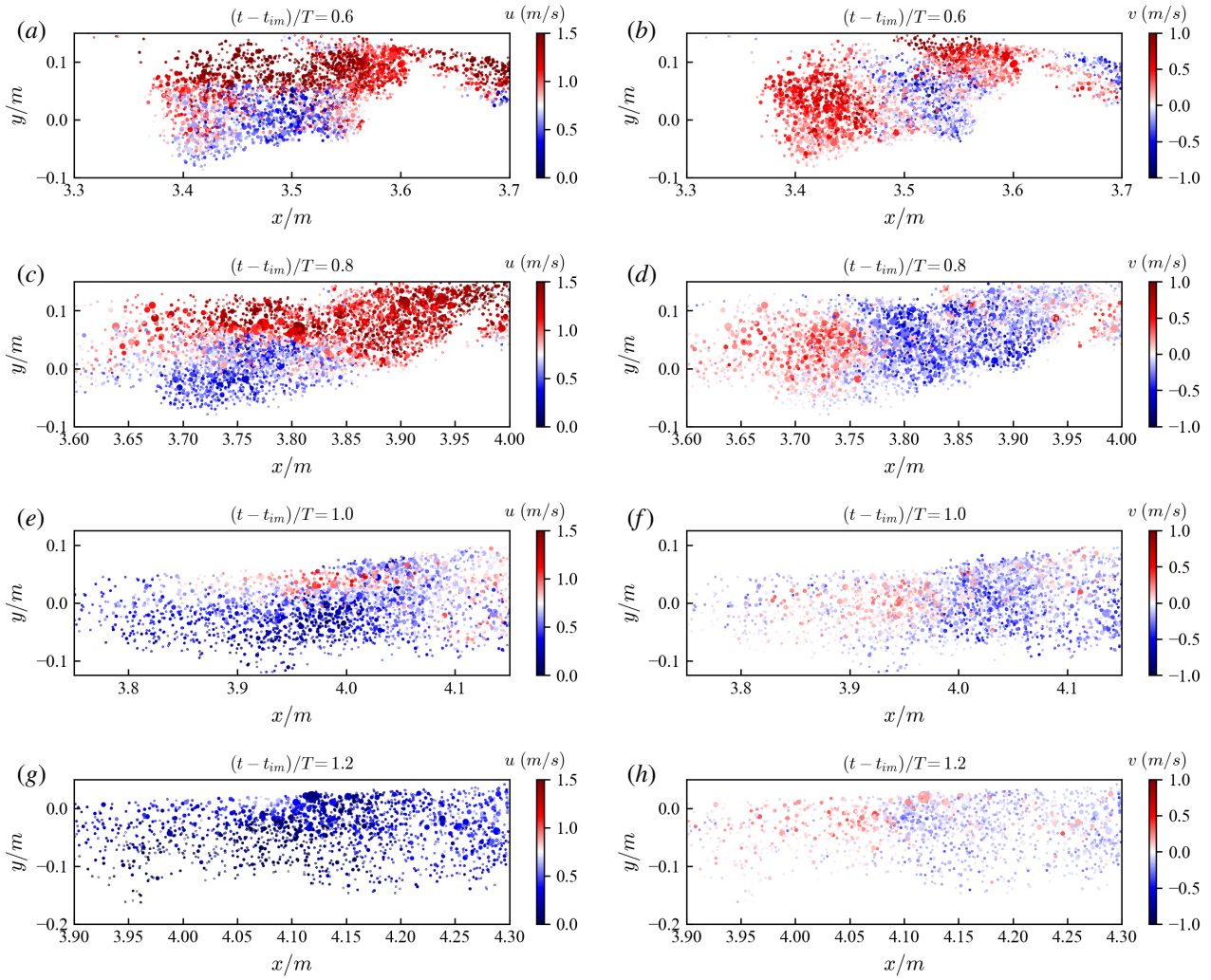

Figure 5.19: The spatial distribution and velocity of the bubbles in the second bubble plume during the active breaking phase for the wave with s/d = 2.13 and fd/c = 0.12 at Re = 100 000 and Bo = 8 600.

5.6 Conclusion

In this chapter, we extended two-dimensional breaking wave simulations to a three-dimensional framework to account for three-dimensional effects on the wave-breaking process and to evaluate the effects of viscosity (represented by Reynolds number, Re) and surface tension (represented by Bond number, Bo) on the characteristics and size distribution of bubbles generated by wave breaking. We analysed the grid convergence of the numerical results by considering three sets of simulations with l_{max} = 11, 12, and 13. We discussed numerical convergence in terms of the energy budget and size distribution of the bubbles and droplets produced by wave breaking. All results converged well, with no significant changes observed as the maximum level of refinement increased from 11 to 13. The numerical results agreed reasonably well with the experimental measurements in terms of the wave shape and maximum wave height before breaking. During the active breaking time, the bubble size distribution follows $N(r,t) \propto r^{-10/3}$. A higher Bo leads to a greater number of bubbles, with the difference being more pronounced in the range of smaller bubbles. The vertical velocity varies with bubble radius, showing varying rise velocities at different bubble radii under the effect of buoyancy, with larger bubbles rising to the free surface at a faster rate. During the active breaking phase, the depth of the bubble plume remains constant, consistent with the initial height of the main cavity. The current computational limitations of three-dimensional simulations preclude a parametric study encompassing a broad range of Re and Bo values. Consequently, future research will focus on comparative analyses of energy budget and air entrainment between two-dimensional and three-dimensional simulations.

Chapter 6

2-D oil dispersion simulations

Contents

The breaking process described herein, including the wave overturning, the phenomenon of splash-up and the mode of gas entrainment and droplet formation, is generally in accordance with the laboratory observations of Li (2017); Li *et al.* (2017). The characteristics of oil droplets dispersed from spills resulting from common oceanic activities are essential for effective oil spill response. Breaking waves, a significant driving force of oil spills, can entrap the oil film into the water column, fragment the oil slick into droplets, and disperse the oil over a wide area. Dispersants, which significantly reduce the interfacial tension between oil and water, are widely used in oil spill response to decrease the overall oil droplet size, thereby mitigating oil spill contamination of the ocean and coastlines and reducing its harm to the marine environment and biology. Therefore, investigating possible influential factors, especially the effects of wave energy and interfacial tension on oil droplet characteristics, is crucial to understanding the oil dispersion process and improving the efficiency of oil spill response.

6.1 Numerical set-up

We solve numerically the partial differential equations with the open-source free software library Basilisk. Basilisk allows to perform direct numerical simulation with no turbulence models required as the Navier-Stokes equations are resolved down to the smallest scales. When dealing with multiphase flow, the variations of density and viscosity inside the domain are described with the help of the Volume of Fluid method. Because we are in presence of a three-phase flow, we cannot use the implicit declaration of phase two as in a two-phase flow. Instead, we declare explicitly three volume fractions corresponding to each phase. Because of the overlap and empty of the phases in a cell, the sum of volume fractions could be in a range of 0 to 3. To respect the physical constrain of $\alpha_a + \alpha_w + \alpha_o = 1$, we normalize the volume fractions of each phase with the sum of volume fractions at each time step

$$\alpha_{i,norm}(x,t) = \frac{\alpha_i(x,t)}{\sum_{i=1}^{3} \alpha_i(x,t)} \tag{6.1}$$

This way we can follow a one fluid description with variable density and viscosity determined in the domain with arithmetic mean

$$\rho(\alpha) = \alpha_a \rho_a + \alpha_w \rho_w + \alpha_o \rho_o \tag{6.2}$$

$$\mu(\alpha) = \alpha_a \mu_a + \alpha_w \mu_w + \alpha_o \mu_o \tag{6.3}$$

Surface tension is acting on the interface between two fluids, but here there is more than one possibility of fluid neighbour for one phase. That is why we decompose the physical surface tension into phase-specific surface

Wave	s (m)	f (Hz)	d (m)	U_{max} (m/s)	t_o (mm)	γ/γ_0
1	0.3962	0.75	0.25	0.934	5	3
2	0.4267	0.75	0.25	1.005	5	3
3	0.4572	0.75	0.25	1.077	5	3
4	0.4877	0.75	0.25	1.149	5	3
5	0.5334	0.75	0.25	1.257	5	3
6	0.5334	0.75	0.25	1.257	5	1
7	0.5334	0.75	0.25	1.257	5	2
8	0.5334	0.75	0.25	1.257	5	4
9	0.5334	0.75	0.25	1.257	5	6
10	0.5334	0.75	0.25	1.257	5	8
11	0.5334	0.75	0.25	1.257	5	10

Table 6.1: Parameter space for a parametric study in two-dimensional oil dispersion simulations. The column labels are as follows: s, wave plate stroke; f, frequency; d, water depth; U_{max}, maximum piston speed; γ/γ_0, the ratio of interfacial tension to the oil-water interfacial tension.

tension just depending on the phase and not the fluid in contact (Chen *et al.*, 2017; Joubert *et al.*, 2022)

$$\gamma_a = (\gamma_{ao} + \gamma_{aw} - \gamma_{wo})/2 \tag{6.4}$$

$$\gamma_w = (\gamma_{wa} + \gamma_{wo} - \gamma_{ao})/2 \tag{6.5}$$

$$\gamma_o = (\gamma_{oa} + \gamma_{wo} - \gamma_{aw})/2 \tag{6.6}$$

Numerical simulations of oil dispersion were performed in the presence of oil slicks on the interface. Five breakers with wave plate stroke s of 0.3962 m, 0.4267 m, 0.4572 m, 0.4877 m, and 0.5334 m were selected to investigate the effects of wave energy on oil droplet sizes. Six cases with interfacial tension γ/γ_0 of 1, 2, 4, 6, 8, 10 were also simulated to investigate the effects of interfacial tension on oil dispersion processes, where γ_0 is the interfacial tension between oil and water. The various cases and corresponding parameters are summarized in Table 6.1. Oil was initially maintained on the free surface centered at x_0 = 1.6 m, with a length of 0.4 m and a thickness of 5 mm. A maximum level of refinement of 16 was used for the oil phase, and 14 was used for the water and air phases in the two-dimensional oil dispersion simulations. The ratio of oil-water density and viscosity were set to the experimental values, which are $877/1018.3$ and $1.07 \times 10^{-5}/1.01 \times 10^{-6}$, respectively.

6.2 Parametric study

The fate of spilled oils is influenced by numerous factors, such as the geometry, position, and thickness of the oil slick. Given the widespread use of dispersants in oil spill mitigation, it is also essential to investigate the effects of interfacial tension. Therefore, this parametric study investigates the effects of wave energy, oil slick thickness, and interfacial tension on the resulting oil dispersion processes.

6.2.1 Effects of wave intensity on the particle statistics

We investigate the influence of breaking wave energy on the characteristic size of oil droplets. We generated five breaking waves with different energy dissipation rates by varying the stroke of the wave plate s from 0.3962 m to 0.5334 m. Each wave is characterized by its specific wave height and energy dissipation. The oil was generally introduced at the undisturbed water surface as a rectangular oil slick. The position of the oil slick was chosen so that it was impacted by the jet of the plunging breaker. The same thickness of the oil film h_o = 5 mm was used when studying the effect of wave energy. All the oil particles were subsequently fragmented into oil droplets or entrained in the water column by splash-ups and turbulence generated by breaking waves.

In the presence of surface-breaking waves and the resulting upper-ocean turbulence, pre-existing oil films can disintegrate under the action of gravitational, viscous, and surface tension forces, forming numerous oil droplets. Turbulence can be characterized by a spectrum of eddies varying in size. The energy contained within the larger eddies undergoes a cascade, propagating through intermediate-scale eddies and ultimately dissipating into heat due to the effects of viscosity. The significant velocity gradients present in these smaller eddies play a crucial role in the disintegration of oil droplets. In comparison, the larger eddies predominantly facilitate the diffusive transport of the oil droplets. To assess the effect of energy dissipation strength on the characteristic droplet size, we induced breaking waves with different energy levels under a constant interfacial tension condition of γ/γ_0 = 3, varying the stroke of wave plate s within the range of 0.3962 m to 0.5334 m. The quantification of the energy dissipation rate per unit volume was derived from the total energy loss during the active breaking period. Figure 6.1 shows the temporal evolution of the three-phase free surface at s = 0.4267 m. The leading edge of the wave crest becomes vertical at t/T = 0.38 (Figure 6.1a) and the initial plunging jet impacts the wavefront at t/T = 0.50 (Figure 6.1b). The jet does not contact the oil slick at the moment of jet impact. As the wave propagates, the jet affects the left portion of the oil slick, causing it to become enrolled beneath the wave crest together with the main air cavity. Due to the lower energy from the wave impact, the

affected oil slick remains continuous for a period of time (Figure 6.1c). The oil phase on the left side of the impact site is entrained, forming elongated oil ligaments that encircle the air cavity. The oil phase on the right side of the impact site interacts with the water phase, resulting in the initial splash-up event (Figure 6.1d). This splash-up gives rise to a stratified liquid film, with the wave phase at the top and the oil phase at the bottom. The first splash-up develops further, with the oil phase settling beneath the wave phase. As this initial splash-up evolves, portions of oil-water patches detach from its tip. Under the influence of gravity, the first splash-up descends and collides with the wavefront. This collision induces rapid free surface expansion, leading to the elongation and dispersion of the oil phase and the generation of numerous oil droplets varying in size. Simultaneously, the air cavity trapped within the liquid and the oil phase behind the advancing wave undergoes disintegration, giving rise to formations such as air bubbles, elongated oil patches, oil ligaments, and additional oil droplets (Figure 6.1e-f). In the late stage at t/T = 1.50, the residual oil phase has been dispersed into small droplets by the region of strong turbulence near the waveform. Simultaneously, some oil droplets located at the rear of the waveform become entrapped within the deeper water column under the action of the vortices, whereas most of the entrained oil particles resurface. The initial oil slick with a width of 0.4 m and a thickness of 5 mm experiences extensive transportation and dispersion across a wide span. The maximum spacing of the oil phase along the streamwise direction and vertical direction is 2.731 m and 0.576 m, respectively.

To better identify the turbulent flow fields during wave breaking, the vorticity field was computed at different times. Figure 6.2 shows the time evolution of a breaking wave at s = 0.4267 m, with the vorticity field displayed in both the water and oil phases. The time evolution indicates that in the pre-breaking stage of wave steepening at $t/T = 0.38$ (Figure 6.2a) and jet impact at t/T = 0.50 (Figure 6.2b), both tips of oil slick spread slightly under the influence of surface tension, causing opposite vorticities in the near-water phase beneath the surface. During the development of the first splash-up generated by the plunging jet impact, negative (clockwise) vorticity is produced and mostly localized around the entrained air cavity and the elongated oil ligaments that encircle the air cavity (Figure 6.2c). Topological changes in the flow, such as jet plunging and reconnection, are responsible for vorticity generation. The splashing process and air entrainment generate bubbles and droplets with associated vortical structure, also related to topological changes (Iafrati, 2009; Deike *et al.*, 2015) (Figure 6.2d). Entrainment between the rear side of the splash and the upper surface of the plunging jet is observed at t/T = 0.86, together with entrapment by subsequent impacts of forward splash created by the jet impact (Figure 6.2e). The circulations generated by the first backward-splash entrainment are observed at t/T = 0.98 (Figure 6.2f), where entrainment between the rear side of the second splash and the upper surface of the first

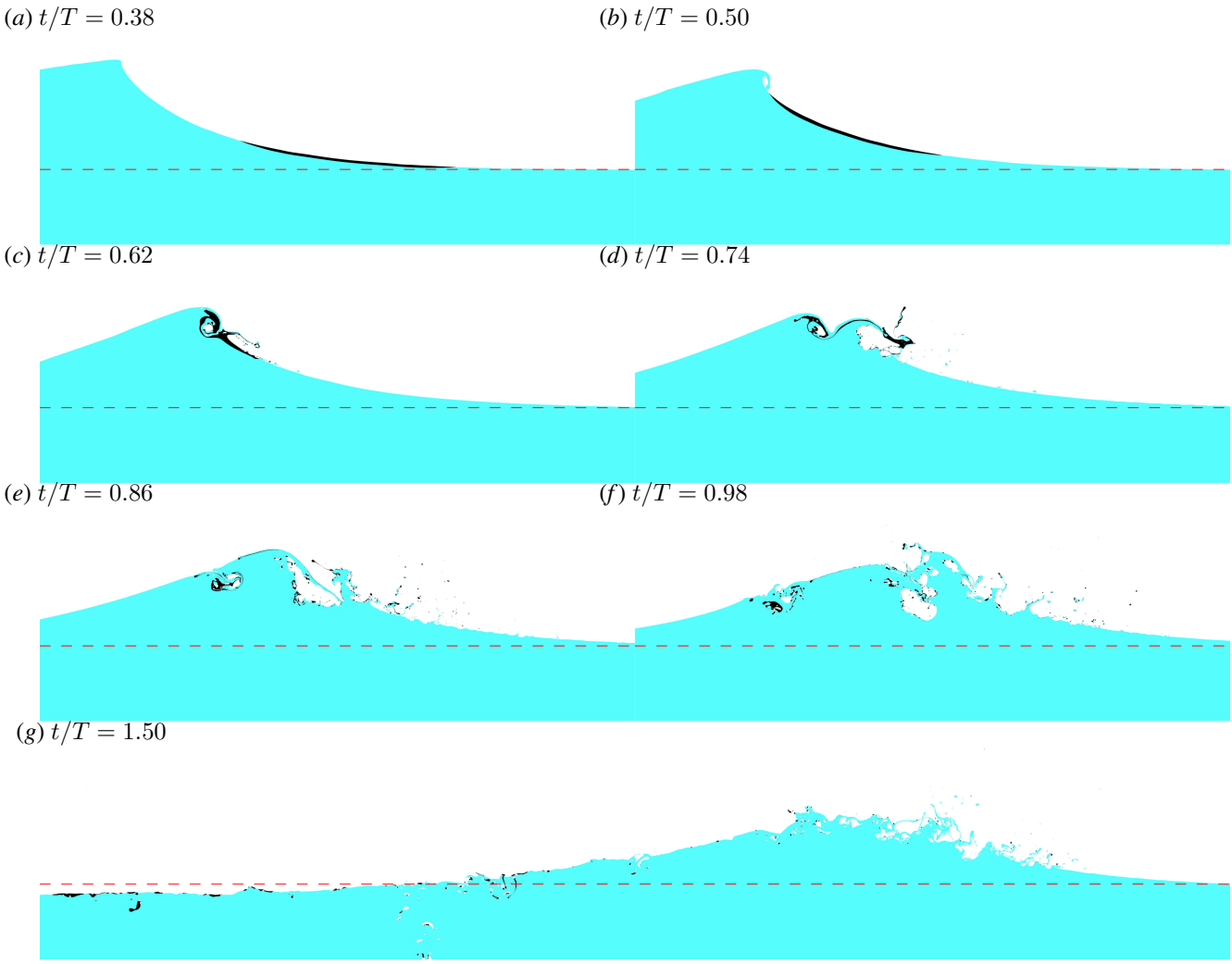

Figure 6.1: The time evolution of the three-phase free surface at s = 0.4267 m.

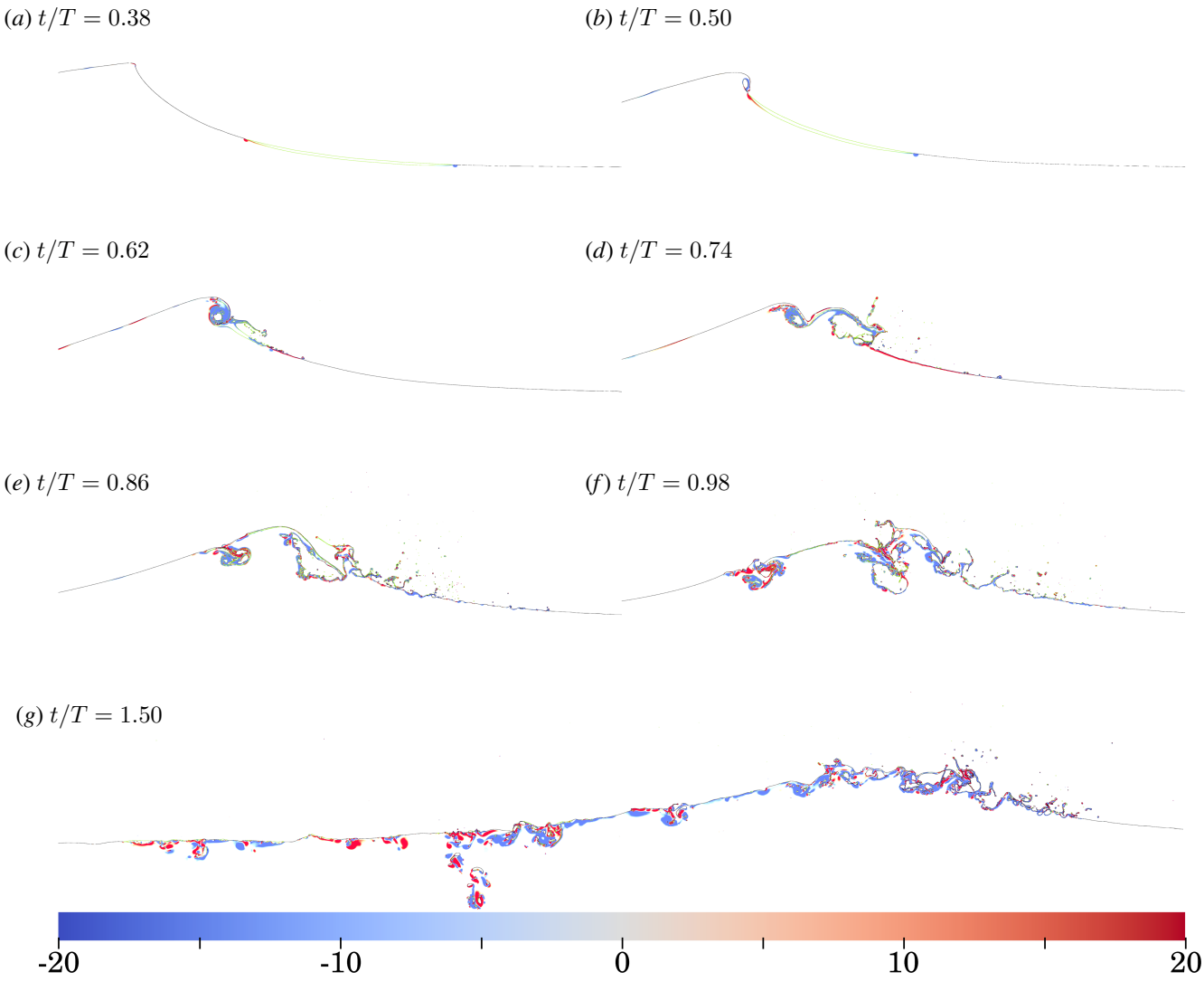

Figure 6.2: Evolution of a breaking wave at s = 0.4267 m and the vorticity field, displayed both in the water and oil.

splash occurs. In the very late stages of the breaking process at t/T = 1.50, entrainment is observed all over the splash and the turbulent breaking regions when the surface bursts into ligaments and droplets in highly energetic waves, and entrapment is observed at the leading edge of the turbulent breaking region in the late stages of the breaking process (Figure 6.2g).

Figure 6.3 shows the evolution of a breaking wave, obtained for s = 0.4267 m, and the vorticity field displayed only in the oil. When the wavefront becomes vertical (Figure 6.3a) and a jet is formed, there is no vorticity within the oil slick. When the plunging jet impacts on the wavefront (Figure 6.3b), there is only a tiny negative vorticity on the side near the jet impact site because of the rising of the free surface. Until t/T = 0.62 when

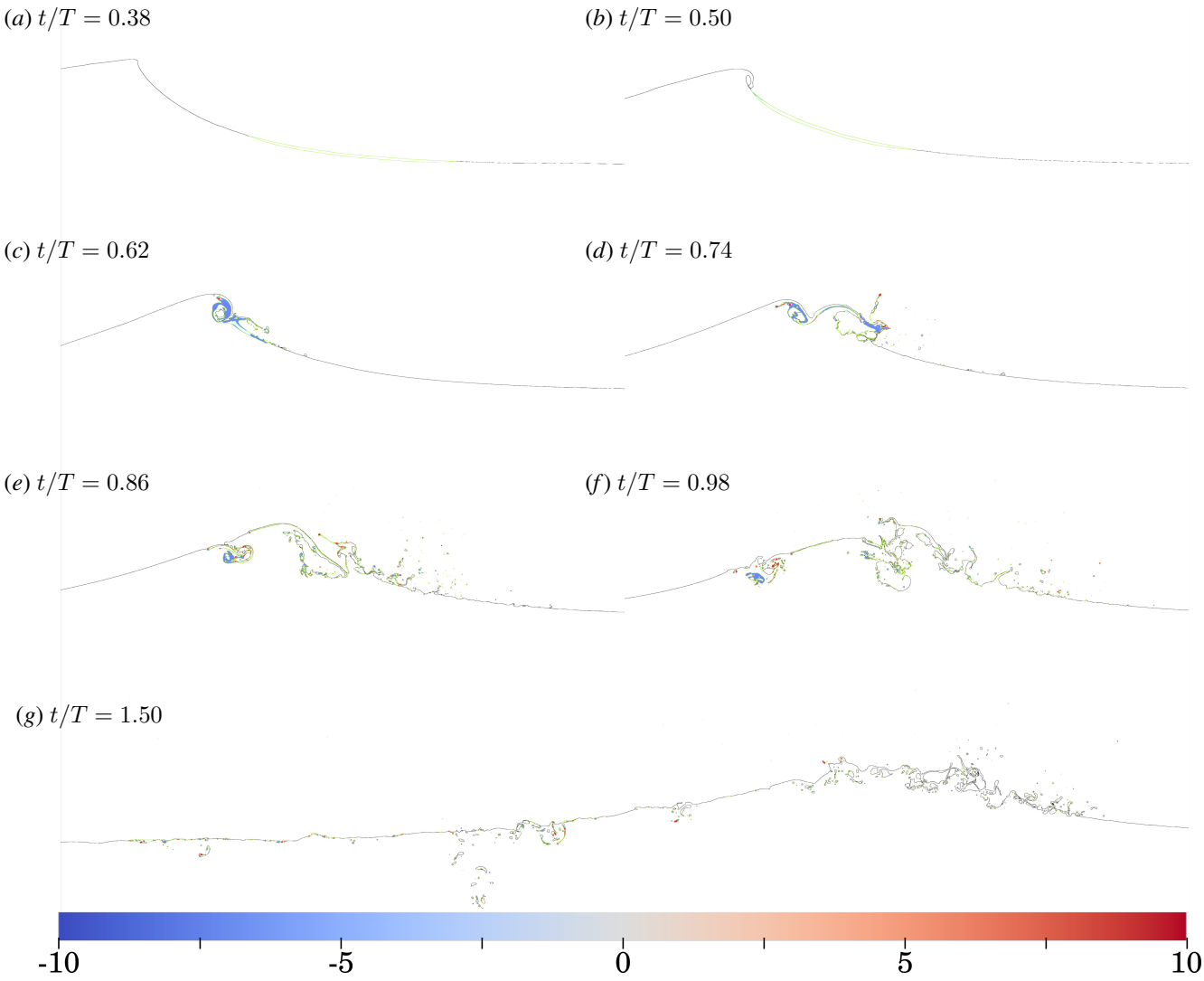

Figure 6.3: Evolution of a breaking wave at s = 0.4267 m and the vorticity field, displayed only in the oil.

the first splash-up is generated (Figure 6.3c), the oil slick was entrapped, surrounding the air cavity. At this time, the negative vorticity can be observed in the majority of the oil slick. At t/T = 0.74, a long oil ligament was produced in the middle of the rising splash-up and stretches (Figure 6.3d). When the tip of the splash-up impacts the free surface (Figure 6.3e), the fragments and droplets mixed with water and oil were generated by the impact of the splash-up. Meanwhile, As the splash-up stretch further (Figure 6.3f), the oil droplets can be formed because of the elongation of the oil ligaments under the effect of surface tension. In the very late stages of the breaking process at t/T = 1.50, the initial oil slick has been fragmented into ligaments and droplets and spreads all over the wave propagation region (Figure 6.3g).

Figure 6.4 shows the time evolution of the three-phase free surface at s = 0.5334 m. The formation and the

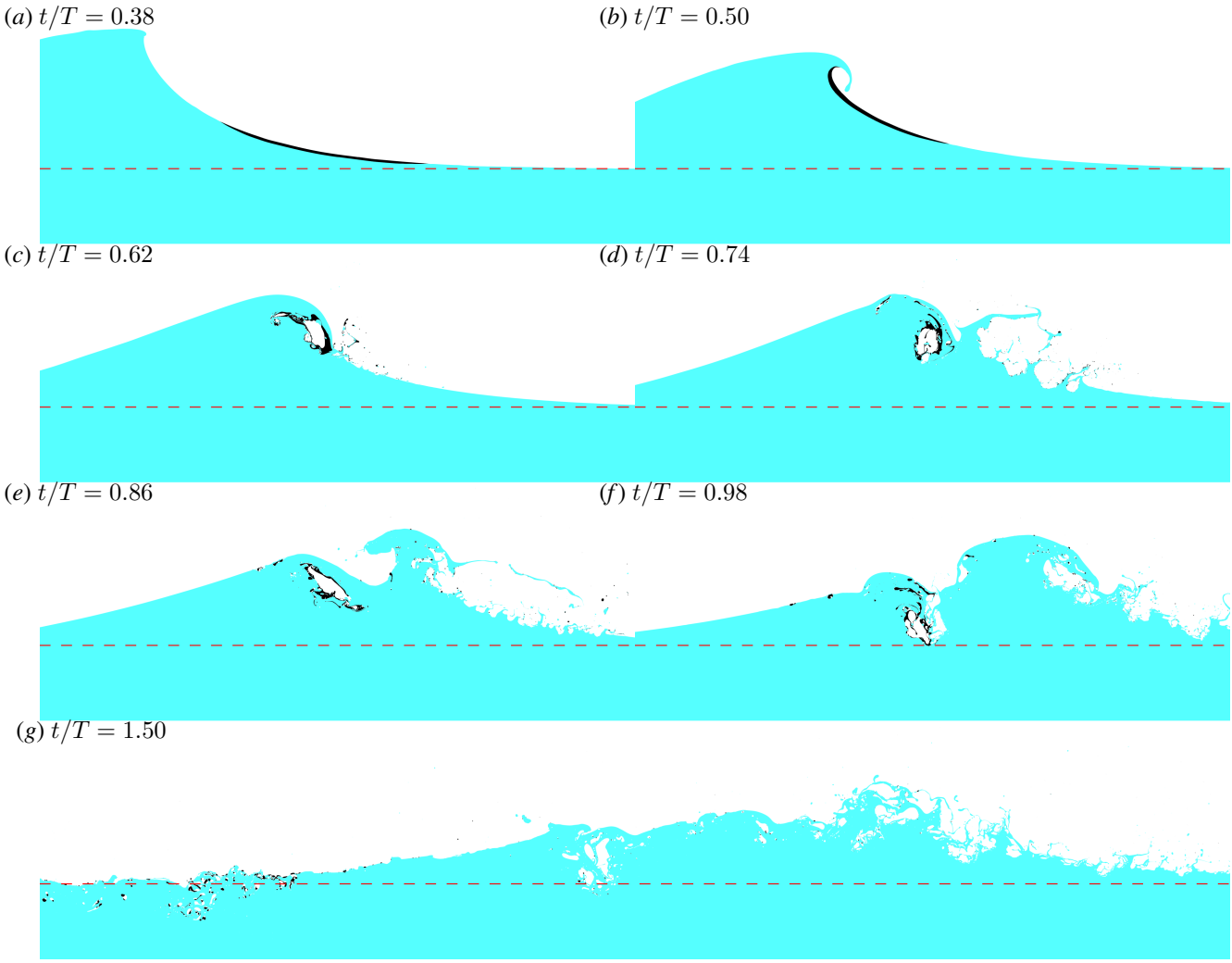

Figure 6.4: The time evolution of the three-phase free surface at s = 0.5334 m.

evolution of the plunging breaker are similar to the description of the plunging breaker obtained for s = 0.4267 m. In this case, the initial plunging jet impacts the oil slick (Figure 6.4b). The splashing process and free-surface stretching become more violent, producing more dispersed oil fragments and droplets (Figure 6.4c-g). When the wave plate stroke s is increased, plunging waves are still observed but the wave becomes higher, leading to a significant increase in air entrapment and a stronger splashing and oil breakup process. For the breaking waves with higher breaking strength, the wave breaking tends to promote wave overturning and subsequent surface turbulence, which enhances the oil breakup and generates smaller oil droplets.

Figure 6.5 shows the evolution of a breaking wave, obtained for s = 0.5334 m, and the vorticity field displayed both in the water and oil. A larger magnitude of the vorticity and smaller eddy structures can be

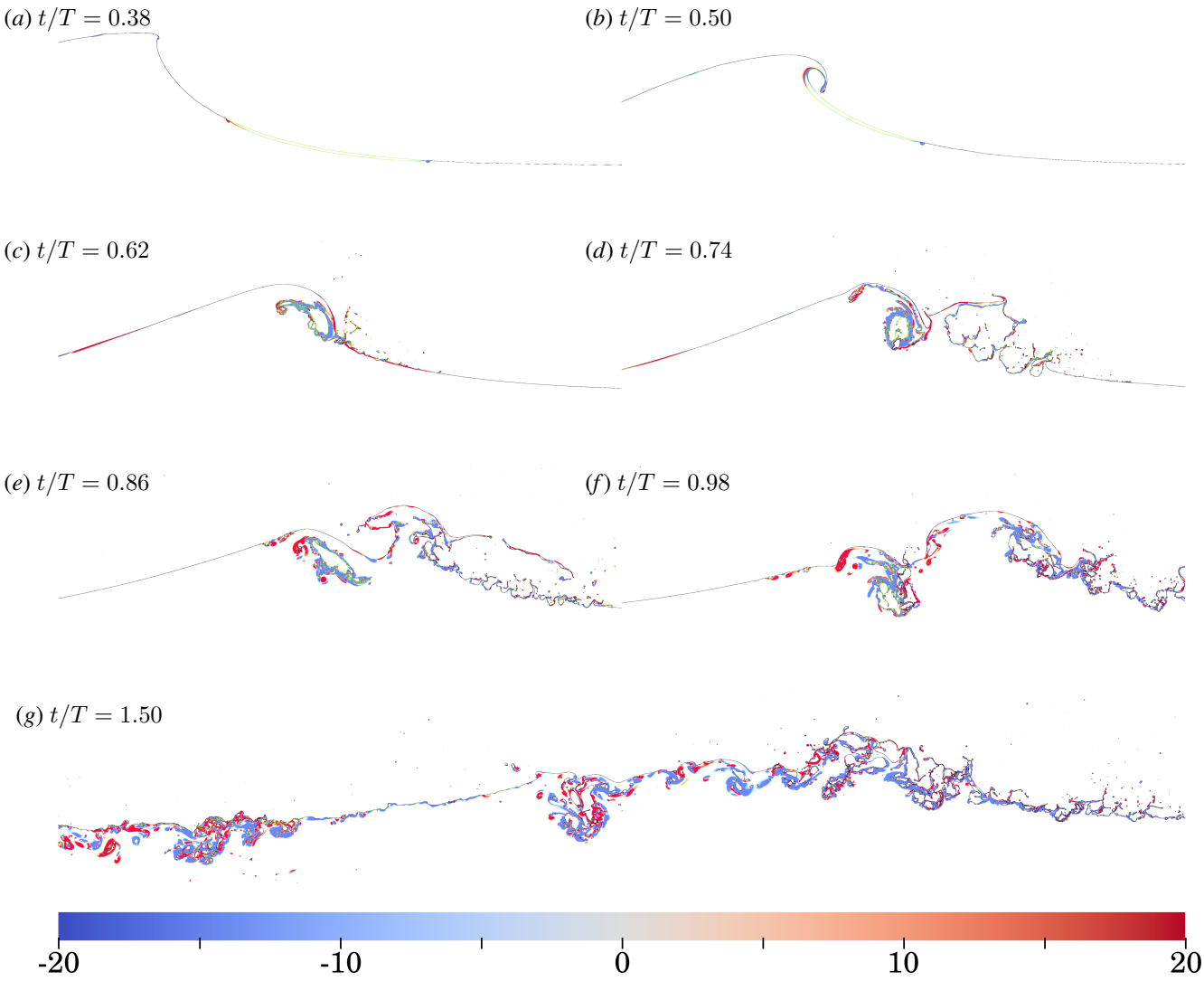

Figure 6.5: Evolution of a breaking wave at s = 0.5334 m and the vorticity field, displayed both in the water and oil.

observed, indicating stronger turbulence and wider turbulent region caused by wave breaking.

Figure 6.6 shows the evolution of a breaking wave, obtained for s = 0.5334 m, and the vorticity field displayed both in the water and oil. A more pronounced negative vorticity within the oil slick can be observed at t/T = 0.50 because of the rising of the left side of the oil slick (Figure 6.6b). At t/T = 0.62, due to the larger air cavity entrapment and stronger impact of the plunging jet on the free surface, the more pronounced vortices can be observed at the left side of the jet impact site, but the jet still cannot penetrate the oil slick (Figure 6.6c). At the right side of the jet impact site, the generated splash-up ruptured violently and shattered into fragments and droplets (Figure 6.6d-f). During the breaking processes, stronger turbulence caused by the larger wave breaking

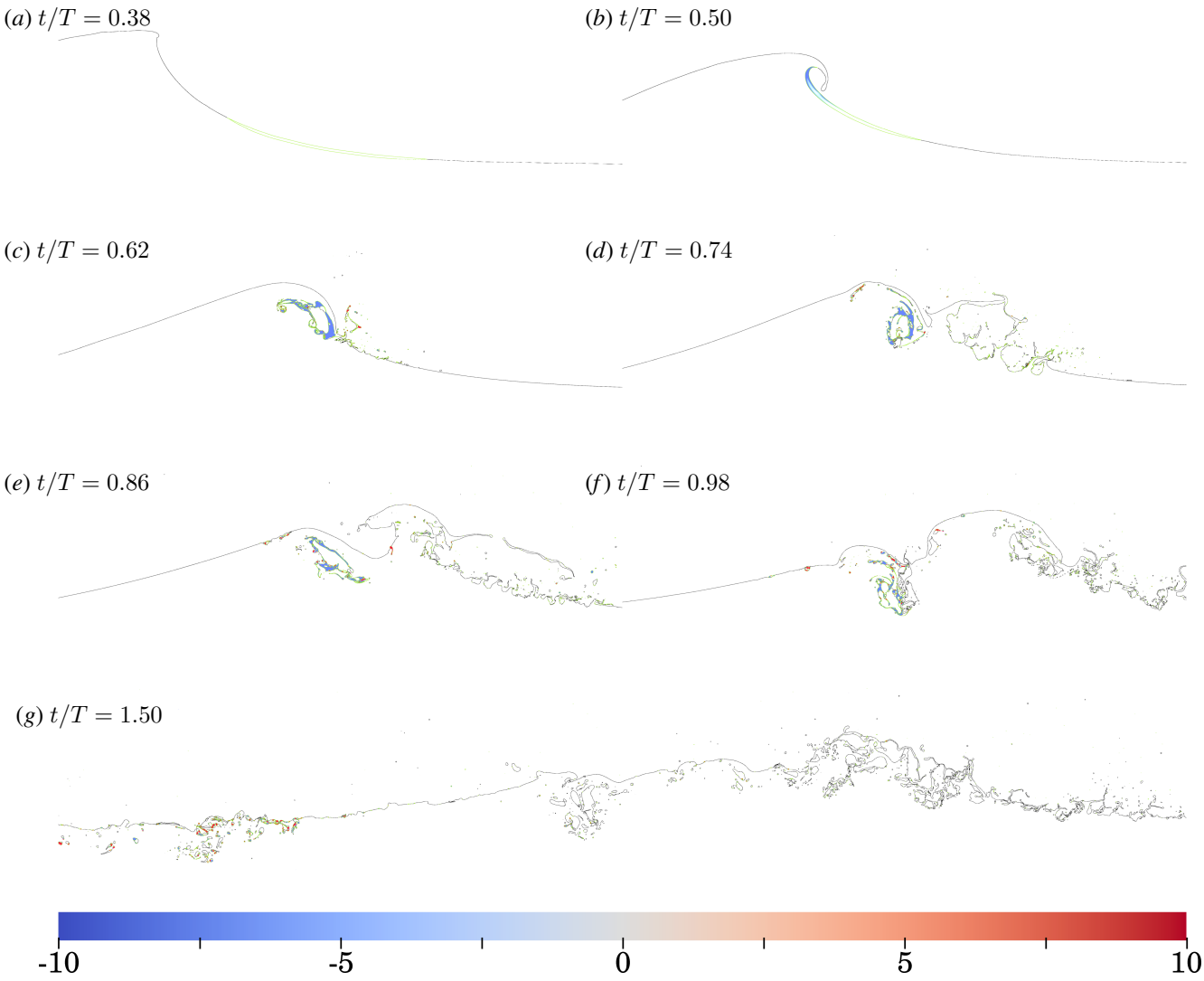

Figure 6.6: Evolution of a breaking wave at s = 0.5334 m and the vorticity field, displayed both in the water and oil.

strength results in the more pronounced elongated oil structures and dispersed oil droplets (Figure 6.6g).

Figure 6.7 shows the time evolution of the surface tension energy normalized by the initial value at t/T = 0.50 in the water phase (Figure 6.7a) and in the oil phase (Figure 6.7b). A general increase in the surface tension energy in the water can be observed as the wave strength increases. The initial surface energy at t/T = 0.50 corresponds to the time which is approximately at the jet impact moment. So the increase of the normalized surface energy corresponds to the increase of the free surface caused by the wave breaking. As can be seen in Figure 6.7(a), the increase rate of the surface energy in the water with time shows some fluctuations, with the rapid increase corresponding to the jet impact and the generation of the splash-ups. After the first increase of the

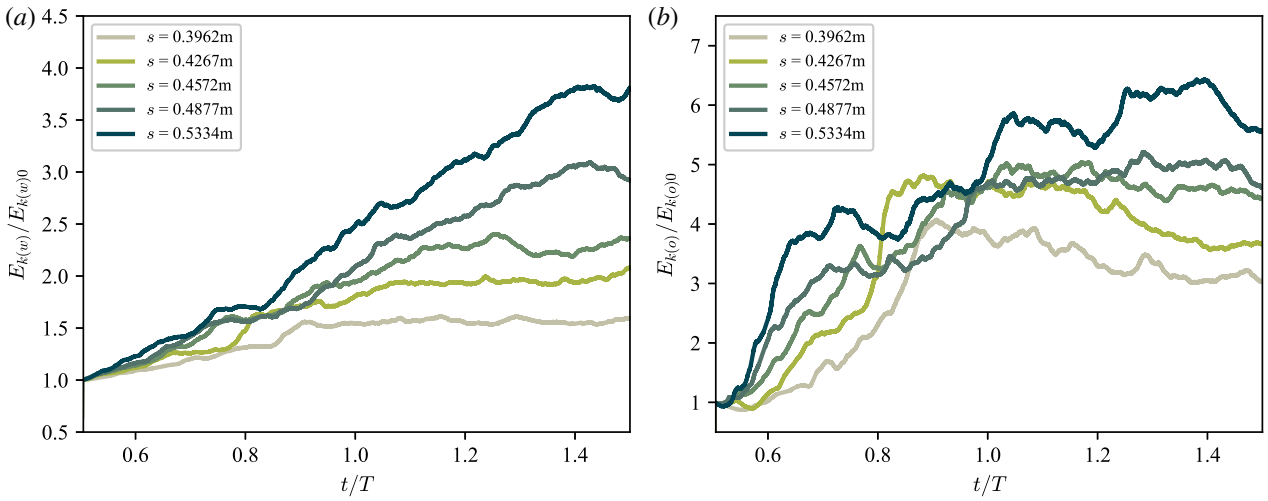

Figure 6.7: Evolution of the surface tension energy of the water phase (a) and oil phase (b) at various wave plate strokes. The surface tension energy is normalized by the initial surface energy at t/T = 0.5.

surface energy caused by the initial splash-up, the weaker breaking waves undergo an obvious second splashing process and then keep a relatively constant surface energy, as can be seen at s = 0.3962 m and s = 0.4267 m. For larger breaking waves, three pronounced splashing processes can be observed and shown in the evolution of the surface energy. For the case with s = 0.5334 m, the largest surface energy can be observed at t/T = 1.4 and it is approximately 4 times the initial surface energy. Figure 6.7(b) shows the evolution of the surface energy in the oil phase. With the increase of the wave plate stroke, a general increase of the surface energy can be observed in the oil phase after wave breaking. After the jet impact, the surface energy in the oil phase presents a rapid increase for all cases, caused by the stretching of the oil slick and the production of the initial splash-up. The first jet impact corresponds to a most significant increase of the surface energy in the oil phase, showing 3 - 4 times the initial surface energy. For weaker breaking waves, the surface energy reaches the maximum and then decreases after the first jet impact. However, for stronger breaking waves, the subsequent splashing processes increase the surface energy in the oil phase even further. For the case with s = 0.3962 m, the maximum surface energy can be observed at t/T = 0.95, which corresponds to the end of the first splash-up, and it increases to 4 times the initial surface energy. For the case with s = 0.5334 m, the maximum surface energy can be observed at t/T = 1.4, corresponding to the end of the third splash-up, and is approximately 6.5 times the initial surface energy.

Next, we examine the relationship between the characteristic droplet size and the energy dissipation rate due to breaking. By generating homogeneous turbulence with different energy levels using an oscillating grid in a

vertical column, Delvigne & Sweeney (1988) fit an empirical relation between the mean and maximum droplet sizes and the mean energy dissipation rate: $d_{50}, d_{max} \propto \epsilon^{-0.50(\pm 0.1)}$. This can be interpreted theoretically by Hinze's formula which assumes that the dynamic pressure forces of turbulent flows are the cause for the droplet breakup. The formula for the maximum droplet size can be obtained as $d_{max} = c(\gamma/\rho)^{3/5}\varepsilon^{-2/5}$. Li & Garrett (1998) proposed a hypothesis that turbulent shear is a dominant force for droplet breakup when oil droplets are sufficiently small. They derived a transitional dissipation rate ϵ_c between the pressure and shear regimes $\epsilon_c = (\alpha_1/c)^{5/3}(\gamma/\mu)^5(\gamma/\rho)^{-1}(\mu_d/\mu)^{5/8}$. This gives the dissipation rate at the transition between the two regimes as $\epsilon_c \approx 2.2 \times 10^4$ $\mathrm{m}^2/\mathrm{s}^3$ and $\epsilon_c \approx 474$ $\mathrm{m}^2/\mathrm{s}^3$ when assuming an intermittency face of 10 in breaking waves for typical water and oil properties. As the typical values of energy dissipation rate in breaking waves range from 0.1 $\mathrm{m}^2/\mathrm{s}^3$ in moderate sea conditions to 10 $\mathrm{m}^2/\mathrm{s}^3$ in stormy sea conditions (Duncan, 1981; Kendall Melville, 1994; Li & Garrett, 1998), it concludes that in natural breaking waves the pressure force must be the breakup mechanism and cannot cause a significant amount of droplet dispersion except in extreme weather conditions or when chemical dispersants are used. Therefore, the characteristic droplet size should hold a scaling law of -2/5 to the turbulence energy level ϵ.

Figure 6.8 (a) shows the time evolution of the energy dissipation rate for various wave-breaking strengths, by varying the wave plate stroke from 0.3962 m to 0.5334 m. These cases have the same frequency of the wave plate f = 0.75 Hz, and we observed a similar impact time t_{im} = 0.50, which is likely to indicate that the impact time is determined by the wave plate frequency (and the wave period of the generated waves). The active breaking period used to determine the averaged or the maximum breaking dissipation rate is selected as one wave period after jet impact from $t_{im} + 0.2T$ to $t_{im} + 1.2T$, which is approximately from t/T = 0.7 to t/T = 1.7 for all cases here.

To elucidate the dearth of turbulent fragmentation, the approximate characteristic droplet size should be used to identify the size distribution of the oil droplets produced by wave breaking. The commonly used characteristic droplet size in the experiment is d_{95}, which indicates that 95% of the total volume of oil is contained in droplets with $d \leq d_{95}$. In the experiments, the subsurface droplet size distribution in the wave-breaking region is usually quantified using oil droplet sampler, high-speed imaging, or digital inline holography technique. Conversely, the information recorded in our simulations contains all the oil phase separating from the initial oil slick in the numerical domain produced by wave breaking, which consists of oil parcels, ligaments, fragments, and droplets. Moreover, in the oil dispersion by breaking waves, the dispersed oil was generally only a small fraction of the total oil mass in the surface slick. All surface oil was submerged by the breaking waves, but the oil lumps

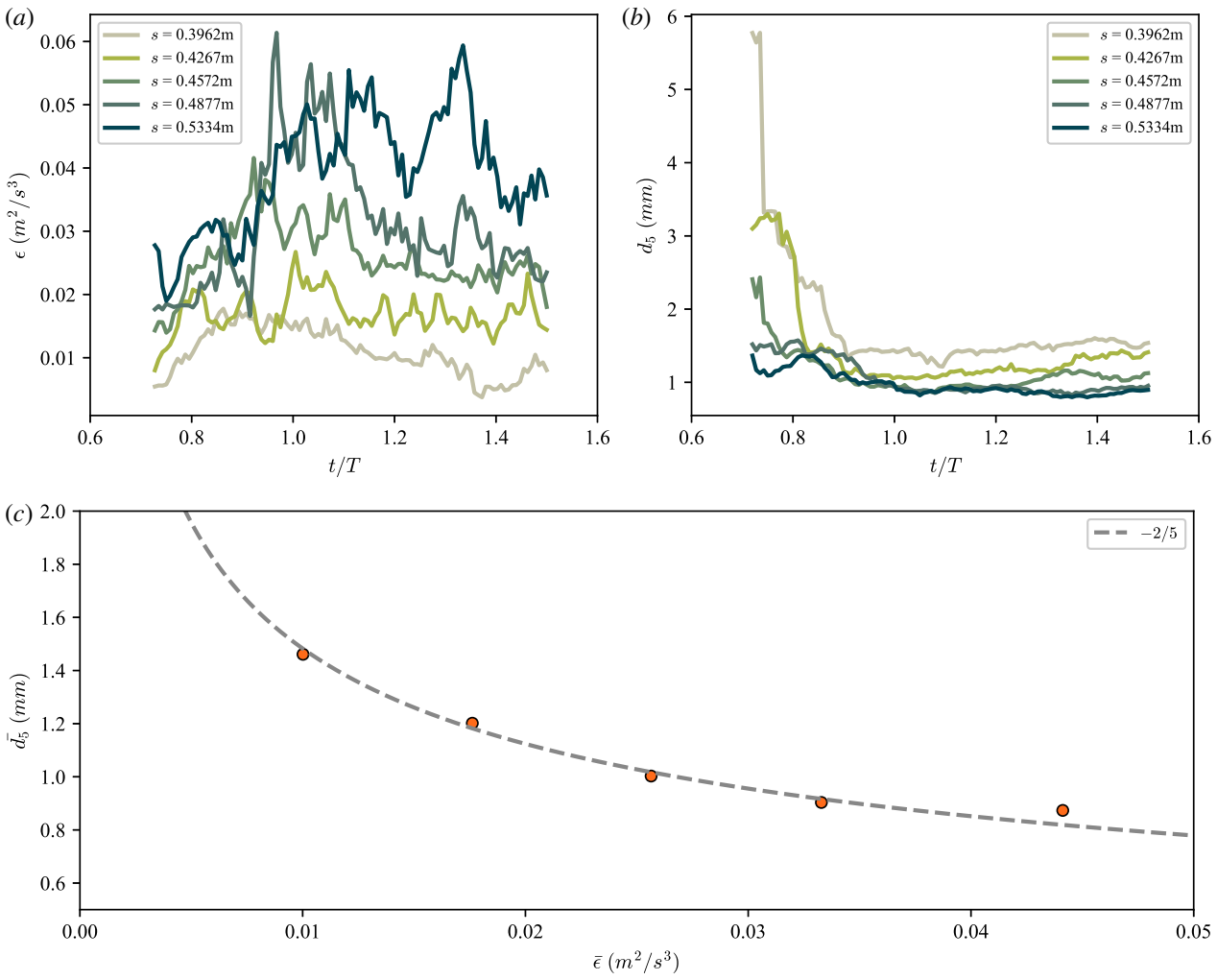

Figure 6.8: Time evolution of (a) the energy dissipation rate ϵ due to breaking at various wave-breaking strengths and (b) the characteristic oil droplet size d_5 at various wave-breaking strengths. (c) The relationship between mean droplet size $\bar{d_5}$ and mean dissipate rate $\bar{\epsilon}$. The mean values were averaged from t/T = 1.0 to t/T = 1.5. The dashed line represents the theoretical scaling of -2/5.

and big oil droplets resurfaced almost immediately after the breaking event. In order to present the oil droplet characteristics and discover their relation to the energy dissipation rate, a droplet size d_5 is used to represent the characteristics of all the circular droplets and eliminate the possible deviation existing in very low droplet number concentration. Noting that the relevance of determining a maximum droplet size using 2D simulations warrants careful justification. This simplified approach essentially reduces the problem to determining the diameter of an infinite cylinder in a two-dimensional turbulent field, which differs significantly from the actual scenario under study. Therefore, we remind that the potential implication of the two-dimensional simplification on the validity and generalizability of this representative droplet size d_5 needs to be treated with caution. To provide a more comprehensive understanding of droplet size determination in turbulent fields, considering factors such as air cavity rupture, future research involving three-dimensional simulations is anticipated. Figure 6.8 (b) shows the time evolution of the characteristic oil droplet size d_5 at various wave-breaking strengths. It is observed that at the early time after wave breaking, d_5 cannot accurately represent the characteristic oil droplet size because of the limited droplet number. The characteristic oil droplet size d_5 becomes stable after t/T = 0.9, so we take the mean droplet size $\bar{d_5}$ and mean dissipate rate $\bar{\epsilon}$ averaged from t/T = 1.0 to t/T = 1.5 to present their relationship.

Figure 6.8 (c) shows the relationship between mean droplet size $\bar{d_5}$ and mean dissipate rate $\bar{\epsilon}$. The numerical results are well-fitted to the theoretical scaling of -2/5, which confirms that the turbulent pressure gradient is the cause of the droplet breakup. Although 2-D direct numerical simulations may not be able to determine the droplet size distribution, it is capable of capturing the energy dissipation information and characteristic droplet size. This confirms the validity of our numerical model to simulate the wave breaking and the associated turbulent flows, as well as the characteristic oil droplets during the wave breaking process.

6.2.2 Effects of interfacial tension on the particle statistics

By validating the capacity of capturing the energy dissipation information and characteristic droplet size in two-dimensional direct numerical simulations, the effect of interfacial tension on the particle statistics was investigated in this part. Figure 6.9 shows how the free surface changes when the plunging jet hits the oil slick. The oil-water interfacial tension affects the shape and motion of the oil and water. At t = 0.7 s, the oil slick edges are rounder with higher interfacial tension. At t = 0.8 s, lower interfacial tension leads to a longer liquid sheet and bigger vorticity around it than higher interfacial tension. At t = 0.9 s, this vorticity detaches from the oil film edge with some air bubbles and moves up to the free surface. Higher interfacial tension causes

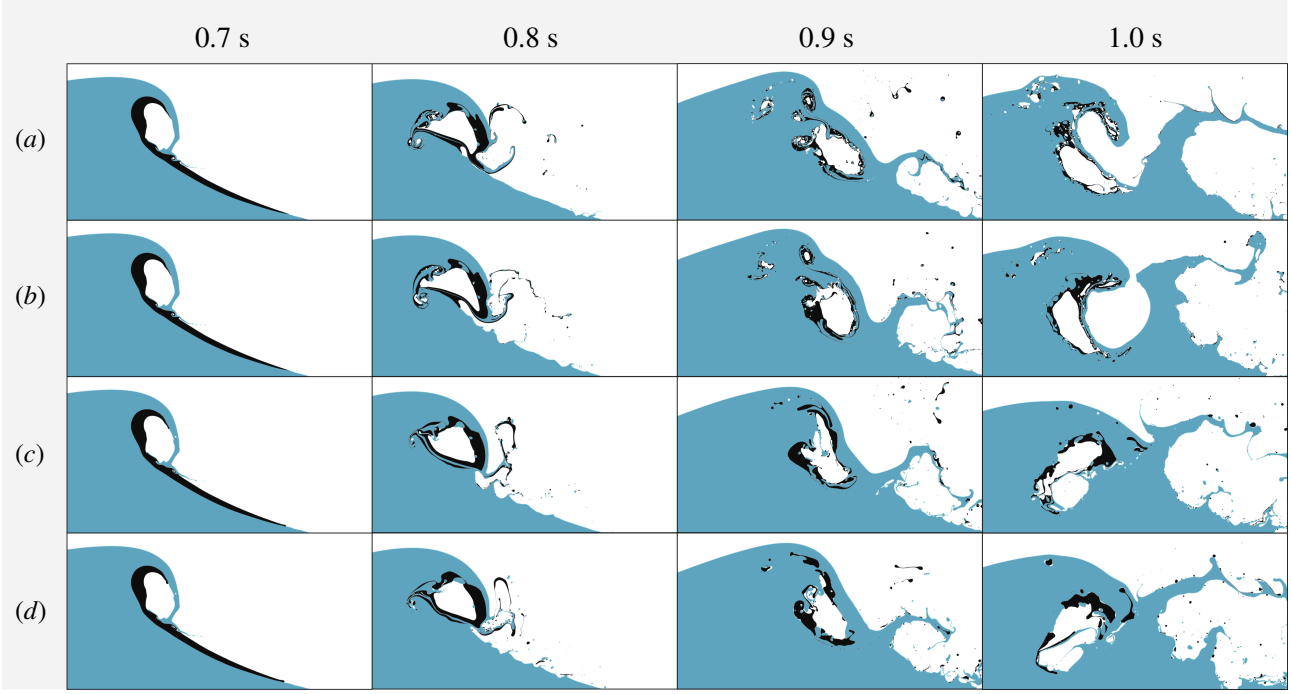

Figure 6.9: Time evolution of three-phase free surface evolution at various interfacial tensions: (a) $\gamma/\gamma_0 = 1$, (b) $\gamma/\gamma_0 = 2$, (c) $\gamma/\gamma_0 = 4$, (d) $\gamma/\gamma_0 = 8$.

less vorticity and more large oil particles detached from the liquid sheet. At $t = 1.0$ s, lower interfacial tension results in a big vortex with air that resurfaces and disrupts the falling jet. Higher interfacial tension produces large oil particles that rise near the free surface but with less impact on it.

Next, we investigate the effect of the oil-water interfacial tension on the energy budget during wave-breaking processes. Figure 6.10 shows the evolution of the kinematic energy and potential gravitational energy of the oil phase in multiple cases with various interfacial tensions between oil and water. For the kinematic energy, there is no evident influence of the interfacial tension on the evolution of the kinematic energy. For these cases with different interfacial tensions, the oil phase reaches its maximum kinematic energy at the same time at around 0.76 s. Then the oil phase loses its kinematic energy as the wave passes through. The oil phase loses almost all the kinematic energy at 2 s. The influence of the interfacial tension on the evolution of the potential gravitational energy can be observed in Figure 6.10(b). The oil phase also reaches its maximum potential gravitational energy at around 0.76 s. Several splash-ups can be generated, and the oil at the front edge of the wave can move with these splash-ups, showing several times the fluctuation. Generally, more potential gravitational energy remains at $t = 2$ s when decreasing the interfacial tension. This can be explained by the phenomenon that the dispersed oil particles distribute at the free surfaces at the smaller interfacial tension, while the oil droplets can be entrained

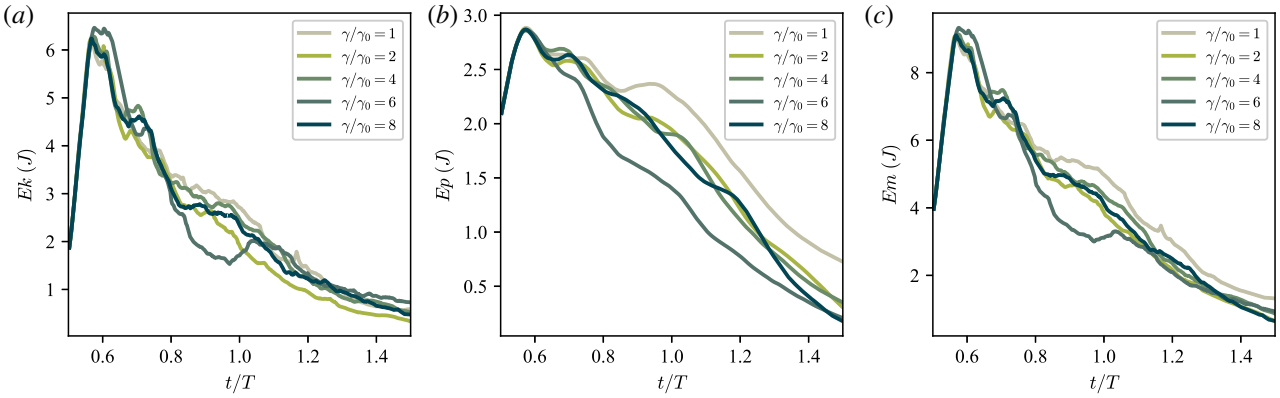

Figure 6.10: Evolution of the kinetic energy (a), gravitational potential energy (b) and the mechanical energy (c) in the oil phase.

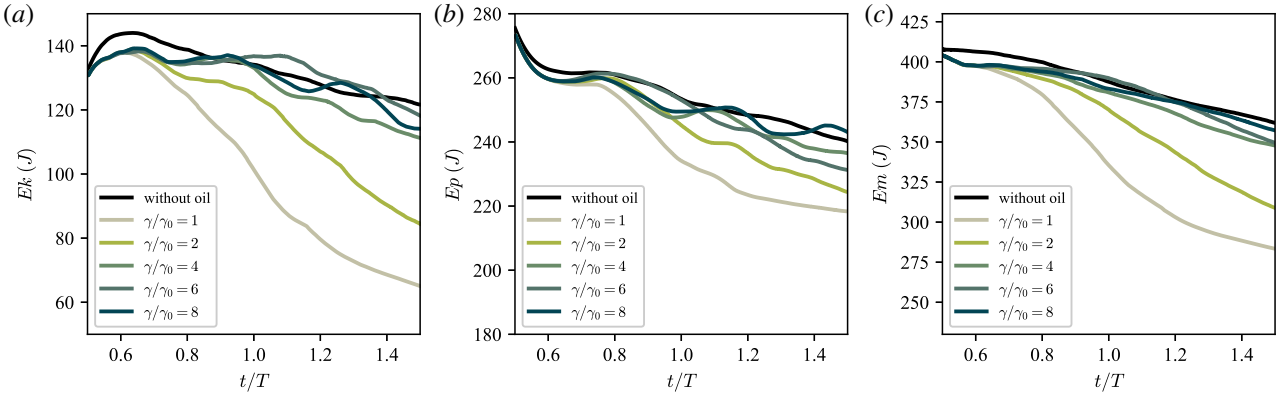

Figure 6.11: Evolution of the kinetic energy (a), gravitational potential energy (b) and the mechanical energy (c) in the water phase.

into the water column for larger interfacial tension.

Figure 6.11 shows the evolution of the kinematic energy and potential gravitational energy of the water phase in multiple cases with various interfacial tensions between oil and water. The energy budget of the case without oil is also presented here for comparison. The evolution of the kinematic energy in the water phase clearly shows the effect of the interfacial tension. Generally speaking, the presence of the oil slick increases the loss of the kinematic energy and the potential gravitational energy in the water. The more kinematic energy and the potential gravitational energy remain for larger interfacial tension. When decreasing the interfacial tension, less kinematic energy and the potential gravitational energy in the water will remain. The effect of the presence of the oil slick on decreasing mechanical energy can be explained by the formation of the droplets. Because the oil and water are immiscible when a wave breaks and impacts the oil slick, abundant oil particles and water

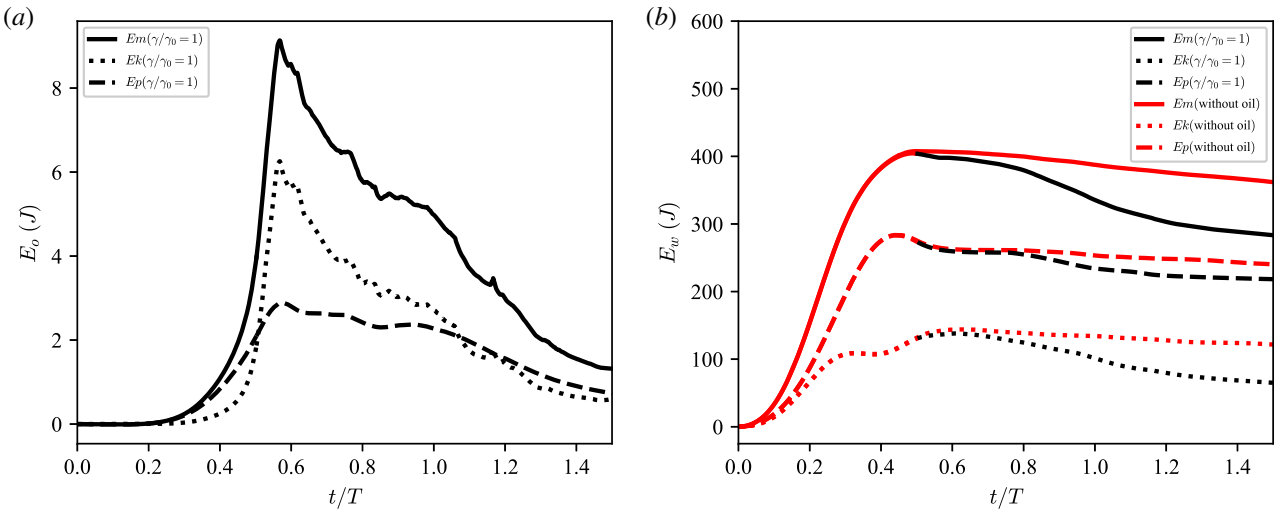

Figure 6.12: (a) The mechanical energy E_m, kinetic energy E_k, and gravitational potential energy E_p in the oil phase at γ/γ_0 = 1. (b) The mechanical energy E_m, kinetic energy E_k, and gravitational potential energy E_p in the water phase at γ/γ_0 = 1; the red lines are the mechanical energy E_m, kinetic energy E_k, and gravitational potential energy E_p in the water phase without the presence of the oil slick.

droplets can be generated. There will be many vortices near these particles, promoting the dissipation of the energy in the water. When decreasing the interfacial tension, smaller particles and ambient vortices can be generated, enhancing the dissipation.

Figure 6.12 shows the energy evolution in the oil and water phases at the physical value of the interfacial tension between oil and water. A mixing depth of the oil equals the penetration depth of the turbulence beneath the breaking wave. The mixing depth varies considerably over the interfacial tension under the same wave condition. the measured drop concentrations show a substantial number of supra-millimeter size drops, the size at which surface tension ceases to be relevant. In addition, these larger drops were significantly larger than the Hinze scale, the size at which turbulent breakup dominates the fragmentation process. Surprisingly, no clear regime change in the distribution is evident at this scale. This suggests that surface tension may have a limited influence on the oil spray generation at the scale of these rather large droplets.

As expected previously the bubbles and droplets should be resolved in 3-D simulations, we still expect that 2-D simulation can at least capture the overall features of the droplet breakups. So instead of analyzing the droplet size distribution which is quite challenging in 2-D simulations, we are going to discuss the characteristic droplet size and its dependence on the surface tension and dissipation rate.

Figure 6.13(a) shows the time-evolved energy dissipation rate under the effect of the interfacial tension. For

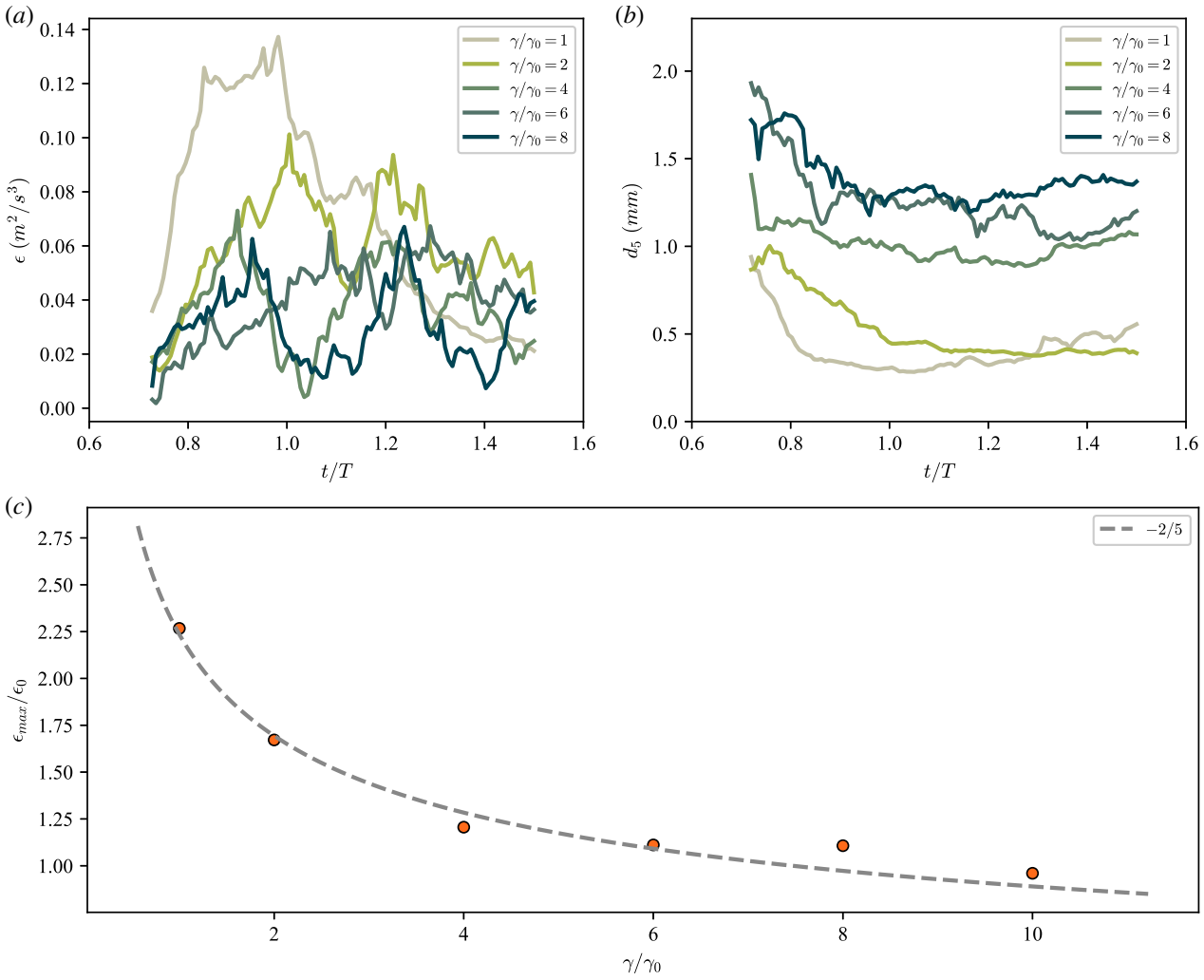

Figure 6.13: Time evolution of the energy dissipation rate ϵ due to breaking (a) and the characteristic oil droplet size d_5 at various interfacial tensions. (c) The relationship between the normalized maximum dissipate rate $\epsilon_{max}/\epsilon_0$ and the normalized interfacial tensions γ/γ_0 during the active breaking stage.

these cases, the plunging jet impacts the wavefront at the approximately same time (t/T = 0.50). As can be seen here, when γ/γ_0 = 1, After the generation of the first splash-up, when the first splash-up impacts the water (t/T = 0.70), the energy dissipation rate rapidly increased. The increase of the three-phase free surface causes the elongation of the oil slick, producing slender oil ligaments. In addition, the break-up of the initial oil slick caused by the wave-breaking turbulence generates a large amount of oil droplets of various sizes. The small eddies caused by oil droplets enhance the energy dissipation, dramatically weakening the energy in the wave. the increase of the energy dissipation rate at t/T = 1.15 corresponds to the second splash-up impact, and then the energy dissipation rate keeps decreasing due to the loss of the wave energy. When increasing the interfacial tension between oil and water, the energy dissipation rate caused by the first splash-up impacting decreases, and the energy dissipation rate due to the second splash-up impacting has the same magnitude as the previous one. Figure 6.13(b) shows the time-dependent characteristic droplet diameter d_5 at various interfacial tension. The interfacial tension significantly varies the corresponding characteristic droplet diameter. Compared with the time-evolved energy dissipation rate in figure 6.13(a), the initial decrease of d_5 can be attributed to the large dissipation rate caused by the first splash-up impact. For γ/γ_0 = 1, the first splash-up impacting dissipates the majority of the energy in the wave, so due to the small energy dissipation level in the subsequent time, d_5 increases a little bit. When the dissipation rate caused by the second splash-up impact is significant, d_5 has a further decrease in the corresponding time. This shows the possible relationship between characteristic droplet diameter and energy dissipation rate.

To examine the relationship between characteristic droplet diameter and energy dissipation rate, we should determine the proper value representing the flow characteristics and the droplet breakup mechanisms from the time-dependent values. As can be seen in figure 6.13, the energy dissipation rate changes a lot with time, and the evolution of the dissipation rate with time is different at different interfacial tension, because of the different free surface evolution as we mention in the previous section. Additionally, the characteristic droplet size is related to the dissipation rate. So the time-averaged dissipation rate cannot reflect the energy feature for droplet breakages. As argued by Li & Garrett (1998), if turbulent shear associated with intermittent high dissipation events causes the disintegration of oil droplets, we should use the peak dissipation rate when calculating oil droplet sizes. For the characteristic droplet diameter d_5, the effect of the interfacial tension and the energy dissipation rate is related to the characteristic droplet diameter d_5. So the minimum diameter during the wave-breaking process is used to consider its relationship with the maximum dissipation rate. Here we take the minimum droplet size from t/T = 0.7 to t/T = 1.5, and we expect that the minor difference in choosing the time period would not

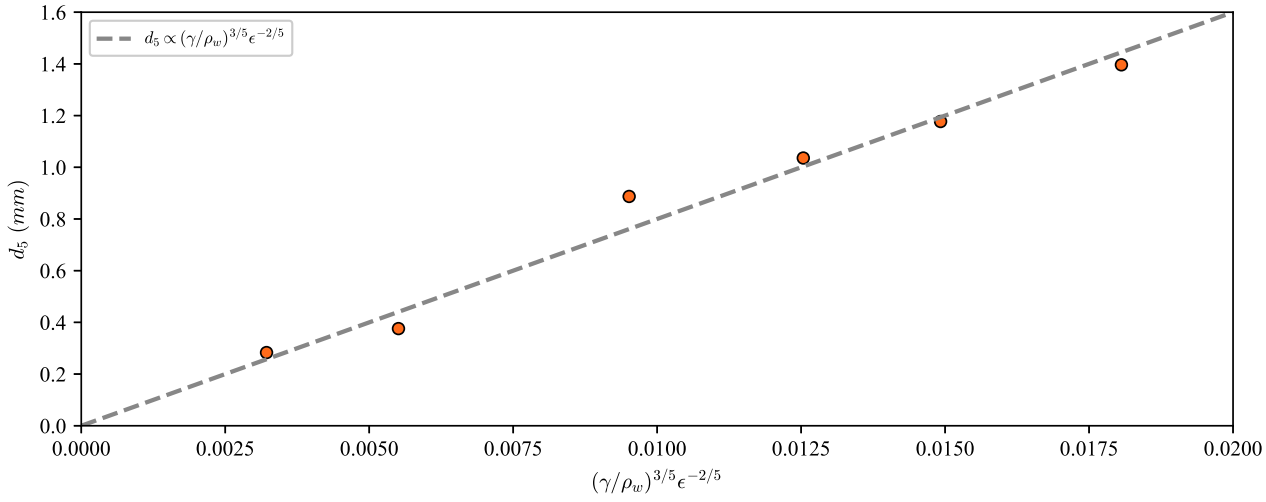

Figure 6.14: The relationship between the characteristic oil droplet size d_5 and the interfacial tensions, water density, and dissipation rate $(\gamma/\rho_w)^{3/5}{\epsilon_{max}}^{-2/5}$ during the active breaking stage.

significantly influence the final result.

Figure 6.13 (c) shows the relationship between the maximum energy dissipation rate and the interfacial tension. Due to the small eddies produced under the condition of the small interfacial tension, the larger energy dissipation rate associated with the strong turbulent patches can be expected. In this figure, a relationship between the dissipation rate on the interfacial tension can be observed, showing that the maximum energy dissipation rate decreases as the interfacial tension increases. This is an empirical result visualized from our numerical results, further theoretical derivation should be conducted to validate this result.

In our cases, the generated droplet sizes in breaking waves are larger than the Kolmogorov scale, so the dominant deforming force for droplet breakups is inertia rather than viscous shear. When surface tension is the dominant restoring force, the droplet diameter d is related both to $\gamma^{3/5}$ and $\epsilon^{-2/5}$. So the oil droplet size depends on the dissipation rate and the interfacial tension, which was identified as $d = C(\gamma/\rho_w)^{3/5}\epsilon^{-2/5}$ (Hinze, 1955).

The maximum energy dissipation rate ϵ_{max} is found to be better to relate the characteristic droplet diameter. Figure 6.14 shows the dependence of characteristic droplet diameter d_5 on the $(\gamma/\rho_w)^{3/5}{\epsilon_{max}}^{-2/5}$. From the figure, Our two-dimensional numerical results accurately show this dependence. However, the scaling law of the dissipation rate and the interfacial tension is an empirical result visualized from our numerical results, so further theoretical derivation should be conducted to validate this result in the future.

6.3 Conclusion

In this chapter, we extended two-dimensional breaking waves direct numerical simulations to three-phase conditions with the oil slick on the water surface. We conducted a parametric study to analyze the quantitative dependence of the characteristic oil droplet size on wave intensity and interfacial tension. With increasing wave plate stroke s, the surface energy of the oil phase generally increases after wave breaking. The jet impact causes a rapid increase in the surface energy of the oil phase in all cases, due to the stretching of the oil slick and the production of the initial splash-up. The first jet impact corresponds to the most significant increase in the surface energy of the oil phase, reaching 3 - 4 times the initial surface energy. For weaker breaking waves, the surface energy reaches a maximum after the first jet impact and then decreases. However, for stronger breaking waves, the subsequent splashing processes further increase the surface energy of the oil phase. Additionally, we identified a strong correlation between the maximum energy dissipation rate and the characteristic droplet diameter d_5, where d_5 depends on $(\gamma/\rho_w)^{3/5}{\epsilon_{max}}^{-2/5}$, aligning with theoretical scaling predictions. This research paves the way for investigating the relationship between wave breaking and oil slick behavior in marine oil spills through numerical simulations, contributing to a deeper understanding of the mechanisms governing oil dispersion and surface spreading. In the next step of our research, we intend to extract the maximum air bubble size information from 2-D breaking wave simulations and compare it to the numerical results from 3-D counterparts. This comparison will help us to strengthen our underlying assumption regarding the validity of the representative droplet size in a 3D breaker. Moreover, the additional analysis of oil film propagation position probability distribution will be integrated into our ongoing research, e.g., the probability of finding oil at some given distance after the passage of a breaking wave.

Chapter 7

Concluding remarks

7.1 Conclusions

Oil spills often occur on the sea surface in nearshore regions with relatively shallow water depths. Wave shoaling and breaking, which occur as waves propagate towards shallow nearshore areas, create more intense dynamic conditions and energy exchange rates. Oil spilled at sea forms oil slicks, which are subsequently entrained into the water and broken up into droplets ranging from submicron to several millimeters by breaking waves. These phenomena significantly affect the fate of the oil film, including its mass transfer, energy exchange, particle distribution, and spatiotemporal evolution. Therefore, investigating the characteristics of the resulting oil droplets is crucial for understanding the oil dispersion process and its interaction with shallow-water breaking waves.

In this study, we employed direct numerical simulations (DNS) to investigate the generation, development, and evolution of breaking waves and their impact on oil slicks by reproducing experimental waves generated by a piston-type wave plate.

First, we performed two-dimensional DNS of breaking waves using the Basilisk solver to gain a detailed understanding of the wave-breaking process, including the evolution of the free surface, velocity, and vorticity fields. We investigated the effect of fluid properties and initial conditions on the dynamics, kinematics, and energy dissipation in the breaking process. A quantitative relationship between the main cavity size and the breaking height is presented based on the investigation of the influence of the Bond number on the evolution of the overturning jet. This reveals the effect of surface tension on the crest overturning process, which thickens the width of the plunging jet and shortens the distance that projects forward ahead of the wave. The resulting wave height can be estimated based on the simplified theory for plane wavemakers, and our numerical results agree

well with this theoretical result. The link between wave height and initial conditions indicates that waves can be classified as non-breaking waves, spilling breakers, and plunging breakers based on the ratio of wave height to water depth H/d. The conventional dissipation scaling of turbulence theory is applied to the wave-breaking process, deriving a link between the energy dissipation rate and the ratio of the breaking-wave crest to water depth H_b/d. By accounting for a threshold behavior, an empirical scaling of the breaking parameter is proposed as $b = a(H_b/d - \chi_0)^n$, where χ_0 = 0.65 represents the breaking threshold and n = 1.5 is a power law determined through the best fit to the numerical results. The proposed scaling laws quantitatively link the kinematics and dynamics of breaking waves to the local wave parameters and initial conditions, which may be of use for future theoretical analysis.

We then extended two-dimensional breaking waves DNS to a three-dimensional framework to account for three-dimensional effects on the wave-breaking process and to evaluate the effects of viscosity (represented by Reynolds number, Re) and surface tension (represented by Bond number, Bo) on the characteristics and size distribution of bubbles generated by wave breaking. The grid convergence of the numerical results is analysed by considering three sets of simulations with l_{max} = 11, 12, and 13, and the numerical convergence is discussed in terms of the energy budget, and size distribution of the bubbles and droplets produced by wave breaking. All results have been proved to be well converged, with no significant changes observed as the maximum level of refinement increases from 11 to 13. The numerical results appear in reasonable agreement with the experimental measurements in terms of the wave shape and maximum wave height before breaking. During the active breaking time, the bubble size distribution follows $N(r,t) \propto r^{-10/3}$. A higher Bo leads to a greater number of bubbles, with the difference being more pronounced in the range of smaller bubbles. The vertical velocity varies with bubble radius, showing varying rise velocities at different bubble radii under the effect of buoyancy, with larger bubbles rising to the free surface at a faster rate. During the active breaking phase, the depth of the bubble plume remains constant, consistent with the initial height of the main cavity.

Finally, we extended the two-dimensional breaking waves DNS to three-phase simulations in the presence of oil slicks on the water surface. Through a parametric study, we analysed the quantitative dependence of the characteristic oil droplet size on the wave intensity and interfacial tension. With increasing wave plate stroke s, the surface energy of the oil phase generally increases after wave breaking. The jet impact causes a rapid increase in the surface energy of the oil phase in all cases, due to the stretching of the oil slick and the production of the initial splash-up. The first jet impact corresponds to the most significant increase in the surface energy of the oil phase, reaching 3 - 4 times the initial surface energy. For weaker breaking waves, the surface energy

reaches a maximum after the first jet impact and then decreases. However, for stronger breaking waves, the subsequent splashing processes further increase the surface energy of the oil phase. Additionally, we identified a strong correlation between the maximum energy dissipation rate and the characteristic droplet diameter d_5, where d_5 depends on $(\gamma/\rho_w)^{3/5}{\epsilon_{max}}^{-2/5}$, aligning with theoretical scaling predictions.

This research paves the way for investigating the complex relationship between wave breaking and oil slick behavior in marine oil spills through numerical simulations, contributing to a deeper understanding of the mechanisms governing oil dispersion and surface spreading.

7.2 Perspectives

This study establishes a relationship between the dissipation rate and wave parameters, providing predictive insights into the dissipation rate of breaking waves in shallow water. By conducting a comparison using available data of breaking dissipation in both deep water and shallow water, we found that there is a clear discontinuity between the deep-water and shallow-water regimes, rendering a single power-law scaling inadequate for capturing both datasets. Therefore, further endeavours should be made to develop a comprehensive breaking parametrization. We mention that the available datasets summarizing both deep water and shallow water breaking dissipation offer valuable insights into this unsolved problem. The data indicate that the breaking threshold varies with the change in the water depth, suggesting the possibility of a varying breaking threshold, particularly in the context of transitioning between deep and shallow water conditions. A determination relation governing the breaking threshold could be proposed to accommodate the different depth regimes. This remains to be explored in future work.

Additionally, the simulation of oil dispersion by breaking waves using the Basilisk solver reconstructs the three-phase interface using an advection equation that considers triple points, where each phase has a distinct volume fraction. This approach can generally capture oil transport due to breaking waves and the associated characteristic droplet size. However, the triple point is unstable using this basic advection scheme because it does not conserve local volume fractions due to overlap and empty zone propagation. Therefore, the treatment of triple points needs improvement, and a modified advection scheme is required to achieve accurate reconstruction of three-phase interfaces.

Furthermore, there remains a need to characterize the interaction between wave breakup and the mechanisms of oil dispersion. To address this, we will utilize current two-dimensional simulations to elucidate the spreading

of oil slicks beyond the distribution of droplets. Specifically, we will quantify the probability of encountering oil at a given distance downstream of a breaking wave. By incorporating the passive tracers to track the Lagrangian transport of the oil phase, we will derive additional statistical quantities that encapsulate the spatial dispersion of the oil distribution, potentially revealing less sensitive aspects to three-dimensional effects, such as the variance of the position of the oil droplets.

Finally, one unresolved issue is the size distribution of crude oil and oil-dispersant mixtures at scales smaller than the resolution of current direct numerical simulations. Specifically, this study did not quantify the size distribution and formation mechanisms of oil droplets at these scales. Some three-dimensional simulations have been initiated to investigate the oil dispersion process, and preliminary analysis shows a generally similar oil trajectory induced by breaking, as well as a scaling law for the droplet size distribution of crude oil to that observed in the experiments. Further analysis of the statistics and mechanisms involved in the generation of oil droplets is deferred to future studies.

Bibliography

Afshar-Mohajer, Nima, Li, Cheng, Rule, Ana M, Katz, Joseph & Koehler, Kirsten 2018 A laboratory study of particulate and gaseous emissions from crude oil and crude oil-dispersant contaminated seawater due to breaking waves. *Atmospheric Environment* **179**, 177–186.

Aulisa, Eugenio, Manservisi, Sandro, Scardovelli, Ruben & Zaleski, Stephane 2007 Interface reconstruction with least-squares fit and split advection in three-dimensional cartesian geometry. *Journal of Computational Physics* **225** (2), 2301–2319.

Banner, ML & Peregrine, DH 1993 Wave breaking in deep water. *Annual Review of Fluid Mechanics* **25** (1), 373–397.

Banner, Michael L & Peirson, William L 2007 Wave breaking onset and strength for two-dimensional deep-water wave groups. *Journal of Fluid Mechanics* **585**, 93–115.

Batchelor, George Keith 1953 *The theory of homogeneous turbulence*. Cambridge university press.

Beji, S 1995 Note on a nonlinearity parameter of surface waves. *Coastal engineering* **25** (1-2), 81–85.

Bell, John B, Colella, Phillip & Glaz, Harland M 1989 A second-order projection method for the incompressible navier-stokes equations. *Journal of computational physics* **85** (2), 257–283.

Blenkinsopp, CE & Chaplin, JR 2007 Void fraction measurements in breaking waves. *Proceedings of the Royal Society A: Mathematical, Physical and Engineering Sciences* **463** (2088), 3151–3170.

Blenkinsopp, Christopher E & Chaplin, John R 2010 Bubble size measurements in breaking waves using optical fiber phase detection probes. *IEEE Journal of Oceanic Engineering* **35** (2), 388–401.

Boswell, Hunter, Yan, Guirong & Mostert, Wouter 2023 Characterizing energy dissipation of shallow-water wave breaking in a storm surge. *Physical Review Fluids* **8** (5), 054801.

Brackbill, Jeremiah U, Kothe, Douglas B & Zemach, Charles 1992 A continuum method for modeling surface tension. *Journal of computational physics* **100** (2), 335–354.

Carratelli, Eugenio Pugliese, Dentale, Fabio & Reale, Ferdinando 2011 On the effects of wave-induced drift and dispersion in the deepwater horizon oil spill. *Monitoring and Modeling the Deepwater Horizon Oil Spill: A Record-Breaking Enterprise, Geophysical. Monograph Series* **195**, 197–204.

Chan, Wai Hong Ronald, Johnson, Perry L, Moin, Parviz & Urzay, Javier 2021 The turbulent bubble break-up cascade. part 2. numerical simulations of breaking waves. *Journal of Fluid Mechanics* **912**.

Chen, Xiaodong, Sun, Yingnan, Xue, Chundong, Yu, Yude & Hu, Guoqing 2017 Tunable structures of compound droplets formed by collision of immiscible microdroplets. *Microfluidics and Nanofluidics* **21**, 1–14.

Clift, Roland, Grace, John R & Weber, Martin E 2005 Bubbles, drops, and particles .

Cokelet, ED 1977 Breaking waves. *Nature* **267** (5614), 769–774.

De Vita, Francesco, Verzicco, Roberto & Iafrati, Alessandro 2018 Breaking of modulated wave groups: kinematics and energy dissipation processes. *Journal of fluid mechanics* **855**, 267–298.

Deane, Grant B 1997 Sound generation and air entrainment by breaking waves in the surf zone. *The journal of the acoustical society of America* **102** (5), 2671–2689.

Deane, Grant B & Stokes, M Dale 2002 Scale dependence of bubble creation mechanisms in breaking waves. *Nature* **418** (6900), 839–844.

Deike, Luc 2022 Mass transfer at the ocean–atmosphere interface: The role of wave breaking, droplets, and bubbles. *Annual Review of Fluid Mechanics* **54**, 191–224.

Deike, Luc, Melville, W Kendall & Popinet, Stéphane 2016 Air entrainment and bubble statistics in breaking waves. *Journal of Fluid Mechanics* **801**, 91–129.

Deike, Luc, Pizzo, Nick & Melville, W Kendall 2017 Lagrangian transport by breaking surface waves. *Journal of Fluid Mechanics* **829**, 364–391.

Deike, Luc, Popinet, Stephane & Melville, W Kendall 2015 Capillary effects on wave breaking. *Journal of Fluid Mechanics* **769**, 541–569.

Delvigne, Gerardus Athenasius Leonardus & Sweeney, C_E 1988 Natural dispersion of oil. *Oil and Chemical Pollution* **4** (4), 281–310.

Derakhti, Morteza & Kirby, James T 2014 Bubble entrainment and liquid–bubble interaction under unsteady breaking waves. *Journal of fluid mechanics* **761**, 464–506.

Derakhti, Morteza & Kirby, James T 2016 Breaking-onset, energy and momentum flux in unsteady focused wave packets. *Journal of Fluid Mechanics* **790**, 553–581.

Diorio, JD, Liu, X & Duncan, JH 2009 An experimental investigation of incipient spilling breakers. *Journal of fluid mechanics* **633**, 271–283.

Drazen, David A & Melville, W Kendall 2009 Turbulence and mixing in unsteady breaking surface waves. *Journal of Fluid Mechanics* **628**, 85–119.

Drazen, David A, Melville, W Kendall & Lenain, LUC 2008 Inertial scaling of dissipation in unsteady breaking waves. *Journal of fluid mechanics* **611**, 307–332.

Duncan, JH 1981 An experimental investigation of breaking waves produced by a towed hydrofoil. *Proceedings of the Royal Society of London. A. Mathematical and Physical Sciences* **377** (1770), 331–348.

Duncan, James H 1983 The breaking and non-breaking wave resistance of a two-dimensional hydrofoil. *Journal of fluid mechanics* **126**, 507–520.

Elliott, AJ, Hurford, N & Penn, CJ 1986 Shear diffusion and the spreading of oil slicks. *Marine Pollution Bulletin* **17** (7), 308–313.

Fang, Shibiao, Lin, Mu, Jia, Sen, Liu, Kuan & Liu, Darong 2022 Deep learning technique for examining the mechanism, transport, and behavior of oil-related hazardous material caused by wave breaking and turbulence. *Environmental Research Letters* **17** (10), 104058.

Fingas, Merv 2014 Oil and petroleum evaporation. *Handbook of oil spill science and technology* pp. 205–223.

Fitzpatrick, Richard 2017 *Theoretical fluid mechanics*. IoP publishing.

Francois, Marianne M, Cummins, Sharen J, Dendy, Edward D, Kothe, Douglas B, Sicilian, James M & Williams, Matthew W 2006 A balanced-force algorithm for continuous and sharp interfacial surface tension models within a volume tracking framework. *Journal of Computational Physics* **213** (1), 141–173.

Fuster, Daniel, Agbaglah, Gilou, Josserand, Christophe, Popinet, Stéphane & Zaleski, Stéphane 2009 Numerical simulation of droplets, bubbles and waves: state of the art. *Fluid dynamics research* **41** (6), 065001.

Fuster, Daniel & Popinet, Stéphane 2018 An all-mach method for the simulation of bubble dynamics problems in the presence of surface tension. *Journal of Computational Physics* **374**, 752–768.

Galvin, Cyril Jerome 1964 *Wave-height prediction for wave generators in shallow water*, , vol. 4. Coastal Engineering Research Center.

Garrett, Chris, Li, Ming & Farmer, David 2000 The connection between bubble size spectra and energy dissipation rates in the upper ocean. *Journal of physical oceanography* **30** (9), 2163–2171.

Grare, Laurent, Peirson, William L, Branger, Hubert, Walker, James W, Giovanangeli, Jean-Paul & Makin, Vladimir 2013 Growth and dissipation of wind-forced, deep-water waves. *Journal of Fluid Mechanics* **722**, 5–50.

Guo, WJ & Wang, YX 2009 A numerical oil spill model based on a hybrid method. *Marine pollution bulletin* **58** (5), 726–734.

Hinze, Julius O 1955 Fundamentals of the hydrodynamic mechanism of splitting in dispersion processes. *AIChE journal* **1** (3), 289–295.

Hirt, Cyril W & Nichols, Billy D 1981 Volume of fluid (vof) method for the dynamics of free boundaries. *Journal of computational physics* **39** (1), 201–225.

Iafrati, A 2009 Numerical study of the effects of the breaking intensity on wave breaking flows. *Journal of Fluid Mechanics* **622**, 371–411.

Iafrati, A 2011 Energy dissipation mechanisms in wave breaking processes: spilling and highly aerated plunging breaking events. *Journal of Geophysical Research: Oceans* **116** (C7), C07024.

Jeong, Jinhee & Hussain, Fazle 1995 On the identification of a vortex. *Journal of fluid mechanics* **285**, 69–94.

Joubert, Nelson, Gardin, Pascal, Popinet, Stéphane & Zaleski, Stéphane 2022 Experimental and numerical modelling of mass transfer in a refining ladle. *Metallurgical Research & Technology* **119** (1), 109.

Kendall Melville, W 1994 Energy dissipation by breaking waves. *Journal of Physical Oceanography* **24** (10), 2041–2049.

Keramea, Panagiota, Spanoudaki, Katerina, Zodiatis, George, Gikas, Georgios & Sylaios, Georgios 2021 Oil spill modeling: A critical review on current trends, perspectives, and challenges. *Journal of marine science and engineering* **9** (2), 181.

Kiger, Kenneth T & Duncan, James H 2012 Air-entrainment mechanisms in plunging jets and breaking waves. *Annual Review of Fluid Mechanics* **44**, 563–596.

Kothe, Douglas B, Mjolsness, Raymond C & Torrey, Martin D 1991 *RIPPLE: A computer program for incompressible flows with free surfaces*. Available to DOE and DOE contractors from OSTI.

Leifer, Ira & De Leeuw, Gerrit 2006 Bubbles generated from wind-steepened breaking waves: 1. bubble plume bubbles. *Journal of Geophysical Research: Oceans* **111** (C6).

Li, Cheng 2017 Dispersion of oil spills by breaking waves. PhD thesis, Johns Hopkins University.

Li, C, Miller, J, Wang, J, Koley, SS & Katz, J 2017 Size distribution and dispersion of droplets generated by impingement of breaking waves on oil slicks. *Journal of Geophysical Research: Oceans* **122** (10), 7938–7957.

Li, Ming & Garrett, Chris 1998 The relationship between oil droplet size and upper ocean turbulence. *Marine Pollution Bulletin* **36** (12), 961–970.

Li, Xiaoyi, Arienti, Marco, Soteriou, Marios & Sussman, Mark 2010 Towards an efficient, high-fidelity methodology for liquid jet atomization computations. In *48th AIAA aerospace sciences meeting including the new horizons forum and aerospace exposition*, p. 210.

Li, Zhengkai, Lee, Kenneth, King, Thomas, Boufadel, Michel C & Venosa, Albert D 2008 Oil droplet size distribution as a function of energy dissipation rate in an experimental wave tank. In *International Oil Spill Conference*, , vol. 2008, pp. 621–626. American Petroleum Institute.

Lin-Lin, Zhu, Hui, Guan & Chui-Jie, Wu 2016 Three-dimensional numerical simulation of a bird model in unsteady flight. *Computational Mechanics* **58** (1), 1–11.

Loewen, MR, O'Dor, MA & Skafel, MG 1996 Bubbles entrained by mechanically generated breaking waves. *Journal of Geophysical Research: Oceans* **101** (C9), 20759–20769.

Lubin, P & Glockner, S 2015 Numerical simulations of three-dimensional plunging breaking waves: generation and evolution of aerated vortex filaments. *Journal of Fluid Mechanics* **767**, 364–393.

Lubin, Pierre, Kimmoun, Olivier, Véron, Fabrice & Glockner, Stéphane 2019 Discussion on instabilities in breaking waves: Vortices, air-entrainment and droplet generation. *European Journal of Mechanics-B/Fluids* **73**, 144–156.

Melville, W Kendall 1996 The role of surface-wave breaking in air-sea interaction. *Annual review of fluid mechanics* **28** (1), 279–321.

Melville, W Kendall & Matusov, Peter 2002 Distribution of breaking waves at the ocean surface. *Nature* **417** (6884), 58–63.

Mostert, Wouter & Deike, Luc 2020 Inertial energy dissipation in shallow-water breaking waves. *Journal of Fluid Mechanics* **890**, A12.

Mostert, Wouter, Popinet, Stéphane & Deike, Luc 2022 High-resolution direct simulation of deep water breaking waves: transition to turbulence, bubbles and droplets production. *Journal of Fluid Mechanics* **942**, A27.

Muin, M, Muslim, AB & Puspitasari, TA 2022 The effect of non-linear wave on oil spill dispersion. In *IOP Conference Series: Earth and Environmental Science*, , vol. 1065, p. 012006. IOP Publishing.

Mukherjee, Biplab, Wrenn, Brian A & Ramachandran, Palghat 2012 Relationship between size of oil droplet generated during chemical dispersion of crude oil and energy dissipation rate: Dimensionless, scaling, and experimental analysis. *Chemical engineering science* **68** (1), 432–442.

Murawski, Jens & Woge Nielsen, Jacob 2013 Applications of an oil drift and fate model for fairway design. *Preventive methods for coastal protection: Towards the use of ocean dynamics for pollution control* pp. 367–415.

Naess, Arvid 1982 On the residence time of oil mixed into the water column by breaking waves. *Society of Petroleum Engineers Journal* **22** (04), 573–584.

New, AL 1983 A class of elliptical free-surface flows. *Journal of Fluid Mechanics* **130**, 219–239.

Pairetti, César, Popinet, Stéphane, Damián, Santiago, Nigro, Norberto & Zaleski, Stéphane 2018 Bag mode breakup simulations of a single liquid droplet. In *ECCM6,ECFD7,Glasgow,UK*, p. 12. Available at: https://hal.science/hal03150888.

Peishi, Q, Zhiguo, S & Yunzhi, L 2011 Mathematical simulation on the oil slick spreading and dispersion in nonuniform flow fields. *International Journal of Environmental Science & Technology* **8**, 339–350.

Perlin, Marc, Choi, Wooyoung & Tian, Zhigang 2013 Breaking waves in deep and intermediate waters. *Annual review of fluid mechanics* **45**, 115–145.

Perlin, Marc, He, Jianhui & Bernal, Luis P 1996 An experimental study of deep water plunging breakers. *Physics of fluids* **8** (9), 2365–2374.

Popinet, Stéphane 2003 Gerris: a tree-based adaptive solver for the incompressible euler equations in complex geometries. *Journal of computational physics* **190** (2), 572–600.

Popinet, Stéphane 2009 An accurate adaptive solver for surface-tension-driven interfacial flows. *Journal of Computational Physics* **228** (16), 5838–5866.

Popinet, Stéphane 2018 Numerical models of surface tension. *Annual Review of Fluid Mechanics* **50**, 49–75.

Rapp, Ronald James & Melville, W Kendall 1990 Laboratory measurements of deep-water breaking waves. *Philosophical Transactions of the Royal Society of London. Series A, Mathematical and Physical Sciences* **331** (1622), 735–800.

Reed, Mark, Johansen, Oistein, Leirvik, Frode & Brørs, Bård 2009 Numerical algorithm to compute the effects of breakingwaves on surface oil spilled at sea. *Final Report Submitted to the Coastal Response Research Center. Report F* **10968**, 131.

Rivière, Aliénor, Mostert, Wouter, Perrard, Stéphane & Deike, Luc 2021 Sub-hinze scale bubble production in turbulent bubble break-up. *Journal of Fluid Mechanics* **917**.

Romero, Leonel, Melville, W Kendall & Kleiss, Jessica M 2012 Spectral energy dissipation due to surface wave breaking. *Journal of Physical Oceanography* **42** (9), 1421–1444.

Scardovelli, Ruben & Zaleski, Stephane 2000 Analytical relations connecting linear interfaces and volume fractions in rectangular grids. *Journal of Computational Physics* **164** (1), 228–237.

Taylor, Geoffrey Ingram 1935 Statistical theory of turbulence-ii. *Proceedings of the Royal Society of London. Series A-Mathematical and Physical Sciences* **151** (873), 444–454.

Tian, Zhigang, Perlin, Marc & Choi, Wooyoung 2010 Energy dissipation in two-dimensional unsteady plunging breakers and an eddy viscosity model. *Journal of fluid mechanics* **655**, 217–257.

Vassilicos, J Christos 2015 Dissipation in turbulent flows. *Annual Review of Fluid Mechanics* **47**, 95–114.

Veron, Fabrice 2015 Ocean spray. *Annu. Rev. Fluid Mech* **47** (1), 507–538.

Wang, Hui, Liu, Shuo, Bayeul-Lainé, Annie-Claude, Murphy, David, Katz, Joseph & Coutier-Delgosha, Olivier 2023 Analysis of high-speed drop impact onto deep liquid pool. *Journal of Fluid Mechanics* **972**, A31.

Wang, Zhaoyuan, Yang, Jianming & Stern, Frederick 2016 High-fidelity simulations of bubble, droplet and spray formation in breaking waves. *Journal of Fluid Mechanics* **792**, 307–327.

Wei, Zhangping, Li, Cheng, Dalrymple, Robert A, Derakhti, Morteza & Katz, Joseph 2018 Chaos in breaking waves. *Coastal Engineering* **140**, 272–291.

Wei, Zhangping, Shi, Huabin, Li, Cheng, Katz, Joseph, Dalrymple, Robert A & Bilotta, Giuseppe 2017 Behavior of oil under breaking waves by a two-phase sph model. *arXiv preprint arXiv:1702.07760* .

Wroniszewski, Paweł A, Verschaeve, Joris CG & Pedersen, Geir K 2014 Benchmarking of navier–stokes codes for free surface simulations by means of a solitary wave. *Coastal Engineering* **91**, 1–17.

Wu, ChuiJie & Wang, Liang 2009 Numerical simulations of self-propelled swimming of 3d bionic fish school. *Science in China Series E: Technological Sciences* **52** (3), 658–669.

Zhang, Bo, Popinet, Stéphane & Ling, Yue 2020 Modeling and detailed numerical simulation of the primary breakup of a gasoline surrogate jet under non-evaporative operating conditions. *International Journal of Multiphase Flow* **130**, 103362.

Zhang, Zhanyang, Schäfer, Tobias & Kress, Michael E 2021 Gnome and lbm model evaluation on ocean oil spill far-field impacts to highly sensitive areas. *arXiv preprint arXiv:2105.05193* .

French extended summary

Introduction

Les déversements accidentels d'hydrocarbures provenant de la production et du transport de pétrole en mer constituent une menace importante pour les écosystèmes marins, entraînant toute une série de conséquences néfastes. La dispersion des hydrocarbures par les vagues déferlantes est un processus qui se produit lorsque les hydrocarbures déversés en mer forment de fines nappes, qui sont ensuite fragmentées en gouttelettes de différentes tailles. Ces gouttelettes sont soumises aux forces turbulentes et aux tourbillons générés par les vagues déferlantes (Delvigne & Sweeney, 1988). Les vagues déferlantes jouent un rôle important dans l'interaction air-mer, notamment dans le transfert de masse, de quantité de mouvement et de chaleur entre l'atmosphère et l'océan. Le déferlement des vagues renforce le transfert d'énergie du champ de vagues de surface vers les courants et la turbulence, en particulier dans les couches supérieures de la colonne d'eau (Melville, 1996). Lorsqu'une vague déferle, elle déclenche le renversement de la vague et l'entraînement de l'air, constituant ainsi une source d'énergie turbulente capable de mélanger les couches supérieures de l'océan. Ce phénomène entraîne la formation de bulles et de gouttelettes, favorisant les échanges air-mer entre les gaz et les particules, comme le pétrole déversé (Cokelet, 1977).

Dans le contexte des vagues déferlantes, les arguments d'échelle suggèrent une relation proportionnelle entre la dissipation d'énergie et les caractéristiques de la vague. La dissipation de la vague par unité de longueur de la crête déferlante, désignée par ϵ_l, devrait être liée à l'expression $b\rho_w c^5/g$ dans les vagues déferlantes en eaux profondes, comme l'indiquent les travaux antérieurs (Duncan, 1981, 1983). Ici, ρ_w est la densité de l'eau, g est l'accélération due à la gravité, et c est la vitesse de phase de la vague déferlante. Il a été démontré que le paramètre de déferlement b, qui quantifie l'ampleur de la dissipation d'énergie pendant le processus de déferlement, est en corrélation avec la pente de la vague et la largeur de bande spectrale dans le cadre de diverses expériences en laboratoire (Kendall Melville, 1994; Deane & Stokes, 2002; Melville & Matusov, 2002). Cette relation est

caractérisée par $(hk)^{5/2}$ à l'aide d'un modèle d'échelle inertielle proposé par Drazen *et al.* (2008), où hk est un paramètre local de pente de rupture. Contrairement aux conditions en eaux profondes, le déferlement des vagues en eaux peu profondes (par exemple, dans les zones littorales) nécessite des considérations distinctes pour relier la dissipation de l'énergie inertielle aux caractéristiques des vagues. Mostert & Deike (2020) a étendu l'échelle inertielle aux vagues solitaires déferlantes en eaux peu profondes, révélant une dépendance de la dissipation d'énergie par rapport à l'amplitude locale et à la profondeur de l'eau. Cela indique que la dissipation de la vague par unité de longueur de la crête déferlante ϵ_l devrait être proportionnelle à $\rho g^{3/2} {h_b}^{7/2}/d_b$, où h_b est l'amplitude de la vague au moment du déferlement et d_b est la profondeur non perturbée au moment du déferlement.

Pour mieux comprendre le transport du pétrole dispersé par les vagues océaniques et les écoulements turbulents, Li (2017) ont effectué des mesures expérimentales dans un canal à vagues pour étudier l'évolution temporelle des distributions de taille des gouttelettes de pétrole de subsurface induites par une seule vague déferlante. Ils ont également cherché à établir des corrélations entre les distributions de taille des gouttelettes d'huile et divers paramètres, tels que la tension interfaciale, la viscosité de l'huile, la densité et les caractéristiques de déferlement des vagues.

Les simulations numériques peuvent jouer un rôle crucial dans l'obtention d'informations hydrodynamiques précises sur les vagues déferlantes et dans l'évaluation de l'influence de la dispersion naturelle sur la propagation des nappes de pétrole formées dans la colonne d'eau. Toutefois, les modèles existants pour les scénarios de marée noire ne permettent pas de résoudre directement la dispersion des gouttelettes d'hydrocarbures résultant du déferlement des vagues. Compte tenu des progrès significatifs des algorithmes numériques et des ressources informatiques, il est désormais impératif de représenter les processus de dispersion des hydrocarbures par des simulations numériques directes afin d'améliorer la précision de la prédiction du devenir des hydrocarbures déversés. Par conséquent, il est essentiel de parvenir à une compréhension globale de l'effet des vagues déferlantes sur la rupture des nappes d'hydrocarbures et la distribution de la taille des gouttelettes qui y est associée. La distribution de la taille des gouttelettes sert de pont entre les processus à petite échelle (tels que la vitesse de montée des gouttelettes, la dissolution et la biodégradation) et les processus à grande échelle qui régissent le transport des hydrocarbures. En tant que première étape dans l'étude des déversements d'hydrocarbures en mer, cette étude se penche sur les mécanismes de dispersion naturelle sous l'influence des vagues déferlantes. Notre objectif principal est de simuler les processus de dispersion d'hydrocarbures sous l'influence de vagues déferlantes, en mettant l'accent sur le transport et le devenir des hydrocarbures déversés. Il est important de noter que dans cette étude, nous supposons que la dispersion des hydrocarbures est

principalement régie par l'étalement horizontal de la nappe superficielle sous l'effet de la gravité, de l'inertie, des forces visqueuses et des forces de tension superficielle, sans tenir compte des processus chimiques et biologiques.

Nous effectuons des simulations numériques directed du déferlement de vagues à l'aide d'un calcul 2 phases et de la dispersion de pétrole à l'aide d'un calcul 3 phases pour étudier l'évolution des vagues expérimentales générées par une plaque à vagues et leur impact sur la rupture des gouttelettes de pétrole. La simulation numérique directe des vagues déferlantes est devenue une option viable ces dernières années, fournissant des informations précieuses sur les prévisions de début de déferlement, la dissipation d'énergie et la génération de bulles et de gouttelettes.

Dans le contexte des vagues déferlantes, nous résolvons les équations de Navier-Stokes incompressibles à densité variable avec une précision spatiale et temporelle de second ordre à l'aide du solveur Basilisk. Nous suivons l'interface air-eau à l'aide d'un schéma de volume de fluide (VOF). La tension superficielle est traitée avec la technique des forces équilibrées. Pour améliorer la précision et l'efficacité des écoulements induits par la tension superficielle, nous mettons en œuvre une méthode généralisée d'estimation de la courbure de la fonction de hauteur (HF) qui traite les incohérences à faible résolution de l'interface. En outre, nous utilisons un schéma de raffinement de maillage adaptatif pour concentrer les ressources de calcul sur les régions de solution critiques, améliorant ainsi l'efficacité du calcul. Pour étudier la relation entre la géométrie de la crête et le taux de dissipation d'énergie dans les vagues déferlantes, nous menons une étude paramétrique approfondie des déferlantes bidimensionnelles en tant qu'analogues informatiques des processus tridimensionnels. Cette étude est nécessaire car l'étude paramétrique approfondie basée sur des simulations tridimensionnelles n'est actuellement pas réalisable en raison de la limitation des ressources informatiques. Nous proposons une analyse dimensionnelle pour les vagues bidimensionnelles générées par une plaque à vagues afin de faciliter cette analyse. Nous reproduisons numériquement une plaque à vagues de type piston pour initier un événement de déferlement unique à l'endroit désiré avec l'énergie désirée en spécifiant la course et la fréquence de la plaque à vagues. Nous analysons les caractéristiques de la vague à différentes intensités de déferlement pendant le déferlement et étudions l'échelle de la dynamique et de la cinématique de la vague aux conditions initiales en utilisant des arguments d'échelle inertielle. L'étude directe de la distribution des bulles n'étant évidemment pas possible dans le cadre d'une étude bidimensionnelle, il est essentiel de réaliser des simulations tridimensionnelles de vagues déferlantes. En faisant varier le nombre de Reynolds Re et le nombre de Bond Bo, nous explorons les effets de la viscosité et de la tension de surface sur la distribution de la taille des bulles et identifions les liens

possibles entre le taux de dissipation d'énergie et la distribution de la taille des bulles et des gouttelettes.

Pour étudier l'interaction d'une nappe de pétrole avec des vagues déferlantes, nous effectuons une simulation numérique directe basée sur une modélisation précise des vagues déferlantes et des régions de turbulence qui en résultent. Pour obtenir des informations dynamiques précises, nous utilisons la fonction VOF et des techniques de maillage adaptatif dans le solveur Basilisk pour modéliser l'évolution de la surface libre en trois phases. Nous effectuons des simulations de dispersion d'hydrocarbures en 2D pour remplacer le processus en 3D afin de faciliter une analyse paramétrique approfondie. Cela nous permet d'explorer les impacts potentiels de l'intensité des vagues et des tensions interfaciales sur la taille caractéristique des gouttelettes de pétrole. Notre étude numérique de la dispersion du pétrole par les vagues déferlantes englobe cinq séries d'intensités de vagues déferlantes et cinq tensions interfaciales différentes. En simulant le mouvement horizontal de la nappe de pétrole en surface, en suivant la distribution verticale des particules de pétrole, en quantifiant leur concentration dans la colonne d'eau et en évaluant le bilan de masse du pétrole déversé, nous dévoilons la dépendance des caractéristiques des gouttelettes à la fois à l'intensité des vagues déferlantes et aux tensions interfaciales.

Cette thèse comprend sept chapitres. Après l'introduction, le chapitre 2 fournit des informations essentielles sur l'étude en cours et une analyse complète des thèmes des vagues déferlantes et de la dispersion des hydrocarbures. Le chapitre 3 détaille le schéma numérique utilisé pour les simulations numériques directes, y compris la méthodologie utilisée pour suivre la surface libre et traiter la tension de surface dans les scénarios à deux et trois phases, et l'approche employée pour identifier le bilan énergétique, les bulles et les gouttelettes. Le chapitre 4 présente les résultats des simulations de vagues déferlantes en 2D, en commençant par une discussion des caractéristiques du déferlement des vagues, y compris le processus de déferlement des vagues et l'analyse du bilan énergétique. Une étude paramétrique est ensuite menée pour évaluer l'influence de la condition initiale et du nombre de Bond sur des aspects critiques tels que la cavité principale, la prédiction du début du déferlement et la dissipation d'énergie due au déferlement. Le chapitre 5 présente les données numériques obtenues à partir de simulations de vagues déferlantes en 3D. Il commence par présenter des informations générales sur les bulles et les gouttelettes, ce qui facilite l'analyse de leur formation et de leur évolution spatio-temporelle, ainsi que de leur distribution de taille. Ensuite, divers panaches de bulles générés à des étapes distinctes de la rupture de la vague sont analysés séparément, dans le but d'étudier les mécanismes de rupture des bulles. Le chapitre 6 présente les résultats des simulations de dispersion d'huile en 2D. Une étude paramétrique est menée pour explorer les effets de la force des vagues et de la tension interfaciale sur les statistiques des particules. Le chapitre 7 clôt la thèse par des remarques finales sur les principaux résultats et perspectives.

Contexte et revue de la littérature

Vagues déferlantes

En tant que processus intermittent fortement non linéaire se produisant sur une large gamme d'échelles, le déferlement des vagues joue un rôle important dans les interactions air-mer en limitant la hauteur des vagues de surface et en améliorant le transfert de masse, de quantité de mouvement et de chaleur entre l'atmosphère et l'océan (Melville, 1996; Perlin *et al.*, 2013). Lors du déferlement des vagues, des altérations notables se produisent à la surface libre, impliquant l'entraînement d'air dans l'océan, l'éjection d'embruns dans l'atmosphère, la production de bulles et d'aérosols (Kiger & Duncan, 2012; Veron, 2015), et la génération de turbulences locales à proximité de la surface libre. Le déferlement des vagues exerce également une influence déterminante sur divers aspects de la partie supérieure de l'océan, tels que la dispersion des marées noires et des contaminants, la détermination de la distribution de la taille des particules et le transport dynamique, ainsi que la santé générale des écosystèmes marins (Delvigne & Sweeney, 1988; Deike *et al.*, 2017; Li *et al.*, 2017). La manifestation la plus visible du déferlement des vagues est l'action initiale de renversement de la crête de la vague, qui forme des embruns et des nuages blancs et s'accompagne généralement de la projection vers l'avant d'un jet d'eau. Les processus associés aux vagues déferlantes ont été largement étudiés, et des progrès significatifs ont été réalisés dans la compréhension de leur géométrie, des critères d'apparition de la déferlante, de la dissipation d'énergie due à la déferlante et de l'entraînement d'air (Perlin *et al.*, 2013; Deike, 2022).

En particulier, les transferts d'énergie impliqués dans les vagues ont été largement étudiés au fil des ans, et la paramétrisation du taux de dissipation dû au déferlement a grandement bénéficié des expériences de laboratoire et des mesures numériques. La paramétrisation dérivée des études expérimentales fondamentales de Duncan (1981) a indiqué que le travail effectué par le whitecap ou le taux de dissipation d'énergie par unité de longueur de la crête de la vague est proportionnelle à la vitesse à la puissance 5

$$\epsilon_l = b\rho c^5/g \tag{7.1}$$

Ici, b est un coefficient sans dimension lié à la force de déferlement des vagues, ρ est la densité du fluide, c est une vitesse caractéristique associée à la vague déferlante et g est l'accélération due à la gravité. Le paramètre de déferlement b a d'abord été supposé être une constante non dimensionnelle, mais des études expérimentales approfondies ont ensuite montré qu'il variait sur plusieurs ordres de grandeur lorsque l'on fait varier la pente de la vague déferlante S (Rapp & Melville, 1990; Tian *et al.*, 2010). Pour établir des relations possibles

entre le paramètre de déferlement b et les conditions initiales des vagues déferlantes, l'échelle de dissipation conventionnelle de la théorie de la turbulence a été appliquée au processus de déferlement des vagues (Duncan, 1981; Drazen *et al.*, 2008; Mostert & Deike, 2020), en suivant la forme du taux de dissipation turbulente basée sur l'analyse dimensionnelle (Batchelor, 1953). Le taux de dissipation de l'énergie turbulente locale pendant le déferlement des vagues peut être estimé comme $\epsilon = \chi(w^3/l)$, où χ est une constante de proportionnalité, w est l'échelle de vitesse représentative et l est l'échelle de longueur intégrale turbulente caractérisant les tourbillons turbulents contenant de l'énergie (Taylor, 1935; Vassilicos, 2015). Par conséquent, le taux de dissipation d'énergie par unité de longueur de la crête est $\epsilon_l = \rho A \epsilon$ en supposant un nuage turbulent de section transversale A. Drazen *et al.* (2008) relie le taux de dissipation de l'énergie turbulente locale aux propriétés de rupture locales par une mise à l'échelle inertielle, c'est-à-dire $\epsilon = \sqrt{gh}^3/h$, où h est la hauteur de rupture et $\sqrt{gh}$ la vitesse balistique de la pointe du brise-roche plongeant. Le nuage de turbulence est supposé être un cercle avec une section transversale de $A = \pi h^2/4$. Ceci indique que le taux de dissipation par unité de longueur de la crête de rupture

$$\epsilon_l = \rho A \epsilon \propto \rho g^{3/2} h^{5/2} \propto (hk)^{5/2} \rho c^5 / g \tag{7.2}$$

où k est le nombre d'ondes et $c = \sqrt{g/k}$ par la relation de dispersion en eau profonde. Cela conduit à $b \propto S^{5/2}$, avec $S = hk$ étant la pente de la vague déferlante. De plus, le comportement seuil de la dissipation d'énergie associée au déferlement des vagues a été identifié par des mesures en laboratoire, révélant que b doit tendre vers zéro pour des pentes suffisamment faibles (Rapp & Melville, 1990; Drazen *et al.*, 2008; Tian *et al.*, 2010; Grare *et al.*, 2013). Pour caractériser ce comportement, Romero *et al.* (2012) a proposé une mise à l'échelle semi-empirique en introduisant un seuil de pente caractéristique

$$b = a(S - S_0)^{5/2} \tag{7.3}$$

avec une constante $a = 0,4$ et une pente critique $S_0 = 0,08$ déterminée sur la base de l'ajustement aux données de laboratoire. Des simulations numériques ultérieures ont constamment validé cette relation d'échelle (Iafrati, 2009; Deike *et al.*, 2016; De Vita *et al.*, 2018). Outre les vagues déferlantes en eau profonde, l'énergie dissipée par les vagues solitaires déferlant sur la pente d'une plage a également été quantifiée par Mostert & Deike (2020). L'échelle de vitesse représentative est considérée comme la vitesse d'impact, qui est calculée de manière balistique comme $w = \sqrt{2gH_b}$, où H_b est l'amplitude de la vague au moment du déferlement. L'échelle de longueur intégrale de la turbulence est estimée être la profondeur non perturbée à la rupture d_b, et la section transversale du nuage de turbulence est supposée être $A = \pi {H_b}^2/4$. Par conséquent, le taux de

dissipation par unité de longueur d'une crête de rupture est donné par

$$\epsilon_l = \rho A \epsilon \propto \rho g^{3/2} {H_b}^{7/2} / d_b \propto (H_b/d_0)^{7/2} (d_b/d_0)^{-1} \rho c^5 / g \tag{7.4}$$

où d_0 est la profondeur non perturbée avant la pente de la plage, et $c = \sqrt{g d_0}$ est dérivé de la relation de dispersion en eau peu profonde. Ces efforts ont permis d'établir un lien entre la dynamique et la cinématique des vagues déferlantes, et une paramétrisation de la dynamique a été développée sur la base de propriétés géométriques.

Bien que de grands progrès aient été réalisés dans les études précédentes sur la dissipation de l'énergie due au déferlement, certaines limitations persistent, nécessitant des recherches supplémentaires pour parvenir à une compréhension globale des vagues déferlantes. Tout d'abord, la majorité des efforts de recherche se sont concentrés sur l'étude des vagues déferlantes en eaux profondes. Cependant, les vagues déferlantes en eaux peu profondes et intermédiaires subissent des changements plus prononcés à la surface libre que les vagues déferlantes en eaux profondes, ce qui introduit des complexités supplémentaires au problème. Actuellement, il existe peu d'études portant sur le déferlement en eaux peu profondes, en particulier dans les cas où le déferlement est uniquement attribué à la non-linéarité dans un réservoir à fond plat. Bien que l'approche de simulation numérique directe (DNS), qui résout tous les processus de déferlement dans les vagues, ait été utilisée avec succès dans les études en eaux profondes (Iafrati, 2011; Deike *et al.*, 2016) et dans les déferlements en eaux peu profondes sur une pente (Mostert & Deike, 2020), les études précédentes ont été limitées par des ressources informatiques restreintes, limitant ainsi la gamme d'échelles de vagues à des nombres de Reynolds et de Bond plus petits. Néanmoins, il est essentiel de considérer les vagues expérimentales en eau peu profonde qui englobent une large gamme d'échelles de longueur, allant du déferlement à l'échelle du mètre à l'entraînement de bulles d'air à l'échelle du micron. Cette recherche vise à caractériser de manière exhaustive les vagues déferlantes expérimentales et à explorer la dispersion des marées noires influencées par les vagues déferlantes. Les vagues déferlantes expérimentales, qui ressemblent à des vagues solitaires, constituent une plate-forme appropriée pour l'analyse des caractéristiques de déferlement dans les eaux peu profondes. Leurs niveaux d'énergie plus élevés les rendent utiles pour valider et développer les théories de déferlement existantes, y compris les critères de déferlement, les lois d'échelle de dissipation du déferlement et les mécanismes d'entraînement de l'air. En outre, la formation et l'interaction des bulles d'air dans la couche mixte de l'océan supérieur fournissent des distributions verticales et horizontales de bulles. La mesure et l'interprétation de la taille des bulles d'air dans la couche supérieure de l'océan sont importantes pour l'évaluation des transports de gaz entre l'atmosphère et l'océan (Melville, 1996; Garrett *et al.*, 2000). Les vagues déferlantes forment des bulles et créent un ensemble

de bulles sous la surface (Deane, 1997). Les formes des nuages de bulles sont détectables à l'aide de diverses techniques sonar et servent à marquer la turbulence de la couche de surface, jouent un rôle dans l'échange de gaz entre l'atmosphère et l'océan et influencent le spectre du bruit ambiant (Banner & Peregrine, 1993). L'objectif de l'étude sur l'entraînement d'air était de caractériser la taille et la distribution spatiale des panaches de bulles et des nuages après le passage d'une vague déferlante. Une solution complète à la formation de bulles proposée par Garrett *et al.* (2000) a illustré le lien entre le spectre de taille et le taux de dissipation de l'énergie turbulente. Garrett *et al.* (2000) a supposé que l'air injecté par les vagues déferlantes à une échelle beaucoup plus grande que l'échelle de Hinze est fragmenté par les fluctuations de pression turbulente, et a proposé une loi de puissance de $r^{-10/3}$ pour le spectre de taille de ces bulles plus grandes, en considérant le niveau de turbulence et le taux moyen d'approvisionnement en air avec un argument de cascade dimensionnelle. Les mesures expérimentales effectuées par Deane & Stokes (2002) ont fourni une description quantitative des mécanismes de formation des bulles, révélant une densité de bulles proportionnelle à $r^{-10/3}$ pour les plus grosses bulles déterminées par la fragmentation turbulente, et une échelle de loi de puissance $-3/2$ pour les plus petites bulles créées par l'impact des jets et des gouttes sur la face de l'onde. Les mesures expérimentales effectuées par Blenkinsopp & Chaplin (2007) ont décrit l'évolution du nuage de bulles généré sous la surface libre et les éclaboussures au-dessus, en analysant la distribution variable dans le temps de la fraction de vide dans les vagues déferlantes. Ils ont révélé des caractéristiques similaires des panaches de bulles et des éclaboussures pour différents types de déferlantes. Les résultats numériques rapportés par Rivière *et al.* (2021) ont révélé une loi de puissance de distribution de la taille des bulles sup-Hinze $\mathcal{N}(r) \propto d^{-10/3}$ et une loi de puissance de distribution de la taille des bulles sub-Hinze $\mathcal{N}(r) \propto d^{-3/2}$, en accord avec le modèle théorique et les simulations numériques. Sur la base de ces résultats favorables, Rivière *et al.* (2021) a proposé un mécanisme alternatif pour la production de bulles sub-Hinze. Contrairement à la cascade auto-similaire de ruptures identifiée dans les bulles super-Hinze par Garrett *et al.* (2000), ils ont soutenu que la loi d'échelle régissant les bulles sub-Hinze est dérivée d'événements de scission de bulles entraînés par capillarité se produisant à l'intérieur de filaments allongés, qui entraînent la création d'au moins une bulle sub-Hinze au cours du processus de fragmentation de la bulle. Alors que l'initiation du phénomène de rupture et la turbulence qu'il génère ont été caractérisées (Rapp & Melville, 1990; Melville & Matusov, 2002; Banner & Peirson, 2007; Drazen *et al.*, 2008; Drazen & Melville, 2009), les échelles de temps et de longueur du processus de transition restent à explorer. La mesure de la turbulence diphasique tridimensionnelle en laboratoire et sur le terrain présente de nombreux défis techniques en termes d'accès au champ d'écoulement turbulent et aux distributions de taille des gouttes et des bulles pendant le temps actif

de la rupture (Mostert *et al.*, 2022). D'un point de vue énergétique, il reste à déterminer les caractéristiques de transition particulières de l'écoulement entièrement tridimensionnel et à étudier la dépendance de ces caractéristiques par rapport au nombre de Reynolds de l'écoulement, ainsi qu'à l'évolution du panache de bulles ingérées. En outre, les détails de la physique de la transition 2-D/3-D dans les vagues déferlantes constituent une question ouverte.

dispersion de l'huile

Les déversements accidentels d'hydrocarbures lors de la production et du transport de pétrole en mer peuvent avoir un large éventail d'effets négatifs sur le milieu marin et constituer une menace sérieuse pour les écosystèmes. Les déversements d'hydrocarbures peuvent également contaminer l'eau et libérer des produits chimiques nocifs dans l'air, ce qui peut avoir un effet dévastateur sur les animaux et les plantes de la zone touchée. Pour faire face aux dangers potentiels des marées noires, des recherches considérables ont été menées pour comprendre et quantifier les processus de marée noire afin de prédire la trajectoire et le devenir des hydrocarbures déversés (Guo & Wang, 2009). Le transport et le devenir des hydrocarbures déversés dans l'eau sont dominés par divers processus physiques, chimiques et biologiques. Les processus d'altération des hydrocarbures les plus courants dans les premières phases d'une marée noire sont l'étalement, l'advection, la diffusion, l'évaporation, l'émulsification, la dissolution et la dispersion. À plus long terme, la photo-oxydation, la biodégradation et la sédimentation apparaissent comme des mécanismes essentiels qui régissent la trajectoire finale des hydrocarbures déversés (Keramea *et al.*, 2021). Principale source d'énergie après un accident de déversement d'hydrocarbures, les processus de dynamique océanique affectent principalement les nappes d'hydrocarbures en termes d'étalement et de dispersion sous les effets combinés du vent, des vagues et des courants. L'étalement est l'expansion horizontale d'une nappe de pétrole due à des forces mécaniques telles que la gravité, l'inertie, la tension visqueuse et interfaciale, et la diffusion turbulente. Lorsque du pétrole brut est déversé à la surface de la mer, il s'étale pour former une nappe de pétrole, dont le mouvement est régi par l'advection et la diffusion turbulente sous l'action des courants et du vent (Guo & Wang, 2009). L'advection des hydrocarbures en surface est causée par les forces du courant de surface et de la traînée du vent sur les hydrocarbures, tandis que l'advection des hydrocarbures en suspension fait référence au mouvement des gouttelettes d'hydrocarbures entraînées dans la colonne d'eau sous l'effet du courant (Fingas, 2014). La dispersion se produit lorsque des vagues ou des turbulences déferlent sur la nappe d'hydrocarbures, produisant des gouttelettes de différentes tailles dans la colonne d'eau. La dispersion naturelle des hydrocarbures déversés

en mer est un processus essentiel pour déterminer la durée de vie prévue à la surface de la mer d'un pétrole brut ou d'un produit pétrolier spécifique dans des conditions environnementales données. Le calcul du temps de séjour des hydrocarbures à la surface de la mer est un élément clé pour évaluer les stratégies alternatives de lutte contre les déversements d'hydrocarbures, déterminer la probabilité d'impact sur les côtes et estimer les effets potentiels sur les oiseaux de mer et les mammifères marins sur la trajectoire de la nappe (Reed *et al.*, 2009). Dans les états de mer caractérisés par un déferlement fréquent des vagues, il est largement reconnu que les vagues déferlantes constituent le principal mécanisme de dispersion naturelle d'une nappe d'hydrocarbures (Naess, 1982). Il est donc hautement souhaitable d'étudier la rupture et le mélange dans l'eau d'une nappe d'hydrocarbures de surface par des vagues déferlantes.

La dispersion des hydrocarbures par les vagues déferlantes est un processus qui se produit lorsque les hydrocarbures déversés en mer forment de fines nappes, qui sont ensuite fragmentées en gouttelettes de différentes tailles par les forces turbulentes et les tourbillons générés par les vagues déferlantes (Delvigne & Sweeney, 1988). Les gouttelettes pénètrent ensuite dans la colonne d'eau, provoquant un mélange de pétrole dans la colonne d'eau. Au cours de ce processus, la taille réduite des gouttelettes est liée à des niveaux d'énergie plus élevés, à une viscosité plus faible et à une tension interfaciale plus faible. Un apport d'énergie élevé à ce stade, tel qu'une tempête, peut disperser la totalité de la nappe dans la colonne d'eau, ne laissant que de très fines traces d'hydrocarbures visibles après le passage de la tempête. Avec le développement des vagues déferlantes, la couche supérieure de la colonne d'eau devient bien mélangée et s'étend jusqu'à une profondeur correspondant approximativement à la hauteur de la vague au moment du déferlement. Les petites gouttelettes sont plus facilement dispersées et diffusées dans la colonne d'eau par les courants de subsurface et la force de mélange turbulente, tandis que les grosses gouttelettes ont tendance à refaire surface et à reformer des nappes. La rupture initiale et la submersion d'une nappe d'hydrocarbures cohérente en surface, ainsi que la rupture secondaire des parcelles d'hydrocarbures en gouttelettes plus petites, dépendent de la structure de la turbulence près de la surface de l'eau. La turbulence joue également un rôle important dans la diffusion verticale des gouttelettes de pétrole dans la colonne d'eau. La turbulence peut être décrite en termes de tourbillons de différentes tailles. L'énergie des grands tourbillons est transférée par l'intermédiaire de tourbillons plus petits vers la classe de taille la plus petite où l'énergie est finalement dissipée en chaleur sous l'influence de la viscosité. Les grands gradients de vitesse des petits tourbillons sont importants pour la rupture des gouttelettes d'huile et pour la probabilité de collision des gouttelettes, tandis que les grands tourbillons sont principalement responsables du transport dispersif des gouttelettes d'huile. L'éclatement en gouttelettes des couches d'hydrocarbures de

surface cohérentes et l'intrusion des gouttelettes dans la colonne d'eau sous l'effet des vagues déferlantes est un ensemble de mécanismes dans lesquels toutes les classes de taille de tourbillon dans les vagues déferlantes jouent probablement un rôle important. De nombreuses études ont été menées pour examiner les mécanismes possibles de génération de gouttelettes de pétrole (Hinze, 1955; Delvigne & Sweeney, 1988; Li & Garrett, 1998; Li *et al.*, 2008; Afshar-Mohajer *et al.*, 2018). L'étude de la dispersion des hydrocarbures induite par les vagues déferlantes a pour but de fournir un modèle de marée noire qui incorpore des équations et des données empiriques sur les effets des vagues déferlantes et de la turbulence sur la taille des gouttelettes d'hydrocarbures, le taux de dispersion verticale et le profil de concentration d'hydrocarbures qui en résulte. Hinze (1955) a supposé que la force de pression dynamique des flux turbulents est la cause de la rupture des gouttelettes, et a obtenu une formule pour la taille maximale des gouttelettes de pétrole qui peuvent survivre à la force de pression en utilisant l'analyse dimensionnelle

$$d_{max} = c(\gamma/\rho)^{3/5}\epsilon^{-2/5} \tag{7.5}$$

où c est une constante empirique. Cependant, Li & Garrett (1998) a soutenu que la formule obtenue par Hinze (1955) n'est valable que pour de grands nombres de Reynolds de gouttelettes, lorsque les nombres de Reynolds de gouttelettes sont petits, le cisaillement visqueux associé à de petits tourbillons turbulents est la cause de l'éclatement. Les études de laboratoire menées par Delvigne & Sweeney (1988) sur la dispersion naturelle de l'huile de surface ont révélé que la taille des gouttelettes dépendait de la viscosité de l'huile et du taux moyen de dissipation de l'énergie. Ils ont émis l'hypothèse que les petits tourbillons dans les écoulements turbulents sont responsables de la division des gouttelettes d'huile. Mukherjee *et al.* (2012) ont étudié les mécanismes de formation des gouttelettes à l'aide d'une analyse sans dimension et d'une analyse de l'équilibre des forces. Ils ont identifié quatre régimes distincts de formation de gouttelettes : pour $d > \eta$, d varie soit avec $\varepsilon^{-2/5}$ ou $\varepsilon^{-1/4}$ et pour $d < \eta$, d varie soit avec $\varepsilon^{-1/2}$ ou $\varepsilon^{-1/4}$ selon que la principale force de rappel contre la rupture des gouttelettes est fournie par la tension superficielle ou par la viscosité de l'huile. Pour $d > \eta$ et $d < \eta$, la force externe qui tente de déformer et de briser la gouttelette est fournie par la différence de pression à travers le diamètre de la gouttelette et le cisaillement visqueux, respectivement.

Le déferlement des vagues est le principal mécanisme par lequel les déversements d'hydrocarbures pénètrent dans l'eau sous forme de gouttelettes, et la génération et la distribution de ces gouttelettes d'hydrocarbures sont des sujets importants dans ce domaine, mais qui ne sont pas encore parfaitement compris. La distribution de la taille des gouttelettes de pétrole dispersé est particulièrement intéressante pour élucider la réduction et la diffusion horizontale du pétrole en surface, l'absorption du pétrole par la vie marine, l'adsorption du pétrole

par les particules en suspension et sa sédimentation ultérieure sur le fond marin. Dans les expériences du canal d'huile à petite échelle pour étudier l'effet des vagues déferlantes sur un film d'huile de surface par (Delvigne & Sweeney, 1988), de l'huile a été versée sur la surface de l'eau dans la section d'essai du canal, ce qui a produit un film d'huile d'une épaisseur de 0,5 mm. Les distributions de taille des gouttelettes ont été obtenues à l'aide d'une série d'échantillonneurs de gouttelettes d'huile, qui consistent en un petit cylindre de verre à sommet plat. Les gouttelettes d'huile échantillonnées sont montées jusqu'au sommet du cylindre de verre après un temps de repos de 20 heures, et des photographies ont été prises du verre supérieur pour permettre le comptage des gouttelettes d'huile. Ces données expérimentales indiquent une distribution de la taille des gouttelettes qui suit la relation suivante

$$N_u(d_o) \propto d_o^{-2.30(\pm 0.06)} \tag{7.6}$$

indépendamment du type d'huile, de l'état d'altération, de l'épaisseur de la couche d'huile et de la température. Dans cette relation, d_o est le diamètre des gouttelettes d'huile, et $N_u(d_o)$ est le nombre de gouttelettes dans un intervalle de taille unitaire Δd autour de d_o. La distribution de la taille des gouttelettes dépend de facteurs tels que la tension interfaciale entre l'eau et l'huile, la viscosité de l'huile, le type et l'intensité des vagues. La dispersion des hydrocarbures par les vagues déferlantes et la distribution de la taille des gouttelettes qui en résulte sont importantes pour évaluer l'impact environnemental des déversements d'hydrocarbures et concevoir des contre-mesures efficaces telles que les dispersants. L'application de dispersants est devenue une mesure importante pour lutter contre les déversements d'hydrocarbures. En réduisant la tension superficielle entre le pétrole et l'eau, les dispersants peuvent aider à fragmenter le pétrole en gouttelettes plus petites, qui peuvent alors être plus facilement dispersées par l'action des vagues et des courants. En outre, l'utilisation de dispersants peut également retarder la formation d'émulsions huile-eau à haute viscosité qui sont difficiles à décomposer et peuvent causer de graves dommages. Il est donc essentiel de comprendre le rôle de la tension superficielle dans la formation et la distribution des gouttelettes de pétrole pour élaborer des stratégies efficaces de lutte contre les marées noires. La dispersion du pétrole par les vagues déferlantes peut être mesurée expérimentalement à l'aide de techniques telles que la vélocimétrie par image de particules (PIV), la fluorescence induite par laser (LIF) et l'imagerie à grande vitesse pour obtenir les champs de vitesse, les distributions de taille des gouttelettes et les profils de surface des vagues déferlantes. Peishi *et al.* (2011) étudie la simulation mathématique de l'étalement et de la dispersion des nappes de pétrole dans des champs d'écoulement non uniformes. La dispersion du pétrole par des vagues déferlantes peut être modélisée à l'aide de méthodes de dynamique des fluides numérique (CFD) qui couplent les équations de Navier-Stokes moyennées par Reynold (RANS) avec des méthodes de volume

de fluide (VOF) pour capturer l'interface eau-air transitoire et le champ d'énergie cinétique turbulente. Un modèle numérique incluant l'étalement et la dispersion a été développé pour décrire le mouvement initial de la nappe de pétrole dans les eaux libres et couvertes de glace. Un modèle d'hydrodynamique des particules lissées (SPH) à deux phases a été développé sur la base de GPUSPH, qui est une implémentation open-source de la méthode SPH faiblement compressible sur les unités de traitement graphique, pour étudier la dispersion du pétrole sous les vagues déferlantes (Wei *et al.*, 2017). Carratelli *et al.* (2011) a fourni une indication des effets du mouvement induit par les vagues du pétrole à la surface de la mer en relation avec la marée noire de Deepwater Horizon. Pour estimer les effets combinés du transport et de l'altération du pétrole, les modèles de dérive saisonnière sont analysés et des conceptions alternatives de fairway sont dérivées à l'aide d'une technique de Monte Carlo (Murawski & Woge Nielsen, 2013). Zhang *et al.* (2021) présentent les résultats de simulation des deux modèles à une échelle limitée (une sous-zone du golfe du Mexique) dans les mêmes conditions de déversement d'hydrocarbures en utilisant des données réelles sur les courants océaniques provenant du modèle couplé unifié d'interface des vagues (UWIN-CM). Muin *et al.* (2022) présente une étude plus approfondie de l'effet des vagues non linéaires sur la dispersion des hydrocarbures dans la baie. Afin d'explorer l'influence du déferlement des vagues en mer sur la formation et le transport de matières dangereuses liées au pétrole, le processus de déferlement des vagues a été simulé dans un canal de laboratoire bidimensionnel, et le processus de comportement des matières dangereuses liées au pétrole a été identifié et suivi (Fang *et al.*, 2022). Toutefois, les méthodes eulériennes traditionnelles présentent l'inconvénient de ne pas résoudre directement les phénomènes de dispersion en un point physique, ce qui entraîne une diffusion numérique. À des fins de calcul, les modèles de marée noire divisent la nappe en éléments lagrangiens ou en particules et suivent leur mouvement, ce qui ne permet pas d'obtenir directement une concentration ou une épaisseur de pétrole à des endroits spécifiques. Elliott *et al.* (1986) ont appliqué le suivi des particules par marche aléatoire (RWPT) pour décrire le mouvement des gouttelettes de pétrole dans la colonne d'eau. Un modèle numérique hybride de marée noire couplé au suivi des particules et à l'approche eulérienne-lagrangienne a été développé par Guo & Wang (2009). La plaque de pétrole initiale est modélisée par la libération de particules et les processus pétroliers sont suivis sur la base d'une valeur critique de l'épaisseur de la nappe de pétrole ou de la concentration de pétrole, avec la capacité de prédire la distribution horizontale et verticale, la concentration dans la colonne d'eau et le bilan de masse du pétrole déversé.

Méthodologie

Schéma numérique

Les équations de Navier-Stokes pour un écoulement multiphasique incompressible avec une densité et une tension de surface variables sont simulées à l'aide de la bibliothèque Basilisk. Le package Basilisk, développé comme le successeur du framework Gerris (Popinet, 2003, 2009), est un programme open-source pour résoudre divers systèmes d'équations aux dérivées partielles sur des maillages cartésiens adaptatifs réguliers avec une précision spatiale et temporelle de second ordre. Un schéma de raffinement de maillage adaptatif (AMR) basé sur un quadtree / octree est utilisé dans les calculs 2-D / 3-D pour améliorer l'efficacité de calcul en concentrant les ressources de calcul sur les domaines de solution importants. La méthode identifie et résout finement les parties actives de l'écoulement simulé tout en utilisant des résolutions locales plus grossières pour les régions à peu près tranquilles. En particulier, l'approche AMR permet plus facilement la résolution directe de la turbulence à petite échelle dans l'eau sans avoir besoin d'un modèle de turbulence (Boswell *et al.*, 2023). Le critère de raffinement est déterminé par un algorithme d'ondelettes, qui estime l'erreur de discrétisation dans les champs de vitesse et de VOF. La boucle temporelle générique est mise en œuvre dans le schéma numérique et le pas de temps est limité par la condition de Courant-Friedrichs-Lewy (CFL). L'écoulement est décrit par les équations de Navier-Stokes incompressibles et à densité variable, le terme de tension superficielle étant traité par une force superficielle continue (Brackbill *et al.*, 1992) qui peut s'écrire comme suit

$$\rho(\partial_t \boldsymbol{u} + (\boldsymbol{u}\cdot\nabla)\boldsymbol{u}) = -\nabla p + \nabla\cdot(2\mu\boldsymbol{D}) + \boldsymbol{f}_\gamma \tag{7.7}$$

$$\partial_t \rho + \nabla\cdot(\rho\boldsymbol{u}) = 0 \tag{7.8}$$

$$\nabla\cdot\boldsymbol{u} = 0 \tag{7.9}$$

où $\boldsymbol{u} = (u, v, w)$ est la vitesse du fluide, $\rho \equiv \rho(x,t)$ est la densité du fluide, p est la pression, $\mu \equiv \mu(x,t)$ est la viscosité dynamique, $\boldsymbol{D}$ est le tenseur de déformation défini comme $D_{ij} \equiv (\partial_i u_j + \partial_j u_i)/2$ et $\boldsymbol{f}_\gamma$ est la force de tension superficielle par unité de volume (Deike *et al.*, 2016).

La méthode VOF a été développée à l'origine par Hirt & Nichols (1981) et a été modifiée par Kothe *et al.* (1991), puis couplée à la conservation de la quantité de mouvement par Fuster & Popinet (2018), avec l'avantage de permettre une résolution spatiale variable et une représentation nette le long de l'interface, tout en limitant l'apparition de courants parasites numériques parasites. L'interface de l'écoulement diphasique est reconstruite par une fonction $\alpha(x,t)$, définie comme la fraction de volume d'un fluide donné dans chaque cellule de la maille

de calcul, en prenant les valeurs 0 ou 1 pour chaque phase. La densité et la viscosité peuvent donc être calculées par des moyens arithmétiques comme suit

$$\rho(\alpha) = \alpha\rho_1 + (1-\alpha)\rho_2 \tag{7.10}$$

$$\mu(\alpha) = \alpha\mu_1 + (1-\alpha)\mu_2 \tag{7.11}$$

où ρ_1 et ρ_2, μ_1 et μ_2 sont respectivement la densité et la viscosité du premier et du second fluide.

L'équation d'advection pour la densité peut être remplacée par une équation d'advection équivalente pour la fraction de volume, qui peut être obtenue en remplaçant l'équation d'advection pour la densité

$$\partial_t \alpha + \nabla \cdot (\alpha \boldsymbol{u}) = 0 \tag{7.12}$$

L'approche de la construction linéaire par morceaux de l'interface (PLIC) est appliquée. La normale de l'interface est calculée par la méthode mixte centrée sur Youngs (MYC) (Aulisa *et al.*, 2007) et l'emplacement de l'interface dans la cellule est calculé sur la base de la méthode Scardovelli & Zaleski (2000).

Pour le suivi des interfaces des écoulements multiphasiques, une fonction similaire de fraction de volume est appliquée. La densité et la viscosité des multiples fluides sont calculées en utilisant les moyennes arithmétiques

$$\rho(\alpha) = \sum_{i=1}^{N} \alpha_i \rho_i \tag{7.13}$$

$$\mu(\alpha) = \sum_{i=1}^{N} \alpha_i \mu_i \tag{7.14}$$

où ρ_i et μ_i sont respectivement la densité et la viscosité de chaque phase. L'équation d'advection pour la fraction volumique d'un écoulement multiphasique décrit le transport d'une phase au sein d'un mélange de phases. Elle peut être construite en considérant des points polyphasés formés par plusieurs phases, où chaque phase a une fraction de volume distincte

$$\partial_t \alpha_i + \nabla \cdot (\alpha_i \boldsymbol{u}) = 0 \tag{7.15}$$

où α_i est la fraction de volume de la phase i. Les champs de fraction volumique α_i sont définis de telle sorte qu'ils satisfont à la condition suivante

$$\sum_{i=1}^{N} \alpha_i = 1 \tag{7.16}$$

où N est le nombre total de phases dans le mélange. Nous avons N = 3 pour les problèmes à trois phases.

Le schéma de conservation de la quantité de mouvement dans les flux de quantité de mouvement advectifs près de l'interface s'est avéré essentiel pour réduire le transfert numérique de quantité de mouvement à travers l'interface, en particulier dans les cas où les différences de densité des phases distinctes sont importantes. Les flux totaux sur chaque face sont obtenus en ajoutant le flux diffusif dû au terme visqueux, qui est calculé par le schéma semi-implicite de Crank–Nicholson (Pairetti *et al.*, 2018). Le schéma de Bell–Collela–Glaz (BCG) d'ordre 2 est utilisé pour la reconstruction de la quantité de mouvement du liquide et du gaz par unité de volume à advecter dans la cellule (Bell *et al.*, 1989). Le limiteur de pente minmod généralisé est employé pour calculer le gradient. La mise en œuvre de l'advection VOF préservant la quantité de mouvement des composantes de vitesse empêche les artefacts causés par la fuite de quantité de mouvement entre les phases denses et légères (Fuster & Popinet, 2018; Zhang *et al.*, 2020).

Bien que les forces de tension superficielle puissent être négligées pour les vagues d'une longueur supérieure au centimètre, qui constituent la majorité des vagues étudiées ici, elles pourraient être importantes pour capturer la cavité principale au moment de l'impact et l'hydrodynamique de la vague après le déferlement. Le processus de déferlement des vagues souligne l'importance de la tension superficielle à petite échelle, qui ne peut être négligée en raison de la forte courbure de la surface libre. La tension superficielle est traitée avec la méthode de Brackbill *et al.* (1992) et la technique des forces équilibrées (Francois *et al.*, 2006) développée par Popinet (2009, 2018). Une version généralisée de l'estimation de la courbure de la fonction de hauteur (HF) est mise en œuvre pour résoudre l'incohérence à faible résolution d'interface, donnant des solutions précises et efficaces pour les écoulements entraînés par la tension superficielle. La force de tension de surface par unité de volume $\boldsymbol{f}_\gamma$ peut être exprimée comme suit

$$\boldsymbol{f}_\gamma = \gamma\kappa\delta_s\boldsymbol{n} \tag{7.17}$$

où γ est le coefficient de tension de surface ; δ_s est la fonction de Dirac de l'interface, indiquant que le terme de tension de surface est concentré sur l'interface ; et κ et $\boldsymbol{n}$ sont les courbures et la normale à l'interface, respectivement.

Les intégrales sur l'ensemble de la phase spécifique sont effectuées numériquement pour identifier le bilan énergétique dans cette phase. L'énergie cinétique E_k et l'énergie potentielle gravitationnelle E_p de l'onde qui se propage sont fournies comme suit

$$E_k = \frac{1}{2}\int_V \rho|\boldsymbol{u}\cdot\boldsymbol{u}|\mathrm{d}V \tag{7.18}$$

$$E_p = \int_V \rho g y\mathrm{d}V - E_{p0} \tag{7.19}$$

où V est le domaine occupé par l'eau dans le système et E_{p0} est l'énergie potentielle gravitationnelle de l'eau immobile au début. L'énergie mécanique E_m de la vague est calculée comme la somme des composantes cinétique et potentielle

$$E_m = E_k + E_p \tag{7.20}$$

La dissipation d'énergie non conservative due à l'action de la viscosité, E_d, peut être calculée directement à partir du tenseur des déformations

$$E_d(t) = \int_0^t \int_v \mu \frac{\partial u_i}{\partial x_j} \frac{\partial u_j}{\partial x_i} \mathrm{d}V \mathrm{d}t \tag{7.21}$$

Ainsi, le budget total d'énergie conservée est donné par $E_t = E_k + E_p + E_d$.

Nous comptons les gouttelettes et les bulles dans un flux en marquant les voisinages connectés. En considérant les régions connectées séparées par des cellules interfaciales, le volume et la position des bulles et des gouttelettes individuelles peuvent être déterminés sans ambiguïté. Dans la pratique, on utilise une implémentation de l'"algorithme du peintre" classique, qui est généralement utilisé dans les éditeurs de graphiques bitmap pour remplir les régions connectées d'une image avec une couleur donnée. Cette méthode est exacte à l'ordre de la résolution des équations de Navier-Stokes et de la méthode VOF associée. Notamment, les erreurs d'advection de la reconstruction de l'interface VOF peuvent être importantes lorsque la structure du liquide est inférieure à deux fois l'espacement de la grille (Li *et al.*, 2010). Comme indiqué dans des études antérieures (Wang *et al.*, 2016; Mostert *et al.*, 2022; Wang *et al.*, 2023), avec plus de 4 cellules de calcul minimum par diamètre de bulle/gouttelette, les bulles/gouttelettes prennent une forme sphérique, conforme à la forme physique des bulles/gouttelettes avec un rapport entre le diamètre et la longueur capillaire inférieur à 0,37 lorsque la tension superficielle domine (Clift *et al.*, 2005). Par conséquent, dans cette étude, les bulles/gouttelettes dont le diamètre est inférieur à quatre cellules de calcul sont considérées comme non résolues et ne sont pas comptabilisées.

Description du problème

Cette étude porte sur la dispersion des hydrocarbures par les vagues déferlantes grâce à des simulations numériques directes de vagues expérimentales. Une série d'expériences de vagues déferlantes a été menée dans un canal à vagues de 6 m de long, 0,3 m de large et 0,6 m de haut pour étudier les processus de déferlement et la dispersion des déversements d'hydrocarbures par les vagues déferlantes (Li *et al.*, 2017; Wei *et al.*, 2018; Afshar-Mohajer *et al.*, 2018). Les vagues déferlantes ont été initialisées en actionnant un générateur de vagues à piston sur une profondeur d'eau constante d. Un événement de déferlement d'une seule vague a été produit

par une seule poussée du générateur de vagues, et sa trajectoire $x(t)$ et la vitesse de la plaque d'onde associée $U(t)$ ont été déterminées par les fonctions suivantes

$$x(t) = \frac{s}{2}(1 - \cos\sigma t), 0 \leq t \leq \frac{1}{2f} \tag{7.22}$$

$$U(t) = s\pi f \sin\sigma t, 0 \leq t \leq \frac{1}{2f} \tag{7.23}$$

où s est la longueur de la course du générateur d'ondes, $\sigma = 2\pi f$ est la fréquence angulaire, et t est le temps. Une seule poussée du générateur d'ondes pendant une demi-période $1/(2f)$ a été appliquée pour produire une onde avec une seule crête. Pendant le mouvement de la plaque d'onde, la course maximale de la plaque d'onde est de s, et la vitesse maximale de la plaque d'onde est de $U_{max} = s\pi f$. Plusieurs types de vagues ont pu être générés en faisant varier la course s, la fréquence f et la profondeur de l'eau d, allant de vagues non déferlantes à des vagues déferlantes de différentes intensités. Par rapport au mouvement conventionnel du générateur de vagues à piston qui produit des vagues sinusoïdales avec un mouvement oscillatoire de $x(t) = s/2 \sin\sigma t$, la trajectoire du piston peut ici accentuer le profil de la vague et favoriser le déferlement de la vague. L'origine du domaine expérimental a été située à la surface de l'eau non perturbée sur la limite gauche, où x représente la direction du courant, et z la direction verticale, la droite et le haut étant positifs. Le générateur de vagues a été initialement placé à $x = 0,535$ m de la limite gauche (voir figure 3.1). L'imagerie à haute vitesse a été mise en œuvre pour visualiser l'impact du jet plongeant et les processus de déferlement qui s'ensuivent pendant le déferlement de la vague. La turbulence produite par le déferlement a été caractérisée à l'aide de la vélocimétrie par images de particules (PIV). Les images PIV ont été traitées pour calculer l'évolution temporelle de la turbulence dans la cuve à vagues. L'holographie numérique en ligne, une technique d'imagerie tridimensionnelle, a été utilisée pour mesurer la taille des gouttelettes et des bulles produites et pour qualifier la distribution de la taille des particules sous la surface. Sur la base des expériences de laboratoire, des simulations numériques directes d'une série de vagues déferlantes ont été réalisées à l'aide du solveur Basilisk.

En tant que processus intermittent fortement non linéaire qui se produit sur une large gamme d'échelles, le déferlement des vagues joue un rôle important dans les interactions air-mer en limitant la hauteur des vagues de surface et en améliorant le transfert de masse, de quantité de mouvement et de chaleur entre l'atmosphère et l'océan (Melville, 1996; Perlin *et al.*, 2013). Lorsqu'une vague déferle, la surface libre subit des changements spectaculaires, entraînant de l'air dans l'océan et éjectant des embruns dans l'atmosphère, avec la production de bulles et d'aérosols (Kiger & Duncan, 2012; Veron, 2015), et la génération de turbulences locales près de la surface libre. Le déferlement des vagues contrôle également le devenir des marées noires et des contaminants

dans la partie supérieure de l'océan, détermine la distribution de la taille des particules et le transport dynamique, et affecte en outre la santé des environnements marins (Delvigne & Sweeney, 1988; Deike *et al.*, 2017; Li *et al.*, 2017). Les processus associés aux vagues déferlantes ont fait l'objet de nombreuses recherches, et les progrès les plus importants ont été réalisés dans la compréhension de la géométrie de la déferlante, des critères d'apparition de la déferlante, de la dissipation due à la déferlante et de l'entraînement de l'air (Perlin *et al.*, 2013; Deike, 2022).

La vague générée par le piston est supposée être suffisamment longue pour l'hypothèse des eaux peu profondes. Cette hypothèse est confirmée par la mesure de la vitesse de la vague. Nos résultats numériques indiquent que la vitesse de la crête de la vague, calculée à partir de la vitesse moyenne de la crête de la vague en mouvement, est supérieure à la vitesse de la vague prévue par la théorie des eaux peu profondes. De plus, la longueur d'onde exacte de la vague est difficile à déterminer, ce qui nous empêche de déterminer avec précision le régime de profondeur d/L (rapport entre la profondeur de l'eau et la longueur d'onde). Dans l'expérience, nous avons mesuré directement la vitesse de la crête de la vague avant le déferlement c_w. En supposant que la fréquence de la plaque d'onde est équivalente à la fréquence de l'onde, et en utilisant la relation de dispersion à une profondeur d'eau de 0,25 m, nous avons calculé que la vitesse maximale de l'onde était de 1,566 m/s. La vitesse de la vague mesurée expérimentalement c_w dépasse largement cette valeur, ce qui suggère que la théorie de la vague linéaire n'est pas applicable dans ce cas. D'autre part, l'estimation de la vitesse de la vague basée sur la théorie de l'onde solitaire donne des valeurs plus proches des mesures expérimentales. Par conséquent, nous concluons que l'onde expérimentale présente des caractéristiques similaires aux ondes solitaires.

La méthodologie numérique suivie dans cette étude implique la simulation de l'écoulement incompressible de deux ou trois fluides non miscibles. Pour saisir avec précision les caractéristiques physiques des profils d'interface triphasés liés aux vagues déferlantes, les équations de Navier-Stokes doivent être résolues numériquement sur des grilles suffisamment fines pour que les effets visqueux et capillaires puissent être conservés. Sur la base de simulations numériques directes (DNS) du mélange eau-air résultant de l'entraînement de gouttelettes et de bulles, et du mélange huile-eau-air résultant de la dispersion de la nappe de pétrole par les vagues déferlantes, en combinaison avec des expériences antérieures menées à l'université Johns Hopkins, nous avons l'intention d'étudier les mécanismes des vagues déferlantes et de la dispersion du pétrole par déferlement en termes de profils de surface libre, de champs de vitesse, de bilan énergétique et de distribution de la taille des bulles et des gouttelettes.

Afin de simuler avec précision les vagues déferlantes et la dispersion du pétrole, nous résolvons les équations

de Navier-Stokes à deux phases avec tension superficielle et en utilisant un transport préservant l'élan de chaque phase. La gravité est prise en compte à l'aide de l'"approche de gravité réduite" (Wroniszewski *et al.*, 2014). Le domaine est discrétisé en utilisant le schéma de raffinement de maillage adaptatif. Une profondeur d'eau constante pour l'interface $\eta(x,y)_{(t=0)} = d$, avec d la profondeur d'eau calme, est utilisée comme condition initiale dans une boîte carrée de taille $L = 6$ m. La nappe de pétrole est placée sur la surface de l'eau non perturbée, avec une longueur de l_o et une épaisseur de h_o. L'onde se propage dans la direction x de gauche à droite. La résolution numérique est donnée par $\Delta = L_0/2^{l_{max}}$, où l_{max} est le niveau maximum de raffinement dans le schéma AMR. Le piston est implémenté en initialisant un champ de fraction de volume à chaque pas de temps, qui correspond à la position et à la vitesse du piston en mouvement. Cette approche a été utilisée efficacement dans des études antérieures (Lin-Lin *et al.*, 2016; Wu & Wang, 2009). Étant donné que le piston mobile est mis à jour à chaque pas de temps, les grilles intersectées par le piston sont affinées au niveau le plus fin en permanence, ce qui garantit une représentation précise de la frontière mobile dans les maillages adaptatifs. Le critère de raffinement est basé sur l'erreur de discrétisation estimée par l'ondelette en termes de champs de vitesse et de VOF. Le maillage correspondant sera affiné si nécessaire lors de l'initialisation de la vague. L'algorithme de raffinement est invoqué à chaque pas de temps pour raffiner le maillage chaque fois que l'erreur estimée de l'ondelette dépasse le seuil prescrit pour les champs de vitesse et de fraction de volume.

Une analyse dimensionnelle des vagues générées par les plaques à vagues est effectuée. La vague générée par la plaque à vagues est supposée dépendre des propriétés du fluide et des conditions initiales. Si le processus ondulatoire est limité aux systèmes air-eau proches de la température et de la pression standard, les rapports de densité et de viscosité cinématique des deux phases sont ceux de l'air et de l'eau dans les expériences, ce qui ne sera pas considéré comme une altération des caractéristiques de l'onde. Les variables dépendantes permettant d'identifier cette onde spécifique peuvent alors être exprimées comme suit

$$f(g, \nu, \rho, \gamma, s, f, d) \tag{7.24}$$

où g [dimension $\mathrm{L/T^2}$] est l'accélération gravitationnelle, ν [$\mathrm{L^2/T}$] est la viscosité cinématique de l'eau, ρ [$\mathrm{M/L^3}$] est la densité de l'eau et γ [$\mathrm{M/T^2}$] est la tension superficielle. La course du piston s [L] et la fréquence f [T] de la plaque d'onde, ainsi que la profondeur d'eau non perturbée d [L] sont appelées conditions initiales. Le théorème de Buckingham peut être utilisé pour construire les paramètres adimensionnels suivants en choisissant ρ, g et d comme variables répétitives

$$\frac{g^{1/2}d^{3/2}}{\nu} = Re, \quad \frac{\rho g d^2}{\gamma} = Bo, \quad \frac{s}{d}, \quad \frac{f}{\sqrt{g/d}} = \frac{fd}{c} \tag{7.25}$$

L'analyse dimensionnelle ci-dessus indique que les caractéristiques des vagues sont déterminées par le nombre de Reynolds Re, le nombre de Bond Bo, s/d et fd/c, où $c = \sqrt{gd}$ est la vitesse de la vague en eau peu profonde. La hauteur maximale de la vague avant déferlement H [L], la crête de la vague déferlante H_b [L] du déferlement plongeant, l'énergie totale par unité de longueur transférée par le mouvement de la plaque de la vague E_l [$\mathrm{ML/T^2}$] et la dissipation de l'énergie de la vague par unité de longueur de la crête déferlante, ϵ_l [$\mathrm{ML/T^3}$] sont d'un intérêt particulier dans le cadre de la présente étude. Ces caractéristiques des vagues doivent être sans dimension pour être reliées aux paramètres sans dimension représentant les propriétés du fluide et les conditions initiales. En utilisant l'analyse dimensionnelle, les paramètres sans dimension pour ces caractéristiques d'ondes sont les suivants

$$\frac{H}{d}, \quad \frac{H_b}{d}, \quad \frac{E_l}{\rho g d^3}, \quad \frac{\epsilon_l}{\rho g^{3/2} d^{5/2}} \tag{7.26}$$

La quantification de l'influence de ces paramètres sans dimension est d'une grande importance pour élucider l'évolution de la forme des vagues, le transfert d'énergie et les mécanismes d'entraînement de l'air.

Résumé des simulations de vagues déferlantes en 2D

Dans les simulations de vagues déferlantes en 2D, nous avons étendu les simulations numériques directes de vagues déferlantes en 2D à des conditions triphasiques avec une nappe de pétrole à la surface de l'eau. Nous avons mené une étude paramétrique pour analyser la dépendance quantitative de la taille caractéristique des gouttelettes d'huile par rapport à l'intensité de la vague et à la tension interfaciale. Avec l'augmentation de la course de la plaque d'onde s, l'énergie de surface de la phase huileuse augmente généralement après le déferlement de la vague. L'impact du jet provoque une augmentation rapide de l'énergie de surface de la phase huileuse dans tous les cas, en raison de l'étirement de la nappe d'huile et de la production du splash-up initial. Le premier impact de jet correspond à l'augmentation la plus significative de l'énergie de surface de la phase pétrolière, atteignant 3 à 4 fois l'énergie de surface initiale. Pour les vagues déferlantes plus faibles, l'énergie de surface atteint un maximum après le premier impact de jet et diminue ensuite. Cependant, pour les vagues déferlantes plus fortes, les processus d'éclaboussures ultérieurs augmentent encore l'énergie de surface de la phase huileuse. En outre, nous avons identifié une forte corrélation entre le taux maximal de dissipation d'énergie et le diamètre caractéristique des gouttelettes d_5, où d_5 dépend de $(\gamma/\rho_w)^{3/5}{\epsilon_{max}}^{-2/5}$, ce qui correspond aux prévisions théoriques de mise à l'échelle. Cette recherche ouvre la voie à l'étude de la relation entre le déferlement des vagues et le comportement des nappes de pétrole dans les déversements

de pétrole en mer par le biais de simulations numériques, contribuant ainsi à une meilleure compréhension des mécanismes régissant la dispersion du pétrole et l'étalement en surface. Dans la prochaine étape de notre recherche, nous avons l'intention d'extraire les informations sur la taille maximale des bulles d'air à partir de simulations de vagues déferlantes en 2D et de les comparer aux résultats numériques de leurs homologues en 3D. Cette comparaison nous aidera à renforcer notre hypothèse sous-jacente concernant la validité de la taille représentative des gouttelettes dans une vague déferlante en 3D. En outre, l'analyse supplémentaire de la distribution de probabilité de la position de propagation du film d'hydrocarbures sera intégrée dans nos recherches en cours, par exemple la probabilité de trouver des hydrocarbures à une distance donnée après le passage d'une vague déferlante.

Résumé des simulations de vagues déferlantes en 3D

Dans les simulations de vagues déferlantes en 3D, nous avons étendu les simulations de vagues déferlantes en deux dimensions à un cadre tridimensionnel afin de tenir compte des effets tridimensionnels sur le processus de déferlement des vagues et d'évaluer les effets de la viscosité (représentée par le nombre de Reynolds, Re) et de la tension superficielle (représentée par le nombre de Bond, Bo) sur les caractéristiques et la distribution de la taille des bulles générées par le déferlement des vagues. Nous avons analysé la convergence de la grille des résultats numériques en considérant trois séries de simulations avec l_{max} = 11, 12, et 13. Nous avons discuté de la convergence numérique en termes de bilan énergétique et de distribution de taille des bulles et des gouttelettes produites par le déferlement des vagues. Tous les résultats ont bien convergé et aucun changement significatif n'a été observé lorsque le niveau maximum de raffinement a augmenté de 11 à 13. Les résultats numériques correspondent assez bien aux mesures expérimentales en termes de forme de la vague et de hauteur maximale de la vague avant le déferlement. Pendant le temps de déferlement actif, la distribution de la taille des bulles suit $N(r,t) \propto r^{-10/3}$. Un Bo plus élevé conduit à un plus grand nombre de bulles, la différence étant plus prononcée dans la gamme des bulles plus petites. La vitesse verticale varie en fonction du rayon de la bulle, montrant des vitesses de montée variables à différents rayons de bulle sous l'effet de la flottabilité, les bulles les plus grosses montant à la surface libre à une vitesse plus rapide. Pendant la phase de rupture active, la profondeur du panache de bulles reste constante, ce qui correspond à la hauteur initiale de la cavité principale. Les limites de calcul actuelles des simulations tridimensionnelles empêchent une étude paramétrique englobant une large gamme de valeurs de Re et Bo. Par conséquent, les recherches futures se concentreront sur des analyses comparatives du bilan énergétique et de l'entraînement d'air entre les simulations bidimensionnelles

et tridimensionnelles.

Résumé des simulations de dispersion d'huile en 2D

Dans les simulations de dispersion d'hydrocarbures en 2D, nous avons étendu les simulations numériques directes de vagues déferlantes en 2D à des conditions triphasiques avec la nappe d'hydrocarbures à la surface de l'eau. Nous avons mené une étude paramétrique pour analyser la dépendance quantitative de la taille caractéristique des gouttelettes d'huile par rapport à l'intensité de la vague et à la tension interfaciale. Avec l'augmentation de la course de la plaque d'onde s, l'énergie de surface de la phase huileuse augmente généralement après le déferlement de la vague. L'impact du jet provoque une augmentation rapide de l'énergie de surface de la phase huileuse dans tous les cas, en raison de l'étirement de la nappe d'huile et de la production du splash-up initial. Le premier impact de jet correspond à l'augmentation la plus significative de l'énergie de surface de la phase pétrolière, atteignant 3 à 4 fois l'énergie de surface initiale. Pour les vagues déferlantes plus faibles, l'énergie de surface atteint un maximum après le premier impact de jet et diminue ensuite. Cependant, pour les vagues déferlantes plus fortes, les processus d'éclaboussures ultérieurs augmentent encore l'énergie de surface de la phase huileuse. En outre, nous avons identifié une forte corrélation entre le taux maximal de dissipation d'énergie et le diamètre caractéristique des gouttelettes d_5, où d_5 dépend de $(\gamma/\rho_w)^{3/5}{\epsilon_{max}}^{-2/5}$, ce qui correspond aux prévisions théoriques de mise à l'échelle. Cette recherche ouvre la voie à l'étude de la relation entre le déferlement des vagues et le comportement des nappes de pétrole dans les déversements de pétrole en mer par le biais de simulations numériques, contribuant ainsi à une meilleure compréhension des mécanismes régissant la dispersion du pétrole et l'étalement en surface. Dans la prochaine étape de notre recherche, nous avons l'intention d'extraire les informations sur la taille maximale des bulles d'air à partir de simulations de vagues déferlantes en 2D et de les comparer aux résultats numériques de leurs homologues en 3D. Cette comparaison nous aidera à renforcer notre hypothèse sous-jacente concernant la validité de la taille représentative des gouttelettes dans une vague déferlante en 3D. En outre, l'analyse supplémentaire de la distribution de probabilité de la position de propagation du film d'hydrocarbures sera intégrée dans nos recherches en cours, par exemple la probabilité de trouver des hydrocarbures à une distance donnée après le passage d'une vague déferlante.

Remarques finales

Conclusions

Les déversements d'hydrocarbures se produisent souvent à la surface de la mer dans les régions littorales où la profondeur de l'eau est relativement faible. Le déferlement et la rupture des vagues, qui se produisent lorsque les vagues se propagent vers les zones littorales peu profondes, créent des conditions dynamiques et des taux d'échange d'énergie plus intenses. Les hydrocarbures déversés en mer forment des nappes d'hydrocarbures, qui sont ensuite entraînées dans l'eau et fragmentées en gouttelettes de taille submicronique à plusieurs millimètres par les vagues déferlantes. Ces phénomènes influencent considérablement le devenir du film d'hydrocarbures, notamment son transfert de masse, son échange d'énergie, la distribution des particules et l'évolution spatio-temporelle. Par conséquent, l'étude des caractéristiques des gouttelettes de pétrole résultantes est cruciale pour comprendre le processus de dispersion du pétrole et son interaction avec les vagues déferlantes en eaux peu profondes.

Dans cette étude, nous avons utilisé des simulations numériques directes (DNS) pour étudier la génération, le développement et l'évolution des vagues déferlantes et leur impact sur les nappes de pétrole en reproduisant les vagues expérimentales générées par une plaque à vagues de type piston.

Tout d'abord, nous avons réalisé des DNS bidimensionnels de vagues déferlantes à l'aide du solveur Basilisk afin d'acquérir une compréhension détaillée du processus de déferlement des vagues, y compris l'évolution de la surface libre, de la vitesse et des champs de vorticité. Nous avons étudié l'effet des propriétés du fluide et des conditions initiales sur la dynamique, la cinématique et la dissipation d'énergie dans le processus de déferlement. Une relation quantitative entre la taille de la cavité principale et la hauteur de rupture est présentée sur la base de l'étude de l'influence du nombre de Bond sur l'évolution du jet de retournement. Ceci révèle l'effet de la tension de surface sur le processus de renversement de la crête, qui épaissit la largeur du jet plongeant et raccourcit la distance qui se projette en avant de la vague. La hauteur de la vague résultante peut être estimée sur la base de la théorie simplifiée pour les faiseurs de vagues planes, et nos résultats numériques concordent bien avec ce résultat théorique. Le lien entre la hauteur de la vague et les conditions initiales indique que les vagues peuvent être classées en vagues non déferlantes, déferlantes déversantes et déferlantes plongeantes sur la base du rapport entre la hauteur de la vague et la profondeur de l'eau H/d. L'échelle de dissipation conventionnelle de la théorie de la turbulence est appliquée au processus de déferlement des vagues, ce qui permet d'établir un lien entre le taux de dissipation de l'énergie et le rapport entre la crête de la vague déferlante et la profondeur de l'eau

H_b/d. En tenant compte d'un comportement de seuil, une échelle empirique du paramètre de déferlement est proposée comme $b = a(H_b/d - \chi_0)^n$, où χ_0 = 0,65 représente le seuil de déferlement et n = 1,5 est une loi de puissance déterminée par le meilleur ajustement aux résultats numériques. Les lois d'échelle proposées relient quantitativement la cinématique et la dynamique des vagues déferlantes aux paramètres locaux de la vague et aux conditions initiales, ce qui pourrait être utile pour de futures analyses théoriques.

Nous avons ensuite étendu le DNS bidimensionnel des vagues déferlantes à un cadre tridimensionnel afin de tenir compte des effets tridimensionnels sur le processus de déferlement des vagues et d'évaluer les effets de la viscosité (représentée par le nombre de Reynolds, Re) et de la tension superficielle (représentée par le nombre de Bond, Bo) sur les caractéristiques et la distribution de la taille des bulles générées par le déferlement des vagues. La convergence de la grille des résultats numériques est analysée en considérant trois ensembles de simulations avec l_{max} = 11, 12, et 13, et la convergence numérique est discutée en termes de bilan énergétique, et de distribution de taille des bulles et des gouttelettes produites par le déferlement des vagues. Tous les résultats ont été prouvés comme étant bien convergents, avec aucun changement significatif observé lorsque le niveau maximum de raffinement augmente de 11 à 13. Les résultats numériques semblent en accord raisonnable avec les mesures expérimentales en ce qui concerne la forme de la vague et la hauteur maximale de la vague avant le déferlement. Pendant le temps de déferlement actif, la distribution de la taille des bulles suit $N(r,t) \propto r^{-10/3}$. Un Bo plus élevé conduit à un plus grand nombre de bulles, la différence étant plus prononcée dans la gamme des bulles plus petites. La vitesse verticale varie en fonction du rayon de la bulle, montrant des vitesses de montée variables à différents rayons de bulle sous l'effet de la flottabilité, les bulles les plus grosses montant à la surface libre à une vitesse plus rapide. Pendant la phase de rupture active, la profondeur du panache de bulles reste constante, ce qui correspond à la hauteur initiale de la cavité principale.

Enfin, nous avons étendu les vagues déferlantes bidimensionnelles DNS à des simulations triphasiques en présence de nappes d'hydrocarbures à la surface de l'eau. Grâce à une étude paramétrique, nous avons analysé la dépendance quantitative de la taille caractéristique des gouttelettes de pétrole par rapport à l'intensité de la vague et à la tension interfaciale. Avec l'augmentation de la course de la plaque d'onde s, l'énergie de surface de la phase huileuse augmente généralement après le déferlement de la vague. L'impact du jet provoque une augmentation rapide de l'énergie de surface de la phase huileuse dans tous les cas, en raison de l'étirement de la nappe d'huile et de la production du splash-up initial. Le premier impact de jet correspond à l'augmentation la plus significative de l'énergie de surface de la phase pétrolière, atteignant 3 à 4 fois l'énergie de surface initiale. Pour les vagues déferlantes plus faibles, l'énergie de surface atteint un maximum après le premier impact de jet

et diminue ensuite. Cependant, pour les vagues déferlantes plus fortes, les processus d'éclaboussures ultérieurs augmentent encore l'énergie de surface de la phase huileuse. En outre, nous avons identifié une forte corrélation entre le taux maximal de dissipation d'énergie et le diamètre caractéristique des gouttelettes d_5, où d_5 dépend de $(\gamma/\rho_w)^{3/5}{\epsilon_{max}}^{-2/5}$, ce qui correspond aux prévisions théoriques de mise à l'échelle.

Cette recherche ouvre la voie à l'étude de la relation complexe entre le déferlement des vagues et le comportement des nappes de pétrole dans les marées noires par le biais de simulations numériques, contribuant ainsi à une meilleure compréhension des mécanismes régissant la dispersion du pétrole et l'étalement en surface.

Perspectives

Cette étude établit une relation entre le taux de dissipation et les paramètres des vagues, ce qui permet de prévoir le taux de dissipation des vagues déferlantes en eaux peu profondes. En effectuant une comparaison à l'aide des données disponibles sur la dissipation des vagues déferlantes en eaux profondes et en eaux peu profondes, nous avons constaté qu'il existe une nette discontinuité entre les régimes d'eaux profondes et d'eaux peu profondes, ce qui fait qu'une seule échelle de loi de puissance ne permet pas de saisir les deux ensembles de données. Par conséquent, des efforts supplémentaires devraient être faits pour développer une paramétrisation complète de la rupture. Nous mentionnons que les ensembles de données disponibles résumant la dissipation de la rupture en eau profonde et en eau peu profonde offrent des indications précieuses sur ce problème non résolu. Les données indiquent que le seuil de rupture varie en fonction de la profondeur de l'eau, ce qui suggère la possibilité d'un seuil de rupture variable, en particulier dans le contexte de la transition entre des conditions d'eau profonde et d'eau peu profonde. Une relation de détermination régissant le seuil de rupture pourrait être proposée pour tenir compte des différents régimes de profondeur. Cette question reste à étudier dans le cadre de travaux futurs.

En outre, la simulation de la dispersion du pétrole par des vagues déferlantes à l'aide du solveur Basilisk reconstruit l'interface triphasique à l'aide d'une équation d'advection qui prend en compte les points triples, où chaque phase a une fraction de volume distincte. Cette approche peut généralement rendre compte du transport d'hydrocarbures dû aux vagues déferlantes et de la taille caractéristique des gouttelettes qui y est associée. Cependant, le point triple est instable en utilisant ce schéma d'advection de base parce qu'il ne conserve pas les fractions de volume locales en raison du chevauchement et de la propagation de la zone vide. Par conséquent, le traitement des points triples doit être amélioré et un schéma d'advection modifié est nécessaire pour obtenir une reconstruction précise des interfaces triphasées.

En outre, il reste nécessaire de caractériser l'interaction entre le déferlement des vagues et les mécanismes de dispersion du pétrole. Pour ce faire, nous utiliserons les simulations bidimensionnelles actuelles pour élucider la propagation des nappes d'hydrocarbures au-delà de la distribution des gouttelettes. Plus précisément, nous quantifierons la probabilité de rencontrer du pétrole à une distance donnée en aval d'une vague déferlante. En incorporant des traceurs passifs pour suivre le transport lagrangien de la phase pétrolière, nous déduirons des quantités statistiques supplémentaires qui encapsulent la dispersion spatiale de la distribution de pétrole, révélant potentiellement des aspects moins sensibles aux effets tridimensionnels, tels que la variance de la position des gouttelettes de pétrole.

Enfin, une question non résolue est celle de la distribution de la taille du pétrole brut et des mélanges pétrole-dispersant à des échelles plus petites que la résolution des simulations numériques directes actuelles. Plus précisément, cette étude n'a pas quantifié la distribution des tailles et les mécanismes de formation des gouttelettes de pétrole à ces échelles. Certaines simulations tridimensionnelles ont été lancées pour étudier le processus de dispersion du pétrole, et une analyse préliminaire montre que la trajectoire du pétrole induite par la rupture est généralement similaire à celle observée dans les expériences, ainsi qu'une loi d'échelle pour la distribution de la taille des gouttelettes de pétrole brut. Une analyse plus approfondie des statistiques et des mécanismes impliqués dans la génération de gouttelettes de pétrole est reportée à des études futures.

Arts et Métiers Sciences et Technologies

Shuo Liu

Direct Numerical Simulation of Shallow-Water Breaking Waves Interacted with Oil Slicks

HESAM UNIVERSITÉ

Résumé : Nous utilisons des simulations numériques directes (DNS) pour étudier l'évolution des vagues déferlantes et leur impact sur les nappes de pétrole en reproduisant les ondes expérimentales générées dans un canal en laboratoire. Tout d'abord, nous avons effectué une DNS bidimensionnelle des vagues déferlantes pour analyser en détails le processus de déferlement des vagues. Nous avons montré l'évolution de la taille de la cavité principale en fonction de la tension superficielle, ainsi que celle dutaux de dissipation d'énergie en fonction du rapport entre la crête de la vague déferlante et la profondeur. Nous avons ensuite réalisé des DNS de vagues déferlantes tridimensionnelles pour évaluer les effets de la viscosité et de la tension superficielle sur la distribution de la taille des bulles générées par le déferlement. Enfin, nous avons étendu la DNS bidimensionnelle des ondes déferlantes à des simulations à 3 phases en présence de nappes de pétrole pour analyser la variation de la taille caractéristique des gouttelettes de pétrole en fonction de la force de rupture des vagues et de la tension interfaciale. Cette recherche ouvre la voie à l'étude de la relation entre le déferlement des vagues et le comportement des nappes d'hydrocarbures lors des marées noires.

Mots clés : Vagues déferlantes, Entraînement d'air, Simulation numérique directe, Taux de dissipation d'énergie, Distribution en tailles des bulles, Dispersion d'huile

Abstract : We employ direct numerical simulations (DNS) to investigate the evolution of breaking waves and their impact on oil slicks by reproducing experimental waves generated by a wave plate. First, we performed two-dimensional DNS of breaking waves to gain a detailed understanding of the wave-breaking process. We derived the dependence of the main cavity size on surface tension and the energy dissipation rate on the ratio of the breaking-wave crest to water depth. We then conducted three-dimensional breaking waves DNS to evaluate the effects of viscosity and surface tension on the size distribution of bubbles generated by wave breaking. Finally, we extended the two-dimensional breaking waves DNS to three-phase simulations in the presence of oil slicks to analyze the dependence of characteristic oil droplet size on the wave breaking strength and interfacial tension. This research paves the way for the investigation of the relationship between wave breaking and oil slick behavior in marine oil spills.

Keywords : Breaking waves, Air entrainment, Direct numerical simulation, Energy dissipation rate, Bubble size distribution, Oil dispersion